HERBIPOLENSIS
15
SILVA

The role of the cytoskeleton in platelet production and the pathogenesis of platelet disorders in humans and mice

◆◆◆◆◆

Die Rolle des Zytoskeletts in der Thrombopoese und der Pathogenese von Thrombozytopathien im Menschen und der Maus

Doctoral thesis for a doctoral degree
at the Graduate School of Life Sciences,
Julius-Maximilians-Universität Würzburg,
Section Biomedicine

submitted by

Simon Stritt
from Stühlingen-Lausheim

Würzburg, 2015

Submitted on: _____

Office stamp

Members of the *Promotionskomitee*:

Chairperson:	Prof. Dr. Jörg Schultz
Primary Supervisor:	Prof. Dr. Bernhard Nieswandt
Supervisor (Second):	Prof. Dr. Manfred Gessler
Supervisor (Third):	Prof. Dr. Antje Gohla

Date of Public Defense: _____

Date of Receipt of Certificates: _____

“The Greater Danger For Most Of Us Lies Not In Setting Our Aim Too High And Falling Short; But In Setting Our Aim Too Low, And Achieving Our Mark.”

- Michelangelo

SUMMARY

Platelets are continuously produced from *megakaryocytes* (MK) in the bone marrow by a cytoskeleton-driven process of which the molecular regulation is not fully understood.

As revealed in this thesis, MK/ platelet-specific *Profilin1* (Pfn1) deficiency results in micro-thrombocytopenia, a hallmark of the *Wiskott-Aldrich syndrome* (WAS) in humans, due to accelerated platelet turnover and premature platelet release into the bone marrow. Both Pfn1-deficient mouse platelets and platelets isolated from WAS patients contained abnormally organized and hyper-stable microtubules. These results reveal an unexpected function of Pfn1 as a regulator of microtubule organization and point to a previously unrecognized mechanism underlying the platelet formation defect in WAS patients.

In contrast, *Twinfilin2a* (Twf2a) was established as a central regulator of platelet reactivity and turnover. Twf2a-deficient mice revealed an age-dependent macrothrombocytopenia that could be explained by a markedly decreased platelet half-life, likely due to the pronounced hyper-reactivity of *Twf2a*$^{-/-}$ platelets. The latter was characterized by sustained integrin activation and thrombin generation *in vitro* that translated into accelerated thrombus formation *in vivo*. To further elucidate mechanisms of integrin activation, *Rap1-GTP-interacting adaptor molecule* (RIAM)-null mice were generated. Despite the proposed critical role of RIAM for platelet integrin activation, no alterations in this process could be found and it was concluded that RIAM is dispensable for the activation of β1 and β3 integrins, at least in platelets. These findings change the current mechanistic understanding of platelet integrin activation.

Outside-in signaling by integrins and other surface receptors was supposed to regulate MK migration, but also the temporal and spatial formation of proplatelet protrusions. In this thesis, *phospholipase D* (PLD) was revealed as critical regulator of actin dynamics and podosome formation in MKs. Hence, the unaltered platelet counts and production in *Pld1/2*$^{-/-}$ mice and the absence of a premature platelet release in the bone marrow of *Itga2*$^{-/-}$ mice question the role of podosomes in platelet production and raise the need to reconsider the proposed inhibitory signaling by α2β1 integrins on proplatelet formation.

Non-muscle myosin IIA (NMMIIA) has been implicated as a downstream effector of the inhibitory signals transmitted via α2β1 integrins. Besides Rho-GTPase signaling, also Mg^{2+} and *transient receptor potential melastatin-like 7* (TRPM7) channel α-kinase are known regulators of NMMIIA activity. In this thesis, TRPM7 was identified as major regulator of Mg^{2+} homeostasis in MKs and platelets. Furthermore, decreased $[Mg^{2+}]_i$ led to deregulated NMMIIA activity and altered cytoskeletal dynamics that impaired thrombopoiesis and resulted in macrothrombocytopenia in humans and mice.

ZUSAMMENFASSUNG

Thrombozyten werden kontinuierlich durch einen Zytoskelett-getriebenen Prozess von *Megakaryozyten* (MK) im Knochenmark gebildet. Die zugrunde liegenden molekularen Mechanismen sind jedoch weitestgehend unverstanden.

In dieser Thesis konnte gezeigt werden, dass eine MK/ Thrombozyten-spezifische *Profilin1* (Pfn1) Defizienz eine Mikrothrombozytopenie verursacht, die das Hauptmerkmal des *Wiskott-Aldrich Syndroms* (WAS) im Menschen ist. Die reduzierte Thrombozytenzahl konnte auf eine beschleunigte Entfernung der Thrombozyten aus der Zirkulation sowie deren vorzeitige Freisetzung im Knochenmark zurückgeführt werden. Sowohl Thrombozyten von Pfn1-defizienten Mäusen, als auch von Patienten mit WAS wiesen abnormal organisierte und hyper-stabile Mikrotubuli auf. Die im Rahmen dieser Thesis gewonnenen Ergebnisse zeigen eine unerwartete Funktion von Pfn1 als Regulator der Mikrotubuliorganisation und weisen auf einen bisher nicht erkannten Mechanismus hin, welcher dem Thrombozytenproduktionsdefekt in Patienten mit WAS zugrunde liegt.

Im Gegensatz hierzu konnte *Twinfilin2a* (Twf2a) als zentraler Regulator der Thrombozytenreaktivität und Lebenspanne etabliert werden. Mäuse mit einer Twf2a Defizienz zeigten eine progressive Makrothrombozytopenie, die durch eine stark reduzierte Lebenspanne der Thrombozyten erklärt werden konnte. Letzteres war höchstwahrscheinlich durch eine erhöhte Empfindlichkeit von Twf2a-defizienten Thrombozyten gegenüber von aktivierenden Stimuli bedingt. Die Hyperreaktivität von Twf2a-defizienten Thrombozyten zeigte sich durch eine verlängerte Aktivierung der Integrine und erhöhter Thrombingenerierung *in vitro* sowie beschleunigter Thrombusbildung *in vivo*.

Um die Mechanismen der Integrinaktivierung besser zu charakterisieren, wurden *Rap1-GTP-interacting adaptor molecule* (RIAM)-null Mäuse generiert. Obwohl RIAM eine zentrale Rolle in der thrombozytären Integrinaktivierung zugeschriebenen wurde, konnten keine Defekte in diesem Prozess in RIAM-null Thrombozyten identifiziert werden. Dies führte zu der Schlussfolgerung, dass RIAM für die Aktivierung von β1 und β3 Integrinen in Thrombozyten nicht benötigt wird. Diese Erkenntnisse verändern das gegenwärtige mechanistische Verständnis der Integrinaktivierung in Thrombozyten.

Die *outside-in* Signalgebung durch Integrine und andere Oberflächenrezeptoren reguliert die Migration sowie die zeitliche und räumliche Bildung von *proplatelets* durch MKs. In dieser Thesis konnte gezeigt werden, dass *Phospholipase D* (PLD) ein zentraler Regulator der Aktindynamik und Podosomenbildung in MKs ist. Die normale Thrombozytenzahl und -Produktion in *Pld1/2*$^{-/-}$ Mäusen sowie die fehlende vorzeitige Freisetzung von Thrombozyten

im Knochenmark von *Itga2*$^{-/-}$ Mäusen, stellen die Funktion von Podosomen in der Thrombozytenproduktion in Frage. Ferner zeigen diese Ergebnisse, dass die Rolle der inhibitorischen Signalgebung durch α2β1 Integrine in der *proplatelet*-Bildung noch einmal überdacht werden muss.

Non-muscle myosin IIA (NMMIIA) wird als Effektorprotein im α2β1 Integrinsignalweg angesehen. Neben Signalen, die durch Rho-GTPasen vermittelt werden, regulieren auch Mg^{2+} und die α-Kinase des *transient receptor potential melastatin-like 7* (TRPM7) Kanals die Aktivität von NMMIIA. Im Rahmen dieser Thesis wurde TRPM7 als Hauptregulator der Mg^{2+} Homöostase in MKs und Thrombozyten identifiziert. Darüber hinaus führten erniedrigte intrazelluläre Mg^{2+} Konzentrationen zu einer veränderten NMMIIA Aktivität und Zytoskelettdynamik. Diese Defekte beeinträchtigten die Thrombopoese und verursachten eine Makrothrombozytopenie im Menschen und der Maus.

TABLE OF CONTENTS

1. INTRODUCTION

1.1. Megakaryocytes

With an average diameter of up to 50-100 µm, *megakaryocytes* (MKs) are the largest cells within the *bone marrow* (BM). Their main function is the production of blood platelets, which maintain the vascular integrity but also play roles in other biological processes. During proplatelet formation, a mature MK is thought to release up to 5000 platelets *in vivo*.[1,2] Under *in vitro* conditions, however, these values are markedly lower as for example only 10% of human MKs (up to 30% for mouse MKs) form proplatelet protrusions in culture, which yields on average 10-100 platelets per $CD34^+$-derived MK.[3]

1.1.1. Megakaryopoiesis

Like all cells of the hematopoietic system, MKs are derived from multipotent *hematopoietic stem cells* (HSC) in the BM. During their maturation, MKs migrate from the osteoblastic niche, which is enriched in collagen I and fibronectin, to the vascular niche close to BM sinusoids, rich in collagen IV, laminin, *von Willebrand-factor* (vWF) and fibrinogen.[4-6] Besides the structural information, these niches are defined by gradients of chemokines such as *interleukin* (IL) 1, IL3, IL6, IL11, c-kit ligand, and *thrombopoietin* (Thpo), calcium and oxygen.[6-9] The key cytokine for megakaryopoiesis, Thpo, and its receptor c-Mpl (*myeloproliferative leukemia virus oncogene*), however, were rather shown to stimulate the generation of MKs by HSC than to regulate MK maturation.[7] In addition, mature MKs were recently shown to regulate HSC quiescence through the secretion of *platelet factor 4* (PF4/ *chemokine (C-X-C motif) ligand* (CXCL) 4) and *transforming growth factor-β1* (TGF-β1), which both negatively regulated HSC cell cycle activity.[10,11]

During their maturation, young MKs undergo several replication cycles without terminal cytokinesis, a process called endomitosis.[12] Polyploidization is enabled through *Runt-related transcription factor 1* (RUNX1)-mediated silencing of *non-muscle myosin heavy chain* (*MYH*) 10 expression. The latter is required for cytokinesis and its inhibition facilitates the switch from mitosis to endomitosis.[13-15] Due to the unique endoreplication process, the multilobed nucleus of a mature MK can contain up to 128 sets of chromosomes (128 N).[16] MK polyploidy is thought to enable the cytoplasmic expansion of mature MKs through an increased protein synthesis.[17] During this phase, platelet-specific granules and the *invaginated*, formerly *demarcation membrane system* (IMS/DMS), are formed.[18,19] The cytoplasmic invaginations, leading to the establishment of the IMS, require highly structured and complex changes in the cytoskeleton of MKs. These cytoskeletal rearrangements are exerted by actin

filament assembly via the *Wiskott-Aldrich-syndrome protein* (WASp)/ *WASp family verprolin-homologous protein* (WAVE) pathway or the *cell division control protein 42* (Cdc42) *interacting protein 4* (CIP4) and are essential to provide sufficient amounts of membranes for platelet formation.[19,20] Furthermore, in a more recent study, Eckly and colleagues showed that some of the membranes of the IMS are derived from the Golgi apparatus and not only from the plasma membrane as previously thought.[21]

1.1.2. Thrombopoiesis

Similar to MK differentiation, migration of MKs towards BM sinusoids is tightly regulated by an elaborate system of chemokines, such as *stromal cell-derived factor-1α* (SDF1α/ CXCL12), *angiopoietin 1* (Ang-1), and Thpo.[22-25] Recently, Niswander and colleagues provided further evidence for an important role of SDF1α and its downstream signaling through the CXCR4 receptor in MK migration, as intravenous administration of SDF1α increased the association of MKs with the endothelium of BM sinusoids and circulating platelet numbers.[23]

MK migration and platelet release strongly depend on cytoskeletal rearrangements, but also on the degradation of *extracellular matrix* (ECM) components, to facilitate the penetration of the basal membrane of the endothelial barrier.[26] Schachtner *et al.* and others have recently shown that MKs form podosomes that mediate the degradation of ECM components through the secretion of *matrix metalloproteases* (MMP) and may serve MK migration.[26-28] Besides MKs, also macrophages, dendritic cells and osteoclasts have been shown to form podosomes.[28] Structurally, podosomes consist of a *filamentous actin* (F-actin)-rich core region (Fig. 1), where the actin remodeling-promoting proteins *actin-related protein* (Arp) 2/3, WASp, *tyrosine kinase substrate with five Src-homology* (SH) *3 domains* (Tks5) and *ArfGAP with SH3 domain, ankyrin repeat and pleckstrin homology* (PH) *domain 1* (ASAP1) can be found (Fig. 1). The core is surrounded by a ring structure consisting of integrins and associated proteins such as vinculin, *talin-1* (Tln-1), paxillin, zyxin, α-actinin and *non-muscle myosin IIA* (NMMIIA).[29,30] Certain conditions further induce the organization of podosome superstructures such as clusters, belts or rosettes.[26,27] Despite a similar structural organization of invadopodia and podosomes, they differ in their lifetime. While podosomes persist for up to 12 minutes, invadopodia could be observed for more than 10 hours. Of note, focal adhesions persist on average for up to one hour.[31] Although podosomes mainly consist of integrins, actin and the respective accessory proteins, microtubules were shown to play a critical role in regulating podosome dynamics and half-life.[32,33] For example, treatment of macrophages with nocodazole (a toxin that induces microtubule disassembly) inhibited podosome formation, which was restored after washout of the toxin.[32,33]

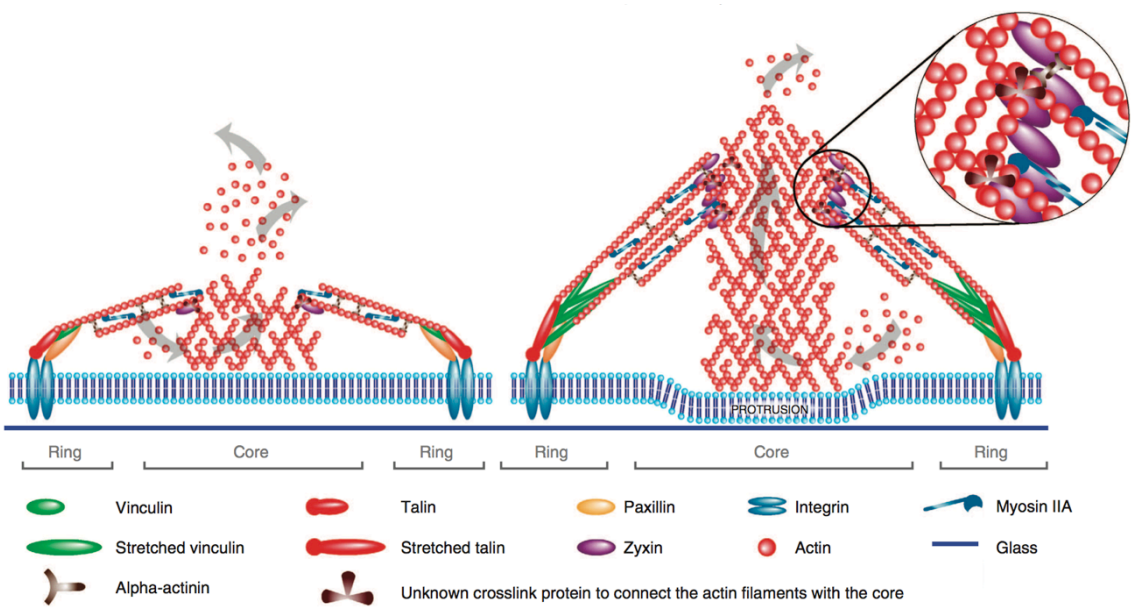

Figure 1 | Schematic model of podosome organization. Podosomes are F-actin-rich protrusions that are characterized by a *filamentous actin* (F-actin)-rich core region and a peripheral ring structure. Podosomes serve cell migration by mediating the degradation of components of the extracellular matrix. While the core mainly consists of F-actin and actin remodeling-promoting proteins such as *actin-related protein* (Arp) 2/3, *Wiskott-Aldrich syndrome protein* (WASp), *tyrosine kinase substrate with five Src-homology* (SH) *3 domains* (Tks5) and *ArfGAP with SH3 domain, ankyrin repeat and pleckstrin homology* (PH) *domain 1* (ASAP1), integrins and associated proteins such as vinculin, talin, paxillin, zyxin, α-actinin and *non-muscle myosin IIA* (NMMIIA) predominate in the ring structure. (taken from van den Dries *et al. Nat Commun* 2013)[34]

Furthermore, microtubules were implicated to stabilize and thereby extend the half-life of podosomes in macrophages and osteoclasts.[33,35] However, in osteoclasts disruption of microtubules did not interfere with podosome formation, but resulted in a reduced organization of podosomes into belts.[36] Despite controlling podosome superstructure and stability, microtubules may in addition also serve the transport of MMPs and integrins to the core.[29]

1.1.2.1. Phospholipase D in podosome formation

Podosome formation and thus actin rearrangement is tightly regulated by various cytoskeletal proteins, such as Arp2/3, WASp, *phospholipase* (PL) D1/2, *profilin* (Pfn) 1 and *Ras-homologue-guanine triphosphatases* (Rho-GTPases) that become activated downstream of lipid signaling cascades.[37-40] Among others, the latter process involves PLD, an intracellular enzyme that catalyzes the conversion of the membrane lipid phosphatidylcholine into choline and *phosphatidic acid* (PA) in response to various stimuli such as hormones, growth factors or neurotransmitter, but also downstream of integrins.[37,41] Moreover, PLD has been reported to interfere with actin dynamics and to play a role in cell migration and phagocytosis by recruiting specific actin-remodeling molecules to the leading edge of cells through the spatially and temporally regulated generation of PA.[38,42] Further evidence for a crucial role of PLD in

actin dynamics was recently provided by Ali *et al.* showing that macrophages deficient in PLD display abnormal actin rearrangements, resulting in reduced numbers of irregularly-shaped podosomes and defective phagocytic capacity.[43] Even though platelets of mice lacking either or both PLD isoforms (PLD1 and PLD2) have been extensively studied, the role of PLD in megakaryo- and thrombopoiesis, in particular during podosome formation of MKs has not been investigated.[44-46]

Located next to BM sinusoids, mature MKs start to form protrusions, so-called proplatelets that reach into the vessel lumen (Fig. 2). Podosomes are also thought to be critical for proper proplatelet formation, as MKs lacking WASp are unable to form podosomes on collagen I, which is considered to account for the premature release of platelets into the BM compartment of *Wasp*$^{-/-}$ mice.[26,27]

1.1.2.2. Proplatelet formation

Proplatelet formation starts at a single spot of the MK membrane from which a pseudopod is extended. This pseudopod tapers into a thin tubule, the proplatelet shaft (2-4 µm diameter) that contains a central microtubule bundle, intermitted by bulbous swellings that contain actin.[47,48] MK polarization is a prerequisite for the directed formation of proplatelet protrusion and Zhang *et al.* revealed that endothelial *sphingosine 1-phosphate* (S1p) and its receptor on MKs (S1pR1) are critical for guided proplatelet-formation into BM sinusoids.[49] Once a proplatelet has passed the endothelial barrier, the dynein-dependent sliding of antiparallel microtubules serves the transport of organelles and granules from the MK body to the sprouting platelets, besides promoting the elongation of proplatelet protrusions.[50-52] In contrast to the microtubule-driven protrusions, actin-dependent branching of existing protrusions increases the number of proplatelet tips and consequently the number of preplatelets that are shed-off by the circulating blood.[48,53,54] The critical role of the actin cytoskeleton for platelet production was further revealed in studies using knockout mouse models for actin-associated proteins.[55,56]

Besides initial reports on proplatelet formation *in situ* using histology and *transmission electron microscopy* (TEM), recent advances in intravital microscopy allowed real time visualization of this process in the BM of living animals.[49,57,58] Although shear forces prevailing in the circulation have been implicated in this process, the precise mechanisms by which larger fragments, so-called preplatelets, are released from proplatelet tips, still remain elusive (Fig. 2).[40,58-60] Recent findings, however, point to a critical role of sphingosine kinase 2-mediated reorganization of the microtubule cytoskeleton, as MKs deficient in this protein show an

altered microtubule stability and cannot sufficiently release preplatelets from proplatelet tips *in vivo* (conference communication of Prof. Steffen Massberg).[61] The shed preplatelets were shown to circulate as beaded or as barbell-shaped platelet pairs and were larger in size than 'normal' platelets.[62,63] These findings supported earlier observations where it was speculated that final platelet maturation occurs in the circulation.[62,63]

Besides the classical lineage commitment that is characterized by the maturation-associated endoreplication and expression of MK markers, very recently a new lineage of *diploid platelet-forming cells* (DPFCs) was identified as the source of the very first platelets in the developing mouse embryo.[64,65] It is still unclear, whether the beforehand-described mechanisms of proplatelet formation by MKs similarly apply for platelet release by DPFCs. Moreover, further studies are required to decipher the role of DPFC-derived platelets in embryogenesis.

1.1.2.3. Rupture-type platelet production

Calculations of platelet consumption and production in humans and mice suggested that platelet production via the classical process of proplatelet formation is sufficient to maintain platelet count in normal physiology.[58,66,67] Furthermore, it was recently shown that aged platelets that have lost sialic acid from their surface are cleared from the circulation by hepatocytes. Thereby, desialylated platelets are recognized by the Ashwell-Morell receptor and signaling-induced phagoycytosis in turn stimulates Thpo production by hepatocytes, thus regulating platelet biogenesis in normal physiology.[68] However, these mechanisms may not be efficient enough to produce sufficient platelet numbers under conditions of increased platelet consumption, such as inflammation/ infection, immune thrombocytopenia, or traumatic blood loss. Nishimura *et al.* recently identified an IL-1α-induced rupture-type mechanism for platelet production that yields 20-fold higher numbers of released platelet particles as compared with the classical mechanism of proplatelet formation during the same period of time (Fig. 2).[69,70] This provides for the first time an explanation of how MKs can maintain platelet mass equilibrium and quickly restore platelet numbers under pathological conditions associated with increased platelet turnover.

The mechanism of rupture-type platelet formation strongly resembles key features of *Fas-ligand* (FasL)-induced apoptosis, including activation of caspase-3, disorganization of the cytoskeleton, and membrane blebbing. However, in stark contrast to typical FasL-induced apoptosis, rupture-type platelet formation is relatively quick (within an hour versus >80 min) and results in the release of a large number of *phosphatidylserine* (PS)-negative particles. These particles carry an increased content of β1-tubulin, which is reminiscent of disor-

ganized α- and β-tubulin expression, and has not been described for apoptotic cells (Fig. 2). The increased formation of membrane blebs was accompanied by a reduction in MK membrane stiffness that could be reverted by caspase inhibitors. The activation of caspase-3 represents a central step in rupture-type platelet release, as caspase-3-deficient MKs could not use this alternative pathway for platelet production.[69,70]

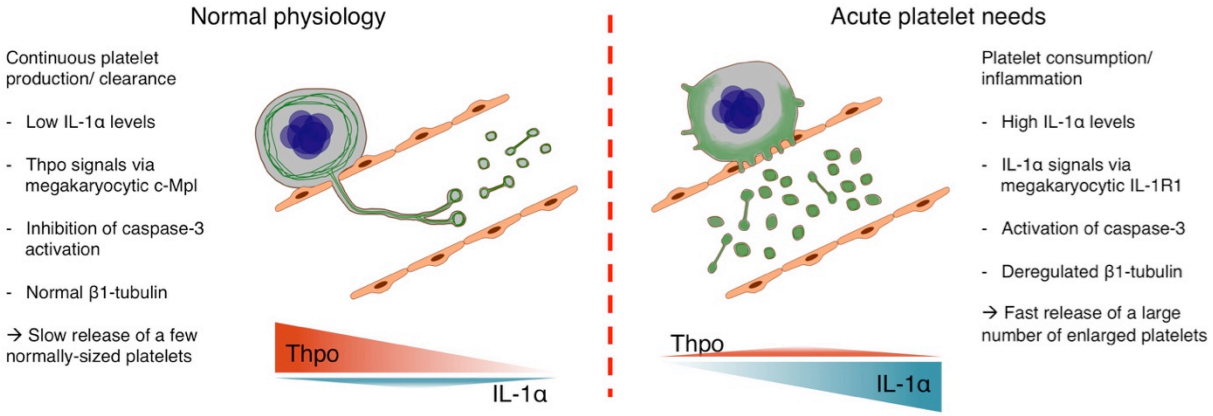

Figure 2 | **Current models of platelet production.** In normal physiology (left panel), platelets are continuously produced by *megakaryocytes* (MKs) via the classical process of proplatelet formation.[40,49,58] Under these conditions, *thrombopoietin* (Thpo) drives megakaryopoiesis by signaling through its receptor c-Mpl, but Thpo is dispensable for proplatelet formation, which is a cell-autonomous process and presumably regulated by the vascular niche.[22-25,71,72] Inhibition of caspase-3 and a well-organized orchestration of microtubule dynamics (green) are prerequisites for proper proplatelet formation and protrusion into *bone marrow* (BM) sinusoids, where preplatelets are released and further mature within the circulation.[14,48,58] Proplatelet formation is a rather slow process with low yields of platelets per period of time, but is sufficient to compensate for the continuous loss of aged platelets. Under conditions of increased platelet loss or consumption (right panel), e.g., as a result of excessive blood loss or in the setting of infection/inflammation, this mechanism might not be sufficient to ensure appropriate platelet supply. Under these conditions, *interleukin-1α* (IL-1α) levels increase rapidly and trigger rupture-type platelet formation via the IL-1R1 receptor on MKs. IL-1α signaling leads to a deregulated expression and organization of β1-tubulin (green) as well as to the activation of caspase-3, which in turn leads to a reduction of MK membrane stiffness. Together, these processes lead to the formation of multiple membrane blebs that are predominantly released into BM sinusoids to quickly replenish platelet numbers.[69] (Nieswandt & Stritt *J Cell Biol* 2015)[70]

1.2. Platelets

With an average size of 2-3 µm and a discoid shape, platelets represent the smallest corpuscular component of the blood. In a healthy human individual 0.15-0.30 x 10^6 and in mice up to 1.0 x 10^6 platelets per µL blood are present in the circulation, respectively. Although these numbers are already quite high, platelets in the circulation only represent two third of the overall platelet population with one third being reversibly sequestered in the spleen. The average life span of a circulating platelet is 10 days in humans and 5 days in mice, respectively. Aged platelets are cleared from the circulation by macrophages in the reticuloendothelial system of the spleen and liver.

1.2.1. Platelet morphology

Platelets are delimited by a plasma membrane that contains embedded *glycoproteins* (GP) and several invaginations, the so-called *open canalicular system* (OCS), remnants of the endoplasmic reticulum represented by the *closed-channel dense tubular system* (DTS) and a highly organized cytoskeleton that preserves cellular integrity and shape.

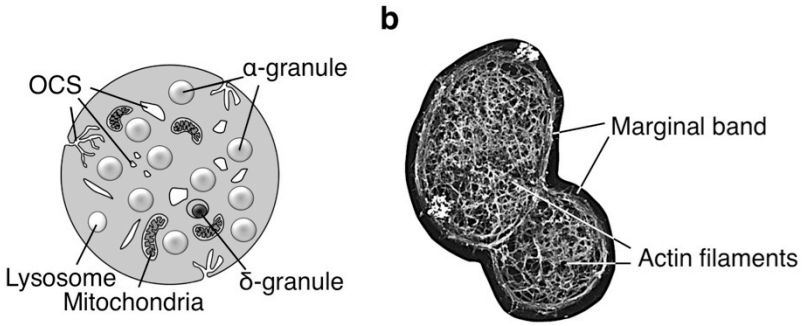

Figure 3 | Platelet morphology. (**a**) Ultrastructural characteristics of platelets. (modified from Fitch-Tewfik & Flaumenhaft *Front Endocrinol* 2013)[73] (**b**) Cytoskeletal organization of platelets (Image by Prof. John Hartwig, Boston, USA).

The OCS is thought to serve three major functions: (1) the uptake of extracellular components and release of granule contents;[74] (2) a membrane reservoir, which is required for filo- and lamellipodia formation and (3) storage site for glycoproteins (Fig. 3a).[75] In contrast, the DTS is primarily believed to serve as a Ca^{2+} reservoir.[76]

In addition, platelets harbor numerous organelles such as α- and dense-granules, lysosomes, peroxisomes, glycogen stores, and mitochondria (Fig. 3a).[76-79] α-granules (40-80 per platelet with an average size of 200-500 nm) are the most abundant granules in the platelet cytoplasm (Fig. 3a) and contain proteins necessary for platelet adhesion (e.g. fibrinogen, fibronectin, vWF), *coagulation factors* (FV, FXIII), PF4, P-selectin or *platelet-derived growth factor* (PDGF), but also glycoproteins such as αIIbβ3 integrins. Dense-granules are smaller (200-300 nm), less numerous (Fig. 3a), but also contain a large number of hemostatically active but inorganic molecules such as catecholamines, *5-hydroxytryptamine* (5-HT, serotonin), *adenosine diphosphate* (ADP), *adenosine triphosphate* (ATP) and Ca^{2+}.[80]

1.3. The cytoskeleton and its implication in platelet production and function

The cytoskeleton consists of a highly interconnected structure of filamentous polymers and associated proteins that enables a eukaryotic cell to cope with deforming forces, allows active transport of intracellular cargos and facilitates the change of cell shape, which is required for movement. This is achieved by integrating specific functions of a multitude of cytoplasmic proteins and organelles. Although the name cytoskeleton indicates that it is a stable and rigid structure it is a highly adaptive and dynamic network, whose components are in a constant equlibrium of assembly and disassembly. This network consists of three major types of filaments: microtubules, intermediate, and actin filaments (microfilaments).[81,82]

1.3.1. Microtubule cytoskeleton

The tubulin cytoskeleton consists of different α- and β-tubulin isoforms that, in their GTP-bound state, form heterodimers and can be further assembled into long and polarized (plus-(β-subunit is exposed) and minus-end (α-subunit is exposed)) protofilaments. Thirteen protofilaments can further associate laterally and thereby build microtubules, which present as long (up to 50 µm in length) hollow cylinders with an average diameter of 24 nm.[83,84] Microtubule polymerization is initiated at a *microtubule-organizing center* (MTOC) that contains a *γ-tubulin-ring complex* (γ-TuRC).[85] The presence of γ-tubulin within the marginal band of platelets suggests that the γ-TuRC also acts as nucleation core for the assembly of microtubules in these cells.[86] Microtubules exist in a steady state of assembly and disassembly termed dynamic instability. In general, assembly can occur at both, the plus- and minus-end even though it occurs much faster at the plus-end.[87] Hydrolysis of the GTP bound to the β-subunit of the polymerized heterodimer decreases the filament stability and leads to microtubule depolymerization. Once the microtubule tip (plus-end) contains GDP-tubulin a rapid depolymerization occurs, which is termed 'catastrophe' that can be rescued by the addition of new GTP-tubulin heterodimers.[88] However, microtubule stability can also be regulated via post-translational modifications such as acetylation, detyrosination, polyglutamylation or polyglycylation.[89] The addition of an acetyl-residue to lysine 40 of the α-tubulin subunit is known to indicate stable microtubules. Acetylation is mostly mediated via the *α-tubulin N-acetyltransferase 1* (α-TAT1), while deacetylation is mainly accomplished by *histone-deacetylases 6/5* (HDAC5/6) and the *nicotinamide adenine dinucleotide* (NAD)-dependent deacetylase *sirtuin-2* (SIRT2).[90-93] Similarly, removal of the C-terminal tyrosine from the α-tubulin subunit leads to the exposure of the preceding C-terminal glutamate, another indicator for stable microtubules. The enzyme mediating the detyrosination still needs to be identified, while the enzyme mediating the addition of a tyrosine, the *tubulin-tyrosine ligase* (TTL) is already known.[89,94] Polyglutamylation and polyglycylation can occur on both the α- and β-tubulin subunits and are mediated via *TTL-like family member enzymes* (TTLLs) that add a γ-linked glutamine or glycine to one or more of the five C-terminal glutamates.[89]

The temporal and spatial coordination of microtubule dynamics is essential as microtubules do not only maintain the structure of the cell, but are also of critical importance for cell migration, mitosis, meiosis, developmental processes and for the transportation of intracellular cargos. The latter is mediated towards the plus-end via kinesins and towards the minus-end via dyneins.[95]

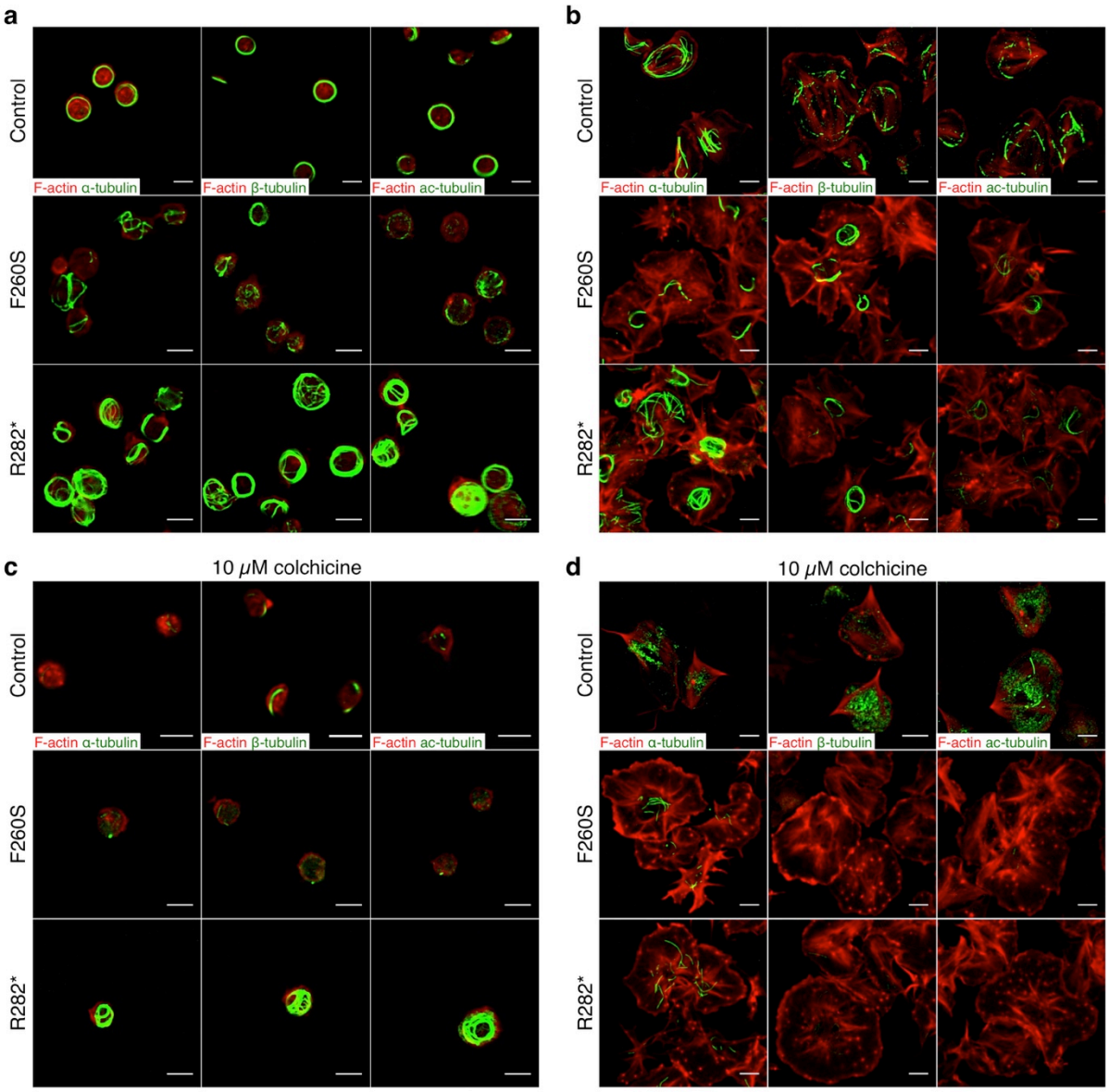

Figure 4 | Variants in *TUBB1* cause distinct alterations of the microtubule cytoskeleton. (**a, b**) Resting (**a**) or on fibrinogen (15 min, 100 µg µL^{-1}) spread platelets (**b**) from healthy controls and patients with a F260S or R282* variant, respectively, were fixed, stained for the indicated proteins and analyzed by confocal microscopy. (**c, d**) Platelets were pretreated (30 min) with 10 µM colchicine and allowed to adhere to poly-L-lysine-coated coverslips (**c**) or to spread (15 min, 100 µg µL^{-1}) on fibrinogen (**d**). Subsequently, platelets were processed for immunostaining and analyzed by confocal microscopy. Scale bars, 3 µm. Experiments were performed in the lab of Dr. Paquita Nurden in Pessac, France (Stritt *et al.*, unpublished observations).

In platelets, microtubules are organized into the characteristic marginal band that consists of 8-12 microtubule coils in the platelet periphery that maintains the discoid shape of resting platelets (Fig. 3b). Consequently, microtubule disassembly, e.g. by incubation below 16°C or treatment with microtubule destabilizing toxins such as colchicine or nocodazole leads to a spherical platelet shape.[78] The critical role of microtubules for maintaining a discoid platelet shape was further confirmed by a knockout mouse model lacking the hematopoietic lineage-specific β_1-tubulin that displayed a macrothrombocyopenia with spherical platelets with a

markedly reduced number of discontinuous microtubule coils within the marginal band.[96] Similarly, in humans a single point mutation changing phenylalanine 260 to a serine causes hereditary macrothrombocytopenia with spherical platelets, a reduced number of microtubules within the marginal band and a bleeding diathesis (Fig. 4).[97] However, this is not true for all patients with variants in *TUBB1*, as patients with a R282* mutation display macrothrombocytopenia, with hyper-aggregable platelets that contain an increased number of aberrantly organized microtubules with an altered stability (Fig. 4).

1.3.2. Actin cytoskeleton

The actin cytoskeleton is involved in many cellular processes such as cell division, exo- and endocytosis, cell motility, cell polarization and the formation of cell protrusions. F-actin is composed of monomeric, *globular actin* (G-actin) molecules, of which in mammals, three isoforms have been identified: the mainly muscle specific α-actin and the ubiquitously expressed β- and γ-actin isoforms.[82] Due to the structure of G-actin molecules, assembly results in polarized filaments, with a barbed (+) and pointed (-) end. The typical helix structure is achieved by a 166° rotation of two parallel F-actin strands, which yields a F-actin microfilament with an average diameter of 7 nm (Fig. 5). Actin filament nucleation can either occur *de novo* mediated by formin family members such as the *mammalian diaphanous 1 protein* (mDia1, DIAPH1) or from pre-existing filaments through the Arp2/3 complex.[98-100] Either activation of formins by small GTPases or binding of *adenomatous polyposis coli* (APC) can overcome the inhibitory effects of Pfn1 and *capping proteins* (CP) on spontaneous actin nucleation.[98,99] Secondly, the Arp2/3 complex (consisting of Arp2, Arp3 and ARPC1-ARPC5) can be activated by binding of WASp family members via their *central/acidic* (CA) region, while the *verproline homology motif* (V) of WASp associates with an actin monomer and the Arp2/3 complex binds to existing actin filaments.[100] The assembly or growth of actin filaments is accelerated by high-energy G-actin monomers, which are bound to ATP, leading to stabilization of the monomers.[101-103] Upon addition to the growing filament, ATP is rapidly hydrolyzed into ADP and *inorganic phosphate* (P_i). Dissociation of the γ-phosphate is a rather slow process, but results in destabilization and is an indicator for the age of the filaments (Fig. 5).[104]

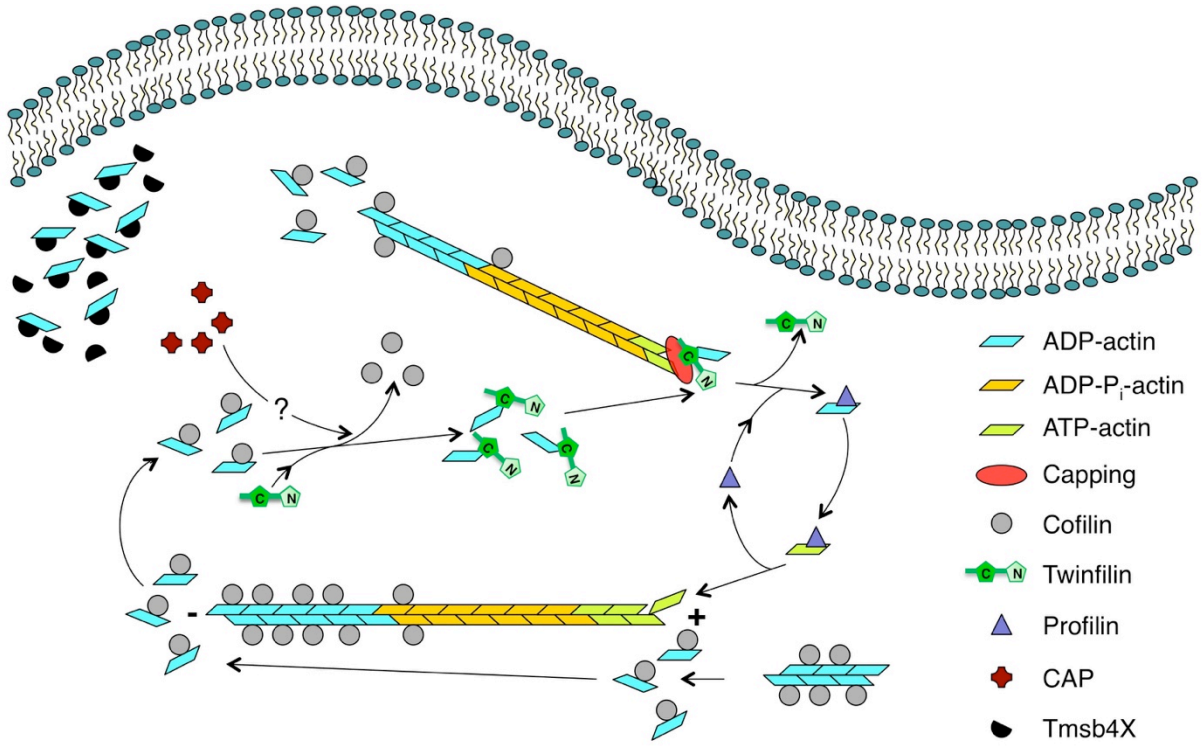

Figure 5 | Schematic overview of a proposed model of actin dynamics (not all involved proteins are depicted). Actin filaments consist of G-actin monomers, which can be divided into three energetic states: ATP-G-actin (bright green), ADP-Pi-G-actin (orange) and ADP-G-actin (light blue). Cofilin (grey) severs and depolymerizes ADP-G-actin from actin filaments. Severing results in free barbed ends (+), on the one hand, providing a new target available for polymerization and on the other hand, providing a new target for disassembly at the newly provided pointed end (-). Twinfilin (light and dark green) competes with cofilin in binding to ADP-G-actin monomers and since twinfilin has a higher affinity for ADP-G-actin, this interaction is preferred. Moreover, twinfilin was shown to interact with heterodimeric capping protein (red). Profilin (dark blue) is a nucleotide exchange factor for G-actin monomers replenishing the pool of high-energy ATP-G-actin bricks for the assembly of actin filaments. Furthermore, twinfilin, profilin as well as cofilin were shown to interact with *phosphatidylinositol-4,5-bisphosphate* (PIP_2, in pink), which results in a down-regulation of the sequestering function of twinfilin and profilin on G-actin monomers and the severing activity of cofilin.[105-107]

Platelets contain over two million actin molecules, which are present in a dynamic monomer-polymer equilibrium.[108,109] Approximately 40% of the total actin monomers are present in the filamentous form in a resting platelet and constitute 2,000-5,000 actin filaments.[110] The remaining 60% monomeric actin is stored in stoichiometric 1:1 complexes with *β4-thymosin* (Tmsb4X), Pfn1, *Twinfilin1/2a* (Twf1/2a), and other actin sequestering proteins and becomes incorporated into filaments upon platelet activation (Fig. 5).[111,112] The actin filaments of resting platelets are highly cross-linked and form a stiff network through numerous actin cross-linking molecules such as *filamin A* (FlnA), spectrins or α-actinin.[113,114] FlnA recruits and positions numerous proteins including *Ras homolog gene family, member A* (RhoA), *Ras-related C3 botulinum toxin substrate 1* (Rac1), *p21/Cdc42/Rac1-activated kinase* (PAK1) and many others. However, the association of FlnA with the cytoplasmic tail of GPIbα was shown to be

of particular importance for the structural organization of resting platelets as more than 90% of FlnA forms complexes with GPIbα.[108,115]

1.3.2.1. Regulation of actin dynamics

The temporal and spatial dynamics of the well-organized cytoskeletal architecture that maintains platelet shape and facilitates the elaborate process of platelet production via proplatelet formation or rupture-type platelet release by MKs (Fig. 2) needs to be tightly regulated. Besides others, the actin nucleating and assembly promoting proteins such as WASp, Arp2/3 or formins, actin monomer sequestering proteins such as Tmsb4X, Pfn1 or Twf1/2a and actin filament severing proteins like cofilin or *cyclase-associated proteins* (CAP) work in concert to control this highly dynamic network (Fig. 5).

1.3.2.2. Profilin

In 1977, Pfn was first identified in calf spleen, but shortly afterwards it was found in all investigated tissues and species.[116] During evolution, multicellular organisms seem to have increased the number of *Pfn* genes or improved the transcriptional regulation, thereby enabling the control of the expression pattern and expanding the functions of Pfns.[117] In mammals, 4 different Pfn isoforms have evolved, partially with a tissue-specific expression pattern. Besides the well-described ubiquitously expressed Pfn1, the brain-specific Pfn2 (with two subisoforms Pfn2a and 2b), and more recently, the mainly testis-specific Pfn3 and 4 were identified.[116,118-121] Remarkably, the sequence homology of Pfns between different species is rather low, however, the structure and functions of the proteins are highly conserved.[122] Despite its small size of only 15 kDa, Pfn harbors, in addition to its actin-binding domain, a domain for binding of phosphatidylinositides, with a strong preference of *phosphatidylinositol-4,5-bisphosphate* (PIP_2) and a *poly-L-proline* (PLP) binding domain, which is required for its interaction with other ligands (Fig. 6).[105,123-125]

Pfn was first identified as a small actin-binding protein (molar ratio of 1:1) and was initially thought to function as an ATP-G-actin sequestering protein, thus interfering with F-actin assembly.[116] This point of view changed dramatically over time, with the observation of Pfn's nucleotide exchange factor activity on G-actin monomers, transforming the low energy ADP-G-actin into polymerization-capable ATP-G-actin monomers.[126] Moreover, Pfns were shown to regulate the addition of new monomers to growing actin filaments. Accordingly, the hitherto mainly sequestering function was replaced by a polymerization-promoting function.[127,128] Further support for this observation is provided by the cellular concentration of Pfn, which is only sufficient to sequester approximately 20% of cellular actin monomers.[129] In conclusion,

Pfns are required to replenish the pool of ATP-G-actin, thus providing new bricks for the assembly of actin filaments. *Profilactin* (profilin bound to ATP-G-actin) can associate with free barbed ends and incorporate new monomers into growing actin filaments (Fig. 5).

As mentioned above, besides its actin-binding domain, Pfn is endowed with a domain that binds to phosphoinositides (preferentially PIP_2), which in turn affects actin and ligand binding, as well as PLCγ1 activity.[105,123,130,131] Beside G-actin and PIP_2, Pfn interacts with a large number of other proteins that contain a PLP stretch (Fig. 6). Among these are for example proteins involved in membrane trafficking, such as synapsin, clathrin, and dynamin, or proteins present in focal contacts, such as *mammalian enabled orthologue* (Mena) or *vasodilator-stimulated phosphoprotein* (VASP).[123,132,133] Furthermore, Pfn is involved in the regulation of signaling pathways of small Rho-GTPases, e.g. as shown by the interaction with N-WASp, *WASp-interacting protein* (WIP), downstream of Cdc42 or mDia1, a known effector of RhoA (Fig. 6).[134-136] The essential role of Pfn in actin dynamics and consequently in development, has been revealed in *Drosophila melanogaster* and mice.[137,138] In *Drosophila*, deletion of *Pfn1* resulted in late, in mice in early embryonic lethality thus indicating an essential biological function in mitosis and signaling.[138] Since the *Pfn1* knockout mouse displayed embryonic lethality, no study on the phenotype of the *Pfn1* knockout in an adult mammalian animal has been reported to date.

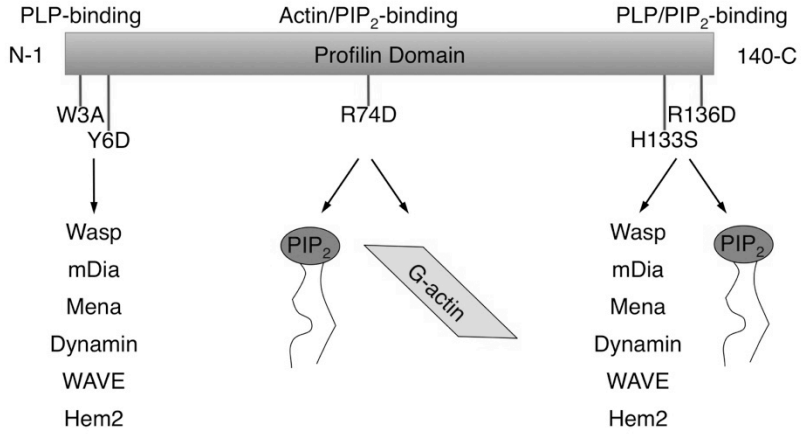

Figure 6 | **Schematic domain architecture and interacting proteins of profilin** (not all interaction partners are depicted). Profilin consists of a N- and C-terminal *poly-L-proline* (PLP) binding domain, a central actin binding site with an overlapping binding site for phosphatidylinositides, exhibiting a strong preference for *phosphatidylinositol-4,5-bisphosphate* (PIP_2) and another PIP_2-binding site that overlaps with the PLP-binding domain in the C-terminus. The N- and C-terminal PLP-binding sites allow the association with the numerous interaction partners of profilin, such as the *Wiskott-Aldrich syndrome protein* (WASp), *mammalian Diaphanous* (mDia), *mammalian Enabled* (Mena), dynamin, *WASp family verprolin-homologous protein* (WAVE) or *hematopoietic protein 2* (Hem2).[123] Binding of profilin to PIP_2 on the one hand prevents phospholipase-mediated hydrolysis to *inositol-1,4,5-triphosphate* (IP_3) and *diacylglycerol* (DAG) and on the other hand inhibits the association with actin monomers. W3A, Y6D, R74D, H133S, and R136D highlight point mutants of profilin that specifically disrupt the function of single domains.[139,140]

1.3.2.3. Twinfilin

The mechanisms by which G-actin monomers are transported from the pointed end of F-actin filaments to places of rapid actin turnover remained enigmatic until Twf was described. Human Twf was first identified in 1994 and initially thought to represent the catalytic domain of the atypical *protein kinase* (PK) C.[141-143] Twf homologues have been identified in human, mouse, and *Caenorhabditis elegans*, but not in plants.[144] With a molecular weight of approximately 40 kDa and consisting of two *actin depolymerizing factor-homology* (ADF-H) domains connected by a short linker region and an additional C-terminal tail, Twf also belongs to the class of small actin-binding proteins (Fig. 5).[145,146] Although the sequence homology of Twf's ADF-H domains and ADF/cofilin is rather low, their crystal structures are almost superimposable.[144,147] While unicellular organisms and lower animals, such as *Saccharomyces cervesiae* or *Drosophila melanogaster* only have one Twf isoform, in mammals the ubiquitously expressed Twf1 and Twf2a, as well as the muscle-specific Twf2b have been identified.[148-150]

Although Twf contains two ADF-H domains, it interacts with G-actin in a molar ratio of 1:1 with an approximately 10-fold higher affinity for ADP-G-actin compared to ATP-G-actin.[107,144] Nevertheless, both ADF-H domains are able to bind G-actin.[149,151] Twf was shown to inhibit actin filament growth by two distinct mechanisms: on the one hand, Twf inhibits barbed end growth by capping of actin filaments barbed ends (Fig. 5) and on the other hand, it inhibits pointed end growth by sequestering G-actin monomers, thus reducing the pool of free monomers. [144,152] Moreover, Twfs interact with heterodimeric CPs and at least in yeast, this interaction was reported to be important for its proper function in actin dynamics (Fig. 5).[153] Of note, binding of CPs to actin filament barbed ends inhibits both depolymerization as well as the addition of new monomers. However, the Twf-CP interaction is thought to localize ADP-G-actin monomers close to places of rapid actin turnover, thus providing new bricks for the growth of actin filaments.[149,153,154] Similarly, upon ADF/cofilin-mediated dissociation of G-actin monomers from actin filaments, Twf is thought to compete with ADF/cofilin in binding of these monomers.[148,151,155] In addition, Twf also interacts with PIP_2 and this interaction in turn inhibits its actin monomer sequestering function.[106]

In vivo, Twf-deficiency in yeast resulted in mild alterations in the cortical actin patches and a defective budding pattern.[144] However, the combination of a cofilin or Pfn functional mutant with a Twf deficiency in yeast resulted in synthetic lethality.[144] In contrast, *Drosophila melanogaster* mutants lacking Twf displayed a reduced body size, were less active, exhibited a retarded development and a *rough eye* phenotype. Most prominent was the aberrant, often bend and rough bristle morphology, which was due to an uncontrolled polymerization of actin.[156] In 2011, Nevalainen *et al.* generated a global Twf2a-deficient mouse line (*Twf2a*$^{-/-}$)

and studied the morphology and histology of different organs. However, they could not find major differences as compared to the corresponding controls, which led to the conclusion that Twf2a is dispensable for mouse development.[150] Nevertheless, they hypothesized that the functionally redundant Twf1 isoform might compensate for the lack of Twf2a.[149,150] Similarly, a MK- and platelet-specific Twf1-deficient mouse did not reveal any defects in MK maturation, thrombopoiesis, platelet function, or actin assembly thus further suggesting that the two Twf isoforms can compensate for each other (Stritt *et al.*, unpublished observations).

1.3.2.4. Transient receptor potential melastatin-like 7 channel

Besides actin filament assembly, also its contraction and organization into superstructures like stress fibers are prerequisites for cell movement. NMMIIA, a member of the myosin-motor superfamily, is an actin-binding/ cross-linking protein that exerts contractile forces, and thus constitutes an important regulator of cytoskeletal reorganization, intracellular trafficking and cell locomotion. Members of the myosin superfamily mediate these effects by generating tension, via sliding and movement of actin filaments.[157] NMMIIA as well as the other myosin family members consist of two heavy chains (230 kDa), two *regulatory light chains* (RLCs; 20 kDa) that serve the regulation of NMMIIA activity and two structure-stabilizing *essential light chains* (ELCs; 17 kDa).[158] The activity of NMMIIA is regulated via serine/threonine phosphorylation of the heavy and light chains.[159-161] While activating phosphorylations occur on Ser19 and Thr18 of the ELCs, phosphorylations on the NMMIIA heavy chain C-term either prevent the formation or lead to the dissociation of myosin cross-linked actin filaments. Besides PKC (Ser1916) and casein kinase II (Ser1943), NMMIIA heavy chain can be phosphorylated by the *transient receptor potential melastatin-like 7* (TRPM7) channel on Thr1800, Ser1803 and Ser1808 (Fig. 7).[159,162,163] Moreover, it has recently been shown that the intracellular magnesium concentration ($[Mg^{2+}]_i$) also contributes to the regulation of actomyosin contractility by modulating the affinity of NMMIIA to actin and the ADP-release from NMMIIA.[164] Of note, Mg^{2+} is the second most abundant cation in mammalian cells and its concentration is critical for many physiological processes including development, cell proliferation, migration, protein synthesis and consequently needs to be tightly regulated.[165]

The ubiquitously expressed TRPM7 channel (213 kDa), consists of six transmembrane domains and a C-terminal atypical serine threonine α-kinase domain (Fig. 7). Four TRPM7 subunits are though to constitute one channel pore by forming a superstructure consisting of their transmembrane domains five and six.[166-169] In normal physiology, the channel pore conducts small inward currents via the influx of divalent Mg^{2+} and Ca^{2+}, but also trace metal cations (Zn^{2+}, Ni^{2+}, Ba^{2+} and Co^{2+}) according to their concentration gradients. However, upon

membrane depolarization when membrane potentials become positively charged, monovalent intracellular cations are rectified outward through TRPM7.[170,171]

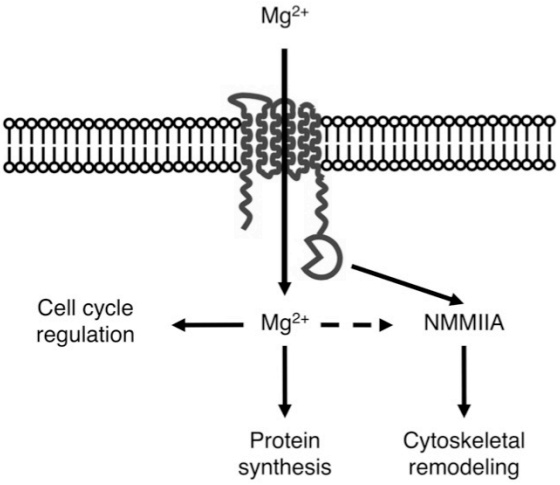

Figure 7 | Schematic model of TRPM7 function. The *transient receptor potential melastatin-like 7* (TRPM7) channel is covalently fused to an α-kinase domain and interferes with cytoskeletal dynamics by both phosphorylation of *non-muscle myosin heavy chain IIA* (NMMIIA) and through the regulation of $[Mg^{2+}]_i$. Besides this, $[Mg^{2+}]_i$ interferes with many cellular processes including development, cell proliferation, migration and protein synthesis.

TRPM7 is ubiquitously expressed with the highest protein levels in the heart, bone, liver and fatty tissue. TRPM7 channel and kinase domain, but not its kinase activity are critical for embryonic development.[172-174] Overexpression or increased channel activity of TRPM7 promoted cell death, thus highlighting the importance of tightly regulated TRPM7 expression levels.[175,176] In contrast, knockdown or cell-specific TRPM7 knockout approaches resulted in impaired cytoskeletal organization, cell migration, proliferation, polarization and survival. In agreement with this, Liu *et al.* described impaired cell polarization and undirected cell locomotion in the developing *Xenopus laevis* embryo in the absence of TRPM7, presumably caused by a dysregulation of the small Rho-GTPases Cdc42 and Rac1, but not RhoA.[177] Together, these defects could partially be explained by increased NMMIIA-mediated contractility of the actin cytoskeleton.[173,177-186] Interestingly, several variants of NMMIIA similarly altered the contractility of the actomyosin complex in MKs, thereby interfering with proplatelet formation in humans and mice.[187] During megakaryopoiesis NMMIIA activity is suppressed by phosphorylation of its C-terminus, enabling MK polyploidization and ultimately proplatelet formation. However, for proper platelet fission and sizing, NMMIIA needs to be re-activated under shear stress in the circulation.[187,188] Although both α-kinase and channel activity of TRPM7 have been proposed to regulate cytoskeletal dynamics, channel activity alone was sufficient to restore cell polarization, morphology and migration.[177,184,189] Consequently, the differential role of the TRPM7 channel versus kinase activity in the regulation of the cytoskeleton still remains unclear.

In line with these findings, the expression of TRPM7 has also been positively correlated to tumor size and tendency of breast cancer cells to metastasize.[186] Likewise, TRPM7 has also been implicated in infract progression during ischemic stroke by inducing a Ca^{2+} overload in

neurons and promoting neuronal cell death.[190] In addition, recent studies by Du *et al.* and Sah *et al*., revealed a role of TRPM7 in the development of atrial fibrillation in mice by regulating myofibroblast dedifferentiation and cardiac automaticity by controlling the expression of *hyperpolarization activated cyclic nucleotide gated potassium channel 4* (HCN4).[179,180,191]

1.3.3. The actin cytoskeleton in the pathogenesis of platelet disorders

The importance of the cytoskeleton for platelet production and function is impressively demonstrated by the clinical symptoms of patients suffering from the *Wiskott-Aldrich-syndrome* (WAS) or *MYH9-related disorders* (MYH9-RD). WAS is an X-linked inherited disorder characterized by microthrombocytopenia, immunodeficiency, eczema and an increased risk of autoimmune disorders and cancer (Online Mendelian Inheritance in Man; Accession number #301000).[192] WAS is caused by mutations within the *WAS* gene that encodes the WAS protein and which was reported to be involved in the signal transduction from membrane receptors to the actin cytoskeleton. The WAS protein was shown to regulate the activity of the Arp2/3 complex, thereby enabling the nucleation of new actin filaments.[193] Consequently, WASp is an important regulator of actin assembly and is constitutively associated with WIP in resting and activated platelets to prevent its degradation.[194-196] The severe phenotype found in these patients underscores the important role of the actin cytoskeleton for the proper function of platelets, but also other cell types. Remarkably, WASp-deficient mice resembled only partially the WAS phenotype. WASp-deficient mice displayed a premature platelet release into the BM, but only a moderate thrombocytopenia with an unaltered platelet size.[27,197] Similarly, a patient carrying a mutation in the *WIP* gene or WIP-deficient mice that also lack WASp in platelets have an unaltered platelet size and suffer from thrombocytopenia partially caused by increased platelet clearance.[196,198,199] The reason for the discrepancy in platelet phenotypes between WAS patients and WASp-deficient mice remains enigmatic and the molecular link between WAS mutations and microthrombocytopenia is unknown.

While a reduced number and size of platelets are the central feature of the WAS, MYH9-RDs are characterized by macrothrombocytopenia with less but bigger platelets, inclusion bodies in leukocytes (Döhle-bodies) and a moderate bleeding tendency.[200] In addition to the hematological symptoms, some patients suffering from MYH9-RD develop hearing loss, cataracts, and renal failure. MYH9-RDs are caused by mutations within the *MYH9* gene on chromosome 22 in humans and chromosome 15 in mice and cause four overlapping syndromes: the May-Hegglin anomaly, Epstein syndrome, Fechtner syndrome, and Sebastian platelet syndrome.[200-202] Of note, while mutations within the NMMIIA head domain mainly affect actin filament sliding and ATPase activity, variants in the tail region impair the protein structure

and actomyosin filament formation.[157] It is rather unlikely that *MYH9*-associated macrothrombocytopenia is attributed to impaired protein expression, since a considerable amount of mutant NMMIIA is found in cells of humans suffering form MYH9-RD, even though often clustered into small aggregates in leukocytes. This suggests that variants in *MYH9* rather affect NMMIIA activity than expression levels, thereby exerting dominant negative effects on thrombopoiesis.[203,204] In line with this, MKs from patients and mutant mice suffering from MYH9-RD displayed markedly reduced numbers of proplatelet extensions with less tips of increased size. Furthermore, treatment with the NMMIIA ATPase inhibitor blebbistatin could not phenocopy MKs from patients with MYH9-RD, but rather supported the notion of an increased NMMIIA activity, since it could restore proplatelet formation of patient MKs.[205,206] Excitingly, similar to the WAS syndrome, MK-specific *Myh9*-deficient knockout mice did not fully reproduce the findings on the patient MKs, showing an increased percentage of proplatelet forming MKs with an reduced number of enlarged proplatelet tips.[56] In contrast, knockin mice, carrying point mutations found in the NMMIIA head and tail domain of patients, recapitulated key features of MYH9-RD also with regards to MK biology.[205]

1.4. The role of platelets in thrombus formation

In normal physiology, platelets never come into contact with components of the thrombogenic ECM such as collagens or laminins. However, upon injury or pathological alterations (e.g. rupture of an atherosclerotic plaque) of the endothelial barrier ECM components become exposed to the flowing blood, activate platelets and allow platelet adhesion. In detail, platelet activation and thrombus formation can be divided into three distinct steps: (I) tethering, (II) activation/ granule release and (III) firm adhesion/ platelet aggregation (Fig. 8). Tethering of platelets occurs under intermediate or high shear forces (1,000-10,000 s^{-1}), which are predominantly present in arterioles or stenosed arteries. During this process, platelets are decelerated by the transient interaction of platelet GPIb-V-IX and vWF immobilized on collagen leading to ‘rolling’ of the platelets (Fig. 8).[207-209] The important role of the vWF-GPIb-complex interaction for thrombus formation is reflected by the severe macrothrombocytopenia and bleeding disorder found in patients suffering from the Bernard-Soulier syndrome, caused by absent or dysfunctional GPIb-V-IX complexes. Interestingly, besides mediating platelet adhesion, the GPIb-complex can also induce intracellular signaling leading to a weak activation of αIIbβ3 integrins.[210] The underlying signaling network is still not completely understood, however, there is evidence that among others, PLD1 may play a role therein.[44]

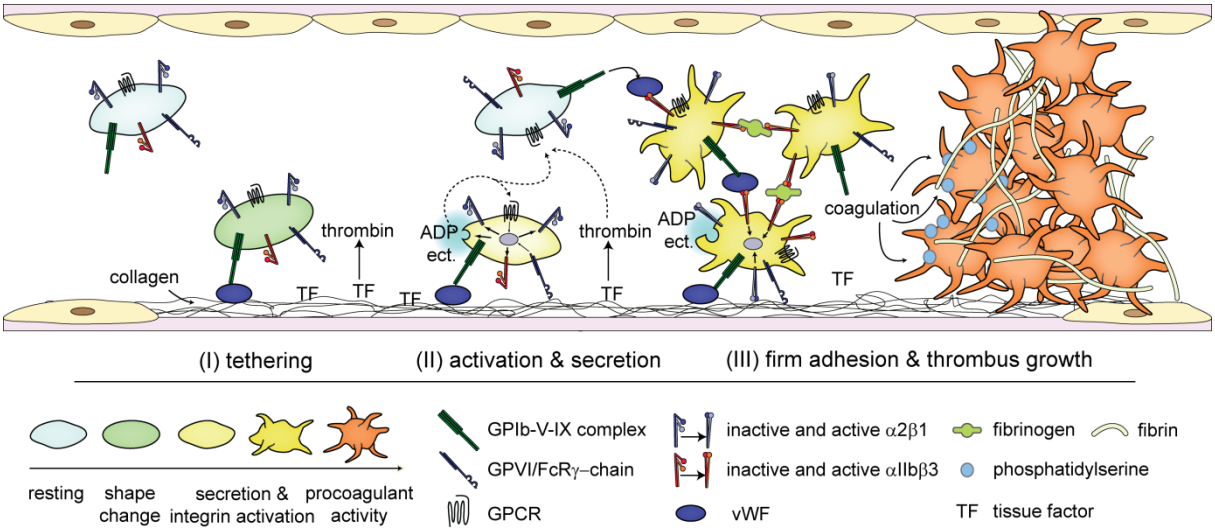

Figure 8 | Schematic overview of thrombus formation. Upon endothelial damage, components of the *extracellular matrix* (ECM) become exposed and under high shear flow platelets tether by the interaction of *glycoprotein* (GP) Ib-V-IX and collagen-bound *von Willebrand factor* (vWF). The interaction of GPVI with collagen leads to the activation of αIIbβ3 and α2β1 integrins and to the release of second wave mediators such as *adenosine diphosphate* (ADP), thromboxane A_2, etc. Locally produced thrombin (triggered by *tissue factor* (TF) and exposure of phosphatidylserine (light blue)) contributes to the cellular activation. Finally, integrins mediate firm adhesion through binding to ECM components and aggregation of platelets via the interaction of fibrinogen and activated αIIbβ3 integrins. (kindly provided by Martina Morowski)[211]

Of note, the affinity of the GPIb-complex towards vWF is too weak to mediate firm adhesion and rather serves the deceleration and localization of platelets in close proximity to the vessel wall, which is reflected by the 'rolling' of platelets and enables the interaction of the platelet GPVI receptor with collagens of the ECM (Fig. 8).[212]

1.4.1. (Hem)immunoreceptor tyrosine-based activation motif signaling in platelets

Cross-linking of the central activating platelet receptor GPVI by collagens induces downstream signaling via the Src family kinases Fyn- and Lyn that phosphorylate the non-covalently associated intracellular *immunoreceptor tyrosine-based activation motif* (ITAM)-bearing *Fc receptor* (FcR) γ chain.[212-214] Fyn- and Lyn-mediated phosphorylation of the YxxL-motifs leads to the recruitment and activation of the *spleen tyrosine kinase* (Syk), that in turn triggers the activation of other downstream signaling molecules, such as the *linker of activated T-cells* (LAT), the *SH2 domain-containing leukocyte protein of 76 kDa* (SLP-76) or *growth factor receptor-bound protein 2* (Grb2), ultimately culminating in the activation of effector molecules such as PLCγ2 or *phosphoinositide-3 kinase* (PI3K).[212-214] Activated PLCγ2 hydrolyses PIP_2 into *inositol-1,4,5-triphosphate* (IP_3) and *diacylglycerol* (DAG). Binding of IP_3 to the IP_3 receptor on the membranes of the endoplasmatic reticulum induces the release of Ca^{2+}. The *stromal interaction molecule 1* (STIM1) serves as a sensor for the Ca^{2+} levels within the

store and induces *store operated Ca^{2+} entry* (SOCE) through *Ca^{2+} release-activated calcium channel protein 1* (Orai1) upon store depletion.[215] The increase in cytosolic Ca^{2+} and locally generated DAG work in concert to activate PKC and *Ca^{2+}-dependent DAG-regulated guanine nucleotide exchange factor I* (CalDAG-GEFI). While CalDAG-GEFI and PI3K play important roles in integrin activation, PKCs are involved in platelet spreading, granule release and contribute to the activation of CalDAG-GEFI (Fig. 9).[216] The hemITAM bearing *C-type lectin receptor 2* (CLEC-2) utilizes a similar signaling pathway, involving Src family kinases and Syk that culminates in the activation of PLCγ2.[213,217,218]

1.4.2. G-protein-coupled receptor signaling in platelets

The temporally and spatially controlled generation and release of second wave mediators leads to the recruitment of additional platelets into the growing thrombus. Among the released second wave mediators, ADP binds to the $P2Y_1$ and $P2Y_{12}$ receptors that activate G_q and G_i, respectively, whereas *thromboxane A_2* (TxA_2) and thrombin stimulate the TxA_2 (TP) and *protease-activated receptors (*PAR) 1/3 or PAR3/4 receptors and signal mainly through G_q and $G_{12/13}$ (Fig. 9).[219-221] Signaling through *G-protein-coupled receptors* (GCPR) leads to amplification of platelet activation by inducing the generation of TxA_2 and release of ADP and ATP. Signaling through G_q culminates in the activation of PLCβ isoforms, generation of IP_3 and DAG via hydrolysis of PIP_2, which subsequently leads to the increase of the cytoplasmic Ca^{2+} concentration, activation of PKC and consequently to the activation of integrins and granule release (Fig. 9 and 10).[221,222] Furthermore, very recently, G_q signaling was shown to be critical for the proper phosphorylation of *protein kinase B* (Akt) downstream of G_i-signaling.[223] In contrast, activation of $G_{12/13}$ family members leads to the activation of Rho-GEFs that activate RhoA and culminates in increased phosphorylation of *myosin light chain* (MLC) through *RhoA kinase* (ROCK)-mediated inhibition of the myosin phosphatase. Activated MLC in turn induces the reorganization of the platelet cytoskeleton, known as shape change.[224] Moreover, stimulation of the G_i-coupled $P2Y_{12}$ receptor inhibits adenylyl cyclase activity and activates PI3K, which in turn generates phosphatidylinositol-3,4,5-triphosphate that activates multiple downstream effectors such as Akt and ultimately leads to integrin activation.[225,226] Interestingly, the epinephrine receptor (α_{2A}) couples to G_i-type G_z proteins and inhibits adenylyl cyclase activity (Fig. 9). However, stimulation of G_z alone is not sufficient to induce platelet activation, but potentiates other responses.[227]

In contrast, activation of thrombin depends on the coagulation cascade. Thrombin catalyzes the conversion of fibrinogen to fibrin and acts as a potent activator of platelets. Its generation can be initiated by two distinct pathways (intrinsic and extrinsic coagulation pathway), both of

which culminate in the cleavage and activation of the proenzyme prothrombin (FII) to thrombin.[228,229]

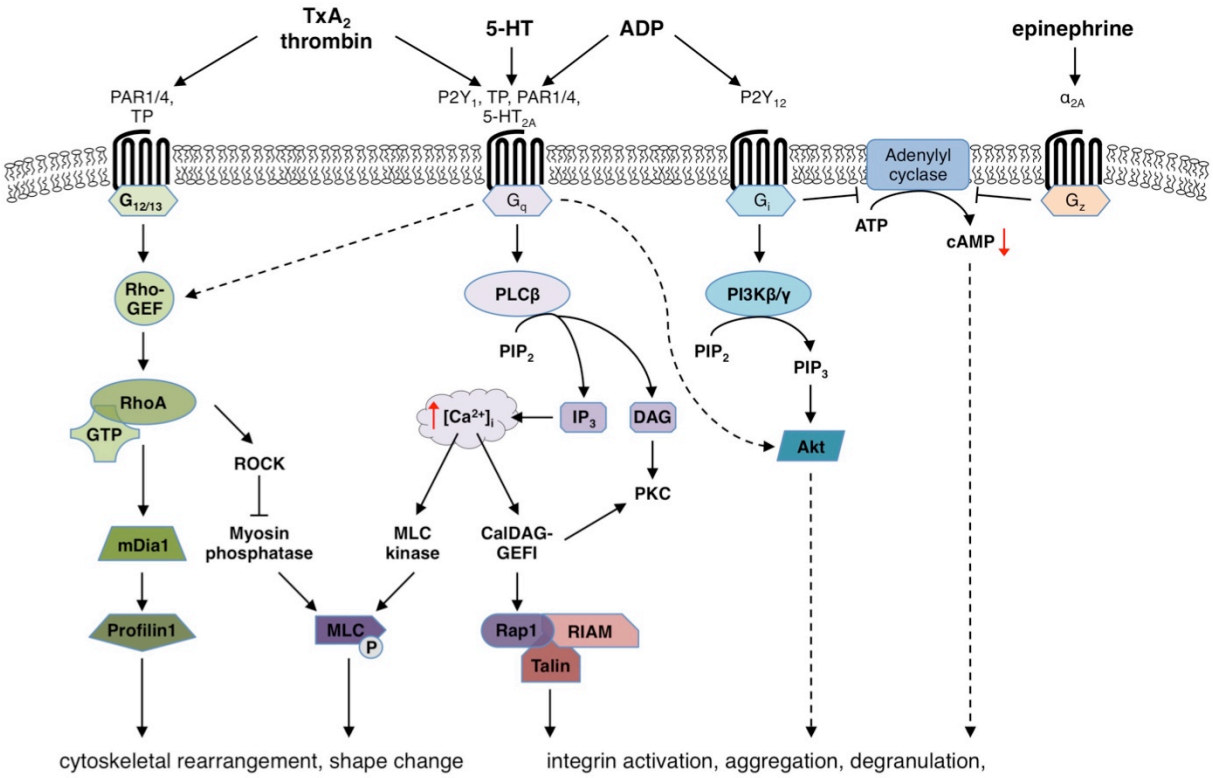

Figure 9 | **G-protein-coupled receptor signaling in platelets.** Second wave mediators of platelet activation in combination with locally produced thrombin, signal through *G-protein-coupled receptors* (GPCR), such as the *thromboxane A2* (TxA_2) receptor TP, $P2Y_{12}$ *adenosine diphosphate* (ADP)-receptor, *serotonin* (5-HT)-receptor 2A, adrenergic α_{2A}-receptor or the *protease-activated receptors 1-4* (PAR1-4) on platelets. GPCR-signaling via $G_{12/13}$, G_q, G_i and G_z protein mediates cytoskeletal rearrangements, shape change as well as integrin activation, aggregation and degranulation. *Rho-specific guanine nucleotide exchange factor* (Rho-GEF); *guanosine triphosphate* (GTP); *mammalian diaphanous 1 protein* (mDia); *RhoA kinase* (ROCK); *myosin light chain* (MLC); *phosphorylation* (P); *phospholipase Cβ* (PLCβ); *phosphatidylinositol-4,5-bisphosphate* (PIP_2); *inositol-1,4,5-triphosphate* (IP_3); *diacylglycerol* (DAG); *protein kinase C* (PKC); *Ca^{2+}-dependent DAG-regulated GEF I* (CalDAG-GEFI); *Ras-proximate-1* (Rap1); *Rap1-GTP-interacting adaptor molecule* (RIAM); *phosphoinositide-3-kinase* (PI3K); *phosphatidylinositol-3,4,5-trisphosphate* (PIP_3); *protein kinase B* (Akt); *adenosine triphosphate* (ATP); *cyclic adenosine monophosphate* (cAMP). (modified from Offermanns *Circ Res* 2006)[221]

Finally, GPVI and PAR signaling act synergistically to fully activate platelets and mediate firm adhesion mainly through binding of α2β1 integrins to collagen and αIIbβ3 integrins to fibrinogen and collagen-bound vWF. Platelet aggregation is mainly mediated through binding and cross-linking of activated αIIbβ3 integrins to fibrinogen. The activation of platelets in general is characterized by a marked rearrangement of the actin and tubulin cytoskeleton, resulting in the formation of membrane protrusions, so-called filopodia and lamellipodia.[230]

1.4.3. Platelet integrin activation

Platelet adhesion and aggregation is essential for hemostasis, however, uncontrolled aggregation responses in injured vessels can cause life threatening disease states such as myocardial infarction or stroke.[231,232] Heterodimeric receptors of the β1 and β3 integrin families are crucially involved in these processes.[233] Platelets express three different β1 and two β3 integrin heterodimers, serving the adhesion to different ECM components, such as collagen (α2β1 integrin), fibronectin (α5β1 integrin), laminin (α6β1 integrin), vitronectin (αvβ3 integrin) or fibrinogen and vWF (αIIbβ3 integrin).[215]

In resting platelets, integrins are expressed in a low-affinity state, but in response to cellular activation they shift to a high-affinity state and efficiently bind their ligands, most notably components of the ECM and other receptors.[234-236] This so-called inside-out activation is triggered by the binding of Tln-1 and kindlins to NPYX-motifs at the intracellular tail of the integrin β-subunit.[237-239] The mechanisms of Tln-1 recruitment to integrins have been extensively studied and the small CalDAG-GEFI-activated GTPase *Ras-proximate-1* (Rap1) and its downstream effector *Rap1-GTP-interacting adaptor molecule* (RIAM) have been implicated therein (Fig. 9 and 10).[240-243]

1.4.3.1. Rap1-GTP-interacting adaptor molecule

RIAM is a member of the *Mig-10/RIAM/Lamellipodin* (MRL) family, which display a characteristic domain architecture consisting of a N-terminal coiled-coil region, a central *Ras-association* (RA) and PH domain and a C-terminal proline-rich domain.[244,245] Due to its interaction with the tryptophan-tryptophan domain of *amyloid beta (A4) precursor protein binding, family B, member 1* (Apbb1), it was initially termed *Apbb1-interacting protein* (Apbb1ip).[246] On protein level, RIAM was shown to be broadly expressed in many tissues and cell types.[238,245,247-249] Subsequently, RIAM was identified as a Rap1-GTP-binding protein that is involved in β1 and β2 integrin activation in T-cells (Fig. 10).[245]

The presence of a RA and an adjacent PH domain suggests that RIAM serves as a proximity detector for Rap1-GTP and PIP_2. In agreement with this, RIAM was found to bind to the C-terminal rod domain of Tln-1, a cytoskeletal protein that associates with β3 integrin tails, which constitutes one of the very final steps of integrin activation.[237,238] A very recent study by Yang and colleagues revealed a novel RIAM binding site on the N-terminal Tln-1 head, which is important for the association with β3 integrin tails.[250] Binding of RIAM to the Tln-1 head inhibits binding of RIAM to the Tln-1 tail, which in turn would sterically block the association of the Tln-1 head with integrin tails. Consequently, masking of the Tln-1 head by RIAM in-

creases the association of Tln-1 with integrin tails.[250] Studies on the platelet αIIbβ3 integrin in cell lines revealed that RIAM, as well as its Rap1 and Tln-1 binding sites are required for αIIbβ3 integrin activation.[240,241] Together, RIAM's RA domain leads to Tln-1 recruitment to membrane microdomains rich in PIP_2, which increases the binding of Tln-1 to the β integrin subunit and ultimately leads to integrin activation (Fig. 10).[242]

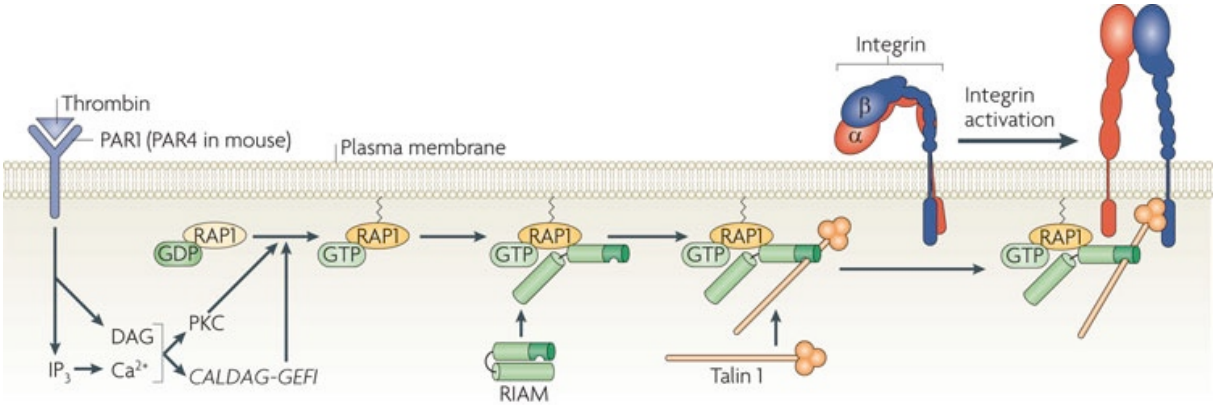

Figure 10 | Mechanism of Talin-1 recruitment to β integrin tails by RIAM. Platelet stimulation and signaling through (hem)ITAM- and/or G_q-coupled receptors (depicted) culminates in the activation of *phospholipase* (PL) C isoforms and consequently in the generation of *inositol-1,4,5-triphosphate* (IP_3) and *diacylglycerol* (DAG) via hydrolysis of *phosphatidylinositol-4,5-bisphosphate* (PIP_2). Subsequently, IP_3 leads to an increase in the cytoplasmic Ca^{2+} concentration and together with DAG work in concert to activate *protein kinase* (PK) C and *Ca^{2+}-dependent DAG-regulated guanine nucleotide exchange factor I* (CalDAG-GEFI). CalDAG-GEFI transforms *Ras-proximate-1* (Rap1) to an active GTP-bound state, which in turn recruits its effector, *Rap1-GTP-interacting adaptor molecule* (RIAM). RIAM binds its binding partner *talin-1* (Tln-1) and recruits it to PIP_2-rich microdomains at the plasma membrane. This enables Tln-1 binding to the β integrin tail and Tln-1-induced activation of integrins. Similarly, kindlin-3 is indispensable for integrin activation, however, the molecular mechanisms and the precise role of Tln-1 and kindlin-3 remain elusive. (taken from Shattil *et al. Nat Rev Mol Cell Biol* 2010)[251]

It is important to note that the above-described findings on the function of RIAM were mostly generated by knockdown and overexpression studies in cancer cell lines *in vitro*, which may not represent the optimal model. In support of this, a recent study by Hernandez-Varas and colleagues revealed that knockdown of RIAM in melanoma cells resulted in only mildly impaired activation of β1 integrins and diminished, but not abolished Tln-1 recruitment.[252]

In addition, RIAM was also shown to interact with Ena/VASP-family members and Pfn, thereby linking RIAM to the actin cytoskeleton.[245] In support of this, overexpression of RIAM increased lamellipodia formation and cell spreading, while RIAM knockdown resulted in reduced F-actin levels and impaired cell migration and invasion.[245,248,252]

2. AIM OF THE STUDY

Despite recent advances in intravital microscopy and the real time visualization of proplatelet formation by MK within the BM of mice, the process of thrombopoiesis as well as the proteins involved in its regulation are still poorly understood. Proplatelet formation requires tightly regulated, highly structured rearrangements of the MK cytoskeleton. Pfn1 and Twf2a belong to the class of small actin-binding proteins and were shown to promote (Pfn1), or inhibit actin assembly (Twf2a). Nevertheless, the role of Pfn1 and Twf2a in megakaryopoiesis and thrombopoiesis are entirely unknown. Therefore, the investigation of the biological roles of Pfn1 and Twf2a in platelet production and function were the first aims of this study.

It is still unclear how MKs reach the vascular niche, where proplatelet formation and release occurs. It is believed that either MKs or their precursors migrate from the osteoblastic to the vascular niche. Functional integrins, the ability to degrade components of the ECM as well as actomyosin contractility are all prerequisites for cell locomotion. RIAM was shown to be critical for platelet αIIbβ3 integrin activation in different *in vitro* cell culture approaches, yet no studies using genetic RIAM knockouts were reported. Thus, to elucidate the role of RIAM in platelet integrin activation, using the first knockout mouse model was a further aim of this thesis.

Integrins are central components of podosomes, which are thought to be critical for the extension of proplatelet protrusions from MKs across the endothelial barrier. PLDs were revealed as important mediators of podosome formation in macrophages. Another aim of this dissertation was to assess the role of PLD1/2 in podosome formation and the requirement of podosomes for proplatelet formation.

Finally, actomyosin contractility is critical for migration, proplatelet formation and platelet abscission within the circulation. Mg^{2+} has been implicated as a regulator of actomyosin contractility and platelet reactivity by controlling Ca^{2+} influx and the affinity of NMMIIA to actin. Interestingly, the regulatory network controlling $[Mg^{2+}]_i$ in MKs and platelets is entirely unknown. TRPM7, a Mg^{2+} and Ca^{2+} permeable cation channel that regulates NMMIIA activity via its α-kinase domain could be involved in MK and platelet Mg^{2+} homeostasis. Hence, in the course of this thesis, the role of TRPM7 in the regulation of MK Mg^{2+} homeostasis as well as the role of $[Mg^{2+}]_i$ in the orchestration of cytoskeletal rearrangements in MKs were analyzed.

3. MATERIALS AND METHODS

3.1. Materials

3.1.1. Chemicals

A23187	AppliChem (Darmstadt, Germany)
Acetic acid	Roth (Karlsruhe, Germany)
Adenosine diphosphate (ADP)	Sigma-Aldrich (Steinheim, Germany)
3-amino-9-ethylcarbazole (AEC) solution	EUROPA (Cambridge, UK)
Agarose	Roth (Karlsruhe, Germany)
Alexa F488	Molecular Probes (Eugene, USA)
Alexa F647	Molecular Probes (Eugene, USA)
Ammonium persulfate (APS)	Roth (Karlsruhe, Germany)
Ampicillin	Roth (Karlsruhe, Germany)
Apyrase (grade III)	Sigma-Aldrich (Steinheim, Germany)
Aquatex® aqueous mounting medium	VWR Int. GmbH (Vienna, Austria)
Adenosine triphosphate (ATP)	Fermentas (St. Leon-Rot, Germany)
β-mercaptoethanol	Roth (Karlsruhe, Germany)
Blebbistatin	Sigma-Aldrich (Steinheim, Germany)
Botrocetin	Pentapharm Ltd. (Basel, CH)
Bovine serum albumin (BSA)	AppliChem (Darmstadt, Germany) Sigma-Aldrich (Steinheim, Germany)
Bromophenol blue	Sigma-Aldrich (Steinheim, Germany)
Cacodylate	AppliChem (Darmstadt, Germany)
Calcium chloride	Roth (Karlsruhe, Germany)
Ciliobrevin D	Merck Millipore (Darmstadt, Germany)
Chloroform	AppliChem (Darmstadt, Germany)
Clodrosomes	Clodronate Liposomes (Haarlem, The Netherlands)
Collagen Horm® suspension + SKF sol.	Takeda (Linz, Austria)
Complete protease inhibitors (+EDTA)	Roche Diagnostics (Mannheim, Germany)
Convulxin (CVX)	Enzo Life Sciences (New York, USA)
Cryo-Gel	Leica Microsystems (Wetzlar, Germany)
Cytochalasin B	AppliChem (Darmstadt, Germany)
Cytochalasin D	AppliChem (Darmstadt, Germany)
Dade® Innovin (tissue factor)	Siemens Healthcare Diagnostics (Deerfield, USA)

4',6-diamidino-2-phenylindole (DAPI)	Invitrogen (Karlsruhe, Germany)
Dimethyl sulfoxide (DMSO)	Sigma-Aldrich (Steinheim, Germany)
Disodiumhydrogenphosphate	Roth (Karlsruhe, Germany)
Dry milk, fat-free	AppliChem (Darmstadt, Germany)
Deoxynucleotide triphosphates (dNTP) mix	Fermentas (St. Leon-Rot, Germany)
DyLight-488	Pierce (Rockford, USA)
DyLight-649	Pierce (Rockford, USA)
Ethylenediaminetetraacetic acid (EDTA)	AppliChem (Darmstadt, Germany)
Ethylene glycol tetraacetic acid (EGTA)	Sigma-Aldrich (Steinheim, Germany)
Eukitt® quick-hardening mounting medium	Sigma-Aldrich (Steinheim, Germany)
Enhanced chemiluminescence (ECL) detection substrate	MoBiTec (Göttingen, Germany)
Eosin	Roth (Karlsruhe, Germany)
Embed-812	EMS (Hatfield, USA)
Ethanol	Roth (Karlsruhe, Germany)
Ethidium bromide	Roth (Karlsruhe, Germany)
Fentanyl	Janssen-Cilag GmbH (Neuss, Germany)
Fibrinogen from human plasma (F3879)	Sigma-Aldrich (Steinheim, Germany)
Fibrinogen from human plasma (F4883)	Sigma-Aldrich (Steinheim, Germany)
Flumazenil	Delta Select GmbH (Dreieich, Germany)
Fluorescein-isothiocyanate (FITC)	Molecular Probes (Oregon, USA)
Fluoroshield™	Sigma-Aldrich (Steinheim, Germany)
Fluorshield™ with DAPI	Sigma-Aldrich (Steinheim, Germany)
GeneRuler DNA Ladder Mix	Fermentas (St. Leon-Rot, Germany)
Giemsa 20x	Sigma-Aldrich (Steinheim, Germany)
Glucose	Roth (Karlsruhe, Germany)
Glutaraldehyde	EMS (Hatfield, USA)
Glycerol	Roth (Karlsruhe, Germany)
Hematoxylin	Sigma-Aldrich (Steinheim, Germany)
Histopaque®-1077 (human PBMCs)	Sigma-Aldrich (Steinheim, Germany)
Histopaque®-1119 (murine PBMCs)	Sigma-Aldrich (Steinheim, Germany)
N-2-Hydroxyethylpiperazine-N'-2-ethanesulfonic acid (HEPES)	Roth (Karlsruhe, Germany)
High molecular weight heparin	Ratiopharm (Ulm, Germany)
Igepal®CA-630	Sigma-Aldrich (Steinheim, Germany)

Immobilon-P transfer membrane, PVDF	Merck Millipore (Darmstadt Germany)
Integrilin® (Eptifibatide)	Millennium Pharmaceuticals Inc. (Cambridge, USA)
Iron-III-chloride hexahydrate ($FeCl_3$ $6H_2O$)	Roth (Karlsruhe, Germany)
Isofluran CP®	cp-pharma (Burgdorf, Germany)
Isopropanol	Roth (Karlsruhe, Germany)
Jasplakinolide	AppliChem (Darmstadt, Germany)
Kanamycin sulfate	Roth (Karlsruhe, Germany
Ketamine	Parke-Davis (Berlin, Germany)
Latrunculin A	AppliChem (Darmstadt, Germany)
Lead citrate	EMS (Hatfield, USA)
Loading Dye solution, 6x	Fermentas (St. Leon-Rot, Germany)
Magnesium chloride	Roth (Karlsruhe, Germany)
Magnesium sulfate	Roth (Karlsruhe, Germany)
Manganase chloride	Roth (Karlsruhe, Germany)
May-Gruenwald's solution	Roth (Karlsruhe, Germany
Medetomidine (Dormitor)	Pfizer (Karlsruhe, Germany)
Methanol	Roth (Karlsruhe, Germany)
Midazolam (Dormicum)	Roche (Grenzach-Wyhlen, Germany)
Midori Green™	Biozym Scientific (Oldenburg, Germany)
Naloxon	Delta Select GmbH (Dreieich, Germany)
3-(N-morpholino) propanesulfonic acid (MOPS)	AppliChem (Darmstadt, Germany)
Nonidet P-40 (NP-40)	Roche Diagnostics (Mannheim, Germany)
Osmium tetroxide	Merck Millipore (Darmstadt, Germany)
PageRuler® Prestained Protein Ladder	Fermentas (St. Leon-Rot, Germany)
Paraformaldehyde (PFA)	Roth (Karlsruhe, Germany)
Phalloidin	AppliChem (Darmstadt, Germany)
Phalloidin-Atto647N	Sigma-Aldrich (Steinheim, Germany)
Phalloidin-FITC	Enzo Life Sciences (New York, USA)
Phalloidin-rhodamine	Invitrogen (Karlsruhe, Germany)
Phenol/chloroform/isoamyl alcohol	AppliChem (Darmstadt, Germany)
Phorbol 12-myristate 13-acetate (PMA)	Sigma-Aldrich (Steinheim, Germany)
Piperazine-N,N′-bis(2-ethanesulfonic acid) (PIPES)	Roth (Karlsruhe, Germany)
Poly-L-lysine	Sigma-Aldrich (Steinheim, Germany)

Potassium acetate	Roth (Karlsruhe, Germany)
Potassium chloride	Roth (Karlsruhe, Germany)
Prolong Antifade	Invitrogen (Karlsruhe, Germany)
Propidium iodide (PI)	Invitrogen (Karlsruhe, Germany)
Propylen oxide	Merck Millipore (Darmstadt, Germany)
Prostacyclin (PGI_2)	Calbiochem (Bad Soden, Germany) Pro-
tease Inhibitor Cocktail	Sigma-Aldrich (Steinheim, Germany)
Proteinase K	Fermentas (St. Leon-Rot, Germany)
Protein G Sepharose	GE Healthcare (Uppsala, Sweden)
Refludan® (Lepirudin)	Bayer Schering Pharma AG (Wuppertal, Germany)
RNase A	Fermentas (St. Leon-Rot, Germany)
R-phycoerythrin (PE)	EUROPA (Cambridge, UK)
Rotiphorese Gel 30% (PAA)	Roth (Karlsruhe, Germany)
Sodium azide	Sigma-Aldrich (Steinheim, Germany)
Sodium chloride	AppliChem (Darmstadt, Germany)
Sodium citrate	AppliChem (Darmstadt, Germany)
Sodiumdihydrogenphosphate	Roth (Karlsruhe, Germany)
Sodium dodecyl sulfate (SDS)	Sigma-Aldrich (Steinheim, Germany)
Sodium hydroxide	AppliChem (Darmstadt, Germany)
Sodium orthovanadate	Sigma-Aldrich (Steinheim, Germany)
Sucrose	Sigma-Aldrich (Steinheim, Germany)
Sulfonic acid, 2N	AppliChem (Darmstadt, Germany)
10x Taq Buffer (+KCl, -$MgCl_2$)	Fermentas (St. Leon-Rot, Germany)
Taq-Polymerase	Fermentas (St. Leon-Rot, Germany)
Taxol	AppliChem (Darmstadt, Germany)
Tetramethylethylenediamine (TEMED)	Roth (Karlsruhe, Germany)
3,3,5,5-tetramethylbenzidine (TMB)	EUROPA (Cambridge, UK)
Thrombin from human plasma	Roche Diagnostics (Mannheim, Germany) Sigma-Aldrich (Steinheim, Germany)
Tissue Freezing Medium®	Jung Leica (Wetzlar, Germany)
Tris(hydroxymethyl)aminomethane (TRIS)	Roth (Karlsruhe, Germany)
Trition X-100	Sigma-Aldrich (Steinheim, Germany)
TRIzol®	Invitrogen (Karlsruhe, Germany)
Tween 20®	Roth (Karlsruhe, Germany)

U46619	Alexis Biochemicals (San Diego, USA)
Uranyl acetate	EMS (Hatfield, USA)
Vectashield hardset mounting medium	Vector Labs, Inc. (Burlingame, USA)
Water, nuclease-free	Roth (Karlsruhe, Germany)
Western Lightning® Plus-ECL	PerkinElmer (Baesweiler, Germany)
Xylazine	Bayer (Leverkusen, Germany)

3.1.2. Cell culture material

Cryo-tubes	Roth (Karlsruhe, Germany)
Dulbecco's phosphate-buffered saline (DPBS)	Gibco (Karlsruhe, Germany)
Dulbecco's Modified Eagle Media (DMEM)	Gibco (Karlsruhe, Germany)
Fetal calf serum (FCS)	Perbio (Bonn, Germany)
Gene Pulser/MicroPulser Cuvettes	Bio-Rad Laboratories (Munich, Germany)
Hirudin	Schering (Berlin, Germany)
Iscove's Modified Dulbecco's Media (IMDM)	Gibco (Karlsruhe, Germany)
Lipofectamine 3000	Invitrogen (Karlsruhe, Germany)
Nonessential amino acids	Gibco (Karlsruhe, Germany)
Penicillin/streptomycin	Gibco (Karlsruhe, Germany)
Polyethylenimine	Sigma-Aldrich (Steinheim, Germany)
Puromycine	Sigma-Aldrich (Steinheim, Germany)
Recombinant mouse IL-3	BioLegend (San Diego, USA)
Recombinant mouse IL-6	BioLegend (San Diego, USA)
Recombinant mouse stem cell factor (SCF)	BioLegend (San Diego, USA)
RetroNectin®	Clontech (Mountain View, USA)
Roswell Park Memorial Institute (RPMI) 1640	Gibco (Karlsruhe, Germany)
StemPro®-34	Gibco (Karlsruhe, Germany)
Thrombopoietin (Thpo)	Biosource (Solingen, Germany)
Tissue culture dishes (100/20 mm)	Greiner (Frickenhausen, Germany)
Tissue culture flasks (T25/75/175)	Greiner (Frickenhausen, Germany)
0.05% Trypsin-EDTA	Gibco (Karlsruhe, Germany)
6/12/24/48/96-well plates	Greiner (Frickenhausen, Germany)

All unstated chemicals were purchased from AppliChem (Darmstadt, Germany), Sigma-Aldrich (Steinheim, Germany) or Roth (Karlsruhe, Germany). *Rhodocytin* (Rhd) was kindly provided by J. Eble (University Hospital Frankfurt, Germany). *Collagen-related peptid*e (CRP)

was a generous gift from Paul Bray (Baylor College, USA). *Annexin V* (Anxa5) was generously provided by Jonathan F. Tait (Medical Center Washington, USA) and conjugated in our lab. Primers were obtained from Metabion (Planegg-Martinsried, Germany)

3.1.3. Kits

3,3'-diaminobenzidine Peroxidase Substrate Kit	Vector Labs, Inc. (Burlingame, USA)
Dynal® Mouse CD4 Negative Isolation Kit	Invitrogen (Karlsruhe, Germany)
MagniSort SVN negative depletion beads	eBioscience Inc. (San Diego, USA)
MicroBCA	Thermo Scientific (Rockford, USA)
Mouse Thrombopoietin DuoSet	R&D Systems (Wiesbaden, Germany)
NucleoSpin® Plasmid	Macherey-Nagel (Düren, Germany)
Plasmid Maxi Kit	Qiagen (Hilden, Germany)
RNeasy Mini Kit	Qiagen (Hilden, Germany)
SuperScript® First-Strand Synthesis System	Invitrogen (Karlsruhe, Germany)
QuickChange® Site-directed Mutagenesis Kit	Stratagene (Amsterdam, Netherlands)
QIAquick Gel Extraction Kit	Qiagen (Hilden, Germany)

3.1.4. Molecular cloning

Competent TOP10 *E. coli*	Iba Lifesciences (Göttingen, Germany)
Fast-Alkine Phosphatase	Fermentas (St. Leon-Rot, Germany)
Polynucleotide kinase (PNK)	Fermentas (St. Leon-Rot, Germany)
T4-DNA Ligase	Fermentas (St. Leon-Rot, Germany)
FastDigest® *BbsI*, *AgeI*, *BamHI*	Fermentas (St. Leon-Rot, Germany)
Restriction Enzymes (*AgeI*, *BamHI*, *NotI*, *SgfI* *EcoRV*, *HpaI*, *SalI*, *NcoI*, *PstI*, *KpnI*, *PmeI*, *BbsI*)	Fermentas (St. Leon-Rot, Germany)

3.1.5. Plasmids

pCMV6-Entry-Pfn1	OriGene (Rockville, USA)
pCMV-AC-Fc-S	OriGene (Rockville, USA)
pCMV-AC-GFP-Actb	OriGene (Rockville, USA)
pCMV-AC-GFP-Tubb1	OriGene (Rockville, USA)
pcoPE	kindly provided by Prof. Axel Rethwilm
pcoPG4	kindly provided by Prof. Axel Rethwilm
pcoPP	kindly provided by Prof. Axel Rethwilm
pF1K-DIAPH1	Promega (Mannheim, Germany)

pIRES2-EGFP	kindly provided by Dr. Attila Braun
pTW22	kindly provided by Prof. Axel Rethwilm
pcDNA3.1-TRPM7	kindly provided by Dr. Vladimir Chubanov
px330	kindly provided by Prof. Cord Brakebusch
px458	kindly provided by Prof. Cord Brakebusch
px459	kindly provided by Prof. Cord Brakebusch

3.1.6. Antibodies

3.1.6.1. Commercially purchased antibodies

Antibody	Host organism	Manufacturer
anti-acetylated-tubulin	mouse	Santa Cruz (Dallas, USA)
anti-α-tubulin (B-5-1-2)	mouse	Sigma-Aldrich (Steinheim, Germany)
anti-β-actin	mouse	Sigma-Aldrich (Steinheim, Germany)
anti-β-actin	rabbit	Sigma-Aldrich (Steinheim, Germany)
anti-β-tubulin	mouse	Sigma-Aldrich (Steinheim, Germany)
anti-CD3	rat	BioLegend (San Diego, USA)
anti-CD11b	rat	BioLegend (San Diego, USA)
anti-CD29 (9EG7)	Rat	BD Biosciences (Heidelberg, Germany)
anti-CD45R/B220	rat	BioLegend (San Diego, USA)
anti-CD105	rat	BioLegend (San Diego, USA)
anti-Diap1	rabbit	Abcam (Cambridge, UK)
anti-Diap2	rabbit	Abcam (Cambridge, UK)
anti-Diap3	rabbit	Cell Signaling (Denver, USA)
anti-FlnA	rabbit	Cell Signaling (Denver, USA)
anti-GAPDH	rabbit	Sigma-Aldrich (Steinheim, Germany)
anti-Glu-tubulin	rabbit	Merck Millipore (Darmstadt, Germany)
anti-RAPH1	rat	Merck Millipore (Darmstadt, Germany)
anti-Ly-6G/C (Gr1)	rat	BioLegend (San Diego, USA)
anti-MagT1	rabbit	Abgent (San Diego, USA)
anti-Myosin IIa	rabbit	Cell Signaling (Denver, USA)
anti-phospho-ASAP	rabbit	Rockland Inc. (Limerick, USA)
anti-Profilin1	mouse	Sigma-Aldrich (Steinheim, Germany)
anti-Profilin1 (B-10)	mouse	Santa Cruz (Dallas, USA)
anti-Profilin1	rabbit	Sigma-Aldrich (Steinheim, Germany)

Antibody	Host organism	Manufacturer
anti-RIAM	rabbit	Epitomics (Burlingame, USA)
anti-Tln (C-20)	goat	Santa Cruz (Dallas, USA)
anti-TER-119	rat	BioLegend (San Diego, USA)
anti-Twf1	rabbit	*
anti-Twf1/2	rabbit	*
anti-Tyr-tubulin (YL1/2)	rat	Merck Millipore (Darmstadt, Germany)
anti-vinculin	rabbit	Santa Cruz (Dallas, USA)
anti-vWF	mouse	DAKO (Hamburg, Germany)
anti-WASp	rabbit	Cell Signaling (Denver, USA)
platelet depletion antibody	rat	Emfret Analytics (Eibelstadt, Germany)

Antibody conjugates	Host organism	Manufacturer
anti-α-tubulin-Alexa F488	mouse	Invitrogen (Karlsruhe, Germany)
anti-CD29-FITC (HMβ1-1)	hamster	BioLegend (San Diego, USA)
anti-mouse IgG-Cy3	donkey	Jackson Immuno (Suffolk, UK)
anti-mouse IgG-Alexa F405	donkey	Jackson Immuno (Suffolk, UK)
anti-mouse IgG-Alexa F488	goat	Invitrogen (Karlsruhe, Germany)
anti-mouse IgG-HRP	rat	DAKO (Hamburg, Germany)
anti-goat IgG-Cy3	donkey	BioLegend (San Diego, USA)
anti-rabbit IgG-Cy3	goat	Jackson Immuno (Suffolk, UK)
anti-rabbit IgG-Alexa F647	goat	Invitrogen (Karlsruhe, Germany)
anti-rabbit IgG-Alexa F488	donkey	Invitrogen (Karlsruhe, Germany)
anti-rabbit IgG-HRP	goat	Cell Signaling (Denver, USA)
anti-rabbit IgG-HRP	donkey	Jackson Immuno (Suffolk, UK)
anti-rat IgG-Cy3	goat	BioLegend (San Diego, USA)
anti-rat IgG-Cy3	donkey	Jackson Immuno (Suffolk, UK)
anti-rat IgG-Alexa F405	donkey	Jackson Immuno (Suffolk, UK)
anti-rat IgG-Alexa F488	goat	Invitrogen (Karlsruhe, Germany)
anti-rat IgG-HRP	goat	Dianova

* Anti-Twf1 and anti-Twf1/2 antibodies were generously provided by Pekka Lappalainen (Helsinki, Finland).

2.1.6.2 Home made monoclonal antibodies (conjugations are not mentioned)

Antibody	Clone	Isotype	Antigen	Described in
p0p3	7A9	IgG2a	GPIbα	253
p0p4	15E2	IgG2b	GPIbα	254
p0p5	13G12	IgG1	GPIbα	255
p0p/B	57E12	IgG2b	GPIbα	256
p0p1	3G6	IgG1	GPIbβ	253
DOM2	89H11	IgG2a	GPV	254
p0p6	56F8	IgG2b	GPIX	254
JAQ1	98A3	IgG2a	GPVI	257
INU1	11E9	IgG1	CLEC-2	258
ULF1	97H1	IgG2a	CD9	254
JER1	10B6	IgG1	CD84	259
LEN1	12C6	IgG2b	α2	247
MWReg30	5D7	IgG1	αIIb	247,253
BAR-1	25B11	IgG1	α5	247
EDL-1	57B10	IgG2a	β3	247,254
JON/A	4H5	IgG2b	αIIbβ3	247,255
JON6	14A3	IgG2b	αIIbβ3	unpublished
WUG 1.9	5C8	IgG1	P-selectin	unpublished
HB.197™	2.4G2	IgG2b	FcgR	260

3.1.7. Buffers and Media

All buffers were prepared and diluted using $aqua_{bidest}$.

- ***Acid-Citrate-Dextrose*** **(ACD) Buffer, pH 4.5**

Trisodium citrate dehydrate	85 mM
Anhydrous citric acid	65 mM
Anhydrous glucose	110 mM

- **Actin-Depolymerization Buffer**

PIPES, pH 6.9	0.1 mM
$MgSO_4$	1 mM
$CaCl_2$	10 mM
Cytochalasin D	5 µM

- **Actin-Stabilization/Lysis Buffer:**

PIPES, pH 6.9	0.1 M
Glycerol	30%
DMSO	5%
$MgSO_4$	1 mM
EGTA	1 mM
Triton X-100	1%
ATP	1 mM
Protease inhibitors	1x

- **Blocking Buffer (Western blot)**

BSA or fat-free dry milk	5%
in Washing Buffer	

- **Blocking Buffer (Immunohistochemistry)**

Tween 20®	0.1%
BSA	3%
Rat serum	0.3%
in PBS	

- **CATCH Buffer**

HEPES	25 mM
EDTA	3 mM
BSA	3.5%
in PBS	

- **Coomassie Staining Solution**

Acetic acid	10%
Methanol	40%
Coomassie Brilliant blue	0.01%

- **Coomassie Destaining Solution**

Acetic acid	10%
H_2O	50%
Methanol	40%

- **Coupling Buffer 2x, pH 9.0**

$NaHCO_3$	167 mM
Na_2CO_3	80 mM

- **Cytoskeleton Extraction Buffer**

1x PHEM special (John Hartwig)	
Triton X-100	0.75%
Phalloidin	1 µM
Taxol	1 µM

- **Cytoskeleton Extraction Washing Buffer**

1x PHEM special (John Hartwig)	
Phalloidin	0.1 µM
Taxol	0.1 µM

- **Cytoskeleton Extraction Fixation Buffer**

1x PHEM special (John Hartwig)	
Glutaraldehyde	1%
Phalloidin	0.1 µM
Taxol	0.1 µM

- **Decalcification Buffer, pH 7.4**

EDTA	10%
in PBS	

- **EDTA Buffer, pH 8.0**

EDTA	1 mM

- **FACS Buffer**

FCS	1%
NaN_3	0.02%
in PBS	

- **Freezing-Medium**

DMEM	
FCS	50%
DMSO	10%

- **IP Buffer**

TRIS/HCl (pH 8.0)	15 mM
NaCl	155 mM
EDTA	1 mM
NaN_3	0.005%

- **Karnovsky Fixation Buffer, pH 7.2**

Paraformaldehyde	2%
Glutardialdehyde	2.5%
Cacodylate	0.1 M

- **Laemmli Buffer (for SDS-PAGE)**

TRIS	40 mM
Glycine	0.95 M
SDS	0.5%

- **LB Medium**

Peptone (pancreatic digested)	10 g L^{-1}
Yeast extract	5 g L^{-1}
NaCl	171 mM

- **LB Plates**

LB-Medium	
Agar	15 g L^{-1}

- **LINKER Buffer**

TRIS/HCl pH 8.0	50 mM
NaCl	100 mM
EDTA	1 mM

- **Low salt PIPES Buffer (for Co-IPs)**

PIPES pH 7.0	20 mM
$MgCl_2$	2 mM
EGTA	1 mM
GTP	1 mM
Protease inhibitors	1 x
Freshly added PMSF	0.5 mM

- **Lysis Buffer**

TRIS base	100 mM
EDTA (0.5 M)	5 mM
NaCl	200 mM
SDS	0.2%
added Proteinase K (20 mg mL^{-1})	100 µg mL^{-1}

- **MK Medium (fetal liver cells):**

IMDM	
FCS	10%
Nonessential amino acids	1%
Penicillin/streptomycin	1%
Thpo	0.5%

- **MK Medium (BM MKs):**

IMDM	
FCS	10%
Nonessential amino acids	1%
Penicillin/streptomycin	1%
Thpo	0.5%
Hirudin	0.1%

- **MK Medium (BM MKs Boston):**

StemPro®-34	
L-Glutamine	2 mM
Nutrient	2.6%
Penicillin/streptomycin	1%

- **PBS/EDTA (for platelet lysates)**

EDTA	5 mM
in PBS	

- **PHEM Buffer, pH 6.8**

PIPES	100 mM
HEPES	5.25 mM
EGTA	10 mM
$MgCl_2$	20 mM

- **PHEM Complete Buffer, pH 7.2**

PHEM Fixation Buffer	
Igepal®CA-630	0.1%
in PHEM	

- **PHEM Fixation Buffer**

PFA	4%
in PHEM	

- **10x PHEM special (John Hartwig), pH 6.9**

PIPES	600 mM
HEPES	250 mM
EGTA	100 mM
$MgSO_4$	20 mM

- ***Phosphate-buffered-Saline*** **(PBS), pH 7.14**

NaCl	137 mM
KCl	2.7 mM
KH_2PO_4	1.5 mM
Na_2HPO_4 x $2H_2O$	8 mM

- **SDS Sample Buffer, 2x**

β-mercaptoethanol (for red. conditions)	10%
TRIS buffer (1.25 M), pH 6.8	10%
Glycerin	20%
SDS	4%
Bromophenolblue	0.02%

- **Separating Gel Buffer (Western Blot), pH 8.8**

TRIS/HCl	1.5 M

- **Solution I (Mini preps)**

Glucose	50 mM
TRIS base	25 mM
EDTA	10 mM

- **Solution II (Mini preps)**

NaOH	0.2 M
SDS	1%

- **Solution III (Mini preps)**

Potassium acetate	3 M

- **Stacking Gel Buffer (Western Blot), pH 6.8**

TRIS/HCl	0.5 M

- **Stripping Buffer (Western Blot), pH 6.8**

TRIS/HCl	62.5 mM
SDS	2%
β-mercaptoethanol	100 mM

- **Sodium-Citrate-Buffer, pH 6.0**

Sodium Citrate	10 mM
Tween 20®	0.05%

- **Storage Buffer, pH 7.0**

TRIS	20 mM
NaCl	0.9%
BSA	0.5%
NaN_3	0.09%

- **50x TAE**

TRIS base	0.2 M
Acetic acid	5.7%
EDTA (0.5 M)	10%

- **TE-Buffer**

TRIS base	10 mM
EDTA	1 mM

- **Transfer-Buffer (semi-dry blot)**

TRIS ultra	48 mM
Glycine	39 mM
Methanol	20%

- ***TRIS-Buffered Saline*** **(TBS), pH 7.3**

NaCl	137 mM
TRIS/HCl	20 mM

- **TRIS-EDTA-Buffer, pH 9.0**

TRIS	10 mM
EDTA	1 mM
Tween 20®	0.05%

- **Tyrode's Buffer, pH 7.3**

NaCl	137 mM
KCl	2.7 mM
$NaHCO_3$	12 mM
NaH_2PO_4	0.43 mM
Glucose	0.1%
Hepes	5 mM
BSA	0.35%
$CaCl_2$	2 mM
$MgCl_2$	1 mM

- **Washing Buffer (ELISA)**

PBS	
Tween 20®	0.05%

- **Washing Buffer (Western Blot)**

TBS	
Tween 20®	0.1%

3.2. Methods

3.2.1. Mutagenesis and molecular cloning

3.2.1.1. Mutagenesis

Mutant *Pfn1* and *DIAPH1* constructs were generated with the help of QuickChange® Site-directed Mutagenesis Kit according to the manufacturer's protocol. Briefly, mutagenesis polymerase chain reaction was performed on the pCMV6-Entry-Pfn1, pF1K-DIAPH1 and pcDNA3.1-TRPM7 vectors with the following primers:

Pfn1_Mut_W3A_for	5' CGATCGCCATGGCCGGGGCGAACGCCTACATCGAC 3'
Pfn1_Mut_W3A_rev	5' GTCGATGTAGGCGTTCGCCCCGGCCATGGCGATCG 3'
Pfn1_Mut_Y6D_for	5' GCCGGGTGGAACGCCGACATCGACAGCCTTATG 3'
Pfn1_Mut_Y6D_rev	5' CATAAGGCTGTCGATGTCGGCGTTCCACCCGGC 3'
Pfn1_Mut_R74E_for	5' CAGAAATGTTCTGTGATCGAGGACTCACTGCTGC 3'
Pfn1_Mut_R74E_rev	5' GCAGCAGTGAGTCCTCGATCACAGAACATTTCTG 3'
Pfn1_Mut_Y129F_for	5' GATCAACAAGAAATGTTTTGAAATGGCCTCTCACC 3'
Pfn1_Mut_Y129F_rev	5' GGTGAGAGGCCATTTCAAAACATTTCTTGTTGATC 3'
Pfn1_Mut_H133S_for	5' GTTATGAAATGGCCTCTAGCCTGCGGCGTTCCCAG 3'
Pfn1_Mut_H133S_rev	5' CTGGGAACGCCGCAGGCTAGAGGCCATTTCATAAC 3'
Pfn1_Mut_R136D_for	5' GCCTCTCACCTGCGGGATTCCCAGTACTGAACG 3'
Pfn1_Mut_R136D_rev	5' CGTTCAGTACTGGGAATCCCGCAGGTGAGAGGC 3'
DIAPH1_Mut_R1213*_for	5' GTCAGGGGCAGCATTCTGACGGAAGAGAGGGCC 3'
DIAPH1_Mut_R1213*_rev	5' GGCCCTCTCTTCCGTCAGAATGCTGCCCCTGAC 3'
Trpm7_Mut_C721G_for	5' CTGGAGTAATTCAACCGGCCTTAAGTTAGCAG 3'
Trpm7_Mut_C721G_rev	5' CTGCTAACTTAAGGCCGGTTGAATTACTCCAG 3'

Subsequent to the PCR, the reaction was incubated with *DpnI* to digest the maternal plasmid DNA, while the newly synthetized, methylated plasmids grossly remained intact. The digested PCR product was then used for transformation of TOP10 *E. coli* cells. Sequencing confirmed the success of the mutagenesis.

3.2.1.2. Molecular cloning of mutant constructs

For the generation of mutant Pfn1 constructs or vectors enabling the expression of fluorophore-tagged cytoskeletal components, standard techniques for molecular cloning as de-

scribed before were used. All ligations were performed at 16°C over night using T4 DNA ligase (Fermentas). First, a *NotI* linker (5' AGCGGCCGCT 3') was inserted into the pIRES2-EGFP vector (kindly provided by Dr. Attila Braun) via blunt end digestion with *EcoRV*. Next, pSSVCV was generated by ligating a 6,502 bp *BamHI-NotI* fragment of the pTW22 vector with a 1,315 bp *BamHI-NotI* fragment of the pIRES2-EGFP vector to insert the IRES-EGFP cassette into the pTW22 vector (kindly provided by Prof. Axel Rethwilm) downstream of the SFFVU3 promoter. Of note, all linkers were purchased as single strand oligos and were by dimerized by heating and cooling in LINKER buffer and phosphorylated using PNK.

Prior to the site-directed mutagenesis, a *BamHI* linker (5' CCGGATCCGG 3') was ligated into the Pfn1 *open reading frame* (ORF)-containing pCMV6 vector (OriGene) downstream of the Pfn1 ORF via EcoRV digestion. The mutant Pfn1 cDNAs were inserted into the viral carrying vector by ligating a 522 bp *BamHI* fragment of the respective pCMV6 W3A, Y6D, R74D, Y129F, H133S and R136D Pfn1 mutants with the *BamHI*-linearized pSSVCV vector. Due to the non-directed ligation, the correct orientation of the inserts was verified by *KpnI* digestion. A correctly inserted mutant yielded a 7,354, 964 and a 21 bp fragment, while an incorrectly orientated insert resulted in a 7,354, 531 and a 454 bp fragment. The newly generated vectors were named pSSW3A, pSSY6D, pSSR74D, pSSY129F, pSSH133S and pSSR136D respectively.

After sequence confirmation of the mutation a 3,825 bp *SgfI-PmeI* fragment of the pF1K vector containing the *DIAPH1* open reading frame or the R1213* variant were gel purified and cloned into a 5,894 bp *SgfI-PmeI* fragment of the pCMV6-Fc-S (PS100054, OriGene) mammalian expression vector. The newly generated vectors were named pSSDIAWT and pSSDIAR1213* respectively.

3.2.1.3. Molecular cloning of fluorophore-conjugated *Tubb1* and *Actb*

To insert the Tubb1-TurboGFP expression cassette (OriGene) into the pSSVCV vector, first a *SalI* linker (5' AAGTCGACTT 3') was cloned into pCMV-AC-GFP-Tubb1 via blunt end digestion with *PmeI* (→pCMV-AC-GFP-Tubb1-SalI link). Subsequently, a 2,116 bp *BamHI-SalI* fragment of the pCMV-AC-GFP-Tubb1-SalI link vector was cloned into a 6,452 bp *BamHI-SalI* fragment of the pSSVCV vector. The resulting vector was named pSSTubb1.

To insert the Actb expression cassette (OriGene) into the foamy viral expression vector, a 1,178 bp *BamHI-XhoI* fragment of the pCMV-AC-GFP-Actb vector was ligated into a 7,163 bp *BamHI-XhoI* fragment of the pSSTubb1 vector. The resulting vector was named pSSActb.

3.2.1.4. Molecular cloning of CRISPR constructs

In order to generate knockout cell lines using the *clustered regularly interspaced short palindromic repeats* (CRISPR) Cas9 technology, each two antiparallel DNA oligos containing *BbsI* restriction sites were designed with the help of ZiFiT Targeter Version 4.2. The oligos (17 bp) were directed against exons of the genes of interest and encoded for the so-called *guide RNA* (gRNA) of the CRISPR-Cas system. The following oligos were purchased, dimerized by heating and cooling in LINKER buffer and phosphorylated using polynucleotide kinase:

RhoA_hogui_Ex3_for	5' ACA CCG GTA GGA GAG GGG CCT CG 3'
RhoA_hogui_Ex3_rev	5' AAA ACG AGG CCC CTC TCC TAC CG 3'
RhoA_hogui_Ex4_for	5' ACA CCG TGC CCA TCA TCC TGG TG 3'
RhoA_hogui_Ex4_rev	5' AAA ACA CCA GGA TGA TGG GCA CG 3'
Bin2_hogui_Ex3_for	5' ACA CCG GTC CTT GTA CAG CTT GG 3'
Bin2_hogui_Ex3_rev	5' AAA ACC AAG CTG TAC AAG GAC CG 3'
Bin2_hogui_Ex4_for	5' ACA CCG CTG TAG ATC TCC TGC AG 3'
Bin2_hogui_Ex4_rev	5' AAA ACT GCA GGA GAT CTA CAG CG 3'
Trpm7_hogui_Ex5_for	5' ACA CCG CTT AAA GAA TGG CAA AG 3'
Trpm7_hogui_Ex5_rev	5' AAA ACT TTG CCA TTC TTT AAG CG 3'
Trpm7_hogui_Ex5.1_for	5' ACA CCG TTA TTT CTG TAC ATG GG 3'
Trpm7_hogui_Ex5.1_rev	5' AAA ACC CAT GTA CAG AAA TAA C 3'

Subsequently, the dimerized and phosphorylated gRNAs were ligated into *BbsI*-linearized px330, px458 and px459 vectors and transformed into TOP10 *E. coli*. Successful insertion of the gRNAs was monitored via double digestion of the Mini DNA with *BbsI* and *AgeI*, as insertion of the gRNA lead to the disruption of the *BbsI* restriction site.

3.2.1.5. Transformation

For transformation chemically competent TOP10 *E. coli* bacteria (Iba Lifesciences; F- mcrA (mrr-hsdRMS-mcrBC) 80lacZ M15 lacX74 recA1 ara 139 (ara-leu)7697 galU galK rpsL (StrR) endA1 nupG) were incubated for 30 min on ice with 10 ng of the ligated vectors. Transformation was then triggered by a 90 s heat shock at 42°C with subsequent incubation on ice for 5 min. Thereafter, bacteria were supplied with 1 mL LB-medium and incubated for 1 h at

450 rpm and 37°C. Positive clones were selected by plating the transformation mixture on LB-agar plates containing antibiotics.

3.2.1.6. Mini preps

Overnight cultures (3 mL LB-medium supplemented with antibiotics) were incubated over night at 37°C and 225 rpm. The next day, cells were pelleted by centrifugation (30 s; 11,000 rpm), resuspended in 200 µL Solution I and lysed by the addition of 250 µL Solution II (5 min). Lysis was stopped and proteins were precipitated by the addition of Solution III. Cell debris was pelleted by centrifugation for 5 min at 11,000 rpm and 4°C and DNA was precipitated by mixing the cleared lysate with 500 µL isopropanol. After another centrifugation step (10 min, 14,000 rpm and 4°C) the DNA pellet was dried by the addition of 500 µL 70% ethanol and reconstituted in TE-Buffer.

3.2.2. Cell culture, virus production and generation of knockout cell lines

3.2.2.1. Cultivation of mammalian cell lines (HEK293FT, MEF, K562, Jurkat)

Adherent *Human Embryonic Kidney* (HEK) 293FT cells and primary or immortalized *Mouse Embryonic Fibroblasts* (MEF) were grown in Dulbecco's modified Eagle medium (containing 10% *fetal calf serum* (FCS), 100 U mL^{-1} of penicillin, 0.1 mg mL^{-1} of streptomycin) at 37°C, 5% CO_2.

Human Jurkat T-cells (clone E6-1) were grown in suspension in RPMI-1640 medium supplemented with 10% FCS and 100 U mL^{-1} of penicillin, 0.1 mg mL^{-1} of streptomycin at 37°C, 5% CO_2.

The human immortalized myelogenous leukemia cell line K562 were grown in suspension in RPMI-1640 medium supplemented with 10% FCS and 100 U mL^{-1} of penicillin, 0.1 mg mL^{-1} of streptomycin at 37°C, 5% CO_2. 10 mL of 2 x 10^5 cells per mL were seeded and the day after stimulated for 72 h either with 1.5% DMSO for erythroid, 100 nM PMA for megakaryocytic or 10 nM staurosporine for monocytic differentiation.

Hematopoietic stem cells were isolated from male mouse BM single cell suspensions using a magnetic bead-based negative depletion kit (anti-rat-IgG Dynabeads, Invitrogen or MagniSort, eBioscience) in combination with (biotinylated) rat-anti-mouse antibodies directed against CD45R/B220, TER-119, CD3, Ly-6G/C and CD11b (each 0.5 µg per 10^7 cells). Experiments were performed according to the manufacturer's protocol. Cells were cultured in Iscove's modified Dulbecco medium (supplemented with 10% FCS, 100 U mL^{-1} of penicillin, 0.1 mg mL^{-1} of streptomycin, 100 ng mL^{-1} mouse SCF, 100 ng mL^{-1} Thpo, 10 ng mL^{-1} mouse

IL-3, 10 ng mL^{-1} mouse IL-6) at 37°C, 5% CO_2 in 12 well cell culture plates coated with 20 µg RetroNectin® CH-296 [1 mg mL^{-1}] in 500 µL sterile PBS.

3.2.2.2. Isolation and immortalization of MEFs

Embryos from time-mated mice (13.5-14.5 days post coitum) carrying the Cre-recombinase under a 4-hydroxytamoxifen-inducible promoter (Cre-ERT) were dissected and heads and all red tissues were removed. The remaining tissues were washed once in sterile PBS, transferred into 1 mL of Trypsin-EDTA solution, minced with a scissor and incubated for 5 min at 37°C. To increase the number of single cells the samples were further homogenized by squeezing through a syringe (26 gauge cannula). To stop the reaction 9 mL culture medium were added and the cells were grown over night. The next day, medium was changed and the day after the superconfluent culture was washed once with PBS, cells were detached by incubation with Trypsin-EDTA solution at 37°C and 3 x 10^5 cells were seeded per 6 cm dish. The remaining cells were either frozen in cryo medium (50% FCS, 40% DMEM, 10% DMSO) or used for genotyping. To immortalize the MEFs, each three days the cells were passaged and 3 x 10^5 cells were seeded per 6 cm dish for 20 consecutive passages. Immortalized clones were cryo preserved.

3.2.2.3. Induction of Cre expression

To induce the expression of the Cre-recombinase and hence ablate expression of *Pfn1* immortalized and primary MEFs (*Pfn1*$^{fl/fl}$ *Cre-ERT*$^{+/-}$ and *Pfn1*$^{fl/fl}$ *Cre-ERT*$^{+/+}$) were seeded in 6 well plates [2 x 10^5 cells per well] and repeatedly treated with 10 µM Z-4-hydroxytamoxifen (each 24 h for three days).

3.2.2.4. Transfection

For expression studies of constructs 5 x 10^5 HEK cells were seeded per well of 6 well plate. The next day, medium was exchanged and cells were transfected by the addition of 100 µL transfection mix (2.5 µg plasmid DNA coding for the different mutants and 7.5 µg polyethylenimine in 100 µL DMEM without supplements incubated for 20 min at *room temperature* (RT)). After 24 h the transfection mix-containing medium was replaced by DMEM supplemented with antibiotics and 10% FCS. After different time points the cells were washed once with PBS and protein lysates were generated or cells were processed for immunostaining and confocal microscopy.

3.2.2.5. Electroporation and generation of knockout cell lines

Transfection of a log phase culture of K562 and Jurkat T-cells was achieved through electroporation. To this end the cells were washed once in serum-free culture medium (1,200 rpm, 5 min) and their concentration was set to 2.5 x 10^7 (K562) or 5 x 10^7 (Jurkat) cells per mL respectively. Each 400 µL were then mixed with 20 µg plasmid DNA, transferred to a 4 mm spacing electroporation cuvette and shot with a Biorad® GenePulser II at 250 V, 950 µF and indefinite resistance using a exponential decay wave form. Subsequently, the cuvette was flicked to obtain a homogenous mixture of the cells and was allowed to rest for 10 min at RT. Next, the cells, without debris, were transferred to 7.6 mL of complete RPMI-1640 culture medium. After 24 h, selection was started by the addition of 1 µg mL^{-1} puromycin, which was resupplemented each 24 h for two days. The surviving cells were subcloned, cultivated and upon expansion some of the cells were used to test for the presence of larger insertions or deletions via PCR.

3.2.2.6. Isolation of genomic DNA from cell lines

The cell pellet was incubated for 2 h at 56°C and 1,400 rpm in 250 µL of lysis buffer. Cellular proteins and lipids were removed by the addition of 250 µL of phenol/chloroform/isoamyl alcohol (25:24:1). Samples were shaken well and centrifuged for 10 min at 10,000 rpm in an Eppendorf 5417R tabletop centrifuge at RT. After the centrifugation, the aqueous nucleic acid containing upper phase was transferred into a new cap containing 250 µL isopropanol to precipitate the DNA/RNA. Subsequently, the nucleic acids were spun down by centrifugation for 15 min at 14,000 rpm and 4°C. The pellet was washed and dehydrated by the addition of 500 µL 70% ethanol with subsequent centrifugation for 15 min at 14,000 rpm. Before dissolving the pellet in 50 µL TE buffer, the pellet was allowed to dry for 30 min at 37°C.

3.2.2.7. Genotyping of mutant cell lines with polymerase chain reaction (PCR)

PCR mix for *RhoA*, *Bin2*, and *Trpm7*:

1.0 µL	DNA sample
2.5 µL	10x Taq Buffer (+KCl, -$MgCl_2$)
2.5 µL	$MgCl_2$ [25 mM]
0.5 µL	dNTPs [10 mM]
0.1 µL	forward Primer [1 µg mL^{-1}]
0.1 µL	reverse Primer [1 µg mL^{-1}]
0.25 µL	native Taq-Polymerase [5 U $µL^{-1}$]
18.05 µL	H_2O

PCR program:

Temperature [°C]	Time [s]	Repeats
96	180	1 cycle
94	30	35 cycles
58	30	35 cycles
72	60	35 cycles
72	300	1 cycle
22	∞	1 cycle

Primer *RhoA* exon 3 (annealing temperature 58°C):

RhoA_Ex3_hu_for: 5' GGC GGG CAC CTG TAG TC 3'

RhoA_Ex3_hu_rev: 5' CAC CGT GCC CTG CCT AG 3'

Expected band size: 661 bp for the *WT* exon three of the *RhoA* gene

Primer *RhoA* exon 4 (annealing temperature 58°C):

RhoA_Ex4_hu_for: 5' CCC ACC TAC AGA GAT GCT CAG 3'

RhoA_Ex4_hu_rev: 5' TTC TCA GGC CAG CAG TCC 3'

Expected band size: 619 bp for the *WT* exon four of the *RhoA* gene

Primer *Bin2* exon 3 (annealing temperature 58°C):

Bin2_Ex3_hu_for: 5' GGC GGG CAC CTG TAG TC 3'

Bin2_Ex3_hu_rev: 5' CAC CGT GCC CTG CCT AG 3'

Expected band size: 436 bp for the *WT* exon three of the *Bin2* gene

Primer *Bin2* exon 4 (annealing temperature 58°C):

Bin2_Ex4_hu_for: 5' CCC ACC TAC AGA GAT GCT CAG 3'

Bin2_Ex4_hu_rev: 5' TTC TCA GGC CAG CAG TCC 3'

Expected band size: 622 bp for the *WT* exon four of the *Bin2* gene

Primer *Trpm7* exon 17 (annealing temperature 58°C):

TRPM7_Ex5_hu_for: 5' CCG ATC CTC TTC AGC CAG TC 3'

TRPM7_Ex5_hu_rev: 5' GGC CTG TAA TCC CAG CTA CTC 3'

Expected band size: 763 bp for the *WT* exon five of the *Trpm7* gene

3.2.2.8. Production of viral particles

To generate viral particles for transduction of different cells (HSCs or MEFs) HEK cells were seeded at a density of 6 x 10^6 per 10 cm dish one day prior to transfection (10 µg of the carrier plasmids, 5 µg pcoPG4, 1 µg pcoPP and pcoPE in 2 mL serum-free DMEM with 51 µg polyethylenimine). The next day, medium was replaced and after another 48 h the supernatant containing viral particles was collected and cleared from cell debris by filtrating through a 0.22 µm filter. The viral particle-containing supernatant was centrifuged for 3 h at 4°C and 10,000 rpm and 40 fold concentrated by resuspending the barely visible pellet in 1 mL PBS. Each 200 µL aliquots were immediately frozen and stored at -80°C.

3.2.2.9. Titration of viral particles

The number of viral particles was determined by seeding 2 x 10^4 cells in 1 mL per well of 12 well plate the day prior to transduction. The next day, serial dilutions (ranging from 10^{-1}-10^{-5}) of the concentrated frozen viral particles were added to the wells. After another 72 h the supernatant medium was discarded, cells were washed once with PBS, trypsinized and washed once more in PBS (1,200 rpm for 5 min). The pellet was resuspended in 500 µL PBS supplemented with 0.1% BSA and the percentage of transduced, GFP-positive cells was determined by flow cytometry.

3.2.3. Genetically modified mice

Conditional Pfn1-deficient mice were generated by intercrossing *Pfn1*$^{fl/fl}$ mice (exon 2 flanked by loxP sites) with mice carrying the Cre-recombinase under the platelet factor 4 (*Pf4*) promoter.[40,261] *Pfn1*$^{fl/fl}$ mice were obtained from EUCOMM (*European Conditional Mouse Mutagenesis Program*, Strain ID EM:03711) and *Pf4-Cre* mice were kindly provided by Dr. Radek Skoda. All mice used in experiments were 12- to 16 weeks old and sex-matched, if not stated otherwise. For experiments on MKs, only male animals were used.

WASp-null[197] and WIP-null[262] mice were maintained on a C57Bl/6 background and were kindly provided by Hérve Falet. Approval for animal research was granted by the Harvard Medical Area Standing Committee, according to the National Institutes of Health standards and as outlined in the Institute for Laboratory Animal Research Guide for Care and Use of Laboratory Animals.

Conditional Twf1-deficient mice were generated by intercrossing *Twf1*$^{fl/fl}$ mice (exon 3 flanked by loxP sites) with mice carrying the Cre-recombinase under the *Pf4* promoter.[261] *Twf1*$^{fl/fl}$ mice were obtained from EUCOMM (Strain ID EM:05232). Constitutive Twf2a-deficient mice were kindly provided by Prof. Pekka Lappalainen and have been described earlier.[150]

Constitutive *PLD1/2* double-deficient mice were kindly provided by Drs. David Stegner and Ina Thielmann and have been described earlier.[45]

Conditional Trpm7-deficient mice were generated by intercrossing *Trpm7$^{fl/fl}$* mice (exon 17 flanked by loxP sites) with mice carrying the Cre-recombinase under the *Pf4* promoter.[172,261] *Trpm7$^{fl/fl}$* mice were generously provided by Prof. David Clapham.

Exons 3 to 6 of *Apbb1ip* gene were replaced with a *LacZ-p(A); Neo-p(A)* cassette by homologous recombination. The replacement leads to a deletion of amino acids 25 – 234 and encompasses the coiled-coiled region, a PLP stretch and parts of the RA-domain. In addition, the deletion induces a frame shift mutation after amino acid 24 of *Apbb1ip* gene and leads to a non-functional protein with a premature stop codon. *Apbb1ip$^{+/-}$* mice were generated by injection of embryonic stem cell clone 16066A-D5 (*Knockout Mouse Project* (KOMP)) into C57Bl/6 blastocysts. Germ-line transmission was obtained by backcrossing the resulting chimeric mice with C57Bl/6 mice.[247] All animal experiments were approved by the district government of Lower Frankonia (Bezirksregierung Unterfranken).

3.2.4. Genotyping of mice

3.2.4.1. Isolation of genomic mouse DNA

A 5 mm² piece of mouse ear was incubated overnight at 56°C and 900 rpm or for 3 h at 56°C and 1,400 rpm in 500 µL of lysis buffer. Cellular proteins and lipids were removed by the addition of 500 µL of phenol/chloroform/isoamyl alcohol (25:24:1). Samples were mixed well and centrifuged for 10 min at 10,000 rpm in an Eppendorf 5417R tabletop centrifuge at RT. After centrifugation, the aqueous nucleic acid containing upper phase was transferred into a new cap containing 500 µL isopropanol to precipitate the DNA/RNA. Subsequently, the nucleic acids were spun down by centrifugation for 15 min at 14,000 rpm and 4°C. The pellet was washed and dehydrated by the addition of 500 µL 70% ethanol with subsequent centrifugation for 15 min at 14,000 rpm. Before dissolving the pellet in 100 µL TE buffer, the pellet was allowed to dry for 30 min at 37°C.

3.2.4.2. Polymerase chain reaction (PCR)

Separate PCR reactions were performed to amplify the *WT*/ floxed *Pfn1*/ *Trpm7* or the targeted *Twf2a*/ *PLD1/2*/ *Apbb1ip* loci and to control the presence of the Cre-recombinase cassette under control of the *Pf4* promoter on Chromosome 9.[261]

PCR mix for *Pfn1*, *Twf2a WT*, *Apbb1ip WT/ KO*:

2.0 µL	DNA sample
2.0 µL	10x Taq Buffer (+KCl, -$MgCl_2$)
1.2 µL	$MgCl_2$ [25 mM]
0.4 µL	dNTPs [10 mM]
0.1 µL	forward Primer [1 µg mL^{-1}]
0.1 µL	reverse Primer [1 µg mL^{-1}]
0.125 µL	native Taq-Polymerase [5 U $µL^{-1}$]
14.075 µL	H_2O

PCR program *Pfn1*, *Trpm7*, *Twf2a WT*, *Apbb1ip WT/ KO*:

Temperature [°C]	Time [s]	Repeats
96	180	1 cycle
94	30	35 cycles
55.5-69.0	30	35 cycles
72	60	35 cycles
72	300	1 cycle
22	∞	1 cycle

Primer *Pfn1* (annealing temperature 55.5°C):

Pfn1_i2_f2: 5’ TTC TGA CTC TGG CTC CCC AG 3’

Pfn1_i2_r2: 5’ GCT AGG AAC GGC TGT GAT GC 3’

Expected band sizes: 187 bp for the *WT* and 221 bp for the floxed *Pfn1* allele

Primer *Twf2a WT* (annealing temperature 69.0°C):

Twf2a_Ex1_for: 5’ CCA GGA CCA AGA GGA GAA CTC CGA C 3’

Twf2a_Int1_rev: 5’ CCC AGC TAT GTA CAA CAG TCT GTT CTG CC 3’

Expected band sizes: 249 bp for the *WT Twf2a* allele

Primer *Apbb1ip WT* (annealing temperature 62.8°C):

Apbb1ip_for: 5’ GAT GCC CTC ATG GCA GAT C 3’

Apbb1ip_rev: 5’ CTA CGG GTG GAG GTG GTA AAG 3’

Expected band sizes: 208 bp for the *WT Apbb1ip* allele

Primer *Apbb1ip KO* (annealing temperature 66.9°C):

Apbb1ip_NeoInF: 5' TTC GGC TAT GAC TGG GCA CAA CAG 3'

Apbb1ip_NeoInR: 5' TAC TTT CTC GGC AGG AGC AAG GTG 3'

Expected band sizes: 282 bp for the targeted *Apbb1ip* allele

PCR mix for *PLD1/2 WT*:

1.0 µL	DNA sample
2.5 µL	10x Taq Buffer (+KCl, -$MgCl_2$)
2.5 µL	$MgCl_2$ [25 mM]
0.5 µL	dNTPs [10 mM]
0.5 µL	forward Primer (1:10 in H_2O, [0.1 µg mL^{-1}])
0.5 µL	reverse Primer (1:10 in H_2O, [0.1 µg mL^{-1}])
0.25 µL	native Taq-Polymerase [5 U $µL^{-1}$]
17.25 µL	H_2O

PCR program *PLD1/2 WT*:

Temperature [°C]	Time [s]	Repeats
96	300	1 cycle
94	30	35 cycles
59-66	30	35 cycles
72	45	35 cycles
72	30	1 cycle
22	∞	1 cycle

Primer *PLD1 WT* (annealing temperature 66.0°C):

PLD1_WT_for: 5´ TGT GCA AGT GCG TGT GGG CA 3´

PLD1_WT_rev: 5´ ACA GGG CAC CCA CAG GAG CA 3´

Expected band size: 283 bp for *WT* samples

Primer *PLD2 WT* (annealing temperature 59.0°C):

PLD2_WT_for: 5´ AAG CAA CAC CAC ACA TTC CA 3´

PLD2_WT_rev: 5´ CTT CCC GAC TCA CAG CTT TC 3´

Expected band size: 445 bp for *WT* samples

PCR mix for *PF4-Cre*:

2.0 µL	DNA sample
2.5 µL	10x Taq Buffer (+KCl, -$MgCl_2$)
2.5 µL	$MgCl_2$ [25 mM]
0.5 µL	dNTPs [10 mM]
1.0 µL	forward Primer (1:10 in H_2O, [0.1 µg mL^{-1}])
1.0 µL	reverse Primer (1:10 in H_2O, [0.1 µg mL^{-1}])
0.25 µL	native Taq-Polymerase [5 U $µL^{-1}$]
15.25 µL	H_2O

PCR program *PF4-Cre*:

Temperature [°C]	Time [s]	Repeats
96	300	1 cycle
94	30	35 cycles
48.5	30	35 cycles
72	45	35 cycles
72	30	1 cycle
22	∞	1 cycle

Primer *PF4-Cre*:

PF4 for: 5´ CCC ATA CAG CAC ACC TTT TG 3´

PF4 rev: 5´ TGC ACA GTC AGC AGG TT 3´

Expected band size: 450 bp for positive samples

PCR mix for *Genetrap (Twf2a KO*, *PLD1/2 KO)*:

1.0 µL	DNA sample
2.5 µL	10x Taq Buffer (+KCl, -$MgCl_2$)
2.5 µL	$MgCl_2$ [25 mM]
0.5 µL	dNTPs [10 mM]
0.05 µL	forward Primer [0.1 µg mL^{-1}]
0.05 µL	reverse Primer [0.1 µg mL^{-1}]
0.25 µL	native Taq-Polymerase [5 U $µL^{-1}$]
18.15 µL	H_2O

PCR program:

Temperature [°C]	Time [s]	Repeats
96	180	1 cycle
94	30	35 cycles
51.4	30	35 cycles
72	60	35 cycles
72	600	1 cycle
22	∞	1 cycle

Primer *Genetrap*:

Genetrap_for: 5´ TTA TCG ATG AGC GTG GTG GTT ATG C 3´

Genetrap_rev: 5´ GCG CGT ACA TCG GGC AAA TAA TAT 3´

Expected band size: 680 bp for positive samples

3.2.4.3. RNA preparation from platelets

For each genotype, at least three animals were bled under isoflurane anesthesia up to 1 mL into 300 µL heparin (in TBS [20 U mL^{-1}]). After blood withdrawal the samples were supplied with another 300 µL heparin [20 U mL^{-1}] and centrifuged for 6 min at 800 rpm in an Eppendorf 5415C centrifuge. The upper phase and the buffy coat, with some erythrocytes was transferred into a tube containing 300 µL heparin [20 U mL^{-1}] and centrifuged once more for 6 min at 800 rpm. Finally, only the upper phase without any erythrocytes was transferred into an empty cap and platelets were pelleted by centrifugation for 5 min at 2,800 rpm (Eppendorf 5417R). The pellets were resuspended and pooled in a total volume of 250 µL IP-buffer supplied with 1% NP-40, vortexed and incubated for 10 min at RT. After the addition of 1 mL TRIzol® reagent, the samples were incubated for 10 min at RT. Further, 250 µL of chloroform were added and the samples were incubated for 10 min at RT and afterwards centrifuged for 10 min at 10,000 rpm (Eppendorf 5417R) and 4°C. The upper phase was then transferred into a tube containing 1 mL of chloroform/isoamyl alcohol (24:1), vortexed for 2 min and centrifuged for 10 min at 10,000 rpm and 4°C. Thereafter, the upper phase was pipetted into a new tube containing 1 mL of ice cold isopropanol, mixed well and incubated for 30 min on ice. The nucleic acids were pelleted by centrifugation for 10 min at 14,000 rpm (Eppendorf 5417R) and 4°C, washed once with 70% ethanol (10 min, 14,000 rpm, 4°C), dried at RT for 30 min and finally resuspended in 20 µL RNase free water. The RNA content of the samples was determined using a NanoDrop (Thermo Scientific) device.

3.2.4.4. RNA preparation from tissues using RNeasy® Kit

Animals were anesthetized, sacrificed by cervical dislocation and organs were immediately removed, washed once with sterile PBS and cut into small pieces of ~30 mg. The tissue pieces were transferred into 600 µL of RLT buffer, homogenized using a stirrer and cell fragments were pelleted by centrifugation for 3 min at 14,000 rpm (Eppendorf 5417R). The supernatant was mixed with an equal volume of 70% ethanol and subsequently 600 µL of the mixture were added onto an RNeasy spin column. The column was centrifuged for 15 s at 14,000 rpm and the procedure was repeated with the residual sample volume. The column was washed once with 700 µL RW1 buffer (15 s, 14,000 rpm) and twice with 500 µL RPE buffer (15 s, 14000 rpm). To elute the RNA, 40 µL of RNase free water were added, incubated for 1 min and finally spun down (1 min, 14,000 rpm). The RNA concentration and quality was assessed using NanoDrop.

3.2.4.5. Semiquantitative reverse transcription PCR (RT-PCR)

For reverse transcription PCR, two different Mastermixes were prepared:

Mastermix 1:

1.0 µg	RNA
2.0 µL	oligo dT Primer [0.5 µg μL^{-1}]
x µL	ad 20 µL H_2O

Mastermix 1 was denaturated for 10 min at 70°C and subsequently cooled on ice.

Mastermix 2:

5.0 µL	5x first strand buffer
2.0 µM	0.1 M DTT [0.1 M]
1.0 µL	dNTPs [10 mM]
0.1 µL	RNAse inhibitors [5 U mL^{-1}]

Mastermix 1 and 2 were pooled and 1 µL of SuperScript® II Reverse Transcriptase [200 U μL^{-1}] was added. Amplification was performed for 1 to 2 h at 42°C in a thermomixer and afterwards the reaction was aborted by incubation of the samples at 70°C for 10 min. The generated cDNAs were stored at -20°C. The mRNA expression levels were determined by PCR, optimal annealing temperature for the used primers was identified via gradient PCR. *Gapdh* expression was determined as control.

PCR mix for semi-quantitative RT-PCR:

2.0 µL	cDNA sample
2.0 µL	10x Taq Buffer (+KCl, -$MgCl_2$)
1.2 µL	$MgCl_2$ [25 mM]
0.4 µL	dNTPs [10 mM]
0.1 µL	forward Primer [1 µg mL^{-1}]
0.1 µL	reverse Primer [1 µg mL^{-1}]
0.125 µL	native Taq-Polymerase [5 U μL^{-1}]
14.075 µL	H_2O

PCR program:

Temperature [°C]	Time [s]	Repeats
96	180	1 cycle
94	30	35 cycles
48-70	30	35 cycles
72	60	35 cycles
72	300	1 cycle
22	∞	1 cycle

RT-PCR Primer:

Pfn1 (annealing temperature 63.0°C):

Pfn1_RT_forw: 5‘ GCC ATC GTA GGC TAC AAG GAC TCG 3‘

Pfn1_RT_rev: 5‘ CCA CCG TGG ACA CCT TCT TTG C 3‘

Expected product sizes: 305 bp for *WT* and 113 bp for *Pfn1*$^{-/-}$ mRNA.

Pfn2 (annealing temperature 62.0°C):

Pfn2_RT_forw: 5‘ GCT ACG TGG ATA ACC TGA TGT GCG 3‘

Pfn2_RT_rev: 5‘ CCC TAA TAC TTA ACA GTC TGC CTA GC 3‘

Expected product size: 436 bp for the *WT* allele.

Pfn3 (annealing temperature 62.5°C):

Pfn3_RT_forw: 5‘ GCA AGC ACA AGT TGC TGG GAC TG 3‘

Pfn3_RT_rev: 5‘ GAC CCG TCT GCA GAA AGG TGT GC 3‘

Expected product size: 224 bp for the *WT* allele.

Pfn4 (annealing temperature 63.0°C):

Pfn4_RT_forw: 5‘ GCT GGG GAC GAA ACA CGT GG 3‘

Pfn4_RT_rev: 5‘ CTT CTC TGT GGC TTC CAC GCA GAC 3‘

Expected product size: 322 bp for the *WT* allele.

Twf1 (annealing temperature 53.2°C):

Twf1_RT_forw: 5‘ TAC CGC ACC CTG CGC CGG A 3‘

Twf1_RT_rev: 5‘ TCT GTA TTT CCC GTT TCT GGC TCG G 3‘

Expected product sizes: 346 bp for the *WT* and 179 bp for the Cre-recombined Twf1 allele.

Twf2a (annealing temperature 58.0°C):

Twf2a_RT_forw: 5‘ CCA GGA CCA AGA GGA GAA CTC C 3‘

Twf2a/b_RT_rev: 5‘ CTT TGA TAA GTC GGA TGG AGC CAG C 3‘

Expected product size: 274 bp for the *WT* allele.

Twf2b (annealing temperature 66.0°C):

Twf2b_RT_forw: 5‘ CAC CAG CAG ACC CAA ACT CTT CCC T 3‘

Twf2a/b_RT_rev: 5‘ CTT TGA TAA GTC GGA TGG AGC CAG C 3‘

Expected product size: 248 bp for the *WT* allele.

GAPDH (annealing temperature 60.8°C):

GAPDH_RT_forw: 5‘ GCA AAG TGG AGA TTG TTG CCA T 3‘

GAPDH_RT_rev: 5‘ CCT TGA CTG TGC CGT TGA ATT T 3‘

Expected product size: 108 bp for the *WT* allele.

DIAPH1 (annealing temperature 55.5°C)

DIAPH1_RT_forw: 5’ CAA GCT GCG GAT GAT GC 3’

DIAPH1_RT_rev: 5’ GGA CAC CTT GGC AGG AAC 3’

Expected product size: 448 bp fragment containing *DIAPH1* c.3637.

MagT1 (annealing temperature 58.0°C)

MagT1_RT_forw: 5’ TCG GAC CGT GCT GGA AGA AA 3’

MagT1_RT_rev: 5’ GAG CTT TAA CAA GAC GAC GG 3’

Expected product size: 255 bp fragment.

Tusc3 (annealing temperature 58.0°C)

Tusc3_RT_forw: 5’ TAC TGG TAG CTT TCC CTT CC 3’

Tusc3_RT_rev: 5’ ATT CTT CGT TAG CCT GCC TG 3’

Expected product size: 263 bp fragment.

Acdp1 (annealing temperature 58.0°C)

Acdp1_RT_forw: 5’ TGT TCG TCA AAG ACT TGG CC 3’

Acdp1_RT_rev: 5’ GGA TCT CCG ACT TGA TGA TC 3’

Expected product size: 261 bp fragment.

Acdp2 (annealing temperature 58.0°C)

Acdp2_RT_forw: 5’ AAG ACT TGG CCT TCG TGG AT 3’

Acdp2_RT_rev: 5’ ACA GGT CTG TCT CAT CCA AG 3’

Expected product size: 270 bp fragment.

Acdp3 (annealing temperature 58.0°C)

Acdp3_RT_forw: 5’ ATA CCA AAC TGG ACG CTG TC 3’

Acdp3_RT_rev: 5’ CAG ACA CCT TGA ATA AGG AG 3’

Expected product size: 267 bp fragment.

Acdp4 (annealing temperature 58.0°C)

Acdp4_RT_forw: 5’ CTA CAC TCG CAT TCC TGT GT 3’

Acdp4_RT_rev: 5’ GAT GAC GTC CTC CAG AGT GA 3’

Expected product size: 289 bp fragment.

Nipa1 (annealing temperature 58.0°C)

Nipa1_RT_forw: 5’ TAG TGA ACG GGT CCA CGT TC 3’

Nipa1_RT_rev: 5’ TTA GCA GAC AGC CCA ACT TG 3’

Expected product size: 267 bp fragment.

Nipa2 (annealing temperature 58.0°C)

Nipa2_RT_forw: 5’ GAA CTA CTC TGC CGT GGT TA 3’

Nipa2_RT_rev: 5’ TCA TAG CCA ATC CCA GAC CA 3’

Expected product size: 262 bp fragment.

Nipa3 (annealing temperature 58.0°C)

Nipa3_RT_forw: 5’ CAA TCT GTA TGT GGG CTT GG 3’

Nipa3_RT_rev: 5’ TTA TGA GAA CGC TCA GAG CC 3’

Expected product size: 233 bp fragment.

Nipa4 (annealing temperature 58.0°C)

Nipa4_RT_forw: 5’ ACC TTG ATC ACC TGG CAA GA 3’

Nipa4_RT_rev: 5’ TCG CAG GTG CAA ATG CAT AG 3’

Expected product size: 259 bp fragment.

Slc41A1 (annealing temperature 58.0°C)

Slc41A1_RT_forw: 5’ CTC CTT TTC CAT TGG ACT GC 3’

Slc41A1_RT_rev: 5’ ATC ATC CGC CAG AGC TCC TT 3’

Expected product size: 246 bp fragment.

Slc41A2 (annealing temperature 58.0°C)

Slc41A2_RT_forw: 5’ CAT GGC TCT GCA GAT ATT GG 3’

Slc41A2_RT_rev: 5’ GTA TGA TGG CTG CCA CAG CT 3’

Expected product size: 311 bp fragment.

Slc41A3 (annealing temperature 58.0°C)

Slc41A3_RT_forw: 5’ GAG ACG TCC CTG ATC ATT GG 3’

Slc41A3_RT_rev: 5’ CAT CGA TTT GCC CCA GTG TT 3’

Expected product size: 226 bp fragment.

Trpm6 (annealing temperature 58.0°C)

Trpm6_RT_forw: 5’ TGT GGG CGG TGC TCA TGA AG 3’

Trpm6_RT_rev: 5’ CAA GCC ATT CGT GCA CGC TG 3’

Expected product size: 450 bp fragment.

Trpm7 (annealing temperature 58.0°C)

Trpm7_RT_forw: 5’ GAG CCC AAC AGA TGC TTA TGG 3’

Trpm7_RT_rev: 5’ GGC CCG CCT TCA AAT ATC AAA G 3’

Expected product size: 550 bp fragment.

Actb (annealing temperature 58.0°C)

Actb_RT_forw: 5’ GTG GGC CGC TCT AGG CAC CAA 3’

Actb_RT_rev: 5’ CTC TTT GAT GTC ACG CAC GAT TTC 3’

Expected product size: 500 bp fragment.

3.2.4.6. Agarose gel electrophoresis

The PCR products were separated on agarose gels with different densities. In parallel, a marker with a range from 100 to 10,000 bp was run on the gels to control the size of the products. 1.5 g of agarose were added to 150 mL TAE buffer and boiled in microwave for approximately 3 min. The dissolved agarose was allowed to cool down to 60°C, DNA was marked by the addition of 50 µL L^{-1} ethidium bromide or Midori Green™ and the gel was poured into a sleigh containing a comb. The cast gel was then laid into a chamber filled with TAE buffer. The PCR products were diluted in 6x Loading Dye and each 20 µL were loaded onto the gels. The samples were separated for 30-45 min at 130 V. For big gels, 4 g agarose in 400 mL TAE buffer were used. The big gels were run at 160 V. Finally, the DNA/ethidium bromide/Midori Green™ was visualized under ultra violet light and pictures were taken with a camera (Herolab GmbH, Germany).

3.2.4.7. Immunoblotting

PRP was prepared as described above. To remove residual serum albumin, platelets were washed twice with 5 mM EDTA in PBS. For Western blotting, platelet counts of washed platelet were determined using a Sysmex KX 21-N cell analyzer (Sysmex Deutschland GmbH) and counts were adjusted to 1.0 x 10^6 platelets per µL using IP-buffer containing 1% NP-40. After an incubation time of 10 min on ice, the samples were mixed with an equal volume of reducing 2x Loading Dye and boiled for 5 min at 95°C. The denatured platelet lysates were then separated by *sodium dodecyl sulfate-* (SDS) *polyacrylamide gel electrophoresis* (PAGE) and blotted onto *polyvinylidene difluoride* (PVDF) membranes and incubated with anti-Pfn1 [1 µg mL^{-1}], anti-Twf1 [1 µg mL^{-1}], anti-Twf1/2 [1 µg mL^{-1}], anti-RIAM [1 µg mL^{-1}], anti-myosin IIa [1 µg mL^{-1}], anti-FlnA [1 µg mL^{-1}], anti-Diap1 [1 µg mL^{-1}], anti-Diap2 [1 µg mL^{-1}], anti-Diap3 [1 µg mL^{-1}], anti-RAPH1 [1 µg mL^{-1}], anti-α-tubulin [0.5 µg mL^{-1}], anti-β-tubulin [0.5 µg mL^{-1}], anti-acetylated-tubulin [0.2 µg mL^{-1}], anti-detyrosinated (Glu)-tubulin [1 µg mL^{-1}], anti-MagT1 [1 µg mL^{-1}], or anti-WASp [1 µg mL^{-1}] antibodies overnight at 4°C. For visualization, horseradish peroxidase-conjugated secondary antibodies and enhanced chemiluminescence solution were used. Detection was performed using a MultiImage® II FC Light Cabinet (Alpha Innotech cooperation) device. GPIIIa, Gapdh or β-actin levels were determined as loading controls.

3.2.4.8. Co-Immunoprecipitation

Washed resting or CRP-treated platelets were lysed by sonification under low-salt conditions in PIPES (pH 7.0) buffer, supplemented with 1 x *protease inhibitors* (PI) and [0.5 mM] *phenylmethylsulphonylfluorid* (PMSF). Platelet lysates were precleared by incubation with protein

G-sepharose for 1 h at 4°C under agitation. WASp was precipitated by incubation of the cleared lysates with mouse anti-WASp antibody (3 µg)-coated protein G-sepharose overnight at 4°C. *Supernatant* (SN) was collected and the sepharose pellet was washed extensively with PIPES buffer supplemented with PI (5 min at 2,800 rpm) before 2x Laemmli buffer was added. Samples (total lysate, *immunoprecipitation* (IP) and SN) were separated by SDS-PAGE and immunoblotted with a rabbit anti-Pfn1 [1 µg mL^{-1}] or a rabbit anti-WASp [1 µg mL^{-1}] antibody.

3.2.5. *In vitro* analysis of platelet function

3.2.5.1. Purification of platelets from whole blood of mice

Mice were bled under isoflurane anesthesia up to 1 mL in 300 µL heparin [20 U mL^{-1}] or ACD buffer. 300 µL of heparin [20 U mL^{-1}] were added and the samples were centrifuged for 6 min at 800 rpm. Subsequently, the upper phase and the buffy coat with some erythrocytes were transferred into 300 µL heparin [20 U mL^{-1}]. To further purify the platelets centrifugation was repeated (6 min, 800 rpm) and only the upper phase without any erythrocytes was pipetted into a new tube containing 2 µL of apyrase [0.02 U mL^{-1}, f.c.] and 5 µL PGI_2 [0.1 µg mL^{-1}, f.c.]. Platelets were spun down (5 min, 2,800 rpm), resuspended in 1 mL of Tyrode's buffer without Ca^{2+}, containing 2 µL of apyrase [0.02 U mL^{-1}, f.c.] and 5 µL PGI_2 [0.1 µg mL^{-1}, f.c.] and allowed to rest for 5 min at 37°C. The washing step was repeated twice, before the pellet was resuspended in an appropriate volume of Ca^{2+}-free Tyrode's buffer containing apyrase [0.02 U mL^{-1}, f.c.] and the platelets were allowed to rest for 30 min prior to experiments.

3.2.5.2. Purification of platelets from whole blood of humans

Fresh blood samples of patients and healthy volunteers were collected in 1/10 volume of acid-citrate-dextrose and centrifuged for 10 min at 200 g. PRP without any erythrocytes was collected, supplemented with 2 µL of apyrase [0.02 U mL^{-1}, f.c.] and 5 µL PGI_2 [0.1 µg mL^{-1}, f.c.], per mL PRP. Prior to immunofluorescence staining the platelets were pelleted by centrifugation for 10 min at 800 g and washed twice with Tyrode's-HEPES buffer containing 2 µL apyrase [0.02 U mL^{-1}, f.c.] and 5 µL PGI_2 [0.1 µg mL^{-1}, f.c.]. The samples were allowed to rest for 30 min at 37°C.

3.2.5.3. Purification of peripheral blood mononuclear cells (PBMC)

3 mL Histopaque®-1077 were added to a 15 mL Falcon tube and 3 mL of whole blood were carefully layered on top (for studies with patients the left overs from platelet purification were used). Samples were centrifuged for 30 min at 400 g and RT with the brake set to 0 allowing the rotor to swing out. Erythrocytes aggregated through crosslinking with polysucrose and

granulocytes became slightly hypertonic and therefore both pelleted during centrifugation. The mononuclear cells got stuck at the interface between the Histopaque-1077 and the platelet-rich plasma. The upper phase was removed to within 0.5 cm of the opaque interface. The mononuclear cell within the opaque interface were immediately supplied with 10 mL DPBS and washed by centrifugation for 10 min at 250 g and RT. The supernatant was discarded, the pellet resuspended in 5 mL DPBS and the cell number was determined with a blood cell analyzer (Sysmex/Coulter). Samples were centrifuged once more for 10 min at 250 g and cells were used for immunoblotting, immunostaining, or DNA extraction for sequencing.

3.2.5.4. Determination of platelet size and count

50 µL of blood was withdrawn from the retro-orbital plexus in 300 µL heparin [20 U mL^{-1}]. The sample was filled up with 650 µL Tyrode's buffer without Ca^{2+} (1:20 dilution). Platelet count and size were assessed by incubating diluted, heparinized blood with fluorophore-conjugated antibodies directed against platelet-specific epitopes and subsequently analyzed using flow cytometry (FACSCalibur, BD Biosciences). *Forward scatter* (FSC) and the counts per second were determined. Alternatively, platelet count and size were measured in heparinized blood in a Sysmex analyzer.

3.2.5.5. Preparation of blood smears

Blood smears were generated by placing a 5 µL drop of venous blood at one end of a glass slide and pulling the blood drop longitudinally across the slide using a second glass slide at a 45° angle. Slides were allowed to dry, fixed with May-Gruenwald's solution and stained with Giemsa's solution according to Pappenheim.

3.2.5.6. Pappenheim stain of blood smears

Air-dried blood smears were stained for 7 min in May-Gruenwald's solution and counterstained for 10 min in Giemsa working solution. Samples were rinsed thoroughly with phosphate buffered saline and allowed to dry. Slides were cleaned with methanol and analyzed with an inverted Leica DMI 4000 B microscope.

3.2.5.7. Platelet glycoprotein expression

The expression levels of the most prominent platelet glycoproteins were determined by incubating heparinized blood with fluorophore-conjugated monoclonal antibodies and fluorescence intensities were analyzed by flow cytometry. The expression levels [*mean fluorescence intensity* (MFI)] of KO platelets were compared with those of WT controls.

3.2.5.8. Integrin recruitment

Surface exposure of the most prominent platelet integrins was determined in resting and activated (thrombin 0.1 U mL^{-1}, f.c.) platelets by incubating heparinized blood/ washed platelets (50,000 μL^{-1}) with fluorophore-conjugated monoclonal antibodies. The relative change in surface prevalence was determined by flow cytometry.

3.2.5.9. Platelet granule content

Surface and cytoplasmic prevalence of vWF, P-selectin, fibrinogen and fibronectin were determined by flow cytometry. To this end, 5 x 10^6 platelets were fixed for 30 min in 1% PFA in PBS or fixed and permeabilized in the presence of 1% PFA and 0.1% NP40 in PBS. Subsequently, platelets were washed with 4 mL PBS, spun down for 5 min at 1,200 rpm and stained with FITC-conjugated monoclonal antibodies for 15 min at RT. The reaction was aborted by the addition of 500 µL PBS.

3.2.5.10. Platelet integrin activation and degranulation

50 µL of blood were withdrawn under isoflurane anesthesia, diluted in 300 µL heparin [20 U mL^{-1}] and washed twice (5 min, 2,800 rpm) with 1 mL of Ca^{2+}-free Tyrode's buffer. After the final washing step, the washed blood or washed platelets was resuspended in an appropriate volume of Ca^{2+}-containing Tyrode's buffer. Washed blood of *WT* and mutant mice was incubated with fluorophore-conjugated antibodies directed against activated β1 integrins (9EG7-FITC) or αIIbβ3 integrins (PE-conjugated JON/A) and against P-selectin (FITC-labeled WUG 1.9). Subsequently, the samples were activated with different agonists such as ADP, U46619 (a stable thromboxane A_2 analogue), thrombin, CRP and the snake venom toxins *convulxin* (CVX) and *rhodocytin* (Rhd). While CVX and CRP activate platelets via GPVI, Rhd signals through the CLEC-2. The other agonists, (ADP, U46619 and thrombin) signal via GPCR. The reaction was stopped after an incubation for 7 min at 37°C and 7 min at RT by the addition of 500 µL PBS. This experiment monitors the signaling-dependent activation of αIIbβ3 integrins and the process of degranulation (determined by P-selectin exposure).

3.2.5.11. Aggregometry

In aggregometry, light transmission of a washed platelet suspension was monitored over time (10 min) using a four-channel aggregometer (APACT, Laborgeräte und Analysensysteme, Hamburg). 1.5 x 10^5 platelets per µL in 150 µL Ca^{2+}-containing Tyrode's buffer supplied with 100 µg mL^{-1} human fibrinogen were activated with different concentrations of agonists (1.6 µL, 100-fold-concentrated), specific for GPVI signaling, such as collagen, CRP and

CVX, or GPCR-related agonists represented by ADP, U46619, thrombin or PAR-4-peptide. For stimulation with thrombin, Ca^{2+}-containing Tyrode's buffer without human fibrinogen was used. Aggregation studies with ADP were performed in platelet-rich plasma [1.5 x 10^5 platelets per µL]. Aggregation was expressed as arbitrary units with the light transmission of 160 µL Tyrode's buffer with Ca^{2+} and fibrinogen set as 100%.

3.2.5.12. Platelet adhesion under flow conditions

Rectangular coverslips (24 x 60 mm) were coated overnight at 37°C with 70 µg mL^{-1} fibrillar type I collagen and prior to the experiment blocked for 1 h with 1% BSA. Mice were bled up to 1 mL in 300 µL heparin [20 U mL^{-1}], the blood was diluted 3:1 with Ca^{2+}-containing Tyrode's and incubated for 5 min at 37°C with DyLight-488-conjugated anti-GPIX derivative [0.2 µg mL^{-1}]. A transparent flow chamber with a slit depth of 50 µm was covered with a collagen-coated and blocked cover slip and perfused for 4 min with the prepared blood using a pulse-free pump and different wall shear rates, reflecting the blood flow in different vessel types (1,000 s^{-1}, 1,700 s^{-1}). Subsequently, the chamber was perfused for 75 s with Tyrode's buffer at the same shear rate and at least five phase-contrast and fluorescent pictures were taken using a Zeiss Axiovert 200 inverted microscope (40x/0.60 objective) equipped with a CoolSNAP-EZ camera (Visitron). The recorded phase-contrast and fluorescence pictures were analyzed off-line using Metavue software.

3.2.5.13. Platelet spreading on fibrinogen

The ability of platelets to adhere and form filo- and lamellipodia on a fibrinogen-coated surface, in response to thrombin, was assessed by a spreading assay. Rectangular coverslips (24 x 50/60 mm) were coated with 10 µg human fibrinogen [100 µL of 100 µg mL^{-1}] overnight at 4°C in a humid chamber. Slides were blocked with 1% BSA in PBS for 1 h at RT. 30 µL of washed platelets [3 x 10^5 per µL] were mixed with 70 µL Ca^{2+}-free Tyrode's buffer, activated with 0.01 U mL^{-1} thrombin and immediately allowed to spread on the fibrinogen-coated coverslips at RT. After different time intervals, the adherent platelets were fixed with 300 µL 4% PFA for 5 min and *differential interference contrast* (DIC) microscopy pictures were taken using an inverted microscope Zeiss HBO 100 (Axiovert 200M, Zeiss). For analysis, the phase abundance of the different spreading stages (1, resting; 2, formation of filopodia; 3, formation of filopodia and lamellipodia; 4, fully spread) was determined. In addition, for visualization of the spreading process, time-lapse videos were recorded by taking pictures every 5 s for 20 min. Similar experiments were performed with the GPVI-specific agonist CRP [6 µg mL^{-1}].

3.2.5.14. Platelet spreading on von Willebrand factor

GPIb signaling was specifically addressed by allowing platelets [3 x 10^5 per µL] to spread on a vWF matrix. Coverslips were coated overnight at 4°C with anti-human vWF antibody [4 µg mL^{-1}], blocked for 1 h with 1% BSA in PBS and afterwards incubated with 100 µL heparinized mouse plasma for 2 h at 37°C. 30 µL washed platelets adjusted to a concentration of 0.3 x 10^6 platelets per µL were mixed with 70 µL Ca^{2+}-containing Tyrode's buffer, incubated for 10 min with integrilin [40 µg mL^{-1}] to block αIIbβ3 integrins. Platelets were stimulated with botrocetin [2 µg mL^{-1}] to enhance GPIb binding and allowed to adhere. Spreading was stopped after the respective time points by the addition of 300 µL 4% PFA in PBS. Analysis was performed by DIC microscopy.

3.2.5.15. Stimulated emission depletion and confocal microscopy

Subsequent to the spreading assays on fibrinogen, CRP or vWF platelets were fixed and permeabilized in PHEM complete buffer for 20 min at RT and blocked for 2 h at 37°C with 5% BSA in PBS. The platelets were further incubated for at least 1 h with fluorophore-labeled antibodies directed against anti-α-tubulin [0.5 µg mL^{-1}], anti-β-tubulin [1 µg mL^{-1}] and anti-acetylated-tubulin [1 µg mL^{-1}] to label the microtubules, anti-profilin1 [1 µg mL^{-1}], anti-myosin IIa [1 µg mL^{-1}], anti-WASp [1 µg mL^{-1}], anti-Diap1 [1 µg mL^{-1}], or anti-vWF [1 µg mL^{-1}] to label the α-granules and Atto647N-conjugated phalloidin [170 nM] to stain for F-actin. After intense washing unlabeled primary antibodies were detected with the respective fluorophore-conjugated secondary antibodies [0.33 µg mL^{-1}]. Confocal (Leica TCS SP5) microscopy and a 100x oil objective was used to determine the number and size of vWF-containing granules per platelet, to evaluate the subcellular localization of proteins, as well as the structure of the cytoskeleton. To visualize the cytoskeleton of resting platelets, 30 µL washed platelets [3 x 10^5 per µL] were mixed with 70 µL PHEM complete buffer and allowed to adhere to poly-L-lysine-coated coverslips and processed as described above. For *stimulated emission depletion* (STED) microscopy (Leica TCS STED) samples were similarly processed as described above for confocal microscopy. Images were further processed using Image J software (National Institute of Health, USA).

3.2.5.16. Platelet clot retraction

Mice were bled up to 700 µL in 70 µL sodium citrate [0.129 mM] and PRP was isolated by centrifugation at 1,800 rpm for 5 min. Plasma was collected and platelets were resuspended in 1 mL Ca^{2+}-free Tyrode's buffer supplemented with 2 µL of apyrase [0.02 U mL^{-1}, f.c.] and 5 µL PGI_2 [0.1 µg mL^{-1}, f.c.]. Platelet count was determined and 7.5 x 10^7 platelets were resuspended in 250 µL plasma. PRP [3 x 10^5 platelets per µL] was recalcified by adding

20 mM $CaCl_2$ and supplemented with 1 µL of red blood cells to visualize the clot. Clot formation was initiated by the addition of 4 U mL^{-1} thrombin (Sigma). Clot formation and retraction was recorded up to 4 h and the residual serum volume was determined.

3.2.5.17. TEM of platelets

Platelets ultrastructure was investigated by TEM. PRP was prepared and mixed in 1:2 ratio with 5% glutaraldehyde in PBS for 10 min at 37°C and for 1 h at RT. Platelets were spun down at 1,500 g for 5 min, washed three times with cacodylate buffer and incubated for 1 h at RT with 1% OsO_4 in cacodylate buffer. Afterwards, the samples were washed twice with cacodylate buffer and H_2O_{bidest} and 2% uranyl acetate (in H_2O) was added for 1 h at 4°C. Then, platelets were dehydrated by a graded ethanol series (3x 70%, 5 min; 3x 95%, 15 min; 3x 100%, 15 min), incubated twice for 10 min with propylenoxide and afterwards transferred in a 1:1 mixture of propylenoxide and epon for 1 h under rotation. After this step, epon was added twice and samples were incubated overnight at RT. Epon was allowed to harden for 48 h at 60°C. Ultrathin sections were prepared, stained with 2% uranyl acetate (in ethanol) and lead citrate (in H_2O) and examined at 80 kV under a EM900 (Zeiss).

3.2.5.18. Platelet actin polymerization

The ability of platelets to incorporate G-actin monomers into F-actin filaments was assessed in a F-actin assembly assay. Washed platelets [5 x 10^5 per µL] were diluted (50 µL: 50 µL) in Tyrode's with Ca^{2+} and stained with 10 µL DyLight-649-labeled a-GPIX antibody derivative by incubation for 3 min at 37°C and 400 rpm in a thermomixer (Eppendorf). Thereafter, the samples were divided into two separate subsets: a resting and an activated sample (ADP+U46, thrombin, CRP, CVX, Rhd; 2 min, 37°C, 400 rpm). After activation, the platelets were fixed for 10 min at 37°C and 400 rpm with 0.55 volumes of 10% PFA and spun down by centrifugation for 5 min at 2,800 rpm (HERAEUS Multifuge 3S-R, Thermo Scientific). The pellets were permeabilized in 55 µL Tyrode's with Ca^{2+} supplied with 0.1% Triton X-100 and stained with 10 µM phalloidin-FITC for 30 min at RT. The reaction was aborted by the addition of 500 µL PBS. To remove residual fluorophore-conjugated phalloidin, the platelets were washed once (5 min at 2,800 rpm) and resuspended in 500 µL PBS. Mean fluorescence FITC-intensity was assessed using flow cytometry.

3.2.5.19. Sedimentation of the actin/microtubule cytoskeleton

190 µL of resting or toxin-treated [10 µM colchicine, 200 ng mL^{-1} TSA] platelets [3 x 10^5 per µL] were lysed by the addition of 20 µL 10x PHEM buffer containing 1% Triton X-100, 60 µM taxol, 20 µM phalloidin and protease inhibitors. 105 µL served as whole cell lysate. Polymer-

ized and soluble fractions were separated by centrifugation for 30 min at 100,000 g and 37°C in a TLA-100 rotor (Beckman Coulter). Total platelet lysates, soluble *supernatant* (S) and insoluble *pellets* (P) were supplemented with SDS-PAGE buffer containing 5% β-mercaptoethanol and incubated for 5 min at 95°C. Samples were separated by SDS-PAGE, blotted onto PVDF membranes and probed with anti-α-tubulin [0.5 µg mL^{-1}], anti-β-tubulin [1 µg mL^{-1}], anti-acetylated tubulin [1 µg mL^{-1}], or anti-β-actin [1 µg mL^{-1}] antibodies.

3.2.5.20. Cold-induced microtubule disassembly

Microtubules were depolymerized by incubation of washed platelets [3 x 10^5 per µL] for 3 h at 4°C. Microtubule reassembly was then allowed by subsequent rewarming at 37°C for 30 min. Samples maintained at 4°C and 37°C, as well as rewarmed platelets were fixed and permeabilized in PHEM buffer supplemented with 4% PFA and 0.1% Igepal CA-630, and allowed to adhere to poly-L-lysine-coated coverslips. Samples were immunostained using an anti-β-tubulin [2.5 µg mL^{-1}], anti-acetylated-tubulin [1.7 µg mL^{-1}] or anti-α-tubulin Alexa F488 antibody [3.33 µg mL^{-1}] and visualized with a Leica TCS SP5 confocal microscope (Leica Microsystems).

3.2.5.21. TEM of the platelet cytoskeleton

The cytoskeleton of resting and spread platelets (15 min either on vWF, fibrinogen or CRP) was visualized by TEM. To prepare samples of resting platelets, washed platelets were spun (5 min at 280 g) onto poly-L-lysine-coated coverslips in PHEM buffer supplemented with 0.75% Triton X-100, 1 µM phalloidin, 1 µM taxol and 0.1% glutaraldehyde. After washing with PHEM buffer containing 0.1 µM phalloidin and taxol, adherent platelets were fixed for 10 min in PHEM buffer supplemented with 1% glutaraldehyde. To prepare samples of spread platelets, washed platelets were spun (5 min at 280 g) onto fibrinogen- [100 µg mL^{-1}], CRP- [10 µg mL^{-1}] or plasma vWF-coated slides in Tyrode's-HEPES buffer, stimulated with 0.01 U mL^{-1} thrombin or 1 U mL^{-1} botrocetin, and incubated for 15 min at RT. To stop the reaction, coverslips were incubated for 5 min with PHEM buffer containing 0.75% Triton X-100, 0.1% glutaraldehyde, 1 µM phalloidin and taxol. After a quick washing step with PHEM buffer containing 0.1 µM phalloidin and taxol, adherent platelets were fixed for 10 min in PHEM buffer supplemented with 1% glutaraldehyde. Coverslips were extensively washed in ultra-pure water, rapidly frozen in a liquid helium-cooled copper block, transferred to a liquid N_2-cooled stage, freeze-dried at -90°C and metal cast with 1.2 nm of tantalum-tungsten with rotation at 45° and 3 nm of carbon at 90° without rotation. Replicas were floated, picked up on formvar-carbon-coated grids and examined in a JEOL 1200-EX TEM at 80 kV.

3.2.5.22. Inductively coupled plasma mass spectrometry (ICP-MS)

The cation content of 4 x 10^7 platelets was analyzed by ICP-MS of platelets from PRP. ICP-MS analysis was performed by ALS Scandinavia AB (Lulea, Sweden).

3.2.6. *In vivo* analysis of platelet function

3.2.6.1. Tail bleeding time

Mice were anesthetized by intraperitoneal injection of triple narcotics (Midazolam [5 µg g^{-1}], Medetomidine [0.5 µg g^{-1}], Fentanyl [0.05 µg g^{-1}]) and a 1 mm segment of the tail tip was removed using a scalpel. Tail bleeding was monitored by gently absorbing blood on filter paper at 20 s intervals without making contact with the wound site. Bleeding was determined to have ceased when no blood was observed on the paper. Experiments were stopped after 20 min by cauterization and anesthesia was antagonized by injection of Atipam [2.5 µg g^{-1}], Flumazenil [0.5 µg g^{-1}] and Naloxon [1.2 µg g^{-1}].

3.2.6.2. $FeCl_3$-induced injury of mesenteric arterioles

The mesentery of 3- to 4-week old anesthetized mice (ketamine/xylazine [100/5 mg kg^{-1}]) was exposed by a midline abdominal. Endothelial damage in mesenteric arterioles was induced by application of a 3 mm^2 filter paper soaked with 20/13% $FeCl_3$. Arterioles were visualized using a Zeiss Axiovert 200 inverted microscope equipped with a 100-W HBO fluorescent lamp source and a CoolSNAP-EZ camera (Visitron). Digital images were recorded and analyzed using the Metavue software. Adhesion and aggregation of fluorescently labeled platelets (Dylight-488–conjugated anti-GPIX derivative) was monitored until complete occlusion occurred (blood flow stopped for > 2 min). Experiments were performed by Sarah Schießl (Twf2a) and Karen Wolf (RIAM) in our laboratory.

3.2.6.3. Determination of platelet life span

The clearance of platelets from the circulation was determined by the retro-orbital injection of 5 µg DyLight 488-labeled anti-GPIX derivative in PBS into mice. The percentage of labeled platelets is determined by daily blood withdrawal (50 µL) and subsequent analysis by flow cytometry.

3.2.6.4. Macrophage depletion with Clodronate

Anesthetized female and male mice were retro-orbitally injected with clodronate-encapsulated or PBS-encapsulated liposomes [2 µL per g body weight]. 50 µL of blood were taken at 0, 24, 48, 72 and 96 h after injection and, subsequently, platelet counts and size were determined by flow cytometry.

3.2.6.5. Splenectomy of mice

Platelet count and size of female and male mice was determined by flow cytometry before surgical splenectomy. The surgical site on anesthetized mice was sterilely prepared and a 1 cm paramedian incision over the left upper quadrant was made. After the spleen was identified, blood supply was stopped by ligation of vascular pedicles with surgical suture material and the spleen was removed. Mice were monitored for 48 h for signs of internal bleeding and infection. After a recovery period of 6 days, platelet counts and size were followed over time by flow cytometry.

3.2.7. *In vitro* analysis of MKs

3.2.7.1. Measurement of Thpo levels in mouse serum

Thpo ELISA was performed according to the manufacturer's protocol (R&D Mouse Thrombopoietin DuoSet). Briefly, a MaxiSorp® 96 well plate was coated overnight at RT with 2 µg mL^{-1} rat anti-mouse Thpo antibody. On the next day, the plate was washed three times with washing buffer and blocked with 1% BSA in PBS for 1 h at RT. Meanwhile, the sera were prepared: Mice were bled from the retro-orbital plexus with heparin-free capillaries and the blood was allowed to clot. The provided Thpo standard was prepared according to the manufacturer's advice. Afterwards the sera were collected and immediately applied as duplicates onto the anti-Thpo-IgG coated 96-well plate and incubated for 2 h at RT. The plate was washed three times, incubated for 2 h with 200 ng mL^{-1} biotinylated goat anti-mouse Thpo antibodies, washed three times and incubated for 20 min at RT with HRP-conjugated streptavidin. After another three washing steps, TMB, a HRP substrate, was added and incubated for 20 min at RT. The reaction was stopped by the addition of 50 µL 2 N H_2SO_4. Intensities and concentrations of the samples were determined using a Multiskan Ascent (96/384) plate reader (MTX Lab Systems).

3.2.7.2. *In vitro* differentiation of MKs from fetal liver cells

The ability of MKs to form proplatelets was investigated by culture, differentiation, enrichment and staining of MKs, derived from fetal liver cells. For this, the livers of 13.5-14.5 days old mouse embryos were isolated from time-mated mice and homogenized in MK-medium using a syringe with 18G and 22G needles. The single cell suspensions were centrifuged (900 rpm, 5 min), resuspended in MK-medium containing Thpo [50 ng mL^{-1}, f.c.] and cultured for 72 h at 37°C and 5% CO_2. On day three of culture, MKs were enriched by a two step BSA density gradient (prepared by overlaying to 37°C prewarmed 3% BSA with an equal volume of 1.5% BSA in PBS). The cultured cells were gently overlaid on the BSA gradient and allowed to

sediment for 45 min at RT. The lowest 500-800 µL contained the biggest cells and the MKs were collected, centrifuged (200 g, 5 min), and finally resuspended in MK-medium supplemented with Thpo [50 ng mL^{-1}, f.c.]. Thereafter, the cells were cultivated overnight at 37°C and 5% CO_2 in 12-well plates. On day four, the percentage of proplatelet-forming MKs was determined by determining the total number of MKs as well as the number of proplatelet-forming MKs under a light microscope.

3.2.7.3. Isolation and *in vitro* differentiation of BM MKs

Hematopoietic stem cells were isolated from male mouse BM single cell suspensions using a magnetic bead-based negative depletion kit (anti-rat-IgG Dynabeads, Invitrogen or MagniSort, eBioscience) in combination with (biotinylated) rat-anti-mouse antibodies directed against CD45R/B220, TER-119, CD3, Ly-6G/C and CD11b (each 0.5 µg per 10^7 cells). Experiments were performed according to the manufacturer's protocol. Cells were cultured in MK medium supplemented with 50 µg mL^{-1} recombinant hirudin and 0.5% Thpo f.c. at 37°C, 5% CO_2 for 3 days, prior to MK enrichment using a two-step BSA density gradient. On day 4, the percentage of proplatelet-forming MKs was determined using a light microscope (Zeiss) or MKs were used for spreading experiments or processed for immunofluorescence staining.

3.2.7.4. MK culture from whole BM (Boston protocol)

A single cell suspension of the BM in StemPro®-34 serum-free medium (Gibco®) including 2 mM L-Glutamine and supplemented with 2.6% StemPro®-34 Nutrient Supplement, 40x (Gibco®) was prepared and passed through a 50 µm cell strainer. Cells were washed once (5 min at 200 g) and resuspended in 5 mL culture medium, supplemented with 50 ng mL^{-1} SCF f.c. After 48 h incubation in 2 wells of a 6 well plate, medium was replaced (5 min at 200 g) by culture media supplemented with 50 ng mL^{-1} SCF and Thpo f.c. After further 48 h medium is replaced by culture media supplemented with 50 ng mL^{-1} Thpo f.c. On the next day, MKs are enriched by a two-step BSA density gradient and resuspended in culture media. Analysis of proplatelet formation, MK spreading, patch clamp measurements, ICP-MS, or preparation of lysates was performed after another 24 h.

3.2.7.5. Electrophysiology

Patch clamp experiments were performed at a whole-cell configuration. Currents were elicited by a ramp protocol from -100 mV to +100 mV over 50 ms acquired at 0.5 Hz and a holding potential of 0 mV. Inward currents were extracted at -80 mV, outward currents at +80 mV and plotted versus time. Data were normalized to cell size as pA pF^{-1}. Capacitance was measured using the automated capacitance cancellation function of the EPC10 (HEKA,

Lambrecht, Germany). Nominally Mg^{2+}-free extracellular solution contained 140 mM NaCl, 3 mM $CaCl_2$, 2.8 mM KCl, 0 mM $MgCl_2$, 10 mM HEPES-NaOH, 11 mM glucose (pH 7.2, 300 mOsm). Intracellular solution contained 120 mM Cs-glutamate, 8 mM NaCl, 1 mM $MgCl_2$, 10 mM HEPES, 10 mM BAPTA, 5 mM EDTA (pH 7.2, 300 mOsm). Experiments were performed in collaboration with Dr. Vladimir Chubanov from the Walther-Straub-Institute for Pharmacology and Toxicology, Ludwig-Maximilians University Munich.

3.2.7.6. MK spreading

In vitro cultivated BM MKs were allowed to adhere and spread at 37°C and 5% CO_2 on coverslips coated with fibrillar collagen type I [50 µg mL^{-1}], fibrinogen [100 µg mL^{-1}] or CRP [6-10 µg mL^{-1}] for the indicated time points. MK spreading was stopped by fixation and permeabilization of the cells using PHEM buffer supplemented with 4% PFA and 0.1% IGEPAL® CA-630. Samples were processed for immunofluorescence staining.

3.2.7.7. Immunofluorescence staining of cultured MKs

To visualize the cytoskeleton, the cultured MKs were spun onto glass slides (Shandon Cytospin 4, Thermo Scientific) or allowed to spread on different matrices, fixed and permeabilized in PHEM buffer supplemented with 4% PFA and 0.1% IGEPAL® CA-630 and blocked with 1% BSA in PBS. F-actin was stained using phalloidin-Atto647N [170 nM] and tubulin was either stained with anti-α-tubulin-Alexa F488 [3.33 µg mL^{-1}] or anti-acetylated-tubulin [2 µg mL^{-1}] antibodies. Anti-phospho-ASAP [10 µg mL^{-1}], anti-WASp [10 µg mL^{-1}], anti-vinculin [4 µg mL^{-1}] or anti-myosin IIa [10 µg mL^{-1}] antibody stainings served as podosome markers. Nuclei were stained using DAPI [1 µg $µL^{-1}$] prior to mounting of samples with Fluoroshield. Visualization was performed with a Leica TCS SP5 confocal microscope (Leica Microsystems).

3.2.7.8. Ultrastructural analysis of MKs using TEM

For TEM on BM samples, the femora of young (6-weeks) and old (12-weeks) mice were isolated and fixed overnight at 4°C in Karnovsky fixation buffer. Thereafter, femora were decalcified for three consecutive days. Contrasting, embedding and analysis of the samples was performed as described above for platelets.

3.2.8. *In vivo* analysis of MKs

3.2.8.1. Sample preparation for histology

Number, structure and location of MKs were assessed using conventional histology as well as specific GPIb-immunostainings and TEM. Spleen and femora of 6- and 12-week-old knockout and WT mice were isolated and fixed overnight in 4% PFA in PBS at 4°C. Femora were decalcified for 2 weeks in decalcification buffer, which was exchanged every two days. After decalcification, spleens and femora were dehydrated in an automated tissue processor (Leica ASP200S) and embedded in paraffin. Using *immunohistochemistry* (IHC), MKs and platelets were specifically stained in these tissues with HRP-conjugated anti-GPIb antibodies.

3.2.8.2. Histology – hematoxylin and eosin (HE) staining of paraffin sections

After embedding in paraffin, 3 µm thick sections of the formalin-fixed paraffin embedded spleens and femora were prepared, immobilized on glass slides and allowed to dry overnight at 37°C. On the following day, deparaffinization and rehydration was performed using xylene (2 x 5 min), followed by a graded alcohol series (100%, 96%, 90%, 80% and 70%, each 2 min) and finally the slides were transferred into H_2O_{bidest} (2 min). Sections were stained with hematoxylin for 15 s and blueing was carried out for approximately 10 min with tap water. As counterstaining 0.05% Eosin (2 min) was used. Slides were washed once with H_2O_{bidest} and dehydrated by a graded alcohol series (70%, 80%, 90%, 96% and 100%, each 2 min) followed by xylene (2 times 5 min). The sections were mounted using Eukitt®, a xylene-based mounting medium. Analysis was performed with an inverted Leica DMI 4000 B microscope.

3.2.8.3. Histology – immunohistochemistry on paraffin sections

3 µm sections of formalin fixed paraffin embedded spleens were cut using a rotation microtome (HM 355, Microm) and incubated overnight at 37°C. The next day, deparaffinization (2 x 5 min xylene) and rehydration (each 2 min 100%, 96%, 90%, 80%, 70% ethanol and H_2O) was performed. Heat induced antigen retrieval was performed in EDTA-buffer (pH 8.0) for 10 min at 97°C in a heat steamer (Braun). After boiling, the samples were allowed to cool down for 20 min at RT and endogenous HRP was blocked by incubating the slides for 10 min in 3% H_2O_2 solution. After three washing steps (1 min each, in washing buffer), the slides were incubated with blocking solution for 1 h at RT. Antibody incubation was performed overnight at 4°C with a 1:1 mixture of HRP-conjugated 13G12 and 7A9 (1:1,000), directed against GPIb, in blocking solution. The next day, the slides were washed three times for 5 min and incubated with the substrates DAB or AEC. Staining was aborted by transferring the slides into washing buffer for 5 min. Counterstaining was performed with hematoxylin for 15 s and blueing was carried out for approximately 10 min with tap water. Slides stained with

AEC were immediately mounted using Aquatex® and a cover slip. After DAB staining, the slides were dehydrated by a graded alcohol series and permanently covered with Eukitt®. Analysis was performed with an inverted Leica DMI 4000 B microscope.

3.2.8.4. Immunostaining on cryosections

Excised spleens were covered with Tissue Freezing Medium® and immediately frozen in liquid nitrogen. Samples were stored at -80°C until further processing. 5 µm thick cryosections were prepared using a cryostat (CM1900, Leica) and immobilized on glass slides. The sections were fixed with ice cold aceton (-20°C) for 20 min, air dried, washed three times (5 min) in PBS and endogenous peroxidase was blocked by incubation for 20 min with 0.03% H_2O_2 in PBS. Thereafter, the sections were incubated for 1 h at RT with blocking buffer and stained for 2 h at RT with a 1:1 mixture of HRP-labeled 15E2 and 3G6 anti-GPIb antibodies (1:750 in blocking buffer). After three washing steps in PBS (each 5 min) detection was carried out using AEC as substrate. Staining intensity was controlled by observing the slides through a light microscope. When the desired intensity was reached, the slides were washed with PBS for 5 min to stop the staining and counterstaining with hematoxylin and blueing in tap water (app. 10 min) was carried out. Analysis was performed with an inverted Leica DMI 4000 B microscope.

3.2.8.5. Immunofluorescence staining on whole femora cryosections

Femora and spleen of mice were isolated, fixed with 4% PFA and 5 mM sucrose for 1 h under agitation, transferred into 10% sucrose in PBS and dehydrated using a graded sucrose series (each 24 h in 10%, 20% and 30% sucrose in PBS, respectively). Subsequently, the samples were embedded in Cryo-Gel and shock frozen in liquid nitrogen. Frozen samples were stored at -80°C. Seven-micrometer-thick cryosections were generated using the CryoJane tape transfer system (Leica Biosystems) and probed with Alexa F488-conjugated anti-GPIb antibodies 7A9 and 13G12 [1.33 µg mL^{-1}], to specifically label platelets and MKs, and Alexa F647-conjugated anti-CD105 antibodies [3.33 µg mL^{-1}] to stain the endothelium. Nuclei were stained using DAPI (4',6-diamidino-2-phenylindole) [1 µg mL^{-1}]. Samples were visualized with a Leica TCS SP5 confocal microscope (Leica Microsystems).

3.2.8.6. Two-photon intravital microscopy of the BM

Mice were anesthetized and a 1 cm incision was made along the midline to expose the frontoparietal skull while carefully avoiding damage to the bone tissue. The mouse was placed on a customized metal stage equipped with a stereotactic holder to immobilize its head.[40,49] Bone marrow vasculature was visualized by injection of tetramethylrhodamine dextran

(8 µg g^{-1} body weight, 2 MDa, Molecular Probes). Platelets and MKs were antibody-stained (0.6 µg g^{-1} body weight anti-GPIX-Alexa F488). Images were acquired with a fluorescence microscope equipped with a 20x water objective with a numerical aperture of 0.95 and a TriM Scope II multiphoton system (LaVision BioTec), controlled by ImSpector Pro-V380 software (LaVision BioTec). Emission was detected with HQ535/50-nm and ET605/70-nm filters. A tunable broad-band Ti:Sa laser (Chameleon, Coherent) was used at 760 nm to capture Alexa F488 and rhodamine dextran fluorescence. ImageJ software (NIH) was used to generate movies. Two-photon intravital microscopy was performed by Judith M. M. van Eeuwijk.

3.2.8.7. Platelet depletion

Circulating platelets were depleted by injection of 1.25 µg anti-GPIbα-antibodies (Emfret) per g body weight and platelet counts were monitored for 10 days. To this end, each day 50 µL of blood were withdrawn from anesthetized mice in 300 µL heparin [20 U mL^{-1}]. Analysis was performed by flow cytometry.

3.2.8.8. Determination of MK ploidy

To determine the ploidy of BM MKs, both femora of mice were isolated and the BM was flushed out in CATCH buffer and homogenized using a syringe with a 22G needle. One-tenth of the suspension was spun down (5 min at 1,200 rpm) and the pellet was resuspended in 400 µL of CATCH:PBS 5% FCS (1:1 mixture), containing 0.02 µg $µL^{-1}$ anti-FcγR antibody (2.4G2) to block unspecific binding sites. Samples were incubated on ice for 15 min and afterwards stained with 200 µL of FITC-conjugated anti-GPIIb antibody (5D7-FITC) for another 20 min on ice. Thereafter, the samples were washed with 1 mL of CATCH:PBS 5% FCS, centrifuged for 5 min at 1,200 rpm, resuspended in 250 µL 5 mM EDTA in PBS and fixed for 10 min on ice by the addition of 250 µL 1% PFA in PBS. Permeabilization in 500 µL of PBS 0.1% Tween 20® (10 min on ice) was performed after a washing step with 3 mL PBS (10 min at 1,200 rpm). After permeabilization the washing step was repeated, the pellet was resuspended in propidium iodide staining solution (50 µg mL^{-1} propidium iodide and 100 µg mL^{-1} RNaseA in PBS) and incubated overnight at 4°C avoiding light exposure. Analysis was performed by flow cytometry and FlowJo software (Tree Star Inc., Ashland, USA).

3.2.9. Flow cytometric analysis of immune cells

$1x10^6$ cells were pelleted in FACS buffer by centrifugation for 3 min at 480 g. The supernatantwas discarded and cells were resuspend in 25 µL FACS buffer supplemented with 2.4G2 antibody (10 µg mL^{-1} f.c.) and incubated for at least 15 min on ice. Next, 25 µL of the diluted antibodies in FACS buffer were added, yielding a total volume of 50 µL. Samples were incu-

bate for 15 min on ice in the dark and cells were washed in FACS buffer. Cells were resuspended in 300 µL FACS buffer and analyzed on a FACSCalibur (BD Biosciences).

3.2.10. Data analysis

The presented results are mean ± standard deviation (s.d.) from at least three independent experiments per group, if not stated otherwise. Differences between *WT* and knockout mice were statistically analyzed using the unpaired Student's *t*-test. *P*-values < 0.05 were considered as statistically significant: $^{***}P < 0.001$; $^{**}P < 0.01$; $^{*}P < 0.05$. Results with a *P*-value > 0.05 were considered as non-significant (NS).

4. RESULTS

4.1. Megakaryocyte-specific Profilin1-deficiency alters microtubule stability and causes a Wiskott-Aldrich syndrome-like platelet defect

4.1.1. *Pfn1*$^{fl/fl\text{-}Pf4Cre}$ mice recapitulate key features of the WAS

Pfn isoform expression in murine platelets was assessed by RT-PCR, which yielded a Pfn1 band at 305 bp, whereas other Pfn isoforms were not detected (Fig. 11a). Since the constitutive knockout of Pfn1 resulted in early embryonic lethality,[138] *Pfn1*$^{fl/fl\text{-}Pf4Cre}$ mice (further referred to as *Pfn1*$^{-/-}$) were engineered that lack Pfn1 expression specifically in MKs and platelets. Complete loss of Pfn1 in mutant platelets (Fig. 11b) and BM MKs (Fig. 11c) was confirmed by Western blot analysis.

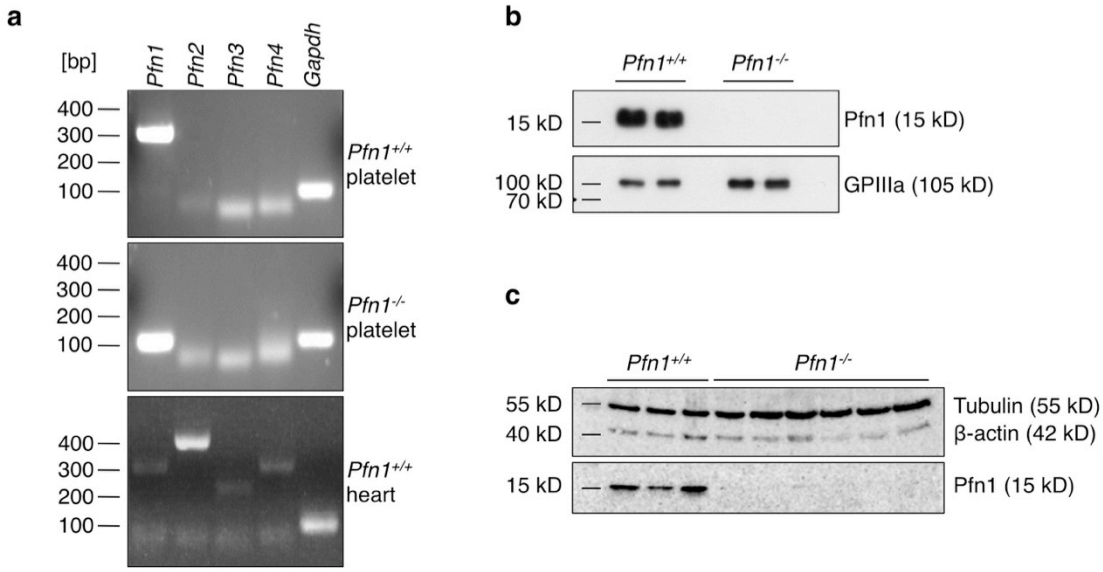

Figure 11 | Pfn1, but not other Pfn isoforms are expressed in platelets. (**a**) RT-PCR of Pfn isoforms in control mouse platelets, *Pfn1*$^{-/-}$ platelets and control heart. Expected band size for Pfn1 in control platelets 305 bp and 113 bp in *Pfn1*$^{-/-}$ platelets. No other isoforms were detected in platelets. (**b**) Whole platelet or (**c**) BM MK proteins were separated by SDS-PAGE and immunoblotted with an anti-Pfn1 antibody. (Bender* & Stritt* *et al. Nat Commun* 2014)[40]

Pfn1$^{-/-}$ mice (12-weeks old) displayed a microthrombocytopenia with a reduction in platelet count of about ~40% (Fig. 12a) and on average smaller-sized platelets (Fig. 12b, forward scatter signal) with a highly variable and frequently very thin platelet shape (Fig. 12c). Analysis of the platelet area on TEM images (Fig. 12d) and blood smears (Fig. 12e) confirmed the reduced size of platelets in *Pfn1*$^{-/-}$ mice. This microthrombocytopenia was also observed in 6-weeks old mice and thus appeared to be an age-independent phenotype (Fig. 12f, g). Of note, heterozygous mice displayed normal platelet counts but still significantly smaller platelets, albeit not as pronounced as in *Pfn1*$^{-/-}$ mice (Fig. 12h, i). Despite the altered platelet morphology and size the distribution of α- and dense granules was not affected (1.53 ± 1.01

in controls versus 1.51 ± 0.93 granules per µm^2 in *Pfn1*$^{-/-}$ platelets). Thus, *Pfn1*$^{-/-}$ mice represent the first mouse model of microthrombocytopenia, a hallmark of WAS in humans,[192] that could not be reproduced in WASp- or WIP-deficient mice which presented with normal-sized platelets.[197,263]

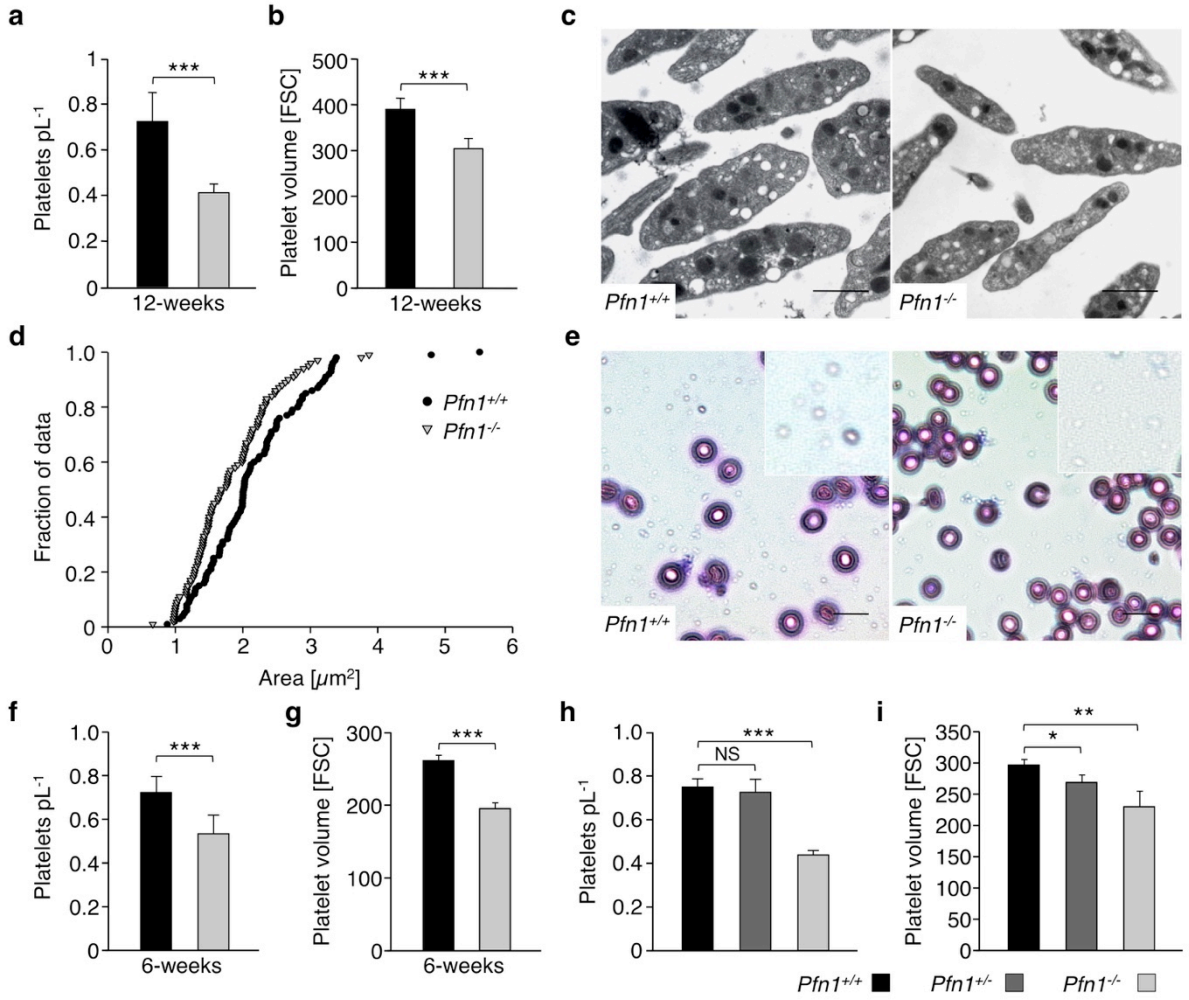

Figure 12 | Microthrombocytopenia in *Pfn1*$^{-/-}$ mice. (**a**, **b**) Fluorescence-activated cell sorter analyses. (**a**) Peripheral platelet counts. (**b**) Platelet size. Values are mean ± s.d. (n = 6). (**c**) TEM analysis of resting platelets. Scale bars, 1 µm. (**d**) Measurement of platelet area by means of TEM images. (**e**) Microthrombocytopenia in *Pfn1*$^{-/-}$ mice shown in blood smears. Scale bars, 10 µm. (**f, g**) Peripheral platelet counts (**f**) and size (**g**) of 6-weeks old mice. Values are mean ± s.d (n = 7). (**h, i**) Peripheral platelet counts (**h**) and size (**i**) of control, *Pfn1*$^{+/-}$ and *Pfn1*$^{-/-}$ mice. Values are mean ± s.d. (n = 5). FSC, *forward scatter*. Unpaired Student's *t*-test: ***$P < 0.001$; **$P < 0.01$; *$P < 0.05$; NS, non-significant. Images are representative of at least 6 individuals. (Bender* & Stritt* *et al. Nat Commun* 2014)[40]

4.1.2. Accelerated clearance and premature release in *Pfn1*$^{-/-}$ mice

Next, the cause of the observed thrombocytopenia was assessed. Reduced platelet numbers could either result from impaired platelet production, accelerated clearance or a combination of both. *Pfn1*$^{-/-}$ mice had a strongly decreased *in vivo* platelet life span (Fig. 13a, $T_{1/2}$ of control platelets: 58.4 h, $T_{1/2}$ of *Pfn1*$^{-/-}$ platelets: 24.7 h). Of note, splenectomy had no long-term effect on platelet counts in *Pfn1*$^{-/-}$ mice (Fig. 13b), thus indicating that the accelerated platelet

clearance is not mediated by splenic macrophages. However, depletion of macrophages within the whole body using clodronate-encapsulated liposomes strongly increased platelet counts in *Pfn1*$^{-/-}$ mice demonstrating that macrophages preferentially remove *Pfn1*$^{-/-}$ platelets from the circulation (Fig. 13c). In agreement with this observation *Pfn1*$^{-/-}$ platelets showed an increased prevalence of surface bound IgA and IgG_1 (Fig. 13d), which might explain the accelerated clearance of *Pfn1*$^{-/-}$ platelets by macrophages. Moreover, it was recently shown that aged, desialylated platelets are removed from the circulation by the Ashwell-Morell receptor on hepatocytes.[68] Hence it would be interesting to determine desialylation of *Pfn1*$^{-/-}$ platelets.

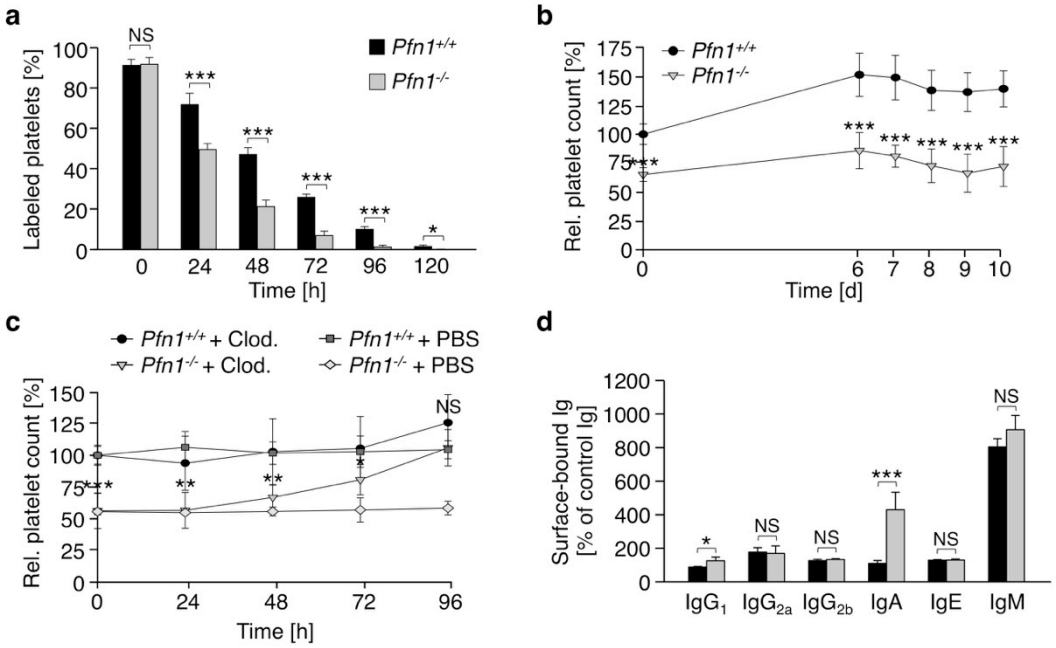

Figure 13 | Altered platelet survival in *Pfn1*$^{-/-}$ mice. (**a**) Platelet life span was measured by injection of a DyLight 488 α-GPIX derivative. Values are mean ± s.d. (n = 5). Platelet counts were monitored over time after (**b**) splenectomy and (**c**) clodronate-encapsulated liposome-mediated macrophage depletion. (**d**) Determination of platelet-bound *immunoglobulins* (Ig) relative to a non-specific Ig. Unpaired Student's *t*-test: ***$P < 0.001$; **$P < 0.01$; *$P < 0.05$; NS, non-significant. (Bender* & Stritt* *et al. Nat Commun* 2014)[40]

Despite the accelerated platelet clearance the mice did not develop splenomegaly (Fig. 14a), suggesting that the thrombocytopenia is not attributed to BM failure. In contrast, the plasma Thpo levels (Fig. 14b) as well as the number of MKs in the spleen (Fig. 14c) and BM (Fig. 14d) were moderately increased in *Pfn1*$^{-/-}$ mice. The increased plasma Thpo concentration is consistent with the reciprocal model of circulating plasma Thpo to MK/ platelet mass. In addition, this finding together with the report on the Ashwell-Morell receptor-mediated regulation of Thpo levels by Grozovsky *et al.* further highlight the need to determine desialylation of *Pfn1*$^{-/-}$ platelets.[68] Furthermore, the increased Thpo concentration in *Pfn1*$^{-/-}$ mice resulted in a slightly elevated ploidy of BM MKs (Fig. 14e), indicating an increased

proportion of mature MKs and excluding defective MK maturation as cause for the observed thrombocytopenia.

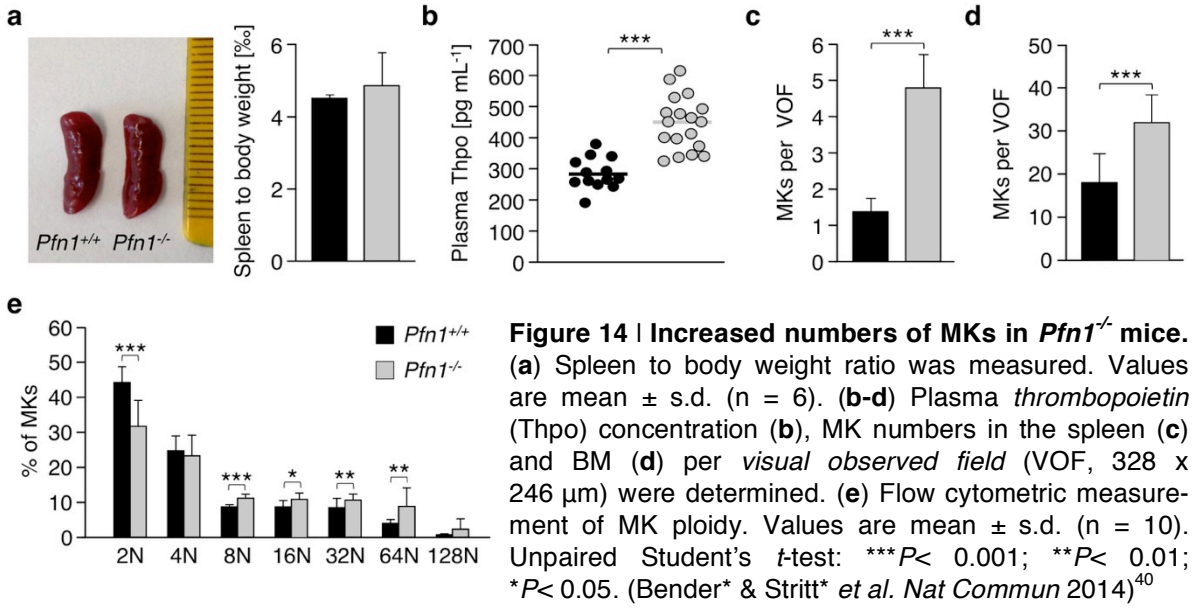

Figure 14 | Increased numbers of MKs in *Pfn1*$^{-/-}$ mice. (**a**) Spleen to body weight ratio was measured. Values are mean ± s.d. (n = 6). (**b-d**) Plasma *thrombopoietin* (Thpo) concentration (**b**), MK numbers in the spleen (**c**) and BM (**d**) per *visual observed field* (VOF, 328 x 246 µm) were determined. (**e**) Flow cytometric measurement of MK ploidy. Values are mean ± s.d. (n = 10). Unpaired Student's *t*-test: ***$P<$ 0.001; **$P<$ 0.01; *$P<$ 0.05. (Bender* & Stritt* *et al. Nat Commun* 2014)[40]

Although the accelerated clearance of *Pfn1*$^{-/-}$ platelets clearly contributed to the observed thrombocytopenia, it was not sufficient to explain a platelet count reduction of 50-60%. Therefore, thrombopoiesis and MK ultrastructure were analyzed. Interestingly, besides the microthrombocytopenia, also the ultrastructure of Pfn1-null BM MKs revealed similarities to that of WASp-null MKs.[27] Pfn1-null BM MKs either could be categorized as (I) MKs with normally distributed granules and a well-developed IMS (Fig. 15a, lower left), a membrane reservoir for future platelets, or as (II) MKs with signs of fragmentation (Fig. 15a, lower and upper right). Strikingly, immunostaining on BM cross-sections of intact femora (Fig. 15b, c) and intravital two-photon microscopy (dashed arrows in Fig. 15d) confirmed that the majority of *Pfn1*$^{-/-}$ MKs released platelets into the BM compartment next to the sinusoids, a defect that was also seen in WASp-deficient mice although to a lesser extent (Fig. 15e and [27]). In addition, two-photon microscopy revealed an increased activity of macrophages within the BM of *Pfn1*$^{-/-}$ mice. This clearly suggests that macrophages remove the prematurely released platelets from the BM. The premature platelet release appeared not to be caused by defective proplatelet formation as revealed by two-photon microscopy (Fig. 15d) and in an *in vitro* proplatelet formation assay (Fig. 15f), nor to an aberrant localization of MKs within the BM (Fig. 15g). It still not clear whether the platelets released into the BM of *Pfn1*$^{-/-}$ mice can make their way into the circulation and contribute to platelet counts.

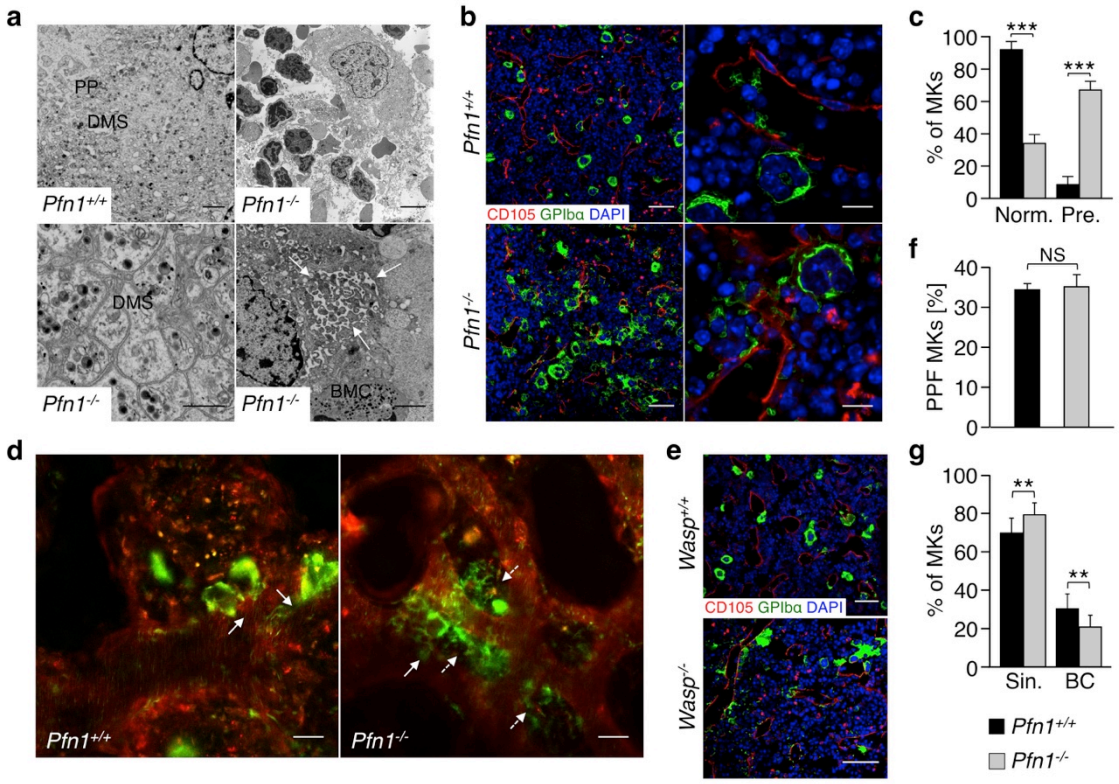

Figure 15 | Premature platelet release into the BM compartment. (**a**) TEM analysis of BM MKs (upper left: control MK). Scale bar, 2 µm (upper left). Scale bar, 1 µm (lower left). Scale bar, 5 µm (upper right). Scale bar, 2 µm (lower right). PP, *proplatelet*; DMS, *demarcation membrane system*; BMC, *BM cell*; black arrows indicate cytoplasmic fragmentation. (**b**) Confocal images of immunostained BM. Scale bars, 50 µm (left panel). Scale bars, 15 µm (right panel). MKs, proplatelets and platelets are shown by GPIbα staining in green color. Endoglin staining (red) labels vessels. DAPI, blue. (**c**) MK morphology was determined on confocal images with immunostained MKs and vessels. Norm, *round MKs*; Pre, *MKs that pre-released proplatelets or platelets into BM*. Values are mean ± s.d. (n = 252 versus 383 MKs). (**d**) Intravital two-photon microscopy of BM MKs in the skull. Arrow shows (normal) proplatelet formation into BM sinusoids; dashed arrow indicates pre-released platelets within the BM. Scale bars represent 25 µm. Two-photon intravital microscopy was performed by Judith M. M. van Eeuwijk. (**e**) Confocal images of immunostained BM from *Wasp*$^{-/-}$ mice. Scale bars, 50 µm (n = 6). (**f**) Normal *proplatelet formation* (PPF) of Pfn1-deficient BM MKs. Values are mean ± s.d. (n = 6). (**g**) MK localization was determined on confocal images with immunostained MKs and vessels. MKs closer than 1 µm to the vessel were counted as MKs at the sinusoids. Sin, *sinusoid*; BC, *BM compartment*. Values are mean ± s.d. (n = 252 versus 383 MKs). Images are representative of at least 6 individuals. Unpaired Student's *t*-test: ***$P < 0.001$; **$P < 0.01$; NS, non-significant. (Bender* & Stritt* *et al. Nat Commun* 2014)[40]

4.1.3. Abolished podosome formation might account for the premature platelet release in the BM of *Pfn1*$^{-/-}$ mice

Podosomes, F-actin-rich matrix contacts, have been proposed as an indicator of MK motility and the ability to extend proplatelets through the basal membrane into the blood stream.[26] To test podosome formation, MKs were allowed to spread on a collagen I matrix and stained for F-actin-rich podosomes and for p-ASAP, WASp or vinculin, as podosomal markers (Fig. 16a-c). *Pfn1*$^{-/-}$ MKs barely formed podosomes as compared to control MKs. In addition, mutant MKs spread on fibrinogen contained an enormous amount of acetylated tubulin,

which has been associated with increased microtubule stability (Fig. 16d).[264] These results suggested that the thrombocytopenia in *Pfn1*$^{-/-}$ mice is caused by both accelerated platelet clearing by macrophages and the premature platelet release into the BM due to altered cytoskeletal dynamics and consequently impaired proplatelet extension through the basal membrane.

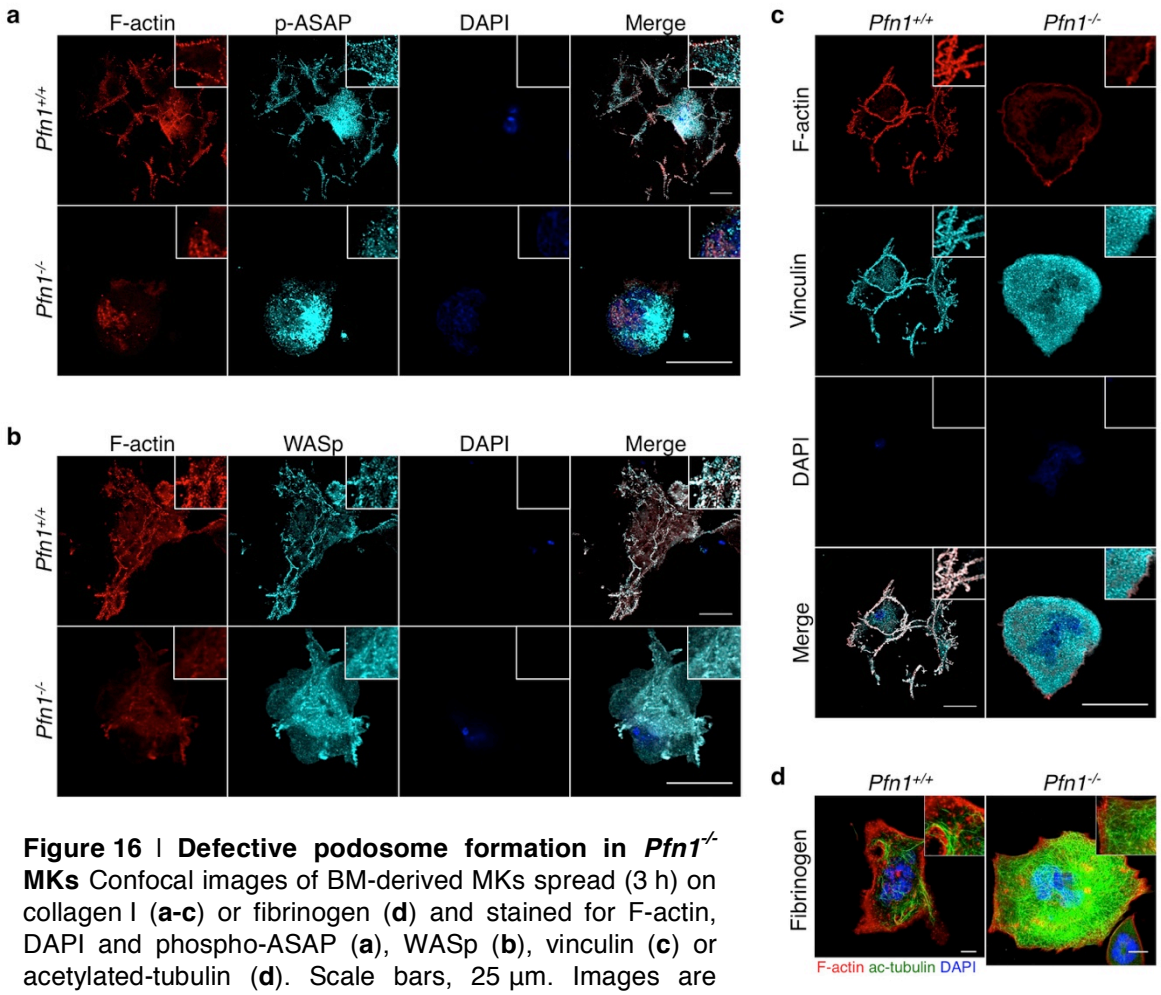

Figure 16 | Defective podosome formation in *Pfn1*$^{-/-}$ MKs Confocal images of BM-derived MKs spread (3 h) on collagen I (**a-c**) or fibrinogen (**d**) and stained for F-actin, DAPI and phospho-ASAP (**a**), WASp (**b**), vinculin (**c**) or acetylated-tubulin (**d**). Scale bars, 25 µm. Images are representative of at least 6 individuals. (Bender* & Stritt* *et al. Nat Commun* 2014)[40]

4.1.4. Cytoskeletal alterations in *Pfn1*$^{-/-}$ platelets

To assess this in more detail, the cytoskeletal organization of circulating *Pfn1*$^{-/-}$ platelets was analyzed. Rapid-freezing electron microscopic analysis of *Pfn1*$^{-/-}$ platelets revealed that their actin scaffold was partially disrupted (Fig. 17a; actin cytoskeleton of *Pfn1*$^{+/+}$ platelets (n = 102): 98% intact, 2% partially disrupted; actin cytoskeleton of *Pfn1*$^{-/-}$ platelets (n = 116): 7.7% intact, 75.9% partially disrupted, 16.4% completely disrupted (as depicted in Fig. 17a)). Since Pfn1 has been described as an important regulator of the actin cytoskeleton,[265] actin levels and assembly in platelets were determined. Total actin content in count-adjusted platelets was reduced (Fig. 17b) and this was also evident by a reduced F-actin content per

platelet (Fig. 17c). Unexpectedly, actin assembly after platelet activation with different agonists was only slightly decreased in *Pfn1*$^{-/-}$ platelets (Fig. 17d). In contrast, other actin-regulatory proteins have been shown to have a more pronounced effect on F-actin assembly.[266] Surprisingly, the total tubulin content was increased in *Pfn1*$^{-/-}$ MKs (Fig. 11c) and platelets (Fig. 17b). This also became evident by a higher number of microtubule coils, organized into a characteristic ring structure, designated as the marginal band (Fig. 17a, e, f).

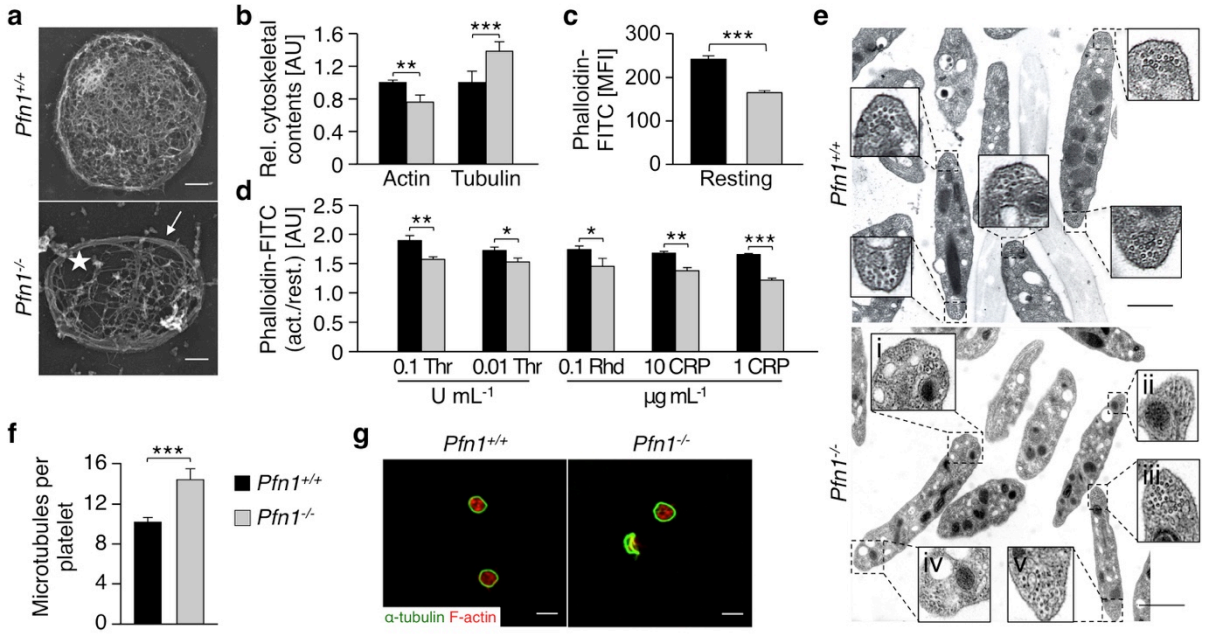

Figure 17 | Pfn1 deficiency causes altered microtubule structure. (**a**) Visualization of the cytoskeleton in resting platelets on poly-L-lysine. Scale bars, 0.5 µm. Asterisk indicates disrupted actin scaffold. Arrow indicates thickened microtubule ring (marginal band). (**b**) Densitometric assessment of β-actin and α-tubulin content of platelet lysates. Values are mean ± s.d. (n = 4). (**c, d**) F-actin content of resting (**c**) or activated platelets (**d**) was determined by flow cytometry. Values are mean ± s.d. (n = 6). Thr, *thrombin*; Rhd, *rhodocytin*; CRP, *collagen-related peptide*. (**e**) TEM analysis of resting control and *Pfn1*$^{-/-}$ platelets. Scale bars, 1 µm. **i**, **ii** and **iv** show altered microtubule distribution as revealed by not perpendicular, but diagonally cut microtubules. **iii** and **v** illustrate mutant platelets with abnormal high numbers of microtubule coils. (**f**) Number of microtubule coils were determined from at least 120 platelets per condition. (**g**) Confocal images of resting platelets. Values are mean ± s.d. (n = 6). Images are representative of at least 6 individuals. Unpaired Student's *t*-test: ***$P < 0.001$; **$P < 0.01$; *$P < 0.05$. Images in **a** were acquired by Prof. John Hartwig, Boston, USA. (Bender* & Stritt* *et al. Nat Commun* 2014)[40]

Furthermore, the marginal band often appeared to have an altered morphology in mutant platelets, most frequently twisted into a figure of eight (Fig. 17g). Next, platelets with twisted microtubules were quantified by analyzing resting platelets on poly-L-lysine stained for α-tubulin. 55.7% of *Pfn1*$^{-/-}$ platelets (n = 582) contained bent or twisted microtubules whereas only 2.7% of control platelets (n = 1037) showed an aberrant morphology of microtubules (Fig. 22d). Together these results reveal a novel and unexpected role of Pfn1 in the regulation of the microtubule cytoskeleton.

4.1.5. Pfn1 co-localizes to microtubules

Next, the localization of Pfn1 in MKs and platelets was analyzed to test whether Pfn1 may directly interfere with microtubule organization. Pfn1 was strongly expressed in the MK body and proplatelets (Fig. 18a), whereas a ring-shaped expression close to the membrane was observed in resting platelets, which was reminiscent of the platelet marginal band (Fig. 18b). A weak Pfn1 localization was found in the platelet cytoplasm, generally in small foci. In human platelets from healthy donors a similar Pfn1 localization was seen (Fig. 18c).

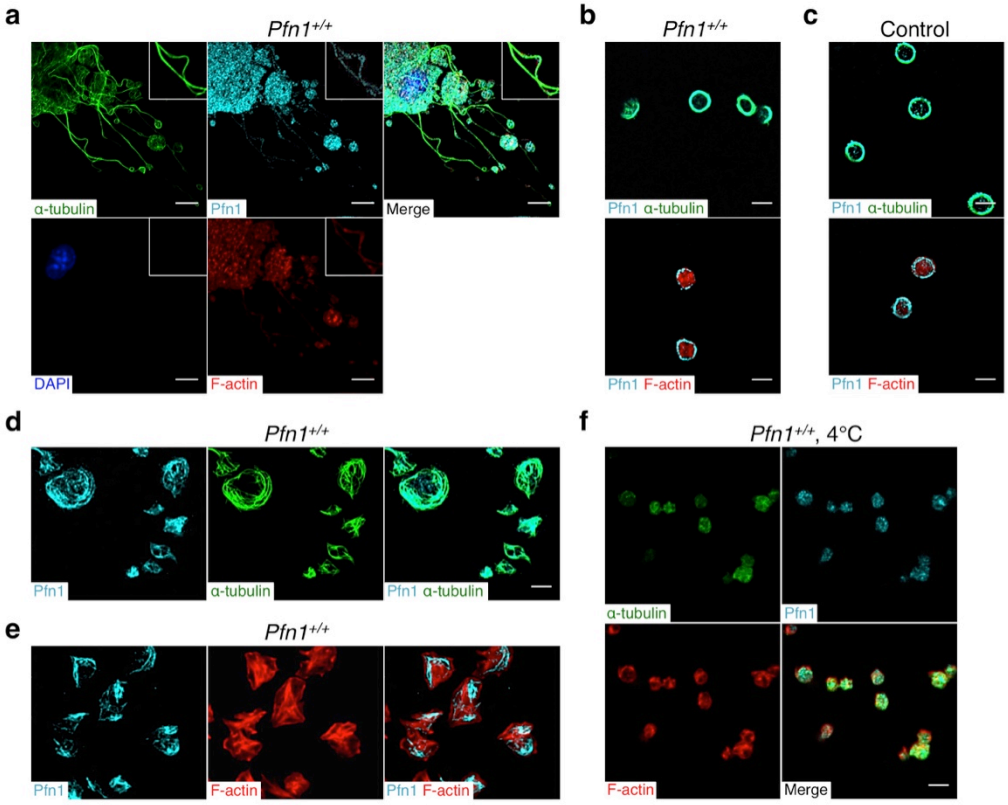

Figure 18 | Pfn1 co-localizes to microtubules. (**a**) Determination of Pfn1 expression in cultured fetal liver-derived *Pfn1*$^{+/+}$ MKs with formed proplatelets. α-tubulin, green; Pfn1, cyan; DAPI, blue; F-actin, red. Scale bar, 10 µm. (**b-f**) Pfn1 localization in resting *Pfn1*$^{+/+}$ mouse (**b**) and human (**c**) platelets, spread mouse platelets (**d, e**) after 15 min on fibrinogen or in resting *Pfn1*$^{+/+}$ platelets after cold-storage for 3.5 h (**f**). Scale bars, 3 µm (in **b-f**). Images are representative of at least 6 individuals. (Bender* & Stritt* *et al. Nat Commun* 2014)[40]

After spreading of mouse platelets on fibrinogen, Pfn1 was redistributed in the cells but still strongly co-localized with α-tubulin (Fig. 18d) and was present in zones devoid of F-actin (Fig. 18e), thus indicating that Pfn1 might be associated to microtubules and interferes with microtubule organization. To further test whether Pfn1 can associate to microtubules its localization was assessed upon cold-induced depolymerization of microtubules in control platelets. After incubation of platelets at 4°C, microtubules were completely disassembled

and Pfn1 was re-localized to the cytoplasm, indicating that the localization of Pfn1 might be microtubule-dependent (Fig. 18f).

4.1.6. Increased stability of microtubules in *Pfn1*$^{-/-}$ platelets

To further investigate the organization and rearrangement of microtubules in *Pfn1*$^{-/-}$ platelets, spreading experiments on different matrices were performed. Mutant platelets showed a delayed and aberrant spreading on fibrinogen with a reduced F-actin content (Fig. 19a, dashed arrows in lower panel) and disorganized microtubules that were randomly dispersed or twisted and failed to constrict into the cell center (Fig. 19a, arrow in lower panels).

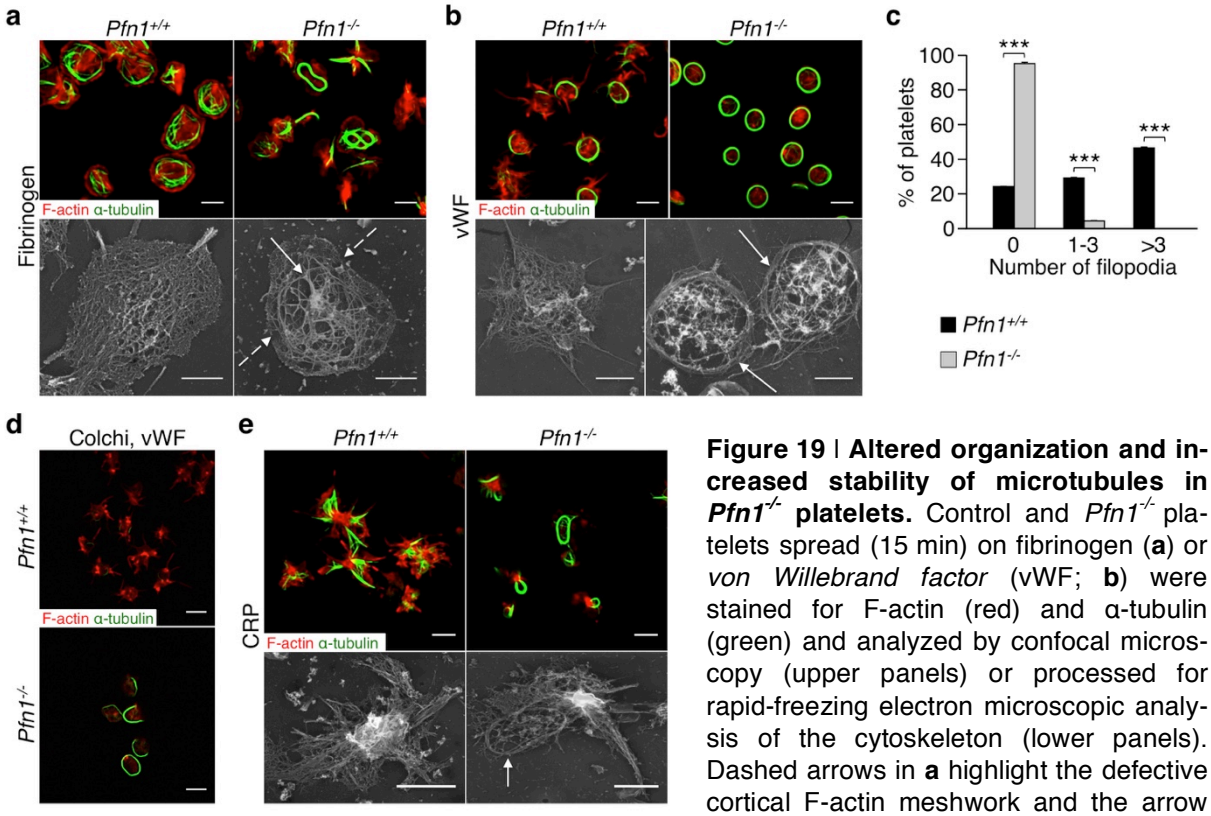

Figure 19 | Altered organization and increased stability of microtubules in *Pfn1*$^{-/-}$ platelets. Control and *Pfn1*$^{-/-}$ platelets spread (15 min) on fibrinogen (**a**) or *von Willebrand factor* (vWF; **b**) were stained for F-actin (red) and α-tubulin (green) and analyzed by confocal microscopy (upper panels) or processed for rapid-freezing electron microscopic analysis of the cytoskeleton (lower panels). Dashed arrows in **a** highlight the defective cortical F-actin meshwork and the arrow indicates disorganized microtubules. Arrows in **b** denote thickened peripheral microtubule coils in *Pfn1*$^{-/-}$ platelets. (**c**) Quantification of filopodia per spread platelet on vWF. Values are mean ± s.d. (n = 6). (**d**) Platelets were pretreated with 10 µM *colchicine* (colchi) and spread (15 min) on vWF. (**e**) Platelets were spread (15 min) on *collagen-related peptide* (CRP). Arrow indicates disintegrated appearing microtubule coils that could not be reorganized upon spreading. Scale bars, 3 µm (in confocal images) Scale bars, 1 µm (in TEM images). Images are representative of at least 6 individuals. Unpaired Student's *t*-test: ***$P < 0.001$. TEM images were acquired by Prof. John Hartwig, Boston, USA. (Bender* & Stritt* *et al. Nat Commun* 2014)[40]

Similarly to fibrinogen-coated surfaces (only 0.8% ± 0.4% of *Pfn1*$^{-/-}$ versus 20.7% ± 0.3% of control platelets formed filopodia at 15 min time point), *Pfn1*$^{-/-}$ platelets could not form filopodia on a vWF matrix (only 0.7% ± 0.5% of *Pfn1*$^{-/-}$ versus 60.0% ± 3.6% of control platelets had formed filopodia at the 15 min time point) and maintained their thick marginal band

(Fig. 19b, arrows in lower panel and Fig. 19c), even after colchicine treatment (Fig. 19d). Likewise, on a surface coated with CRP spread platelets could not reorganize their microtubule coils (Fig. 19e, arrow in lower panel). This represented the first evidence that Pfn1 is crucial for filopodia formation in platelets.

4.1.7. Hyper-acetylated microtubules as consequence of their increased stability

Microtubules in *Pfn1*$^{-/-}$ platelets were highly acetylated (Fig. 20a, b) and could withstand disassembly upon incubation at 4°C (Fig. 20c) or treatment with the microtubule-destabilizing toxin, colchicine (Fig. 20d), suggesting an increased microtubule stability. Therefore, it was tested whether toxin-induced stabilization of microtubules could mimic the tubulin phenotype observed in *Pfn1*$^{-/-}$ platelets.

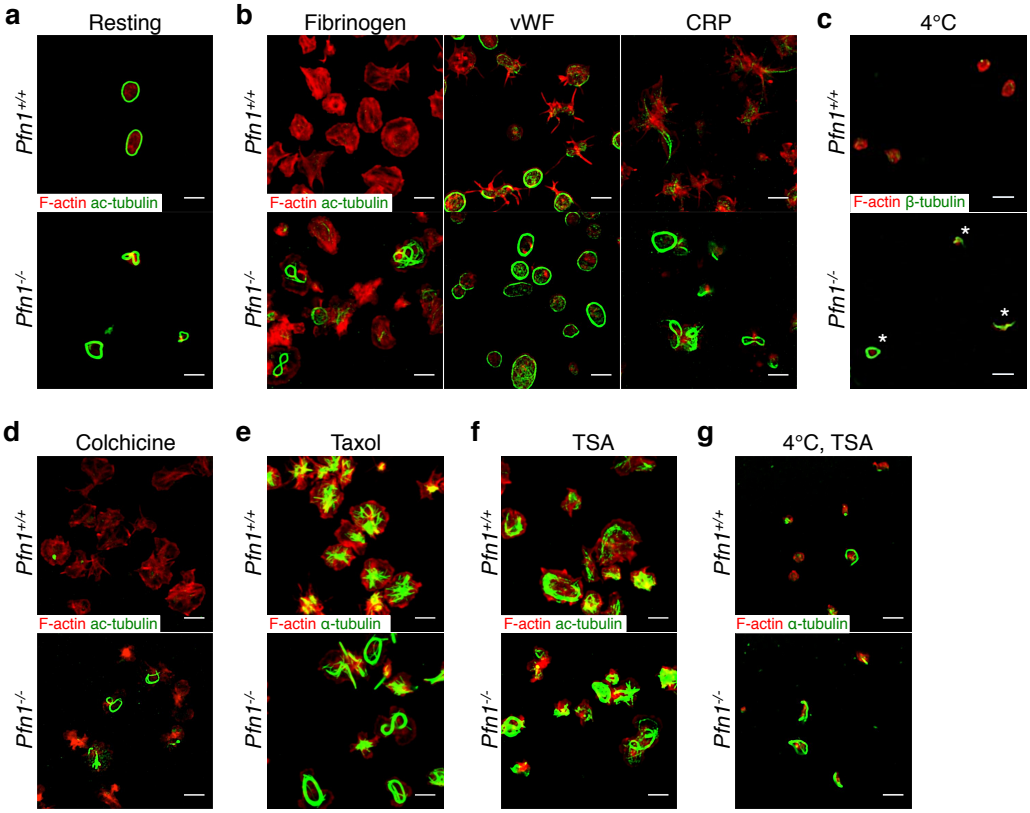

Figure 20 | Acetylation causes aberrant organization of microtubules in *Pfn1*$^{-/-}$ platelets. (**a, b**) Resting (**a**) or spread (**b**) platelets were stained for acetylated-tubulin (green). vWF, *von Willebrand factor*; CRP, *collagen-related peptide*. (**c, d**) Microtubules were challenged by cold-incubation (**c**) or colchicine (10 µM) treatment (**d**). (**e-g**) Pre-treatment of platelets with 10 µM taxol (**e**) or 200 ng mL^{-1} *trichostatin A* (TSA; **f, g**) interfered with microtubule organization (**e**) and increased microtubule acetylation (**f**) and stability upon cold-challenge (**g**). Scale bars, 3 µm. Images are representative of at least 6 individuals. (Bender* & Stritt* *et al. Nat Commun* 2014)[40]

Treatment with the microtubule stabilizing toxin taxol led to a moderate increase of radially organized microtubules in control platelets, whilst spread *Pfn1*$^{-/-}$ platelets maintained the

circular or twisted microtubules (Fig. 20e). Thus, taxol alone is not sufficient to reproduce the microtubular alterations of spread *Pfn1*$^{-/-}$ platelets. In contrast, preincubation with the histone-deacetylase inhibitor *trichostatin A* (TSA) could partially mimic the *Pfn1*$^{-/-}$ microtubule phenotype by preserving hyper-acetylated and disorganized microtubules in spread control platelets and increasing microtubule acetylation in *Pfn1*$^{-/-}$ platelets (Fig. 20e). These highly acetylated microtubules in control and *Pfn1*$^{-/-}$ platelets were also less prone to cold-induced disassembly (Fig. 20f). Furthermore, isolation of the tubulin cytoskeleton after treatment with colchicine or the histone deacetylase inhibitor TSA via ultracentrifugation was performed and the different fractions were tested for tubulin and acetylated tubulin sedimentation. These results revealed an increased amount of sedimented and acetylated (Fig. 21a) tubulin in the insoluble fraction after colchicine treatment in samples of *Pfn1*$^{-/-}$ platelets supporting the microscopic findings that microtubules cannot be rearranged in mutant platelets. Hence, it was concluded that hyper-acetylated, stiff microtubules might cause the aberrant microtubule organization in *Pfn1*$^{-/-}$ platelets. Additionally, the altered microtubule stability and organization appears to be independent of the actin cytoskeletal defects as control platelets pre-incubated with *latrunculin A* (Lat A) disassembled their microtubules upon cold-storage at 4°C (Fig. 21b).

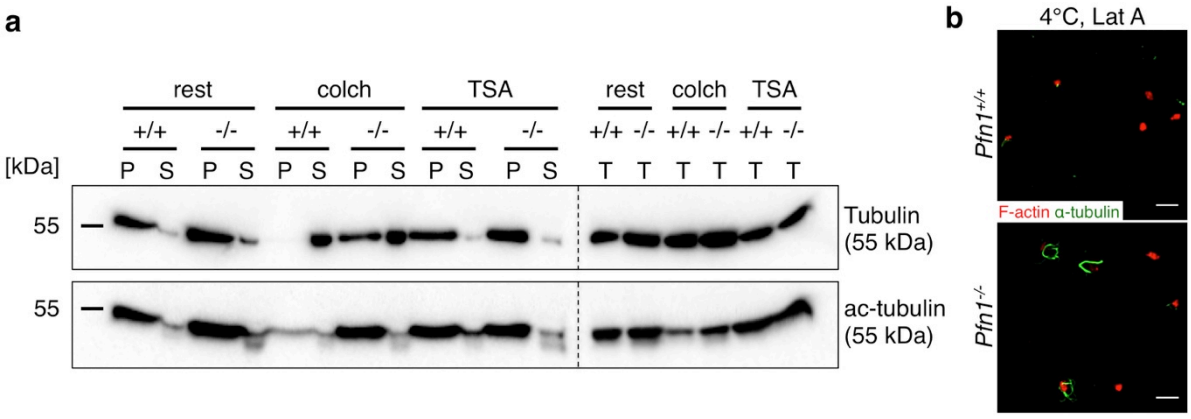

Figure 21 | Increased microtubule stability in *Pfn1*$^{-/-}$ platelets. (**a**) Tubulin cytoskeleton was isolated via ultracentrifugation and immunoblotted against tubulin or acetylated-tubulin. Insoluble fraction (*pellet*, P), soluble fraction (*supernatant*, S); rest: *resting*, colch: 10 µM *colchicine*, TSA: 200 ng mL^{-1} TSA, *trichostatin A*, a deacetylase inhibitor; T: *total protein*; +/+ *Pfn1*$^{+/+}$ and -/-, *Pfn1*$^{-/-}$. (**b**) Resting platelets were pre-treated with 2.5 µM *latrunculin A* (LatA), challenged by cold-incubation and stained for acetylated-tubulin (green). Scale bars, 3 µm. Images are representative of at least 6 individuals. (Bender* & Stritt* *et al. Nat Commun* 2014)[40]

4.1.8. Microtubule stability determines platelet size

Next, it was examined whether the increased microtubule stability could account for the reduced size of *Pfn1*$^{-/-}$ platelets. Determination of the area delimited by the marginal band in control platelets showed a decrease in platelet size after treatment with taxol (74.41% ±

2.33%, compared to DMSO control 100%), TSA (81.53% ± 5.44%), or the combination of both (65.62% ± 1.59%; untreated *Pfn1*$^{-/-}$ platelets 60.8% of control, Fig. 22a, b). Measurement of the F-actin content in toxin-treated resting platelets showed that the toxins did not interfere with the actin cytoskeleton (Fig. 22c). These results suggested that increased microtubule stability might contribute to the smaller size and aberrant organization of microtubules in *Pfn1*$^{-/-}$ platelets (Fig. 22d). Of note, it has been recently shown that antagonistic microtubule motor proteins maintain the platelet marginal band under resting conditions and that functional changes can lead to microtubule coiling accompanied by platelet shape change.[267] Therefore, it is tempting to speculate that the small *Pfn1*$^{-/-}$ platelets might exhibit an imbalanced microtubule motor protein function, consequently leading to twisted or bent microtubules. However, further studies are required to test this hypothesis.

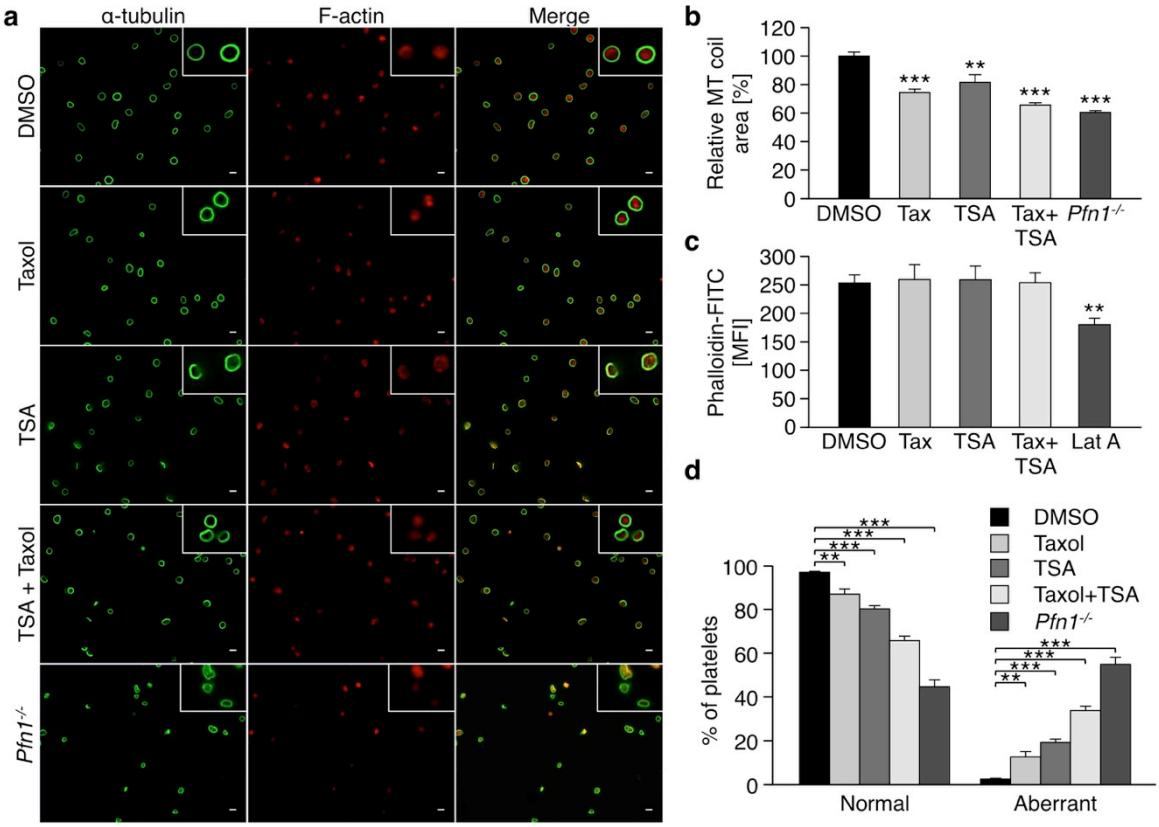

Figure 22 | Toxin-mediated stabilization decreases platelet size. (**a**) Control platelets were treated with 10 µM taxol and/or 200 ng mL^{-1} *trichostatin A* (TSA) for 30 min, fixed on poly-L-lysine-coated slides and stained for α-tubulin (green) and F-actin (red). Scale bars, 3 µm. (**b**) The relative platelet area was quantified using the *microtubule* (MT) coil as a measure. Values are mean ± s.d. (n = 5). (**c**) F-actin content of toxin-treated platelets was determined by flow cytometry. (**d**) Normal and aberrant shape of platelet microtubules was quantified. Values are mean ± s.d. (n = 5). Images are representative of at least 5 individuals. Unpaired Student's *t*-test: ***P< 0.001; **P< 0.01. (Bender* & Stritt* *et al. Nat Commun* 2014)[40]

4.1.9. Unaltered cytoskeletal rearrangements in *Wasp*$^{-/-}$ platelets

Pfn1$^{-/-}$ mice are the first animal model displaying a microthrombocytopenia and thus represent a unique system to study the molecular causes and (patho-)physiological consequences of this hematopoietic defect. In humans, microthrombocytopenia is the central hallmark of the WAS, that was interestingly not reproduced in WASp-deficient mice, which have normally-sized platelets.[197,263] Although, analysis of *Wasp*$^{-/-}$ mouse platelets revealed an increased content of tubulin similar to *Pfn1*$^{-/-}$ platelets (Fig. 17b and 23a), microtubule stability or reorganization during spreading or cold-induced microtubule disassembly were not affected in these cells (Fig. 23b, c).

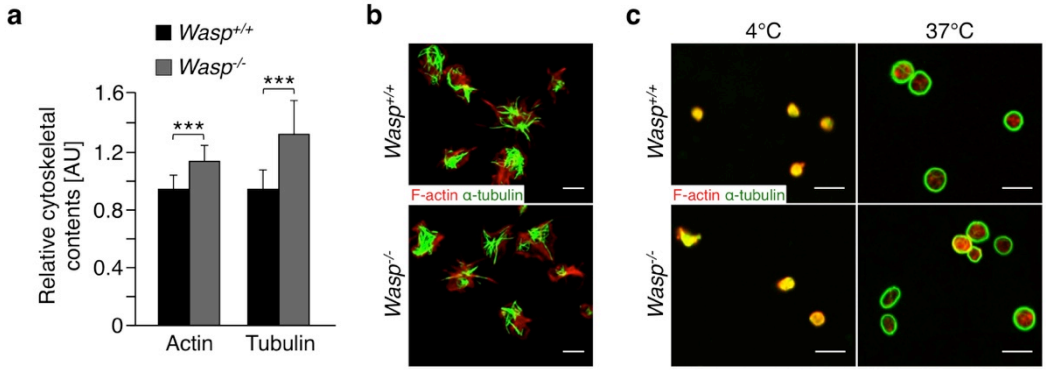

Figure 23 | *Wasp*$^{-/-}$ platelets can normally reorganize their microtubules. (**a**) Densitometry of actin and tubulin via Western blot using count-adjusted platelets. Values are mean ± s.d. (n = 3). (**b, c**) Platelets were allowed to spread (15 min) on a fibrinogen-coated surface (**b**) or chilled at 4°C (**c**) and fixed on a poly-L-lysine-coated surface. F-actin is highlighted in red and α-tubulin in green. Scale bars, 3 µm. Images are representative of at least 3 individuals. Unpaired Student's *t*-test: ***$P < 0.001$. Images in **c** were acquired by Dr. Markus Bender. (Bender* & Stritt* *et al. Nat Commun* 2014)[40]

4.1.10. Altered microtubule rearrangement in WAS patients' platelets

To assess whether an increased microtubule stability may contribute to microthrombocytopenia in human WAS, blood samples of four WAS patients were analyzed. Patient 1 was a 2-years old male carrying a c.290C>T p.Arg86Cys mutation in the *WAS* gene. At the day of consultation, the patient had a platelet count of 11 x 10^3 µL^{-1} and the mean platelet volume could not be determined with an automated blood cell analyzer (Sysmex), presumably due to an aberrant platelet morphology and size. Patient 2 was a 7-years old male with a c.336T>G p.Leu101Arg mutation in the *WAS* gene. During the first year of his life he suffered from severe brain hemorrhage due to low numbers of circulating platelets, which was the reason for subsequent therapeutic splenectomy. At the day of consultation, he presented with a platelet count of 128 x 10^3 µL^{-1} and a mean platelet volume of 7.5 fL as determined by a Sysmex analyzer. In contrast to patient 1 and 2, patient 3 (male, 5-months old, c.559+1G>A splice-site mutation in intron 6 of the *WAS* gene) suffered from eczema, petechiae, lymphocytopenia, recurrent infections, anisocytosis and required platelet transfusions due to low

platelet numbers (32 x 10^3 μL^{-1} at the day of consultation). Patient 4 was a 18-years old male with a frame shift mutation in exon 10 (c.1075delC p.Pro360His fsX85) of the *WAS* gene and had a history of recurrent infections and arthritis. At the day of consultation he presented with a platelet count of 29 x 10^3 μL^{-1}. The analysis of the cytoskeletal organization of WAS patients' platelets revealed an increased content and highly altered organization of the microtubules (Fig. 24a and 25a). Three major microtubule organization types could be distinguished: (I) platelets with a normally organized, but thickened marginal band, (II) platelets that contained microtubules in the platelet center (Fig. 24a and 25a, arrows) and (III) platelets with twisted and disorganized microtubules (Fig. 24a and 25a, dashed arrows). While platelets of healthy controls (Fig. 24a and 25a) displayed a discoid shape, the platelets of patients were often curved in shape, most probably attributed to misarranged microtubules (Fig. 24a and 25a).

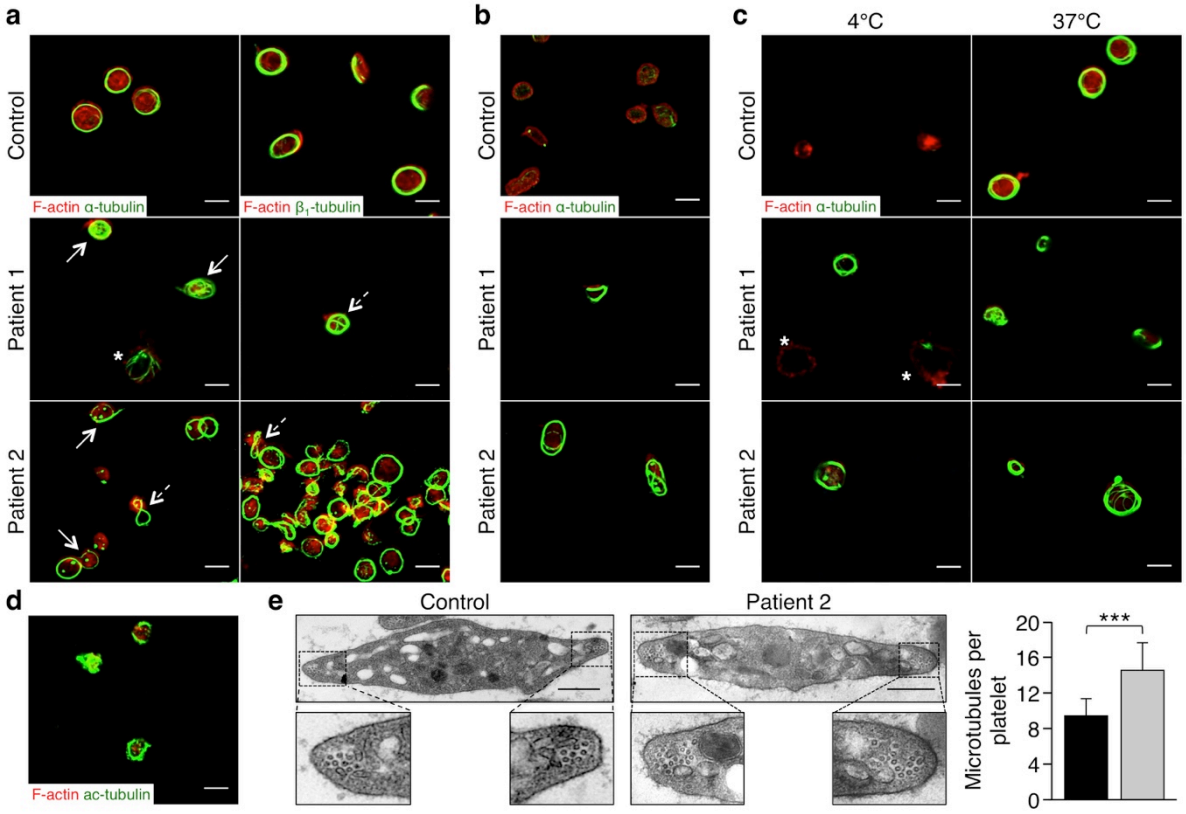

Figure 24 | Platelets of WAS patients resemble the microtubule phenotype of *Pfn1*$^{-/-}$ platelets. (**a**) Poly-L-lysine-immobilized resting platelets from two male WAS patients were stained for F-actin (red) and different tubulin isoforms (green) and analyzed by confocal microscopy. Patient 1: 2 years, without therapeutic intervention, carrying a R86C mutation in Exon 2 in the *WAS* gene; Patient 2: 7 years, underwent therapeutic splenectomy in his first year of life, carrying a L101R mutation in Exon 3 of the *WAS* gene. Microtubules in WAS patients' platelets were challenged with 10 µM colchicine (**b**) or by incubation at 4°C for 3.5 h (**c**). (**d**) Resting platelets of patient 2 were stained for acetylated tubulin (green) and F-actin (red). (**e**) TEM revealed an increased number and aberrant organization of the microtubules in the WAS patients' platelets (grey bar) as compared to healthy controls (black bar). Values are mean ± s.d. (n = 46 platelets). Scale bars, 3 µm (in **a-d**). Scale bars, 1 µm (in **e**). Unpaired Student's *t*-test: ***$P < 0.001$. (Bender* & Stritt* *et al. Nat Commun* 2014)[40]

Next, control and WAS patients' platelets were challenged with colchicine (Fig. 24b and 25b) or chilled at 4°C (Fig. 24c and 25c). Contrary to control samples, under both tested conditions microtubules of WAS patients' platelets were still prominently visible, disorganized, bent or twisted (Fig. 24b, c and 25b,c) and highly acetylated (Fig. 24d and 25d). Similar to *Pfn1*$^{-/-}$ platelets, electron-microscopic analyses of platelets from patient 2 and 3 showed an increased number of microtubules (10.58 ± 2.04 in controls versus 14.86 ± 2.66 in patients) with an altered organization (Fig. 24e and 25e). Even though the splenectomy of patient 2 resulted in increased platelet numbers, the microtubule cytoskeleton was still severely altered and disorganized. Of note, *WASP* heterozygosity in case of a female carrier moderately affected microtubule stability and organization (Fig. 25a-c, e).

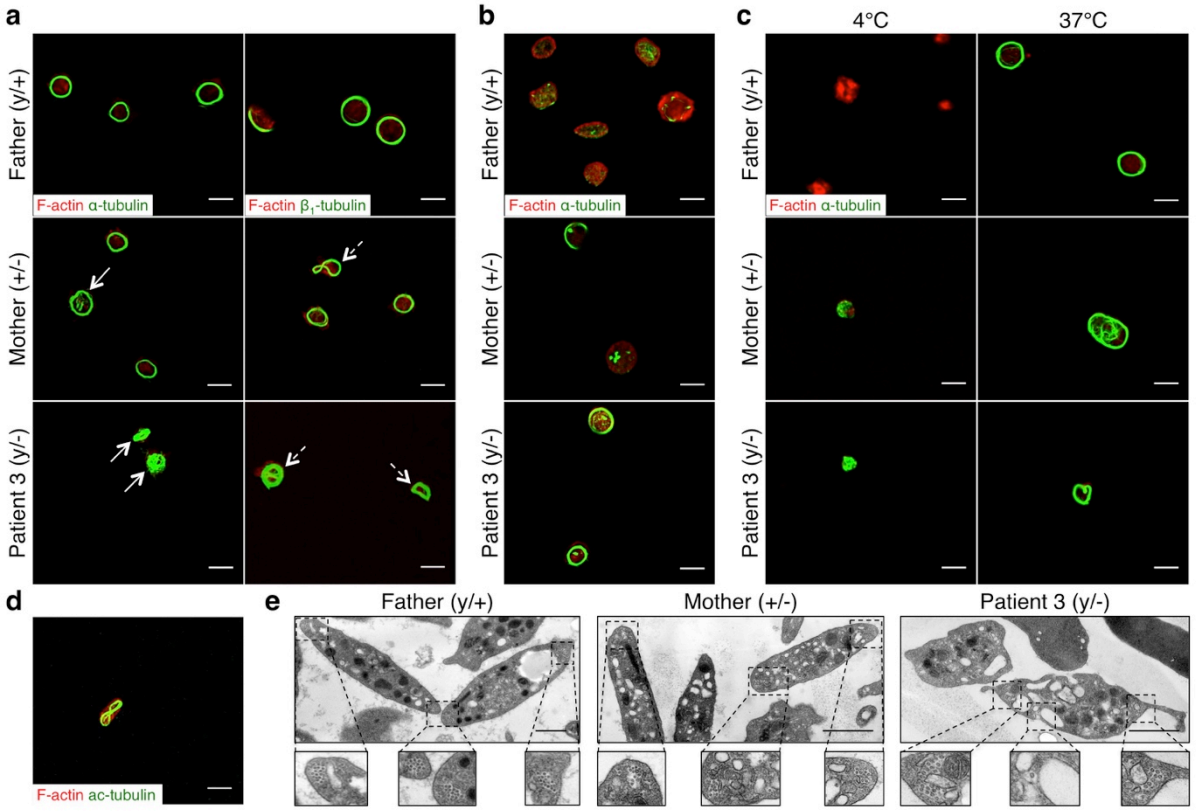

Figure 25 | Platelets of WAS patients and carriers resemble the microtubule phenotype of *Pfn1*$^{-/-}$ platelets. (**a**) On poly-L-lysine-immobilized resting platelets of a WAS family consisting of a healthy father (*WASP*$^{y/+}$), a heterozygous mother (carrier, *WASP*$^{+/-}$) and a son, patient 3 suffering from WAS (*WASP*$^{y/-}$) were stained for F-actin (red) and different tubulin isoforms (green) and analyzed by confocal microscopy. Father: 30 years, healthy; Mother 26 years, normal platelet numbers with a decreased mean platelet volume; patient 3: 5 months, requiring blood transfusions, carrying an IVS6+1G>A splice-site mutation in intron 6. Platelet microtubules were challenged with 10 µM colchicine (**b**) or by incubation at 4°C for 3.5 h (**c**). (**d**) Resting platelets of patient 3 were stained for acetylated tubulin (green) and F-actin (red). (**e**) TEM revealed an increased number and aberrant organization of the microtubules in the WAS patients' platelets as compared to healthy controls. Scale bars, 3 µm (in **a-d**). Scale bars, 1 µm (in **e**). (Bender* & Stritt* *et al. Nat Commun* 2014)[40]

4.1.11. Pfn1 is mis-localized in platelets of WAS patients

Due to the striking similarities between murine Pfn1-deficient platelets and human platelets from WAS patients, localization of Pfn1 was assessed. Interestingly, Pfn1 did not co-localize to the marginal band in platelets of WAS patients 1, 3 and 4 suggesting that WASp and Pfn1 interact with each other in human platelets (Fig. 26a). To test this hypothesis co-immunoprecipitation of WASp was performed on sonificated human platelets and could prove that WASp and Pfn1 interact directly or indirectly with each other (Fig. 26b). Despite the striking co-localization of Pfn1 to microtubules in the marginal band, no direct interaction could be observed in a commercially available microtubule-associated protein fraction (Fig. 26c). Together, these data reveal that platelets from WAS patients display defective microtubule reorganization as observed in *Pfn1*$^{-/-}$ platelets.

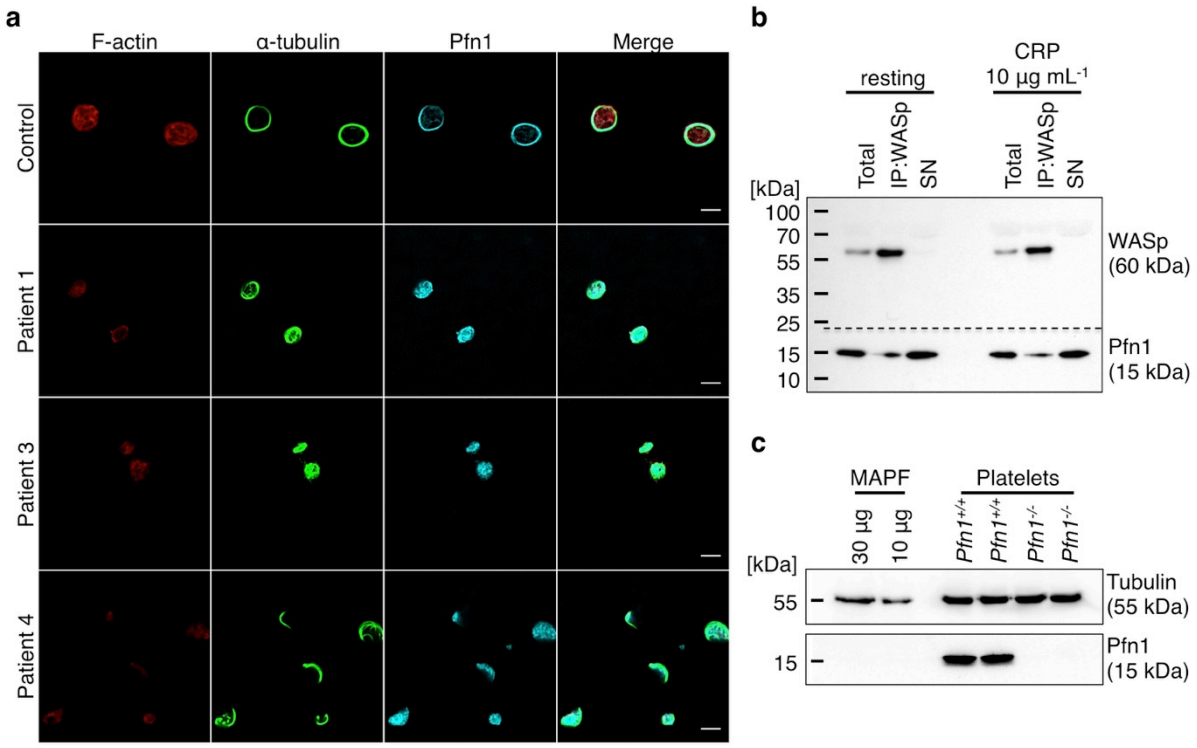

Figure 26 | Mis-localization of Pfn1 in platelets of WAS patients. (**a**) Resting platelets of healthy human controls and WAS patients 1, 3 and 4 were immobilized on poly-L-lysine and stained for F-actin (red), α-tubulin (green) and Pfn1 (cyan). Scale bars, 3 µm. (**b**) WASp was precipitated from sonificated resting or 10 µg mL^{-1} *collagen-related peptide* (CRP)-activated human platelet lysates using a mouse anti-WASp antibody. Samples were separated by SDS-PAGE and immunoblotted with a rabbit anti-Pfn1 or a rabbit anti-WASp antibody. (**c**) A commercially purchased protein fraction of *microtubule-associated proteins* (MAPF; #MAPF-A, Cytoskeleton Inc.) and platelet lysates of *Pfn1*$^{+/+}$ and *Pfn1*$^{-/-}$ platelets were separated by SDS-PAGE, immobilized on a PVDF membrane and probed for tubulin and Pfn1. (Bender* & Stritt* *et al. Nat Commun* 2014)[40]

4.1.12. Altered WASp levels in carriers' PBMCs

In the course of the studies on WAS patients' platelets, WASp expression levels in PBMCs were determined, serving as internal control (Fig. 27a). Interestingly, in two analyzed female carriers the overall WASp expression levels were increased in PBMCs as compared with healthy controls, whereas in the male patients virtually no WASp expression could be detected (Fig. 27a). Taking a closer look at the dot plot for the WASp expression levels, it became evident that two distinct cell populations (WASp^{low} (Pop1) and WASp^{high} (Pop2)) could be identified in the PBMC samples of female carriers (Fig. 27b), which is in line with previous reports.[268] Interestingly, quantification revealed markedly reduced expression of WASp in 7.3% of lymphocytes and 67.1% of monocytes. In stark contrast, in 92.7% of lymphocytes and 32.9% of the measured monocytes an increased WASp expression was detected, which has not been described so far. Together these observations suggest that WASp plays a more important role in the development of lymphocytes than for monocytes.

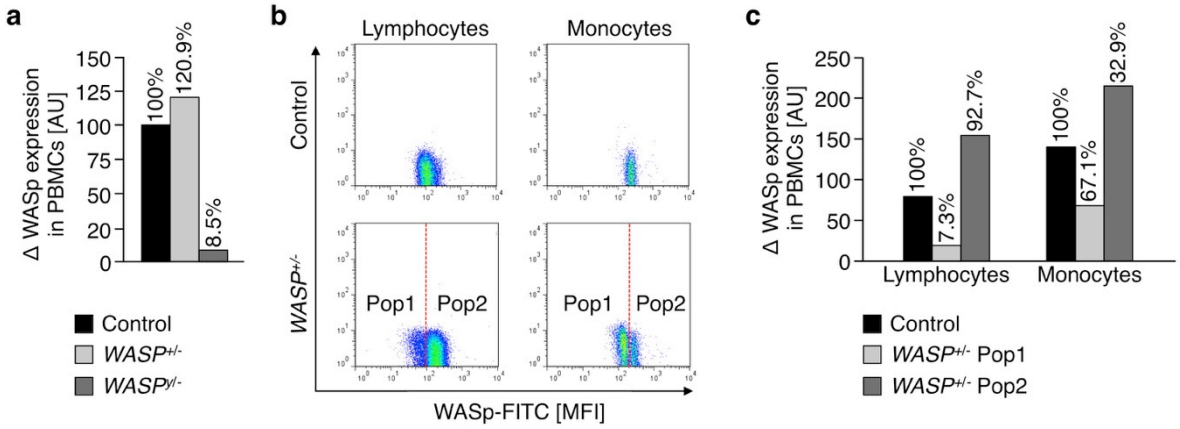

Figure 27 | Increased WASp expression in PBMCs of WAS carrier. (**a**) Relative WASp expression levels in *peripheral blood mononuclear cells* (PBMC) of a healthy control, WAS carrier (*WASP*$^{+/-}$) and a WAS patient (*WASP*$^{y/-}$). PBMCs were isolated from whole blood and intracellular WASp was stained. Analysis was performed by flow cytometry. Values on top of bars indicate relative WASp expression as % of control. (**b**) Representative dot plots of WASp expression profile in lymphocytes (left panel) and monocytes (right panel), respectively. (**c**) Relative WASp expression levels in the WASp^{low} (Pop1) and WASp^{high} (Pop2) populations of the female carrier. Values on top of bars indicate the percentage of carrier's cells within the WASp^{low} (Pop1) and WASp^{high} (Pop2) cell populations, respectively. (Stritt *et al.*, unpublished observation)

4.2. Twinfilin2a is a central regulator of platelet reactivity and turnover

Similarly to Pfn1, Twf2a also belongs to the group of small actin-binding proteins, but was proposed to rather inhibit than promote actin assembly. However, in contrast to Pfn1 far less is known about the molecular role of Twf2a. The first report on a Twf2a knockout mouse (further referred to as *Twf2a*$^{-/-}$) in 2011 by Nevalainen *et al.* did not reveal any developmental or histological alterations. Consequently, the authors concluded that Twf2a is dispensable for mouse development and suggested that Twf1 may compensate for the lack of Twf2a.[150] However, in this initial description blood cells, particularly platelets, were not analyzed.

4.2.1. *Twf2a*$^{-/-}$ mice develop a age-dependent macrothrombocytopenia

The expression of different Twf isoforms in platelets was analyzed by RT-PCR (Fig. 28a). Heart cDNA from *WT* mice served as positive control and *Gapdh* expression was determined as loading control. Both, *Twf1* and *Twf2a* were prominently expressed in platelets while, *Twf2b* could not be detected (Fig. 28a). The prominent expression of *Twf2a* in platelets, together with the finding that MK/ platelet-specific Twf1 deficiency neither affected megakaryopoiesis, thrombopoiesis, nor platelet function (Stritt *et al.*, unpublished observation), strongly suggested compensatory mechanisms and redundant functions of the different Twf isoforms in MKs and platelets. Nevertheless, the role of Twf2a in platelet production and function is entirely unknown.

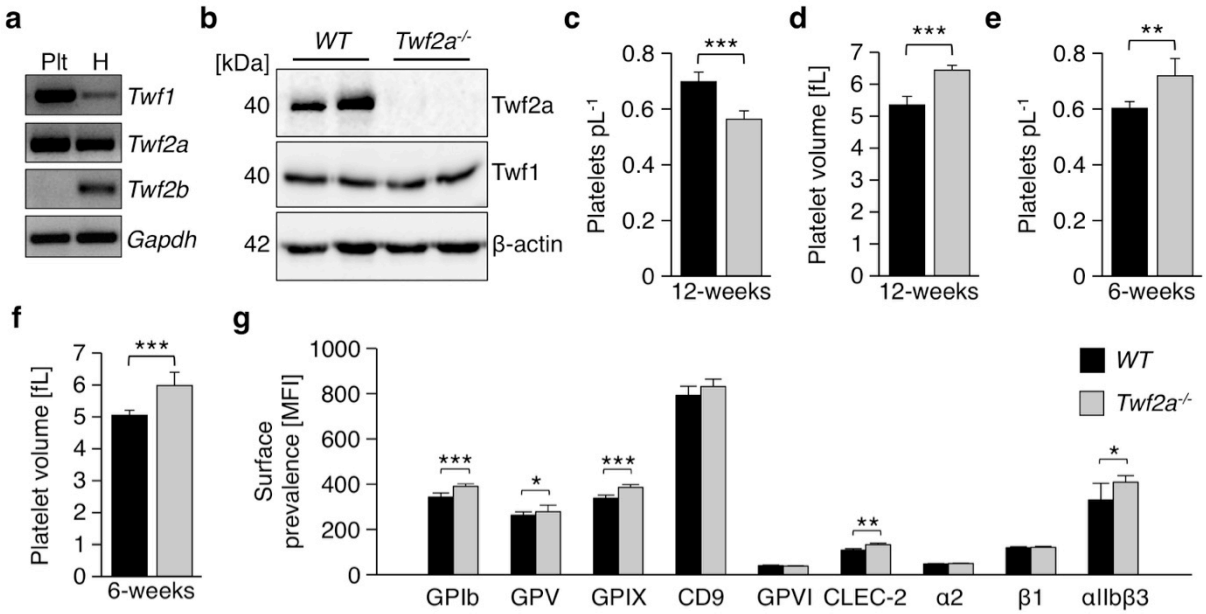

Figure 28 I **Age-dependent macrothrombocytopenia in *Twf2a*$^{-/-}$ mice.** (**a**) Assessment of Twf isoform expression in *WT platelets* (Plt). *WT heart cDNA* (H) and *Gapdh* was used as control. (**b**) Immunoblot on platelet lysates proves efficiency of the targeting strategy. (**d-f**) Platelet count (**c, e**) and size (**d, f**) of 12- (**c, d**) and 6-weeks (**e, f**) old mice. (**g**) Surface prevalence of major platelet glycoproteins assessed by flow cytometry. Values are mean ± s.d. (n = 6). Unpaired Student's *t*-test: ***P< 0.001; **P< 0.01; *P< 0.05. (Stritt *et al.*, unpublished observation)

Western blot analysis on platelet lysates confirmed effective ablation of Twf2a expression on protein level, whereas no compensatory upregulation of Twf1 was observed (Fig. 28b). Assessment of platelet count and size revealed an age dependent macrothrombocytopenia (Fig. 28c-d), while at younger ages a macrothrombocytosis with both, an increased platelet number and size was observed (Fig. 28e-f). In line with the increased platelet size, the surface prevalence of major platelet glycoproteins was slightly increased (Fig. 28g), while the distribution and number of white cells in the blood (Fig. 29a), spleen (Fig. 29b, c), lymph nodes (Fig. 29b, d) and thymus (Fig. 29b, e, f) were grossly unaltered.

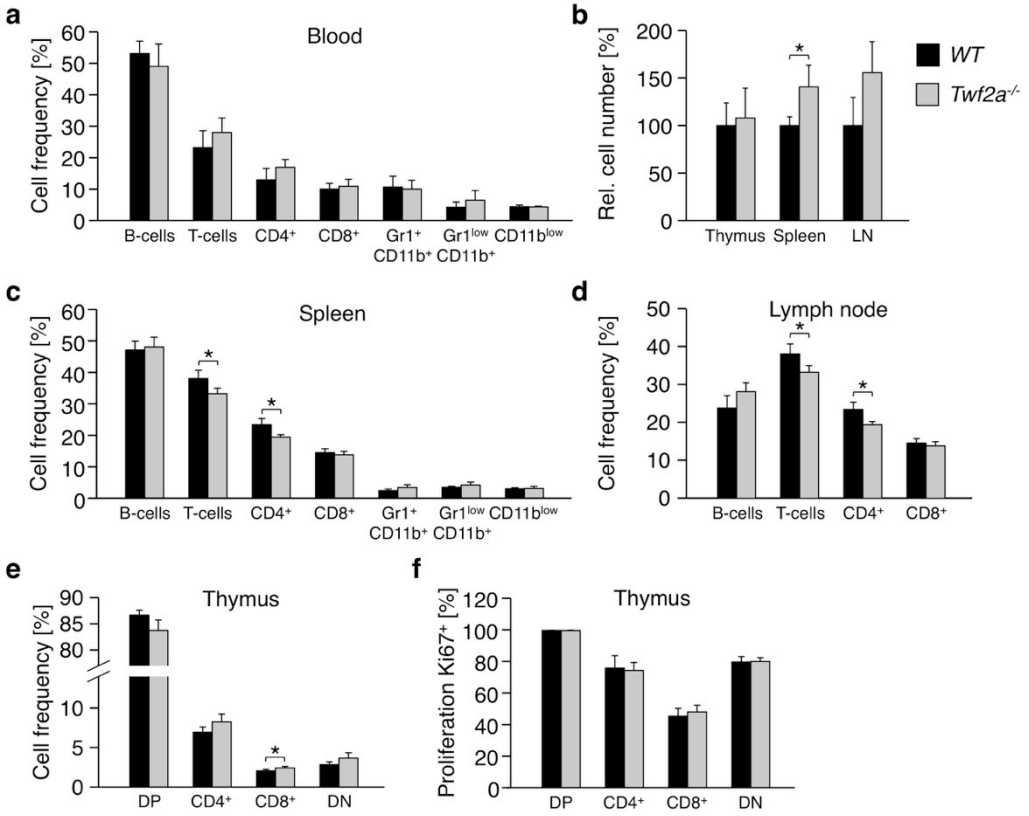

Figure 29 | Normal numbers and distribution of leukocytes in *Twf2a*$^{-/-}$ mice. (**a**) Determination of the distribution of white cell populations in the blood. (**b**) Total cell numbers of lymphatic tissues were determined by flow cytometry. (**c-e**) Determination of lymphatic cell populations in the spleen (**c**), lymph node (**d**) and thymus (**e**). (**f**) Assessment of T-cell proliferation within the thymus. Experiments on immune cells were performed in collaboration with Dr. Timo Vögtle. Values are mean ± s.d. (n = 6). Unpaired Student's *t*-test: **P*< 0.05. (Stritt *et al.*, unpublished observation)

4.2.2. Twf2a is a critical regulator of platelet life span

Next, the cause of the observed thrombocytopenia was analyzed. *Twf2a*$^{-/-}$ mice had a markedly decreased platelet life span ($T_{1/2}$ of control platelets: 48.6 h, $T_{1/2}$ of *Twf2a*$^{-/-}$ platelets: 22.3 h) *in vivo* (Fig. 30a). Assessment of the presence of platelet-bond autoantibodies revealed no gross differences between platelets of control and *Twf2a*$^{-/-}$ mice (Fig. 30b), thus excluding that autoantibodies account to the accelerated clearance of *Twf2a*$^{-/-}$ platelets. In

agreement with this, depletion of macrophages within the whole body using clodronate-encapsulated liposomes increased platelet counts in *WT* mice and similarly, although to a lesser extent in *Twf2a*$^{-/-}$ mice, clearly demonstrating that Twf2a-deficient platelet are not preferentially removed from the circulation by macrophages (Fig. 30c, d). Similarly, splenectomy had no long-term effect on platelet counts in *Twf2a*$^{-/-}$ mice (Fig. 30e, f), thus strongly suggesting alternative, macrophage-independent mechanisms of platelet clearance.

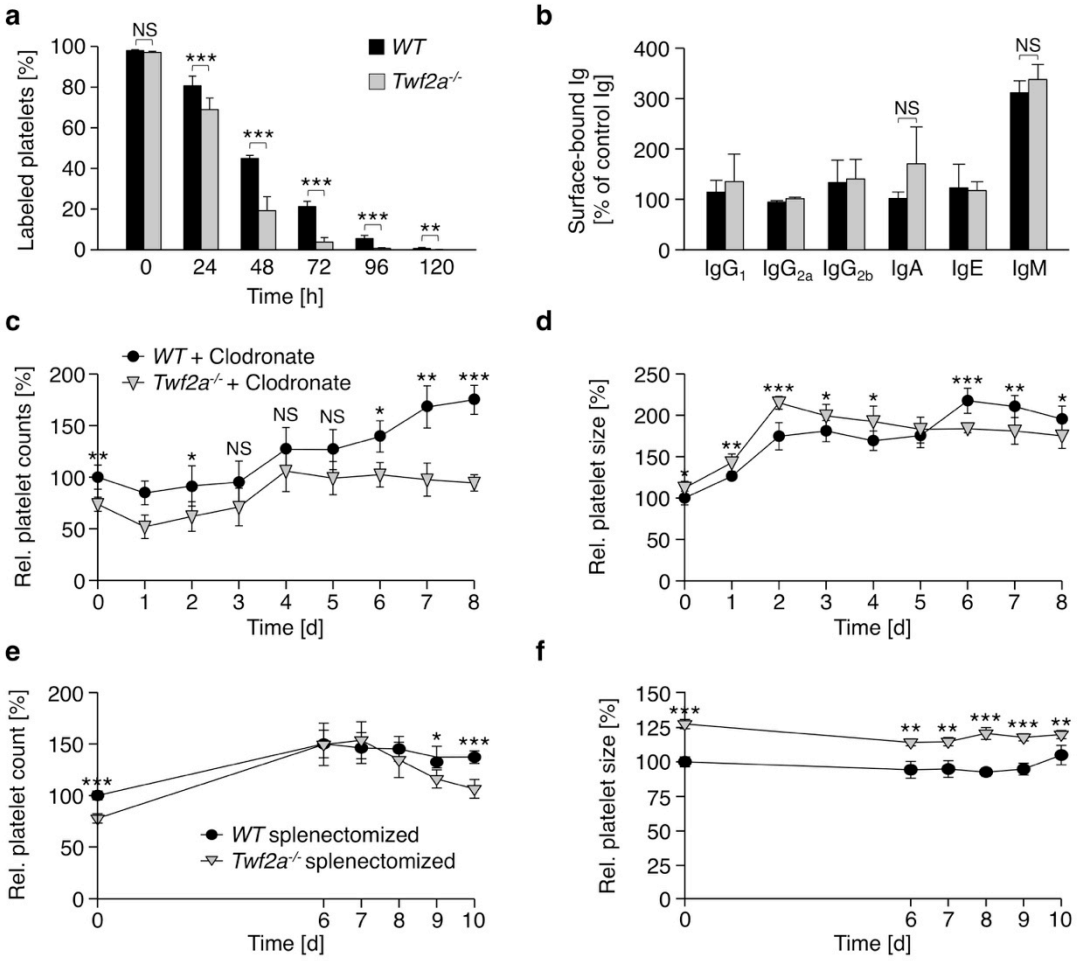

Figure 30 | Markedly reduced life span of *Twf2a*$^{-/-}$ platelets. (**a**) Platelet life span was measured by injection of a DyLight 488 α-GPIX derivative. (**b**) Determination of platelet-bound *immunoglobulins* (Ig) relative to non-specific Igs. (**c-f**) Platelet counts (**c, e**) and size (**d, f**) were monitored over time after clodronate-encapsulated liposome-mediated macrophage depletion (**c, d**) and splenectomy (**e, f**). Values are mean ± s.d. (n = 6). Unpaired Student's *t*-test: ***P< 0.001; **P< 0.01; *P< 0.05; NS, non-significant. (Stritt *et al.*, unpublished observation)

In addition, it was recently shown that aged, desialylated platelets are cleared from the circulation by the Ashwell-Morell receptor on hepatocytes.[68] Hence, it would be interesting to determine the sialylation status of *Twf2a*$^{-/-}$ platelets to further elucidate a possible contribution of this alternate platelet clearance mechanism.

4.2.3. Twf2a is a negative regulator of platelet reactivity

Since Twf2a-deficient platelet were neither opsonized with antibodies (Fig. 30b) nor preferentially cleared by macrophages (Fig. 30c-f), this strongly suggested that the observed thrombocytopenia might be a result of excessive platelet activation or consumption.

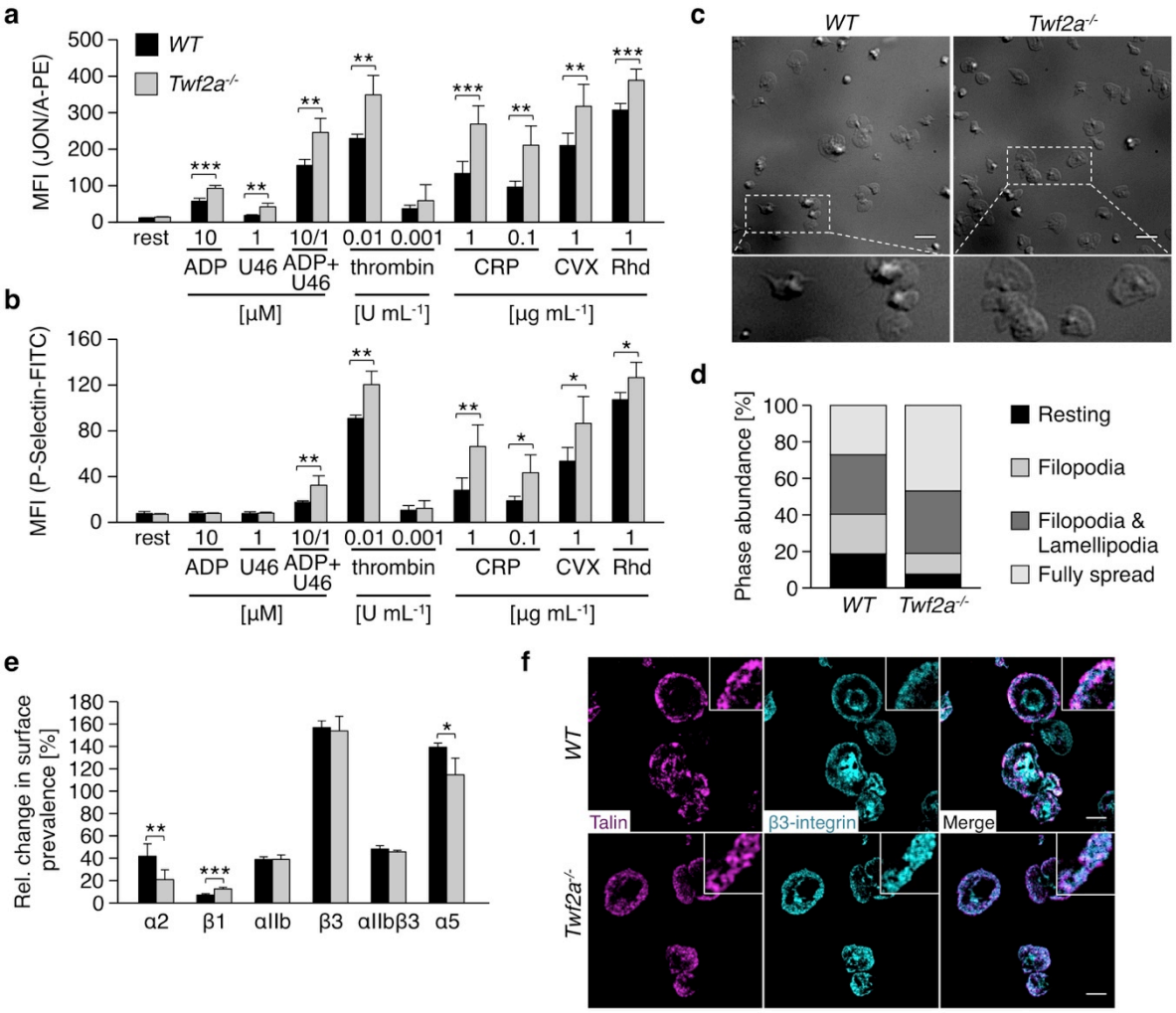

Figure 31 | Increased integrin activation in *Twf2a*$^{-/-}$ platelets. (**a, b**) Platelet αIIbβ3 integrin activation (**a**) and P-selectin exposure (**b**), serving as a measure for α-granule release, were determined by flow cytometry. Rest, *resting*; ADP, *adenosine diphosphate*; U46, *U46619*, a stable thromboxane A_2 analogue; CRP, *collagen-related peptide*; CVX, *convulxin*; Rhd, *rhodocytin*. (**c, d**) Washed platelets were allowed to spread (15 min) on fibrinogen (100 µg mL^{-1}), analyzed by differential interference contrast microscopy (**c**) and phase abundance (**d**) was determined. Scale bars, 3 µm. (**e**) Integrin surface recruitment upon platelet activation (0.1 U mL^{-1} thrombin) was determined by flow cytometry. (**f**) Tln-1 recruitment to β3 integrin tails was assessed by immunostaining and confocal microscopy. Scale bars, 3 µm. Values are mean ± s.d. (n = 6). Images are representative of at least 6 individuals. Unpaired Student's *t*-test: ***P< 0.001; **P< 0.01; *P< 0.05. (Stritt *et al.*, unpublished observation)

To test this directly, platelet integrin inside-out activation (Fig. 31a) and degranulation, evidenced by the surface prevalence of P-selectin (Fig. 31b), was determined. Interestingly, *Twf2a*$^{-/-}$ platelets displayed a pronounced hyper-reactivity towards all tested agonists with both increased integrin activation and α-granule release (Fig. 31a, b). In line with this, integrin outside-in signaling as assessed in a spreading assay on fibrinogen was accelerated (Fig. 31c) with an increased proportion of fully spread platelets after 15 min (Fig. 31d).

Increased surface recruitment of integrins upon activation represents a possible explanation for the enhanced inside-out and outside-in integrin activation and accelerated spreading of Twf2a-deficient platelets. However, integrin recruitment was normal in *Twf2a*$^{-/-}$ platelets, thus excluding elevated integrin copy numbers on the platelet surface as a cause for the observed hyper-reactivity (Fig. 31e). Moreover, Tln-1 recruitment to the tails of β integrins is a key step in integrin activation. In spread Twf2a-deficient platelets Tln-1 and β3 integrin co-localization was more pronounced than in controls and the width of the cortical zone of co-localization was doubled (0.54 µm ± 0.13 µm for controls and 1.08 µm ± 0.18 µm in *Twf2a*$^{-/-}$ platelets) (Fig. 31f).

In agreement with the increased reactivity of *Twf2a*$^{-/-}$ platelets, the overall amount of newly generated thrombin (Fig. 32a) and the peak concentrations (Fig. 32b) were increased, whereas the velocity of thrombin production, measured as the time to peak concentration was indistinguishable from controls (Fig. 32c).

Unexpectedly, PS exposure on the outer membrane leaflet, which is a prerequisite for the pro-coagulant activity of platelets,[269] was reduced in Twf2a-deficient platelets upon stimulation with different agonist (Fig. 32d). However, there's growing evidence that factors other than PS exposure on platelets regulate thrombin generation.[269] In line with the reduced exposure of PS on the platelet surface, also mitochondrial depolarization was less pronounced in Twf2a-deficient platelets upon stimulation with different agonists (Fig. 32e, f).

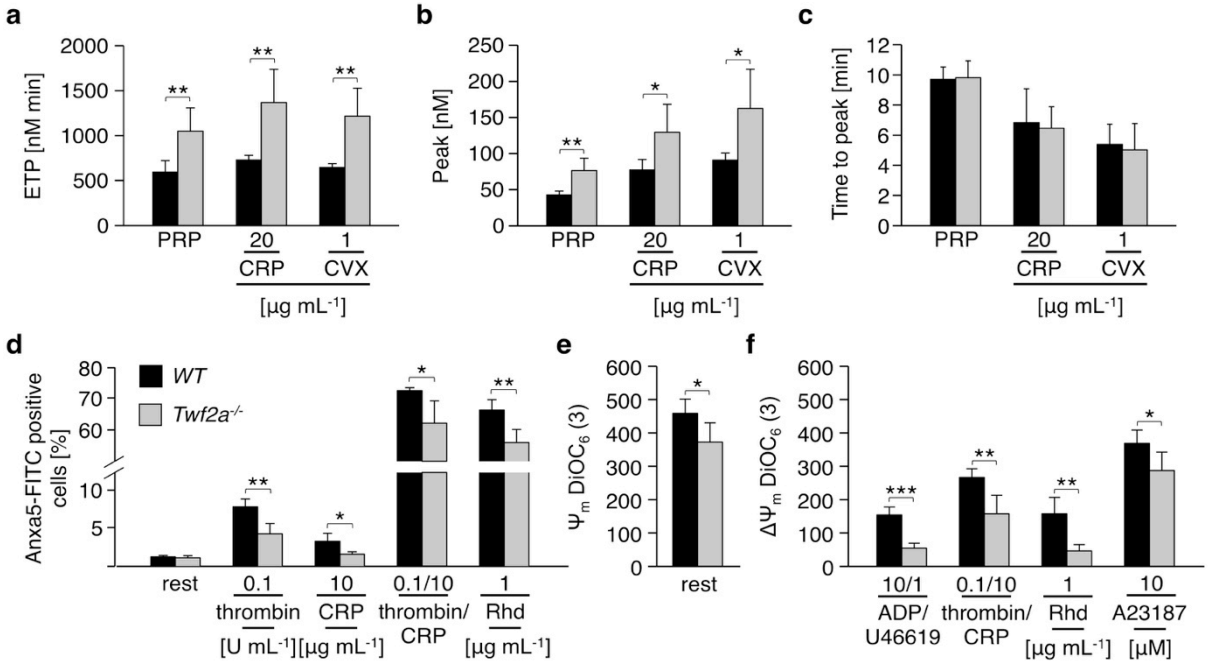

Figure 32 | *Twf2a*$^{-/-}$ platelets are less prone to apoptosis. (**a-c**) Citrate-anti-coagulated PRP remained untreated (PRP), or platelets were stimulated for 10 min at 37°C with *collagen-related peptide* (CRP; 20 µg mL^{-1}) or *convulxin* (CVX; 1 µg mL^{-1}). Thrombin generation was triggered with tissue factor/$CaCl_2$. *Endogenous thrombin potential* (**a**; ETP), maximal thrombin concentration (**b**), and the time to the peak concentration (**c**) were determined. Thrombin generation was determined by Sarah Schießl. (**d-e**) Platelet apoptosis was assessed using Anxa5-FITC binding to exposed phosphatidylserine (**d**) or the mitochondrial membrane potential sensor *3,3′-dihexyloxacarbocyanine iodide* ($DiOC_6$ (3)); **e, f**). Rest, *resting*; ADP, *adenosine diphosphate*; Rhd, *rhodocytin*, A23187, *ionophore*. Values are mean ± s.d. (n = 6). Unpaired Student's *t*-test: ***P< 0.001; **P< 0.01; *P< 0.05. (Stritt *et al.*, unpublished observation)

4.2.4. Twf2a interferes with integrin closure

It has previously been reported that the prevalence of activated platelet αIIbβ3 integrins and the exposure of PS are critically linked. For example, upon sustained Ca^{2+} signaling, which triggers PS exposure on the outer membrane leaflet,[270] αIIbβ3 integrins can be switched back to their low-affinity state, through Ca^{2+}-mediated activation of calpain and cleavage of the cytoplasmic tails of β3 integrins.[270-272]

To assess the role of Twf2a in the dynamics of integrin closure, time course experiments were performed and the percentages of platelets with activated αIIbβ3 integrins (quadrant Q1), PS exposure (Q3), or both (Q2) were determined. In line with the findings on the decreased PS exposure on *Twf2a*$^{-/-}$ platelets (Fig. 32d), an increased percentage of platelets with activated integrins (events in Q1 and Q2) was determined after both, 5 min (39.1% ± 3.7% for controls and 43.9% ± 2.9% for *Twf2a*$^{-/-}$ platelets; *P< 0.05) and 30 min (30.5% ± 3.1% for controls and 39.0% ± 2.3% for *Twf2a*$^{-/-}$ platelets; **P< 0.01) upon simultaneous stimulation with thrombin and CRP (Fig. 33). Together, these results strongly suggest that Twf2a deficiency interferes with Ca^{2+} signaling and thereby delays PS exposition, calpain

activity and consequently integrin closure. The observed hyper-reactivity of *Twf2a*$^{-/-}$ platelets may cause an increased intravascular consumption of platelets and therefore account for the progressing macrothrombocytopenia.

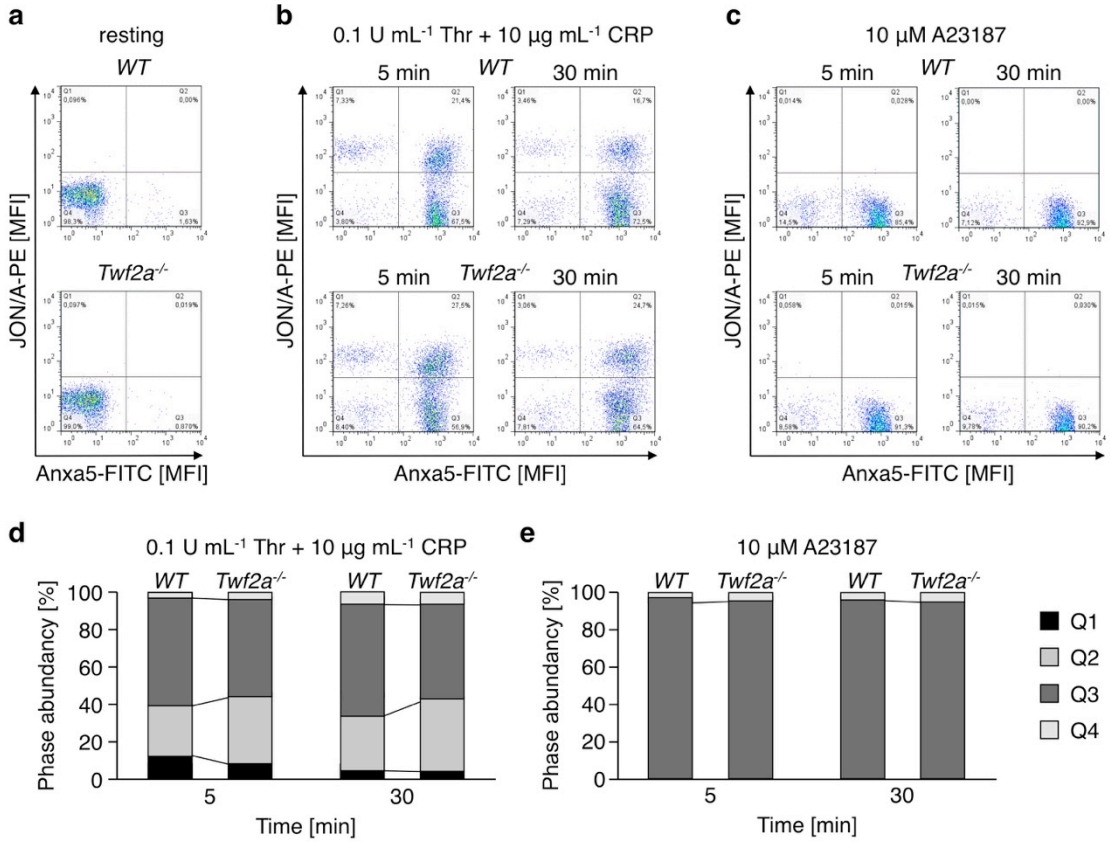

Figure 33 | Delayed integrin closure in Twf2a-deficient platelets. (**a-c**) Washed platelets remained untreated or were stimulated with different agonists for different periods of time. Activation of αIIbβ3 integrins (JON/A-PE) and phosphatidylserine exposure on the outer leaflet of the platelet membrane (Anxa5-FITC) was determined by flow cytometry. Images are representative of at least 6 individuals. (**d, e**) Relative number of events per quadrant. Q1, JON/A$^+$ Anxa5$^-$ (upper left); Q2, JON/A$^+$ Anxa5$^+$ (upper right); Q3, JON/A$^-$ Anxa5$^+$ (lower right); Q4, JON/A$^-$ Anxa5$^-$ (lower left). Values are mean (n = 6). (Stritt *et al.*, unpublished observation)

4.2.5. Accelerated arterial thrombus formation in *Twf2a*$^{-/-}$ mice

To investigate whether the platelet hyper-reactivity observed *in vitro,* can similarly be observed *in vivo*, arterial thrombus formation was analyzed in *Twf2a*$^{-/-}$ mice.

Upon $FeCl_3$-induced damage of the endothelium in mesenteric arterioles, platelet adhesion (7.4 min ± 2.9 min in control and 4.8 min ± 3.1 min in *Twf2a*$^{-/-}$ mice) and vessel occlusion (15.6 min ± 6.3 min in control and 10.6 min ± 2.4 min in *Twf2a*$^{-/-}$ mice) occurred at earlier time points in Twf2a-deficient mice than in controls (Fig. 34). This is in line with the observed hyper-reactivity and increased thrombin generation *in vitro* (Fig. 31 and 32a-c).

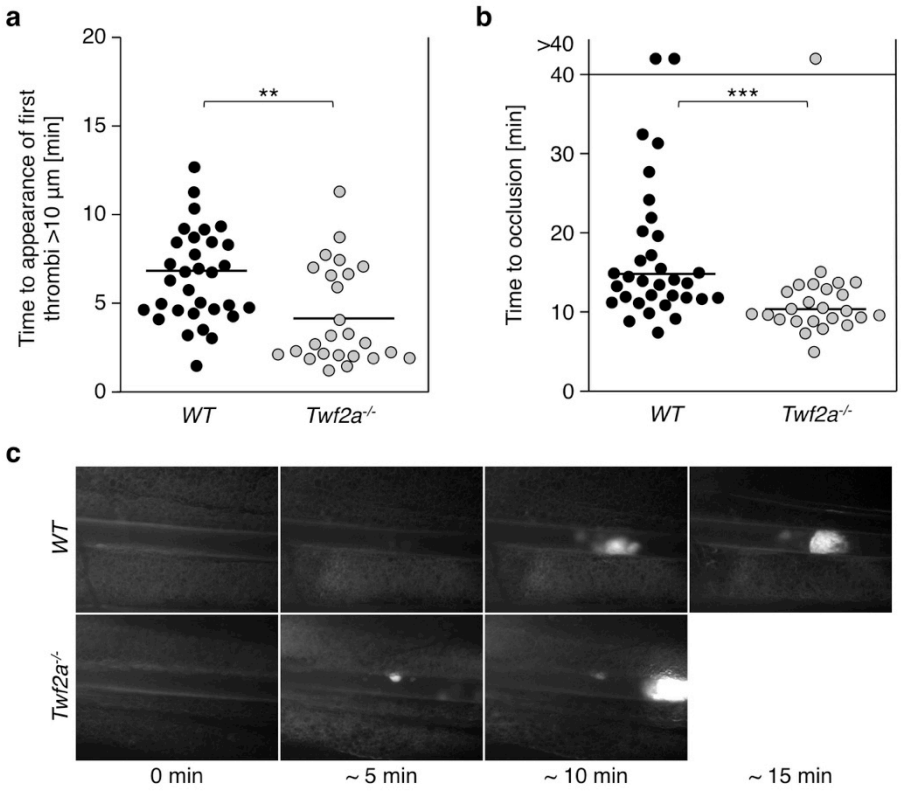

Figure 34 | Twf2a is a critical regulator of platelet reactivity *in vivo*. (**a, b**) Accelerated adhesion of platelets (**a**) and occlusion of mesenteric arterioles (**b**) in Twf2a-deficient mice upon $FeCl_3$-induced injury of the endothelial barrier. Each symbol represents 1 mesenteric arteriole (n = 12 individuals). Horizontal lines represent mean. $FeCl_3$ model was performed by Sarah Schießl. Unpaired Student's *t*-test: ***$P < 0.001$; **$P < 0.01$. (Stritt *et al.*, unpublished observation)

4.2.6. Twf2a is a positive regulator of actin filament assembly in platelets

Rearrangements of the actin cytoskeleton are known to be critical for integrin activation and Twf2a was shown to be a central regulator of these dynamics. However, there are some controversies on its precise function; i.e. whether Twf2a acts as an actin assembly inhibiting or promoting molecule.[106,145,151,156] Morphological analyses revealed no cytoskeletal alterations, but a mildly enlarged size of resting Twf2a-deficient platelets (Fig. 35a). Similarly, spread *Twf2a*$^{-/-}$ platelets displayed an increased size and a slightly thickened cortical actin cytoskeleton (Fig. 35b). Remarkably, after 30 min of spreading Twf2a-deficient platelets were almost devoid of microtubules while they were still prominently visible in platelets from controls (Fig. 35b). To address this in more detail, microtubule stability was assessed by incubating platelets in the cold, which led to the disassembly of microtubules in both, *WT* and Twf2a-deficient platelets (Fig. 35c). Similarly, upon re-warming to 37°C microtubules were normally reassembled to form the marginal band (Fig. 35c). Interestingly, when challenging microtubules with the disassembly promoting toxin colchicine, microtubules in *WT* platelets ap-

peared slightly less sensitive and were partially still present while they were completely depolymerized in *Twf2a*$^{-/-}$ platelets (Fig. 35d).

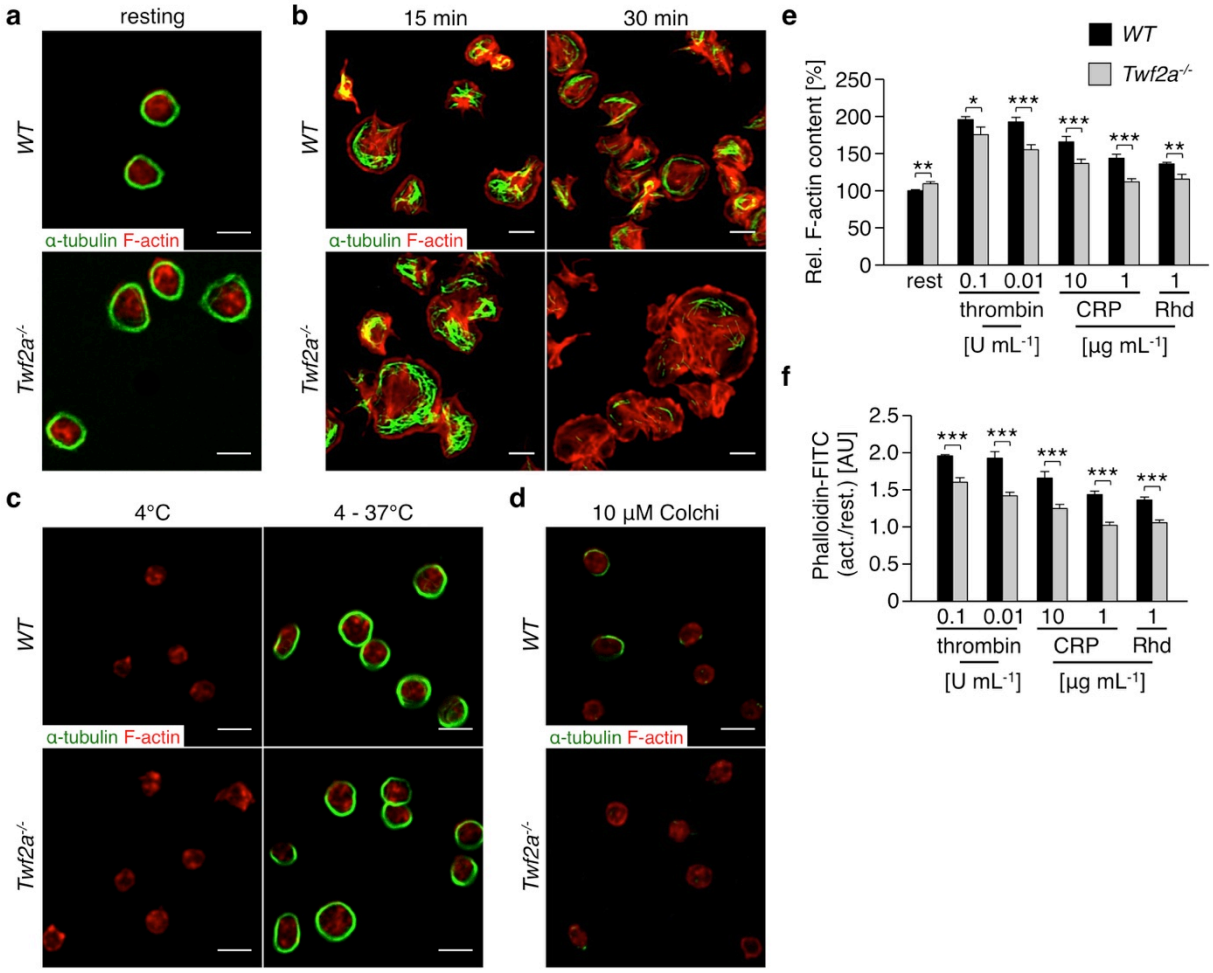

Figure 35 | **Aberrant cytoskeletal rearrangement in *Twf2a*$^{-/-}$ platelets.** (**a, b**) Resting (**a**) or on fibrinogen spread (**b**) platelets were stained for F-actin (red) and α-tubulin (green) after the indicated time points. (**c, d**) Resting platelets were subjected to cold-induced microtubule disassembly by incubation for 3 h at 4°C with or without subsequent rewarming (**c**), or were treated with 10 µM colchicine (**d**) and processed for confocal microscopy. Analysis was performed by confocal microscopy. Scale bars, 3 µm. Images are representative of at least 6 individuals. (**e, f**) Relative F-actin content (**e**) and the ratio of the MFI(Phalloidin-FITC) of activated versus resting platelets (**f**) was determined by flow cytometry. Values are mean ± s.d. (n = 6). CRP, *collagen-related peptide*; Rhd, *rhodocytin*. Unpaired Student's *t*-test: ***$P < 0.001$; **$P < 0.01$; *$P < 0.05$. (Stritt *et al.*, unpublished observation)

This unexpected finding of a role of Twf2a in the regulation of microtubule dynamics and stability certainly requires further investigation, but is not entirely unique as there's growing evidence that the small actin-binding protein Pfn1 is a critical regulator of microtubule stability in platelets.[40] Besides altered microtubule dynamics, resting *Twf2a*$^{-/-}$ platelets displayed an increased F-actin content (Fig. 35e) and an impaired assembly upon stimulation (Fig. 35f). The impaired F-actin assembly in Twf2a-deficient platelets (Fig. 35e, f) contradicts reports on an inhibitory role of Twfs in actin assembly from previous studies. These results showed for

the first time an F-actin assembly-promoting role of Twf2a during platelet activation, presumably via its interaction with CPs.

4.2.7. Interference with cytoskeletal dynamics cannot rescue or reproduce the hyper-reactivity of *Twf2a*$^{-/-}$ platelets

To test whether the observed cytoskeletal alterations could account for the hyper-reactivity platelets of controls and *Twf2a*$^{-/-}$ mice remained untreated (DMSO) or were pretreated with colchicine or latrunculin A. Subsequently, platelets were stimulated with different agonists and activation of αIIbβ3 integrins and degranulation were assessed by flow cytometry. Pretreatment with the microtubule depolymerizing toxin colchicine did neither interfere with the ability of platelets to activate their αIIbβ3 integrins, nor with the release of α-granules (Fig. 36a, b). In contrast, pretreatment with the F-actin destabilizing toxin latrunculin A strongly impaired αIIbβ3 integrin activation and to a lesser extent degranulation (Fig. 36a, b). Latrunculin A pretreatment diminished the hyper-reactivity of Twf2a-deficient, but also the reactivity of control platelets, thus confirming the critical role of the actin cytoskeleton in integrin activation. This finding is further supported by studies on Tln-1, which provides the link between integrins and the cytoskeleton.[273] MK-/platelet-specific Tln-1-deficiency resulted in completely abolished platelet integrin activation thus strongly suggesting that the association of integrins with the actin cytoskeleton represents a prerequisite for their activation.[236] However, this issue is still under debate.

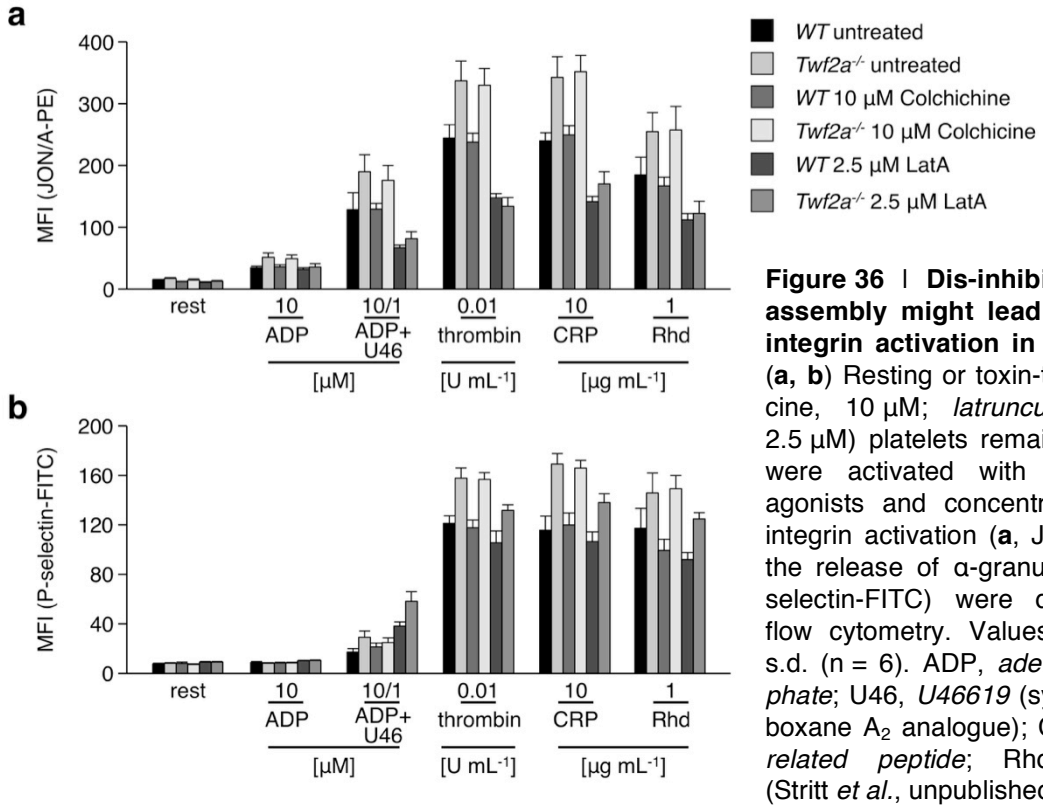

Figure 36 | Dis-inhibition of actin assembly might lead to increased integrin activation in *Twf2a*$^{-/-}$ mice. (**a, b**) Resting or toxin-treated (colchicine, 10 µM; *latrunculin A* (LatA), 2.5 µM) platelets remained resting or were activated with the indicated agonists and concentrations. αIIbβ3 integrin activation (**a**, JON/A-PE) and the release of α-granules (**b**, anti-P-selectin-FITC) were determined by flow cytometry. Values are mean ± s.d. (n = 6). ADP, *adenosine diphosphate*; U46, *U46619* (synthetic thromboxane A_2 analogue); CRP, *collagen-related peptide*; Rhd, *rhodocytin*. (Stritt *et al.*, unpublished observation)

4.2.8. Increased fragmentation of BM MKs in *Twf2a*$^{-/-}$ mice

In order to elucidate the contribution of the markedly reduced platelet life span to the age-dependent development of thrombocytopenia in Twf2a-defcient mice in more detail, histological sections of the bone marrow and spleens were prepared (Fig. 37a, d). Quantification revealed an increased number of BM MKs in *Twf2a*$^{-/-}$ mice with an aberrant morphology (Fig. 37b) and in line with this, plasma Thpo levels were slightly reduced (Fig. 37c). In contrast, the architecture of the spleen and the number of splenic MKs were indistinguishable from controls (Fig. 37d-f). To take a closer look at the aberrant appearance of the MKs in the BM of *Twf2a*$^{-/-}$ mice, whole femora cryosections and immunostainings were performed and revealed signs of increased MK fragmentation as compared to control (Fig. 37g). Assessment of MK ploidy and ultrastructure confirmed this finding, as the majority of MKs in the BM of *Twf2a*$^{-/-}$ mice was very mature and formed proplatelets (Fig. 37h, i). In line with this, *in vitro* assessment of platelet production using fetal liver cell-derived MKs revealed an increased fraction of Twf2a-deficient proplatelet-forming MKs as compared with control (Fig. 37j, k). In addition, immunostaining showed an increased size of proplatelet tips and a decreased content of microtubules in Twf2a-deficient MKs (Fig. 37k).

In summary, these results reveal a critical role of Twf2a in the regulation of platelet life span, integrin activation and closure and thrombopoiesis. These defects can presumably be explained through a reduced cortical tension in the absence of Twf2a. The observed macrothrombocytopenia most likely resulted from accelerated platelet consumption within the circulation due to a marked hyper-reactivity and impaired integrin inactivation and cannot be fully compensated by an increased platelet production by Twf2a-deficient MKs.

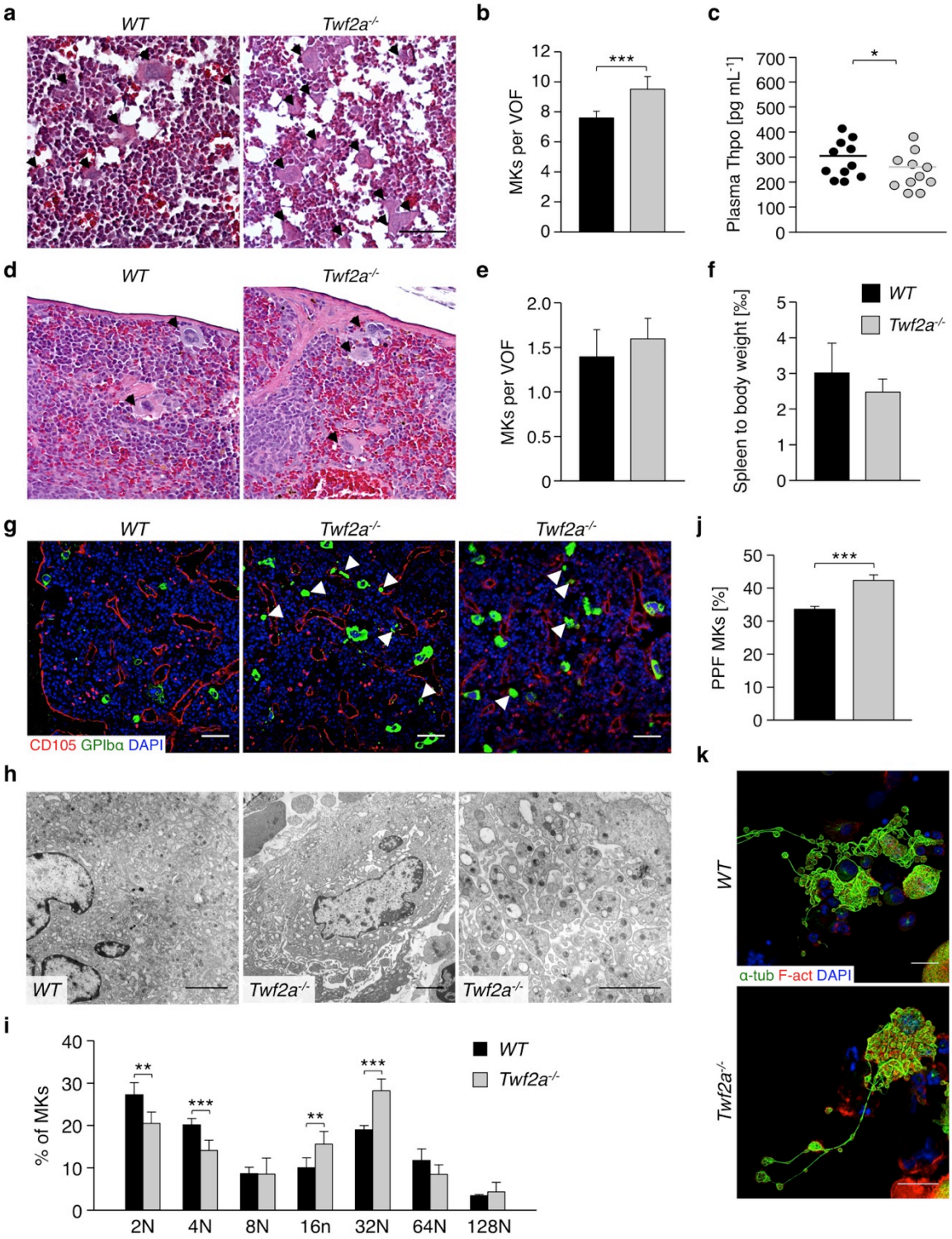

Figure 37 | Increased MK numbers and proplatelet formation compensate for the accelerated platelet clearance in *Twf2a*$^{-/-}$ mice. (**a-f**) Hematoxylin and eosin stained histological sections of femora (**a**) and spleens (**d**) were prepared and *megakaryocyte* (MK) numbers were quantified (**b, e**). (**c**) Plasma *thrombopoietin* (Thpo) levels were determined in control and *Twf2a*$^{-/-}$ mice. (**f**) Twf2a-deficient mice do not display splenomegaly. (**g-i**) MK morphology (**g, h**) and maturation (**i**) were analyzed by confocal (**g**), *transmission electron microscopy* (TEM) (**h**) and flow cytometry (**i**). CD105, red; GPIbα, green; DAPI, blue. Scale bars, 50 µm (confocal images). Scale bars, 3 µm (TEM images). (**j**) *Proplatelet formation* (PPF) of *fetal liver cell-derived* (FLC) MKs was analyzed. (**k**) Confocal microscopy images of FLC-derived MKs immunostained for α-tubulin (green), F-actin (red) and DAPI (blue). Scale bars, 25 µm. Images are representative of at least 6 individuals. Values are mean ± s.d. (n = 6). Unpaired Student's *t*-test: ***P< 0.001; **P< 0.01; *P< 0.05. (Stritt *et al.*, unpublished observation)

4.3. Rap1-GTP-interacting adaptor molecule (RIAM) is dispensable for platelet integrin activation and function in mice

To further decipher the mechanisms leading to the increased and sustained integrin activation in *Twf2a*$^{-/-}$ platelets, literature analysis for proteins involved in both, integrin activation and cytoskeletal rearrangements was performed. Among the identified candidates, RIAM, which is encoded by the *Apbb1ip* gene, was shown to be critical for platelet αIIbβ3 integrin activation in different *in vitro* cell culture approaches by recruiting Tln-1, but also for cell spreading and lamellipodia formation.[238,241,245,248] However, up to date no studies using genetic RIAM knockouts have been reported.

4.3.1. *RIAM-null* mice are viable and healthy

The *Apbb1ip* gene (Fig. 38a) was targeted by applying a *VelociGene Definitive Null Allele Design*, where exons 3 to 6 of the *Apbb1ip* gene were replaced with a *LacZ-p(A); Neo-p(A)* cassette by homologous recombination, thus abolishing Apbb1ip expression. *Apbb1ip*$^{+/-}$ mice were intercrossed to obtain *Apbb1ip*$^{-/-}$ (further on referred to as *RIAM-null*) and the respective control mice. *RIAM-null* mice were born at a normal Mendelian ratio (Fig. 38b), viable and fertile and appeared overall healthy. Western blot analysis confirmed strong expression of RIAM in control but not in *RIAM-null* platelets (Fig. 38c). Platelet counts (Fig. 38d), size (Fig. 38e) and the distribution of red and white blood cells (Fig. 38f) were indistinguishable from controls, suggesting that RIAM is not essential for hematopoiesis.

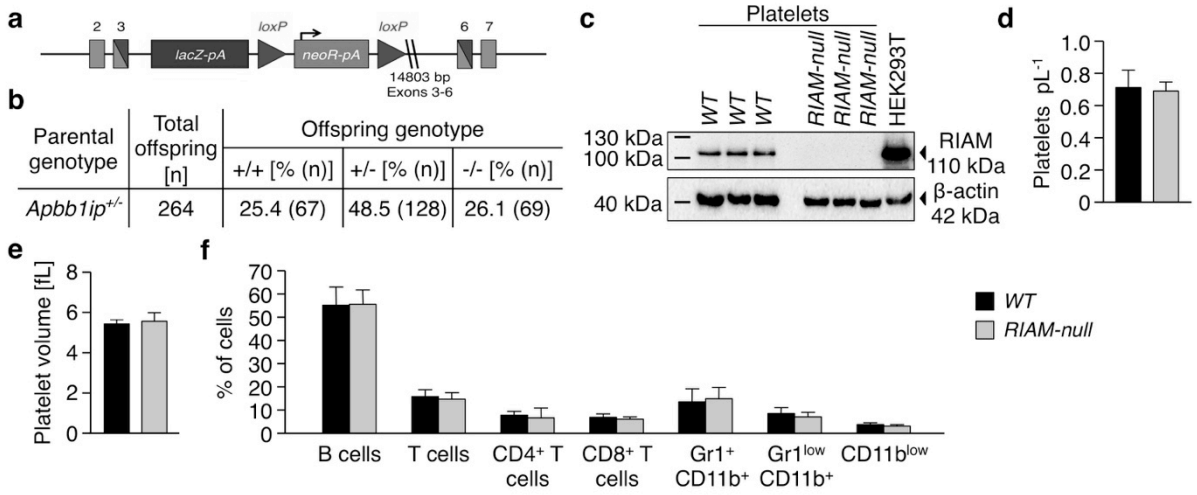

Figure 38 | Normal platelet numbers and size in *RIAM-null* mice. (**a**) Targeting strategy of *Apbb1ip* ES-cell clone A16066A-D5. (**b**) Distribution of genotypes in litters from heterozygous parent animals. (**c**) Western blot analysis reveals the absence of RIAM protein in *RIAM-null* platelets. (**d**) Unaltered platelet number and (**e**) size in RIAM-deficient mice as assessed by flow cytometry and with an automated blood cell analyzer. (**f**) Normal distribution of white cells in *RIAM-null* mice. Values are mean ± s.d. (n = 6). Unpaired Student's *t*-test. (Stritt *et al. Blood* 2015)[247]

4.3.2. Unaltered inside-out integrin activation in *RIAM-null* platelets

Flow cytometric analyses showed that control and *RIAM-null* platelets display comparable surface expression levels of β1 and β3 integrins both under resting conditions and upon stimulation with thrombin (Fig. 39a). Similarly, the expression of major platelet surface glycoproteins was indistinguishable from controls (Fig. 39b).

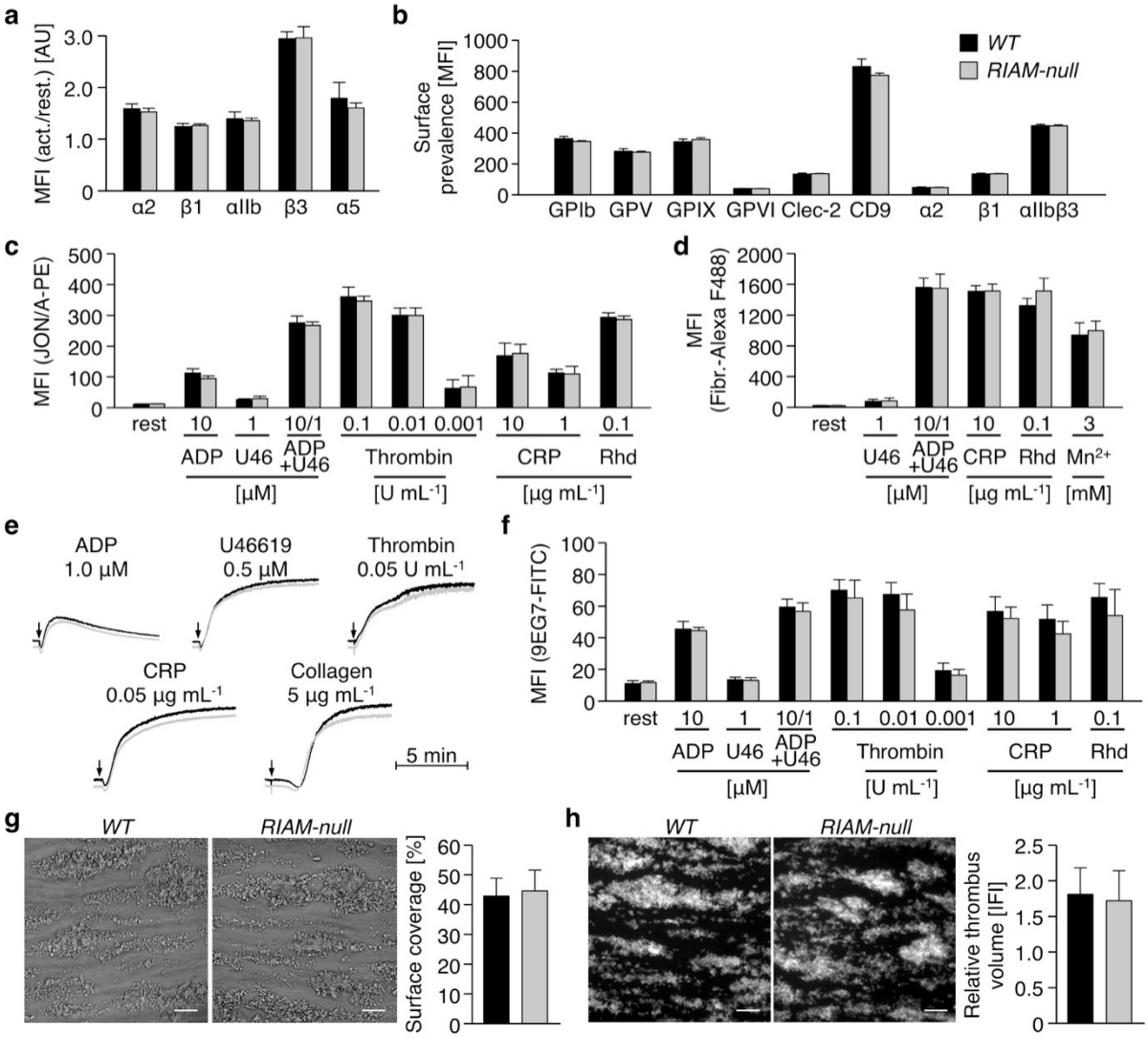

Figure 39 | Unaltered inside-out activation of integrins in *RIAM-null* platelets. (**a**) Integrins are normally recruited to the surface of *RIAM-null* platelets upon stimulation with thrombin (0.01 U mL^{-1}). (**b**) Normal surface prevalence of major glycoproteins in *RIAM-null* platelets. (**a-e**) Unaltered activation of platelet (**c**) αIIbβ3 integrin (JON/A-PE) translates into normal (**d**) fibrinogen-binding and (**e**) aggregation responses of *RIAM-null* platelets as determined by (**a-d**) flow cytometry or (**e**) turbidometric aggregometry. For aggregation studies with thrombin, *collagen-related peptide* (CRP), collagen and U46619 washed platelets (1.5 x 10^5 platelets per μL^{-1}) were used; aggregation studies with ADP were performed in platelet-rich plasma (1.5 x 10^5 platelets per μL^{-1}). U46, *U46619*, a stable thromboxane A_2 analogue; Rhd, *rhodocytin*. (**f-h**) Activation of platelet (**f**) β1 integrin (9EG7-FITC), as well as (**g**) adhesion and (**h**) thrombus formation of *RIAM-null* platelets under flow (1000 s^{-1}) on collagen I (70 μg mL^{-1}) was indistinguishable from *WT* controls. Scale bars in **g** and **h** represent 25 μm. (**a-d** and **f-h**) Values are mean ± s.d. (n = 6). Curves in **e** represent light transmission over time, with platelet-rich plasma set as 0% and platelet-poor plasma as 100% aggregation. The presented results are representative of at least three independent experiments with at least n = 5 individuals per group. Unpaired Student's *t*-test. (Stritt *et al. Blood* 2015)[247]

Next, agonist-induced αIIbβ3 integrin activation was determined using the JON/A-PE antibody[255] and, remarkably, found to occur with the same efficiency in *RIAM-null* and *WT* platelets in response to all tested agonists (Fig. 39c). Similar results were obtained for the binding of Alexa F488-conjugated fibrinogen (Fig. 39d). These results were entirely unexpected given previous studies where a knockdown of RIAM was associated with impaired cell adhesion and αIIbβ3 integrin activation.[238,240,241] Of note, time course experiments have also been performed for platelet fibrinogen-binding and obtained comparable results at all tested time points for control and mutant platelets, strongly suggesting that integrin disengagement is not affected by RIAM deficiency (Fig. 39d). In agreement with these data, *RIAM-null* platelets displayed normal aggregation responses to different agonists (Fig. 39e).

Besides αIIbβ3 integrins, RIAM has been implicated in β1 integrin activation and adhesion of Jurkat T-cells.[245] However, activation of β1 integrins, as assessed by binding of the 9EG7 antibody,[274] was comparable between *RIAM-null* and control platelets (Fig. 39f). Consistently, *RIAM-null* platelets showed normal adhesion (Fig. 39g) and aggregate formation (Fig. 39h) on collagen in a flow adhesion assay, which is known to be highly dependent on functional α2β1 integrins.[236,239,275]

4.3.3. Platelet outside-in signaling and arterial thrombus formation are not affected by RIAM deficiency

RIAM has recently been implicated in integrin outside-in signaling in melanoma cells.[252,276] To assess the role of RIAM in integrin outside-in signaling in platelets, control and *RIAM-null* platelets were allowed to spread on fibrinogen but no differences in adhesion, extent or kinetics of spreading (Fig. 40a) or cytoskeletal rearrangements were observed (Fig. 40b).

Likewise, integrin outside-in signaling dependent clot retraction was indistinguishable between *WT* and *RIAM-null* mice (Fig. 40c, d), excluding an essential role of RIAM in this process.

To investigate the role of RIAM in platelet integrin function *in vivo*, a tail bleeding time assay was used and comparable bleeding times for control (7.2 min ± 1.9 min) and *RIAM-null* mice (6.8 min ± 2.1 min) were found (Fig. 40e). Consistently, pathological thrombus formation, as assessed by intravital microscopy of $FeCl_3$-injured mesenteric arterioles was indistinguishable between control and *RIAM-null* mice, resulting in similar occlusion times (16.4 min ± 3.8 min versus 15.3 min ± 4.9 min, respectively) for both groups (Fig. 40f, g).

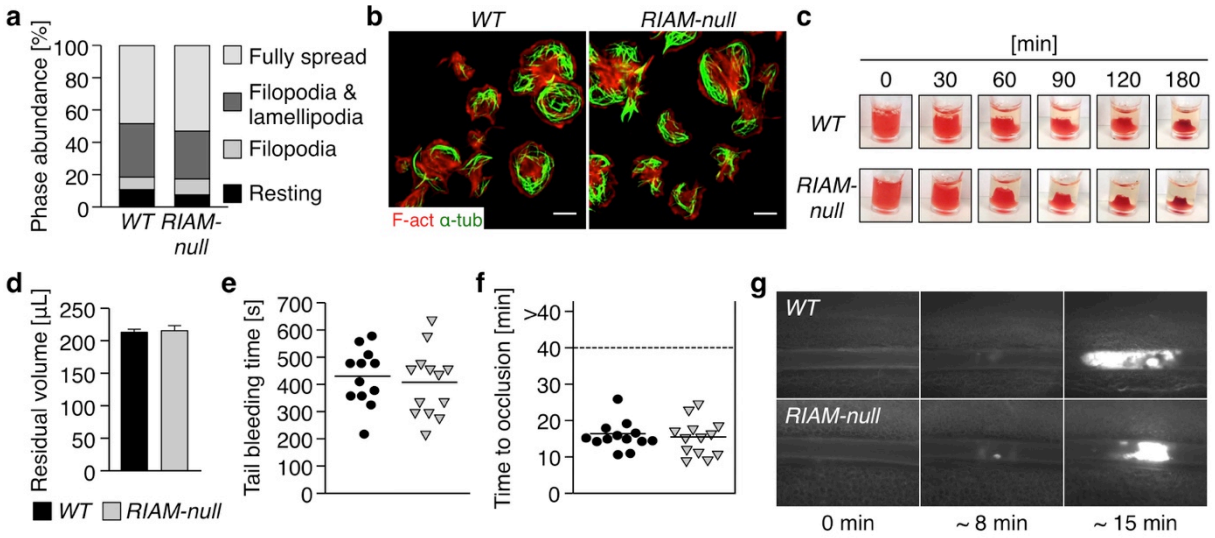

Figure 40 | RIAM deficiency does not affect platelet outside-in signaling and *in vivo* thrombus formation. (**a, b**) *RIAM-null* platelets display normal (**a**) spreading and (**b**) reorganization of filamentous actin (red) and α-tubulin (green) cytoskeleton on a fibrinogen-coated (100 µg mL^{-1}) surface. Values are mean (n = 6). Quantification of phase abundance (**a**) was performed on differential interference contrast microscopy. Images in **b** were acquired by confocal microscopy. Scale bars, 3 µm. (**c**, **d**) Platelet clot retraction of *RIAM-null* platelets was indistinguishable from *WT* controls. Values are mean ± s.d. (n = 6). Unpaired Student's *t*-test. (**e-g**) *In vivo*, RIAM deficiency neither interfered with (**e**) normal hemostasis as assessed by a tail bleeding time assay, nor with (**f**, **g**) arterial thrombus formation upon $FeCl_3$-induced damage of the endothelium. Each symbol in **e** represents one individual. Each symbol in **f** represents one mesenteric arteriole. Horizontal lines in **e** and **f** represent mean. $FeCl_3$ model was performed by Karen Wolf. The presented results are representative of at least three independent experiments with at least n = 3 individuals per group. Unpaired Student's *t*-test. (Stritt *et al. Blood* 2015)[247]

4.4. Phospholipase D is a central regulator of collagen I-induced cytoskeletal rearrangement and podosome formation in megakaryocytes

Besides playing the key role in platelet adhesion at sites of vascular injury, integrins are critical for cell locomotion. As described above, Pfn1-deficient MKs prematurely released proplatelets and platelets into the BM compartment, a defect that has been ascribed to impaired podosome formation and consequently the inability to penetrate the endothelial barrier. PLD that was shown to be important for podosome formation in macrophages served as model to investigate the role of MK podosomes in thrombopoiesis.

4.4.1. Impaired podosome formation and reduced F-actin content in Pld1/2 double-deficient BM MKs spread on collagen I

Since both, PLD1 and PLD2 modulate the actin cytoskeleton via the regulated generation of PA, MK podosome formation was examined in PLD single- and double-deficient mice (further referred to as *DKO*), to identify possible phenotypic compensations through redundant functions of PLD1 and PLD2.[45] To this end, purified primary BM MKs of *WT* and PLD-deficient mice were allowed to adhere and spread on different ECM components. Upon spreading on a native equine tendon collagen I-coated surface, *WT* MKs formed prominent podosomes aligned into belts along the collagen fibers (Fig. 41a).[26,27] In stark contrast spread PLD2- and double-deficient MKs were almost devoid of F-actin (Fig. 41a, c) and the few detectable fibers showed an aberrant distribution and organization into big podosomes close to the cell cortex (Fig. 41b). The similar reduction in F-actin in spread *Pld2*$^{-/-}$ and *DKO*, but not in *Pld1*$^{-/-}$ MKs (Fig. 41c), points, to a specific role of PLD2 in the organization and dynamics of the actin cytoskeleton. Consequently, the reduced F-actin staining intensity in spread *DKO* MKs can be attributed to the absence of PLD2, rather than PLD1. However, it is important to note that podosome formation was impaired in all three mutants, thus pointing to a common function of PLD isoforms in F-actin bundling. The diminished abundance of actin filaments could not be ascribed to a reduced protein level of actin, as this was indistinguishable between *WT* and mutant MKs (data not shown). Despite the reduced content of F-actin in spread PLD2-deficient and *DKO* MKs (Fig. 41c), the mean area covered by the spread cells was comparable for *WT* and mutant MKs on a collagen I matrix (Fig. 41d). In addition, MK perimeter (Fig. 41e) and aspect ratio (major axis : minor axis; Fig. 41f), serving as shape descriptors, were normal in spread mutant MKs. This finding stands in contrast to previous reports on macrophages, neutrophils or adenocarcinoma cells where deficiency in either PLD isoform has been associated with reduced cell spreading and decreased formation of lamellipodia.[37,43,277] However, in agreement with previous studies the number of podosomes

was dramatically reduced in all three mutant MKs compared to *WT* controls, thus indicating an essential role of PLD in MK podosome formation (Fig. 41g).[43] Furthermore, quantification of podosome diameter revealed a decreased size in PLD single-deficient MKs, whilst in double-deficient MKs two distinct populations of podosomes could be distinguished: (1) smaller than those in controls or (2) with a markedly increased diameter (Fig. 41h). The cut-off was set to 1.5 µm to distinguish the two populations of podosomes. Of note, only 2.8% ± 0.1% of *DKO* MKs (versus 100% of *WT* MKs) displayed normally shaped podosomes with a fluorescence intensity of the F-actin staining comparable to that of *WT* MKs.

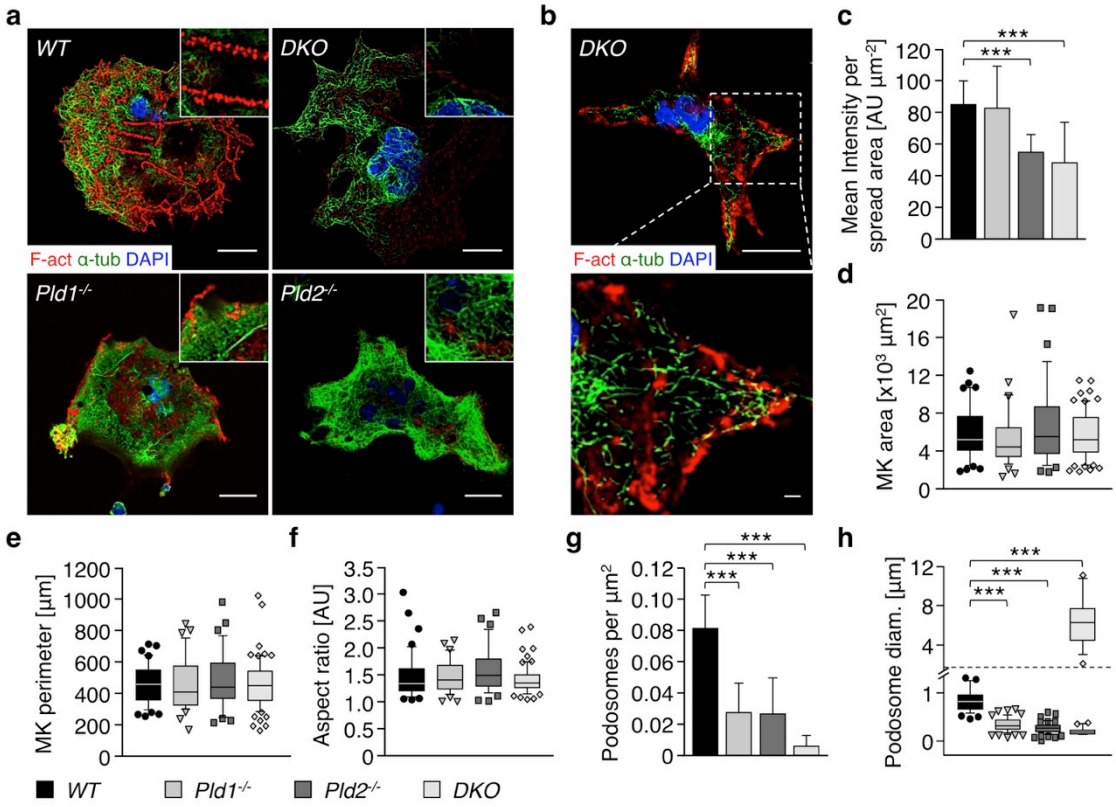

Figure 41 | Impaired podosome formation and reduced F-actin content in PLD double-deficient BM MKs spread on a collagen I matrix. (**a**) *Wild-type* (*WT*), *Pld1*$^{-/-}$, *Pld2*$^{-/-}$ and *Pld1/2*$^{-/-}$ (*DKO*) BM MKs were allowed to spread for 180 min on a native equine tendon collagen I-coated (50 µg mL^{-1}) surface. MKs were stained for F-actin (red) and α-tubulin (green). Nuclei are labeled in blue (DAPI). Images were acquired with a confocal microscope. Scale bars, 20 µm. (**b**) Aberrant podosomes in spread *DKO* MKs on collagen I. Scale bar, 20 µm (upper panel). Scale bar, 2 µm (lower panel). (**c-h**) The mean (**c**) intensity of the F-actin staining, (**d**) surface, (**e**) perimeter, (**f**) aspect ratio (major axis : minor axis), (**g**) number of podosomes and (**h**) podosome size of spread *WT*, *Pld1*$^{-/-}$, *Pld2*$^{-/-}$ and *DKO* MKs (collagen I, 180 min) was quantified with the help of ImageJ software. Values are mean ± s.d. (n = at least 100 MKs per condition). Box plots display 1st and 3rd quartile and whiskers mark minimum and maximum values unless exceeding 1.5 x IQR of at least 100 MKs/ podosomes per condition; symbols represent outliers and the horizontal line displays median. Unpaired Student's *t*-test: ***P< 0.001. (Stritt *et al. J Thromb Haemost* 2014)[39]

4.4.2. FIPI treatment abolished podosome formation of BM MKs on collagen I

Similarly, *5-fluoro-2-indolyl deschlorohalopemide* (FIPI, 750 nM) treatment, which blocks PLD activity, led to a severe reduction of the subcortical and irregularly organized cortical actin in MKs, thus clearly revealing a critical function of the lipase activity in the regulation of MK podosome formation (Fig. 42).

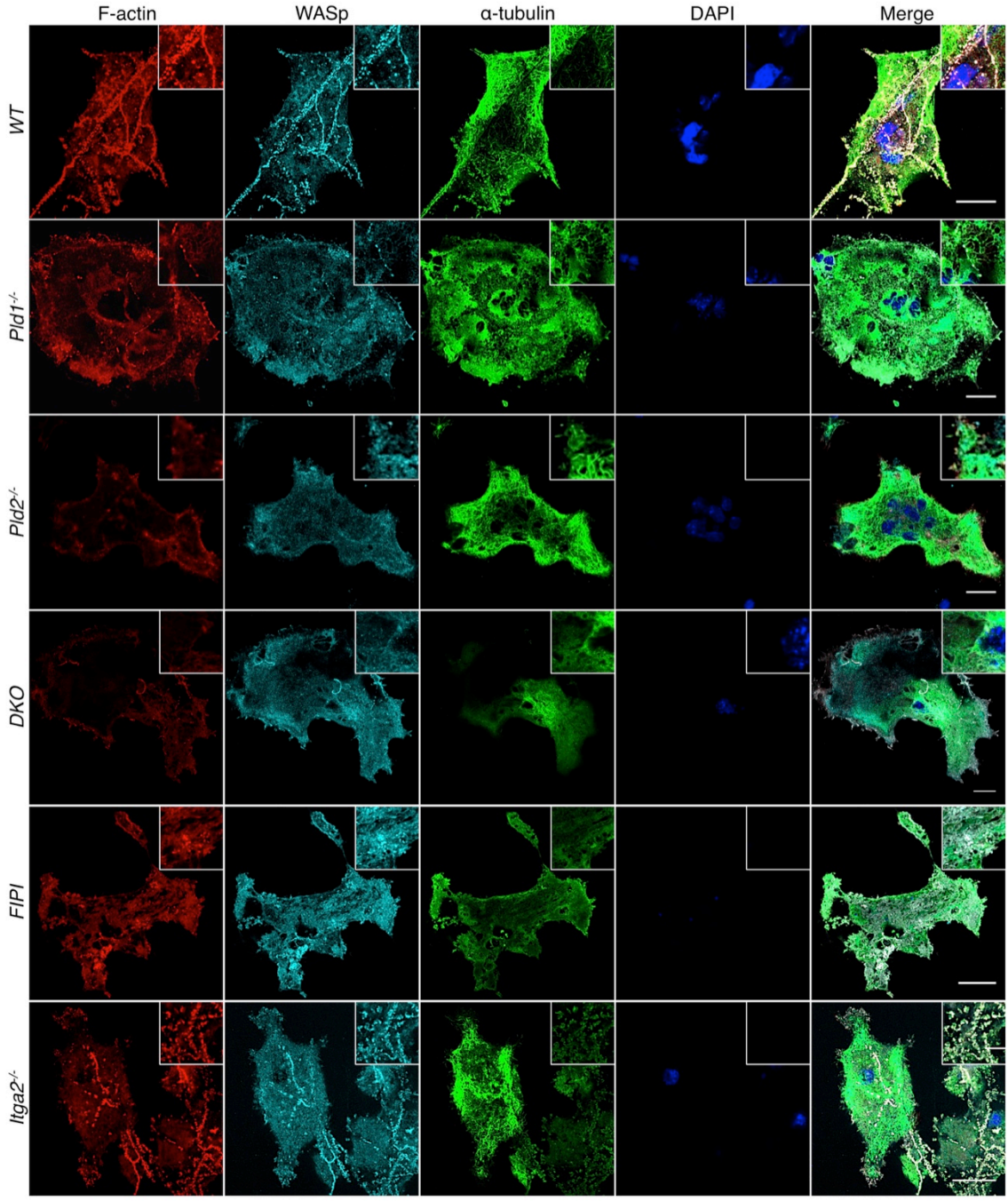

Figure 42 | Impaired podosome formation and aberrant localization of WASp can be phenocopied by FIPI treatment of *WT* BM MKs. *WT*, *Pld1*$^{-/-}$, *Pld2*$^{-/-}$, *DKO, 5-fluoro-2-indolyl deschlorohalopemide* (FIPI, 750 nM)-treated and *Itga2*$^{-/-}$ BM MKs were allowed to spread for 180 min on a native equine tendon collagen I-coated (50 µg mL^{-1}) surface. MKs were stained for F-actin (red), WASp (cyan) serving as a podosome marker and α-tubulin (green). Nuclei are labeled with DAPI (blue). Images were acquired by confocal microscopy and are representative of at 100 MKs per condition. Scale bars, 20 µm. (Stritt *et al. J Thromb Haemost* 2014)[39]

Moreover, ablation of PLD activity by genetic or pharmacologic approaches resulted in almost completely abolished podosome formation in macrophages.[43] Together, these results revealed cooperative functions of PLD1 and PLD2 in MK podosome formation and podosome size determination on collagen I.

4.4.3. Decreased number and aberrant morphology of *DKO* BM MKs *in vivo*

As podosome formation is important for cell migration, the impact of PLD-deficiency on MK number, localization and morphology in the BM was assessed. While MK number was slightly decreased in *Pld1*$^{-/-}$ and *DKO* mice (Fig. 43a, b), MKs were more distant from the BM sinusoids in all PLD mutant mouse strains compared to the *WT* control (Fig. 43a, c). In *Pld2*$^{-/-}$ and *DKO* mice signs of increased MK fragmentation were observed, reminiscent of a premature platelet release within the BM (Fig. 43a, d).

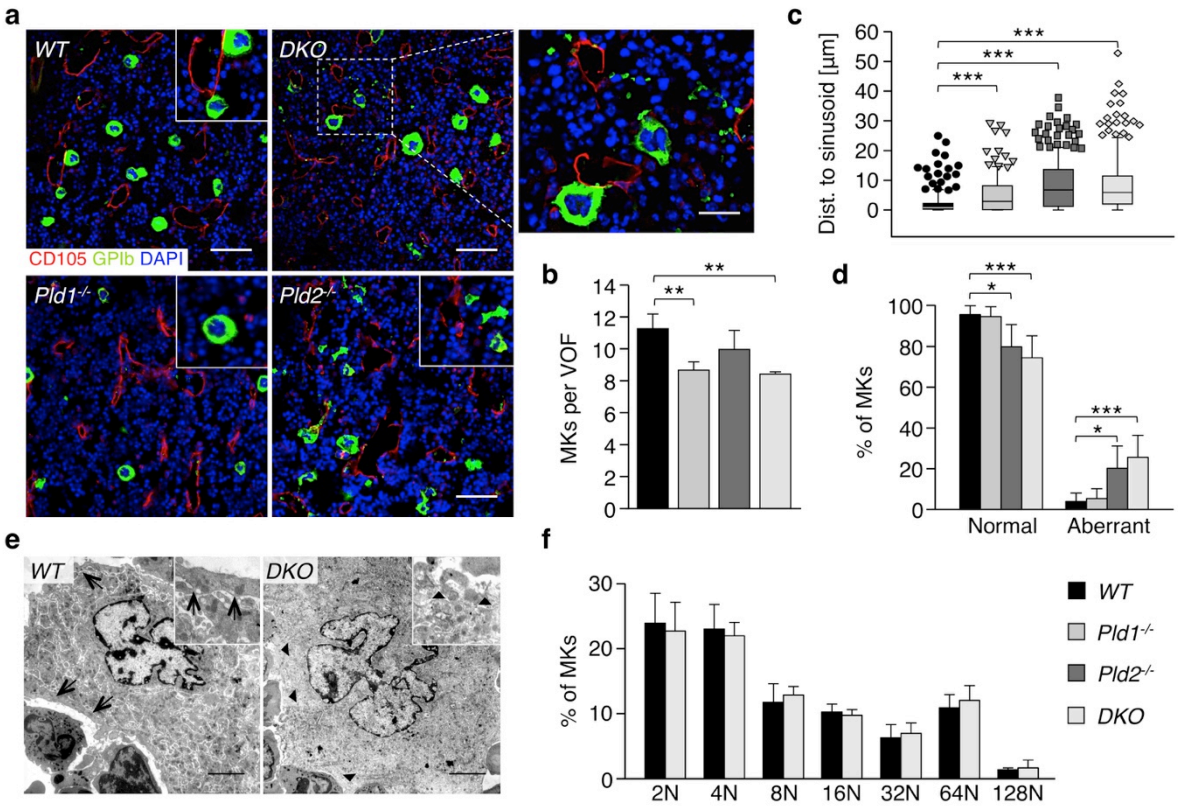

Figure 43 | Morphological alterations of PLD double-deficient BM MKs *in vivo*. (**a**) Cryo sections (7 µm) of whole *WT*, *Pld1*$^{-/-}$, *Pld2*$^{-/-}$ and *DKO* femora were probed with anti-CD105 (red), anti-GPIbα (green) antibodies and counterstained with DAPI (blue). Scale bars, 50 µm. (**b-d**) Quantification of (**b**) BM MKs per *visual observed field* (VOF, 294 x 221 µm), (**c**) distance of MKs from vascular sinusoids and (**d**) MK morphology in histological sections. Values are mean ± s.d. (n = at least 300 MKs per condition). (**e**) Transmission electron microscopy of native BM MKs. Scale bars, 20 µm. (**f**) BM MK ploidy was assessed in whole BM single-cell suspensions by flow cytometry. Values are mean ± s.d. (n = 6); Box plots display 1st and 3rd quartile and whiskers mark minimum and maximum values unless exceeding 1.5 x IQR of at least 300 MKs per condition; symbols represent outliers and the horizontal line displays median. Unpaired Student's *t*-test: ***P< 0.001; **P< 0.01; *P< 0.05. (Stritt *et al. J Thromb Haemost* 2014)[39]

This observation was underscored by a reduced demarcation of *Pld2*$^{-/-}$ and double-deficient MKs in histological sections. Similarly, in TEM experiments the boundaries of *DKO* MKs were difficult to define from surrounding BM cells (Fig. 43e, arrow heads). A reduction in the thickness or an absence of the typical peripheral zone (Fig. 43e, arrows) in the *DKO* MKs (Fig. 43e, arrow heads) might explain this morphological alteration. This suggested that defective MK maturation may contribute to the altered morphology of *DKO* MKs. Therefore, MK ploidy was determined but was found to be grossly normal for *DKO* animals, thus indicating that PLD is dispensable for MK development and maturation (Fig. 43f). Consequently, PLD single-deficient and *DKO* mice had normal numbers of circulating platelets,[44,45] despite the severe morphological and functional alterations, which were most pronounced in double-deficient MKs. In summary, these findings identified a specific function of PLD1 in the determination of BM MK numbers and revealed PLD2 as a regulator of MK morphology.

4.4.4. Unaltered platelet production by *DKO* MKs *in vivo* and *in vitro*

To investigate whether PLD double-deficiency affects platelet production upon challenge, circulating platelets in *WT* and *DKO* mice were depleted by injection of anti-GPIbα-antibodies and the platelet count was monitored for 9 days.

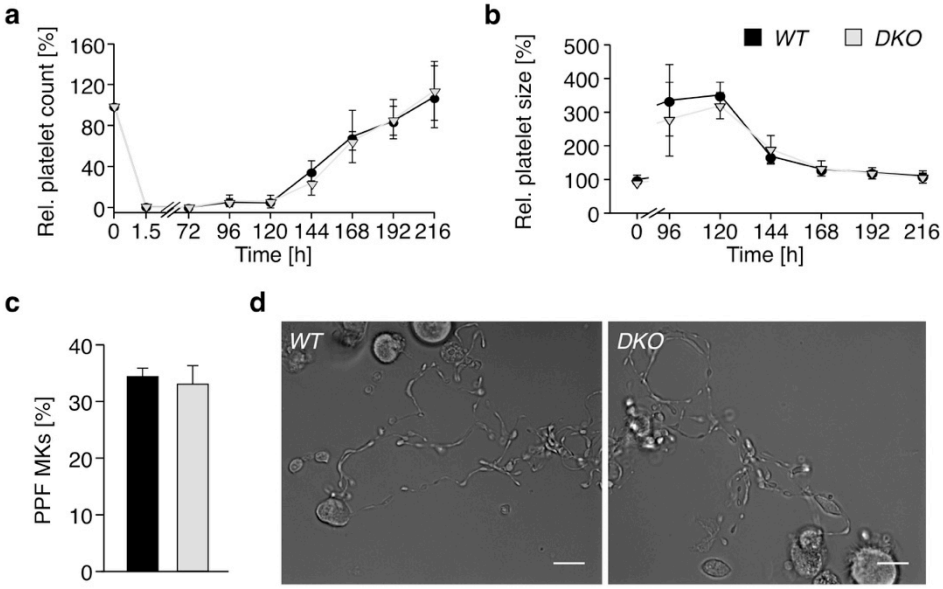

Figure 44 | Normal platelet production in PLD *DKO* mice. (**a-b**) Platelet (**a**) count and (**b**) size in *WT* (black circles) and *DKO* (grey triangles) mice were monitored for 9 days post platelet depletion with an anti-GPIbα antibody. Values are mean ± s.d. (n = 6). (**c-d**) The (**c**) percentage of *proplatelet-forming* (PPF) MKs was determined by counting the total number of MKs as well as the number of PPF MKs and (**d**) representative images were acquired with the help of a differential interference contrast microscope. Values are mean ± s.d. (n = at least 100 MKs per condition). Scale bars, 20 µm. Unpaired Student's *t*-test. (Stritt *et al. J Thromb Haemost* 2014)[39]

Surprisingly, platelet recovery was normal in *DKO* mice (Fig. 44a) and in both groups, platelet size increased initially and returned to normal with similar kinetics (Fig. 44b). In addition, *in vitro* proplatelet formation of PLD double-deficient MKs was indistinguishable from controls (Fig. 44c, d). These results indicated that the defective podosome formation observed *in vitro* can be compensated *in vivo*, presumably due to the stimulation of additional signaling pathways in MKs.

4.4.5. Additional stimuli compensate for podosome formation in *DKO* mice *in vivo*

This hypothesis was supported by an unaltered spreading dynamic with a normal F-actin content and organization in PLD-deficient MKs on fibrinogen (Fig. 45a-e) or CRP (Fig. 45f-j). Of note, MK spreading on fibrinogen is primarily mediated via αIIbβ3 integrin outside-in signaling and might represent an alternative pathway that could compensate *in vivo* for the defects observed in *DKO* MKs spread on collagen I. Furthermore, the grossly normal spreading of double-deficient MKs on CRP (Fig. 45f-h), suggests that above described defects in the actin cytoskeleton are not related to GPVI signaling and are most likely attributed to a cooperative role of PLD1 and PLD2 in the regulation of the MK actin cytoskeleton upon stimulation through collagen I.

In addition, this role of PLD appears specific for MKs, as PLD-deficient platelets spread on collagen I showed normal rearrangement and organization of the actin cytoskeleton (Fig. 45k). While podosome density in *DKO* MKs spread on CRP was normal (Fig. 45l), it was slightly decreased on fibrinogen (Fig. 45d). In contrast, podosome diameter was unaltered in spread MKs on fibrinogen (Fig. 45e) but slightly increased on CRP (Fig. 45j). The aberrant podosome size in spread PLD-deficient MKs on collagen I and CRP suggests a role of PLD in podosome size determination downstream of GPVI (Fig. 41h and 45j), while podosome numbers rather seem to depend on PLD function downstream of other receptors (Fig. 41g and 45d).

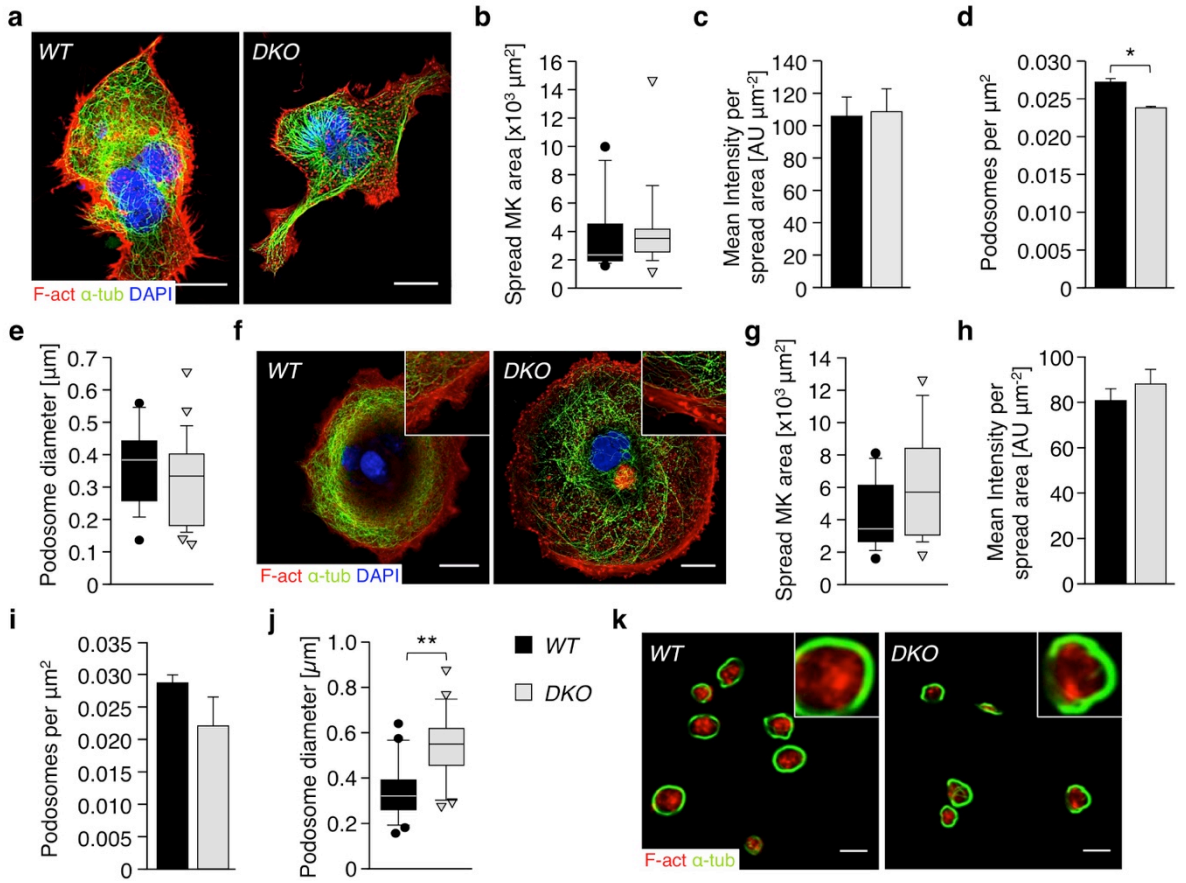

Figure 45 I **Slightly altered rearrangement of the actin cytoskeleton in PLD *DKO* BM MKs on CRP and fibrinogen.** BM MKs spread on (**a-e**) fibrinogen or (**f-j**) *collagen-related peptide* (CRP; 180 min) were stained for F-actin (red), α-tubulin (green) and nuclei were visualized with DAPI (blue). The mean (**b, g**) surface, (**c, h**) intensity of the F-actin staining, (**d, i**) number of podosomes and (**e, j**) podosome size of spread *WT* and *DKO* MKs (**b-e** fibrinogen; **g-j** CRP (180 min)) was quantified with the help of ImageJ software. Values are mean ± s.d. (n = at least 100 MKs per condition). Box plots display 1st and 3rd quartile and whiskers mark minimum and maximum values unless exceeding 1.5 x IQR of at least 100 MKs/ podosomes per condition; symbols represent outliers and the horizontal line displays median. Scale bars, 20 µm. (**k**) Platelets were allowed to spread for 30 min on 50 µg mL^{-1} collagen I and were stained for F-actin (red) and α-tubulin (green). Analysis was performed by confocal microscopy. Scale bars, 3 µm. Unpaired Student's *t*-test: $^{**}P < 0.01$; $^{*}P < 0.05$. (Stritt *et al. J Thromb Haemost* 2014)[39]

4.4.6. MK α2β1 integrins are dispensable for podosome formation on collagen I

The fact that PLD-deficient MKs showed aberrant podosome formation on collagen I, but only to a much lesser extent on CRP, strongly suggested that podosome formation might depend on α2β1 integrins. However, *Itga2*$^{-/-}$ MKs spread on collagen I displayed normal podosome density (Fig. 42 and 46a) with a mildly reduced diameter (Fig. 46b) and unaltered F-actin staining intensity (Fig. 46c). In line with the absence of α2β1 integrins the mean spread surface (Fig. 46d) and the perimeter (Fig. 46e) of *Itga2*$^{-/-}$ MKs was reduced. However, shape descriptors such as the aspect ratio (Fig. 46f), roundness (Fig. 46g), or circularity (Fig. 46h) for *Itga2*$^{-/-}$ MKs were indistinguishable from controls, suggesting rather delayed than impaired spreading as cause for the observed alterations.

Interestingly, *Wasp*$^{-/-}$ MKs spread on a collagen I matrix displayed a similarly reduced F-actin content and impaired podosome formation as PLD-deficient MKs.[26,27] Since PLD has been shown to indirectly couple to WASp via Grb2 these data suggest that PLD and WASp might act in concert to regulate MK actin dynamics and podosome formation in response to collagen I-mediated signaling.[38]

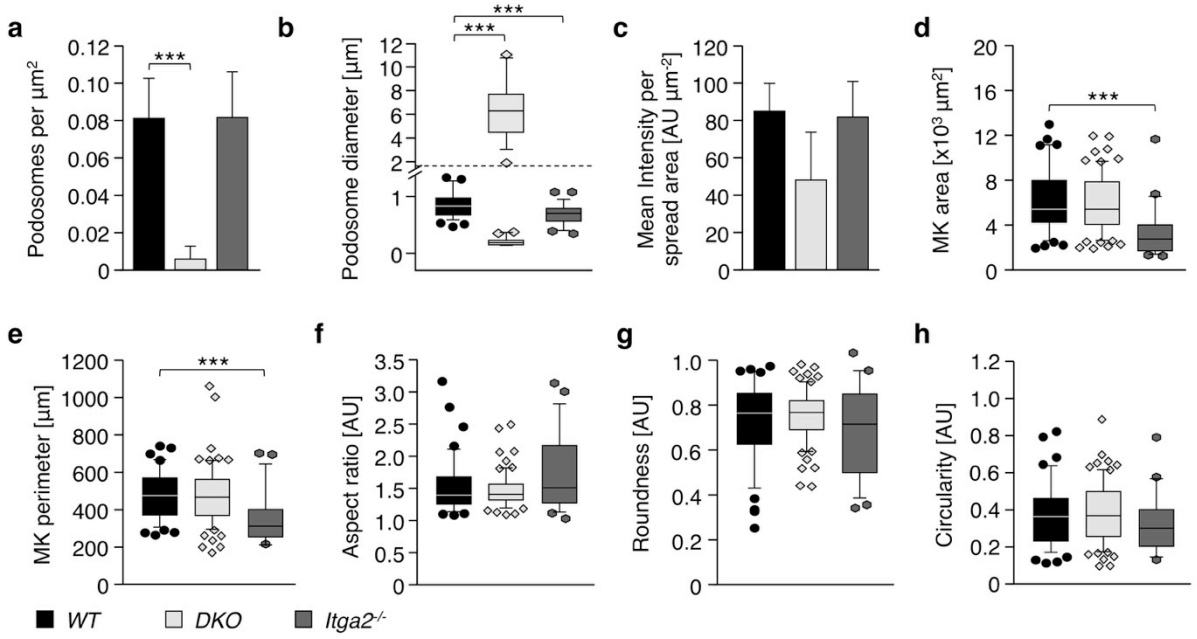

Figure 46 | Normal podosome numbers but decreased spreading and podosome diameter in *Itga2*$^{-/-}$ MKs on collagen I. *Wild-type* (*WT*), *Pld1/2*$^{-/-}$ (*DKO*) and *Itga2*$^{-/-}$ BM MKs were allowed to spread for 180 min on a native equine tendon collagen I-coated (50 µg mL^{-1}) surface. MKs were stained for F-actin (red) and α-tubulin (green). Nuclei are labeled with DAPI (blue) and images were acquired by confocal microscopy. The mean (**a**) number of podosomes, (**b**) podosome size, (**c**) intensity of the F-actin staining, (**d**) MK surface, (**e**) perimeter, (**f**) aspect ratio (major axis : minor axis), (**g**) roundness and (**h**) circularity of spread *WT*, *DKO* and *Itga2*$^{-/-}$ MKs was quantified with the help of ImageJ (NIH) software. Values are mean ± s.d. (n = at least 100 MKs per condition). Box plots display 1st and 3rd quartile and whiskers mark minimum and maximum values unless exceeding 1.5 x IQR of at least 100 MKs/ podosomes per condition; symbols represent outliers and the horizontal line displays median. Unpaired Student's *t*-test: ***P< 0.001. (Stritt *et al.,* unpublished observation)

Taken together, these results show that PLD deficiency leads to aberrant MK morphology and defective collagen I-induced podosome formation, thus indicating a specific role of PLD in this process. These defects did, however, not affect platelet production by MKs probably due to compensatory mechanisms that require further investigation.

4.5. Defects in TRPM7 channel function result in deregulated thrombopoiesis through altered cellular Mg^{2+} homeostasis and cytoskeletal architecture

Besides the degradation of ECM components, regulated actomyosin contractility is a prerequisite for cell migration, proplatelet formation and platelet abscission within the circulation.[187,188] Mg^{2+} has been implicated as regulator of actomyosin contractility and platelet reactivity by controlling Ca^{2+} influx and the affinity of NMMIIA to actin.[164] Interestingly, the regulatory network controlling $[Mg^{2+}]_i$ in MKs and platelets is entirely unknown.

4.5.1. TRPM7 is the major Mg^{2+} channel in murine platelets

TRPM7 was identified as the key Mg^{2+} channel and Magnesium transporter 1 (MagT1) as the major transporter to regulate $[Mg^{2+}]_i$ in murine platelets (Fig. 47a) and MK- and platelet-specific Trpm7 knockout mice were generated (Fig. 47b, c). The absence of typical TRPM7 currents confirmed the efficiency of the targeting strategy in primary BM MKs (Fig. 47d).

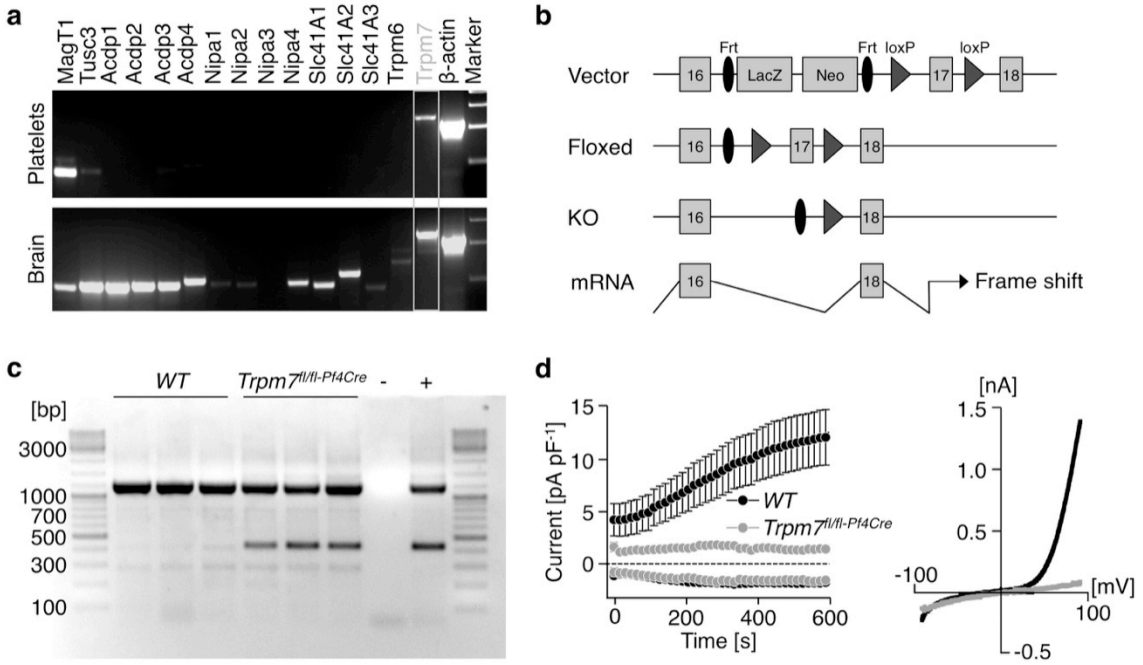

Figure 47 | TRPM7-expression is abolished in primary *Trpm7*$^{fl/fl\text{-}Pf4Cre}$ BM MKs. (**a**) Expression profiling of Mg^{2+} transporters and channels in platelets by RT-PCR. (**b**) Targeting strategy of *Trpm7*$^{fl/fl\text{-}Pf4Cre}$ mice. (**c**) Genotyping of *Trpm7*$^{fl/fl\text{-}Pf4Cre}$ mice yields a 1,200 bp product for the floxed, 1,000 bp product for the *WT* and a 400 bp fragment for the recombined allele. (**d**) Whole cell patch clamp measurements of primary BM MKs confirmed the efficiency of the targeting strategy. Measurements have been conducted in absence of extracellular Mg^{2+} to enhance current sizes. Currents were elicited by a ramp protocol from -100 to +100 mV over 50 ms acquired at 0.5 Hz. Left panel: Inward current amplitudes were extracted at -80 mV, outward currents at +80 mV and plotted versus time of the experiment. Values are normalized to cell size as pA pF^{-1} and represent mean ± SEM. Depletion of intracellular Mg^{2+} leads to the characteristic TRPM7-like currents in *WT* MKs (black circles, n = 13), whereas TRPM7 currents were abolished in *Trpm7*$^{fl/fl\text{-}Pf4Cre}$ MKs (grey circles, n = 10). Right panel: Representative current-voltage relationships at 600 s. *WT* cells show an $I\,V^{-1}$-relationship characteristic for TRPM7 (black trace), which are absent in *Trpm7*$^{fl/fl\text{-}Pf4Cre}$ MKs (grey trace). Patch clamp measurements were performed in collaboration with Dr. Vladimir Chubanov, Munich, Germany. (Stritt *et al.*, submitted)

4.5.2. Abolished TRPM7 channel, but not kinase activity leads to the development of macrothrombocytopenia in mice

Unexpectedly, *Trpm7*$^{fl/fl\text{-}Pf4Cre}$ mice developed a severe macrothrombocytopenia (Fig. 48a, b) with enlarged and spherical platelets often containing large vacuoles as revealed by electron microscopy (Fig. 48c).

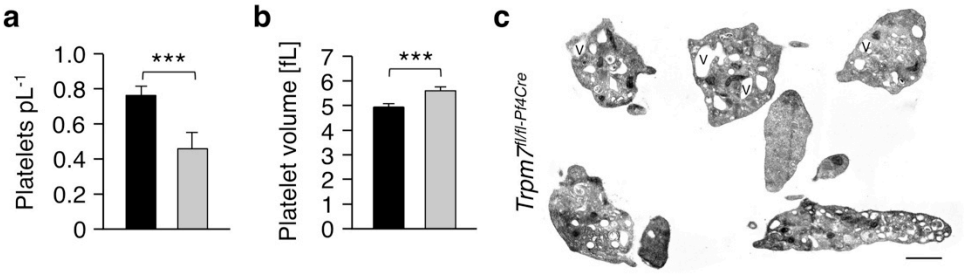

Figure 48 | *Trpm7*$^{fl/fl\text{-}Pf4Cre}$ mice display a macrothrombocytopenia. (**a, b**) Peripheral platelet count (**a**) and size (**b**) were determined with an automated blood cell analyzer. Values are mean ± s.d. (n = 7). Unpaired Student's *t*-test: ***P< 0.001. (**c**) TEM analysis of resting platelets. V, *vacuole*. Scale bar, 1 µm. (Stritt *et al.*, submitted)

In contrast, mice carrying a kinase-dead mutation in *Trpm7*^{174} (*Trpm7*^{KI}) showed normal platelet counts, size and morphology, thus suggesting that the lack of TRPM7 channel function accounts for the macrothrombocytopenia in the mutant mice (Fig. 49).

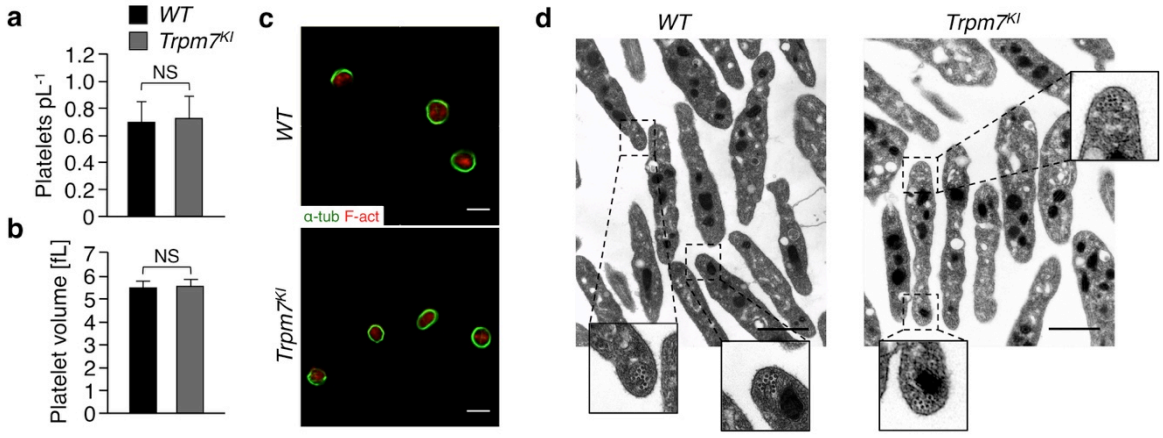

Figure 49 | Trpm7 α-kinase activity does not account for macrothrombocytopenia. (**a, b**) Trpm7 kinase-dead mice display a normal platelet count (**a**) and size (**b**) as determined with an automated blood cell analyzer. (**c, d**) Confocal (**c**) and transmission electron microscopy (**d**) revealed a normal platelet morphology. α-tubulin, green; F-actin, red. Scale bars, 3 µm (for confocal images). Scale bars, 1 µm (for TEM images). All images are representative of at least 5 animals. Unpaired Student's *t*-test: NS, non-significant. (Stritt *et al.*, submitted)

4.5.3. Decreased $[Mg^{2+}]_i$ and aberrant granules in *Trpm7*$^{fl/fl\text{-}Pf4Cre}$ platelets

In line with this, intracellular Mg^{2+} concentration in *Trpm7*$^{fl/fl\text{-}Pf4Cre}$, but not in *Trpm7*^{KI} platelets, was decreased (Fig. 50a) and granules with an aberrant morphology that appeared less electron dense were observed (Fig. 50b). However, assessment of the granule content by

immunostaining and flow cytometry revealed normal to slightly increased levels of α-granular proteins, reflecting the increased size of *Trpm7*$^{fl/fl\text{-}Pf4Cre}$ platelets (Fig. 50c-e).

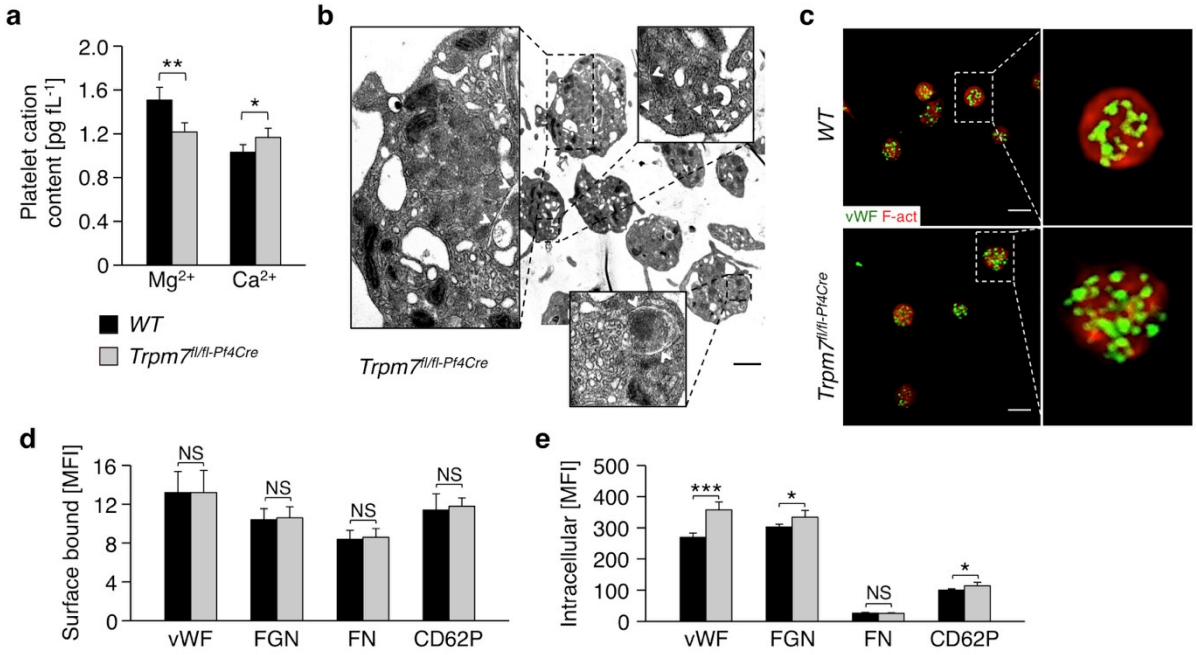

Figure 50 | TRPM7-deficiency perturbs cation homeostasis in platelets and granules. (**a**) Total platelet cation content was determined by inductively coupled plasma mass spectrometry. (**b**) Transmission electron microscopy revealed aberrant granules with a reduced electron density. Scale bar, 1 µm (for TEM images). (**c-e**) Immunostaining and confocal microscopy of resting platelets (**c**) and flow cytometric analyses under resting (**d**) or permeabilized (**e**) conditions showed a mildly increased number of α-granules and content of α-granular proteins. vWF, green; F-actin, red. FGN, *fibrinogen*; FN, *fibronectin*; CD62P, *P-selectin*. All images are representative of at least 5 animals. Scale bars, 3 µm (for confocal images). Values are mean ± s.d. (n = 5). Unpaired Student's *t*-test: ***$P < 0.001$; **$P < 0.01$; *$P < 0.05$; NS, non-significant. (Stritt *et al.*, submitted)

4.5.4. Impaired proplatelet formation accounts for the thrombocytopenia in *Trpm7*$^{fl/fl\text{-}Pf4Cre}$ mice

A mildly reduced platelet life span in *Trpm7*$^{fl/fl\text{-}Pf4Cre}$ mice ($T_{1/2} = 43.55$ h for *WT* versus $T_{1/2} = 35.67$ h for *Trpm7*$^{fl/fl\text{-}Pf4Cre}$ mice) however, was insufficient to explain the observed thrombocytopenia (Fig. 51).

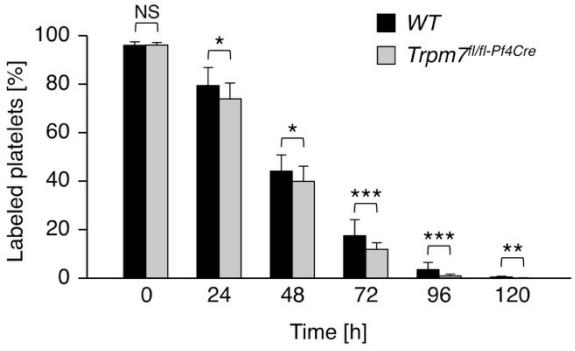

Figure 51 | Mildly accelerated clearance of TRPM7 platelets. Platelet life span was measured by injection of a DyLight 488-conjugated anti-GPIX derivative. Values are mean ± s.d. (n = 5). Unpaired Student's t-test: ***$P < 0.001$; **$P < 0.01$; *$P < 0.05$; NS, non-significant. (Stritt *et al.*, submitted)

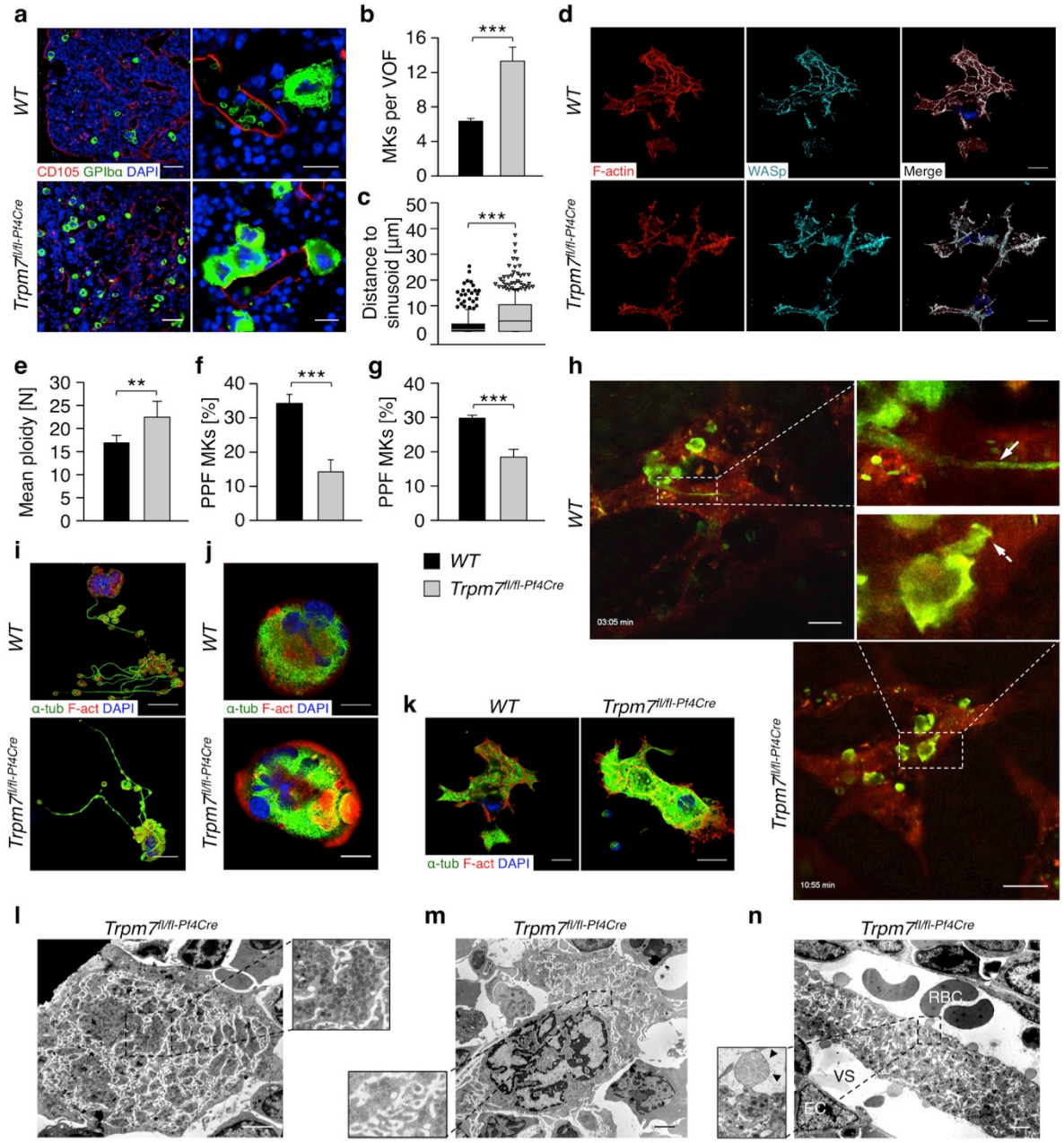

Figure 52 | Impaired proplatelet formation and fragmentation accounts for the thrombocytopenia in TRPM7-deficient mice. (**a**) Confocal microscopic images of immunostained BM. Scale bars, 50 µm (in the left panel). Scale bars, 15 µm (in the right panel). MKs, proplatelets and platelets are shown by GPIb staining in green color. Endoglin staining (red) labels vessels. DAPI, blue. (**b**) Quantification of BM MKs per *visual observed field* (VOF, 328 x 246 µm). Values are mean ± s.d. (n = 6; each 20 VOF were analyzed). (**c**) Distance of MKs to BM sinusoids. Values are mean ± s.d. (n = 6; 300 MKs). (**d**) Confocal images of BM-derived MKs spread (3 h) on collagen I and stained for F-actin (red), DAPI (blue) and WASp (cyan). Scale bars, 25 µm. (**e**) Mean ploidy of primary BM MKs. Values are mean ± s.d. (n = 6). Percentage of *proplatelet-forming* (PPF) fetal liver- (**f**) and BM-derived (**g**) MKs *in vitro*. Values are mean ± s.d. (n = 7). (**h**) Intravital two-photon microscopy of BM MKs in the skull. Arrow shows a normal-sized proplatelet in a BM sinusoid; dashed arrow indicates bulky proplatelet. Rhodamine dextran labels vessels (red) and anti-GPIX antibodies label MKs and platelets (green). Scale bars, 25 µm. (**i-k**) Confocal microscopy of *in vitro* cultured fetal liver- (**i**) or BM-derived resting (**j**) or spread (**k**) MKs (50 µg mL^{-1} collagen I; 3 h) revealed altered cytoskeletal architecture. α-tubulin (green) and F-actin (red) stain the cytoskeleton. DAPI, blue. Scale bars, 25 µm. (**l-n**) TEM analysis of *Trpm7*$^{fl/fl\text{-}Pf4Cre}$ BM MKs. EC, *endothelial cell*; VS, *vascular sinusoid*; RBC, *red blood cell*. Arrow heads in **n** indicate apoptotic blebs. Scale bars, 2.5 µm. All images are representative of at least 5 animals. Unpaired Student's t-test; ***P< 0.001; **P< 0.01; *P< 0.05. (Stritt *et al.*, submitted)

Immunostaining of whole femora BM sections (Fig. 52a) revealed an increased number of MKs in the mutant mice (6.3 ± 0.3 for *WT* versus 13.3 ± 1.6 for *Trpm7*$^{fl/fl\text{-}Pf4Cre}$ mice; Fig. 52b), which were also located further from BM sinusoids than in controls (Fig. 52c). In contrast to previous reports, the formation of podosomes, F-actin rich structures that are thought to serve cell migration and proplatelet protrusion,[278] was unaltered in *Trpm7*$^{fl/fl\text{-}Pf4Cre}$ MKs (Fig. 52d) suggesting that other defects must account for their more distant localization from BM sinusoids (Fig. 52c).

Interestingly, mutant MKs displayed an increased mean ploidy as compared with control (16.9 N ± 1.6 N versus 22.4 N ± 3.4 N for *Trpm7*$^{fl/fl\text{-}Pf4Cre}$ mice; Fig. 52e) thus excluding impaired MK maturation as cause of thrombocytopenia. Despite the increased ploidy *in vivo*, a decreased proplatelet formation for both fetal liver- (Fig. 52f) and BM-derived (Fig. 52g) *Trpm7*$^{fl/fl\text{-}Pf4Cre}$ MKs was found *in vitro.* This was further confirmed *in vivo* by intravital two-photon microscopy of the BM (Fig. 52h). Therefore, the cytoskeletal architecture of *Trpm7*$^{fl/fl\text{-}Pf4Cre}$ MKs was analyzed and an increased content and aberrant organization of microtubules in proplatelet-forming, resting and spread MKs was found (Fig. 52i-k). Electron microscopy revealed a non-homogeneous distribution of granules, tortuous membrane complexes and aberrantly sized proplatelets in mutant MKs (Fig. 52l, m). Furthermore, thick and densely packed proplatelets in BM sinusoids with signs of apoptosis reflecting impaired proplatelet fragmentation and release of preplatelets from *Trpm7*$^{fl/fl\text{-}Pf4Cre}$ MKs were observed (Fig. 52n).

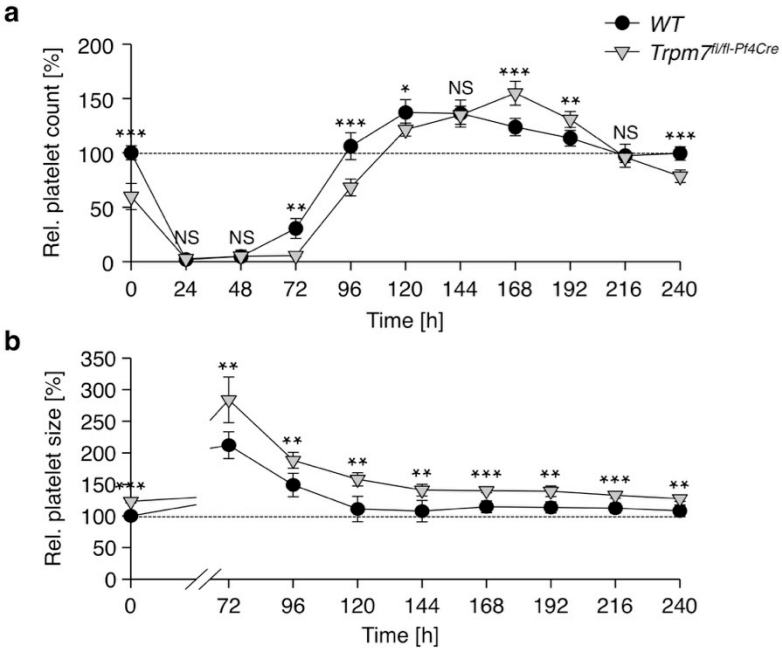

Figure 53 | Impaired platelet production in *Trpm7*$^{fl/fl\text{-}Pf4Cre}$ mice. Platelet (**a**) count and (**b**) size in control (black circles and *Trpm7*$^{fl/fl\text{-}Pf4Cre}$ (grey triangles) mice were monitored for 10 days after platelet depletion with an anti-GPIbα antibody. Symbols are mean ± s.d. (n = 5). Unpaired Student's t-test; ***$P < 0.001$; **$P < 0.01$; *$P < 0.05$; NS, non-significant. (Stritt *et al.*, submitted)

In line with the impaired proplatelet formation (Fig. 52f, g) the recovery of platelet counts after antibody-induced platelet depletion was delayed in *Trpm7*$^{fl/fl\text{-}Pf4Cre}$ mice (Fig. 53).

Although splenomegaly was not observed in *Trpm7*$^{fl/fl\text{-}Pf4Cre}$ mice, an increased number of MKs in an expanded red pulp in the spleen and decreased plasma Thpo levels were found, which further indicates deregulated megakaryopoiesis (Fig. 54).

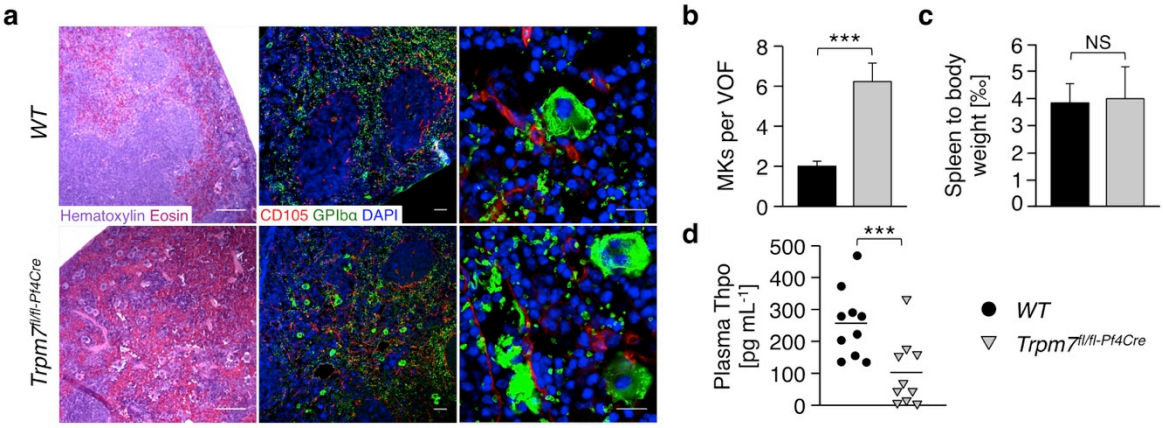

Figure 54 | Aberrant architecture of the red and white pulp in spleens of *Trpm7*$^{fl/fl\text{-}Pf4Cre}$ mice. (**a**) Hematoxylin-eosin and immunostaining on spleen sections reveals an expansion of the red pulp. Scale bar, 25 µm (in the left panel). Scale bar, 50 µm (in the mid panel). Scale bar, 15 µm (in the right panel). MKs and platelets are shown by GPIb staining in green color. Endoglin staining (red) labels vessels. DAPI, blue. (**b**) Quantification of splenic MKs per *visual observed field* (VOF, 328 x 246 µm). Values are mean ± s.d. (n = 6; each 20 VOF were analyzed). (**c**) Normal ratio of spleen to body weight in *Trpm7*$^{fl/fl\text{-}Pf4Cre}$ mice. Values are mean ± s.d. (n = 6). (**d**) In line with the increased number of MKs plasma *thrombopoietin* (Thpo) levels were decreased in *Trpm7*$^{fl/fl\text{-}Pf4Cre}$ mice. Each symbol represents one individual (n = 10). Horizontal lines represent mean. All images are representative of at least 5 animals. Unpaired Student's t-test; ***$P < 0.001$; NS, non-significant. (Stritt *et al.*, submitted)

4.5.5. Decreased NMMIIA stability in platelets and MKs of *Trpm7*$^{fl/fl\text{-}Pf4Cre}$ mice

NMMIIA has been described as a downstream effector of Trpm7[159,278] and importantly, abnormal function of NMMIIA has been associated with impaired formation and fragmentation of proplatelets in humans and mice.[187] Analysis of NMMIIA localization revealed a homogeneous distribution in the cell body and a significant accumulation in proplatelets of mature MKs from controls (Fig. 55a), while it predominated at the cell cortex in *Trpm7*$^{fl/fl\text{-}Pf4Cre}$ MKs. Moreover, similar alterations of NMMIIA localization were observed in platelets (Fig. 55b). Surprisingly, upon spreading of *Trpm7*$^{fl/fl\text{-}Pf4Cre}$ MKs (Fig. 55c) or platelets (Fig. 55d, e) a rapid degradation of NMMIIA was observed that could be rescued either by pretreatment with the NMMIIA inhibitor blebbistatin or by Mg^{2+} supplementation (Fig. 55e-h). In addition, besides preventing the degradation of NMMIIA, blebbistatin pretreatment or Mg^{2+} supplementation restored NMMIIA localization to microtubules in platelets and to podosomes in spread *Trpm7*$^{fl/fl\text{-}Pf4Cre}$ MKs (Fig. 55f-h).

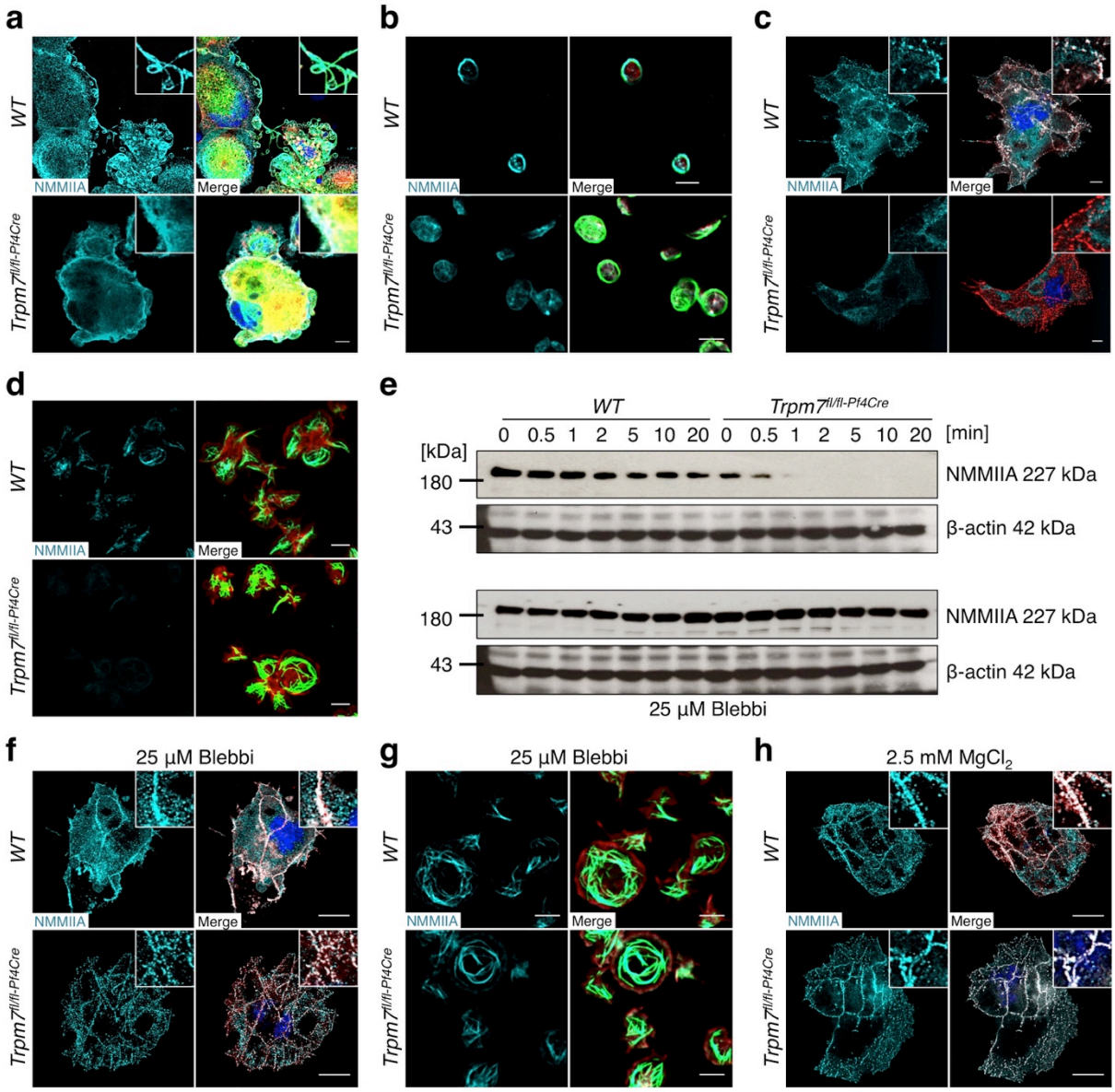

Figure 55 | Altered localization and decreased stability of NMMIIA upon stimulation of *Trpm7*$^{fl/fl\text{-}Pf4Cre}$ platelets and BM-derived MKs. (**a-d**) Localization of NMMIIA (cyan) in proplatelet-forming fetal liver-derived (**a**) and on collagen I(50 µg mL^{-1}) spread BM-derived MKs (**c**) or resting (**b**) and on fibrinogen (100 µg mL^{-1}) spread (**d**) platelets. The MK/ platelet cytoskeleton was immunostained for α-tubulin (green) and F-actin (red). DAPI, blue. (**e**) Untreated or blebbistatin-pretreated (25 µM) platelets were stimulated with 0.5 µg mL^{-1} convulxin, lysed after the indicated time points and processed for immunoblotting. β-actin served as loading control. (**e-h**) Pretreatment of platelets (**e, g**) and BM-derived MKs with 25 µM blebbistatin (**f**) or 2.5 mM $MgCl_2$ (**h**) prevented the degradation of NMMIIA (**c, d**) and restored its localization. Scale bars, 10 µm (**a, c**). Scale bars, 25 µm (**f, h**). Scale bars, 3 µm (**b, d, g**). All images are representative of at least 5 animals. (Stritt *et al.*, submitted)

4.5.6. Dysregulated Mg^{2+} homeostasis alters NMMIIA function and leads to macrothrombocytopenia in *Trpm7*$^{fl/fl\text{-}Pf4Cre}$ mice

These results strongly suggested that deregulated Mg^{2+} homeostasis[164] or phosphorylation of NMMIIA by TRPM7 α-kinase[159,278] may cause an increased NMMIIA activity that accounts for the impaired proplatelet-formation.[164,187] In support of this, either inhibition of NMMIIA activity or Mg^{2+} supplementation (Fig. 56a, b) could almost fully restore proplatelet formation of *Trpm7*$^{fl/fl\text{-}Pf4Cre}$ MKs *in vitro*. According to a previous report,[182] Mg^{2+} supplementation should restore $[Mg^{2+}]_i$ in mutant MKs, which cannot be fully achieved through upregulation of *MagT1* expression under normal culture conditions (Fig. 56c, d). Besides increasing cortical tension,[279,280] blebbistatin treatment also interfered with the prevalence of microtubules in proplatelet protrusions (Fig. 56e, f).

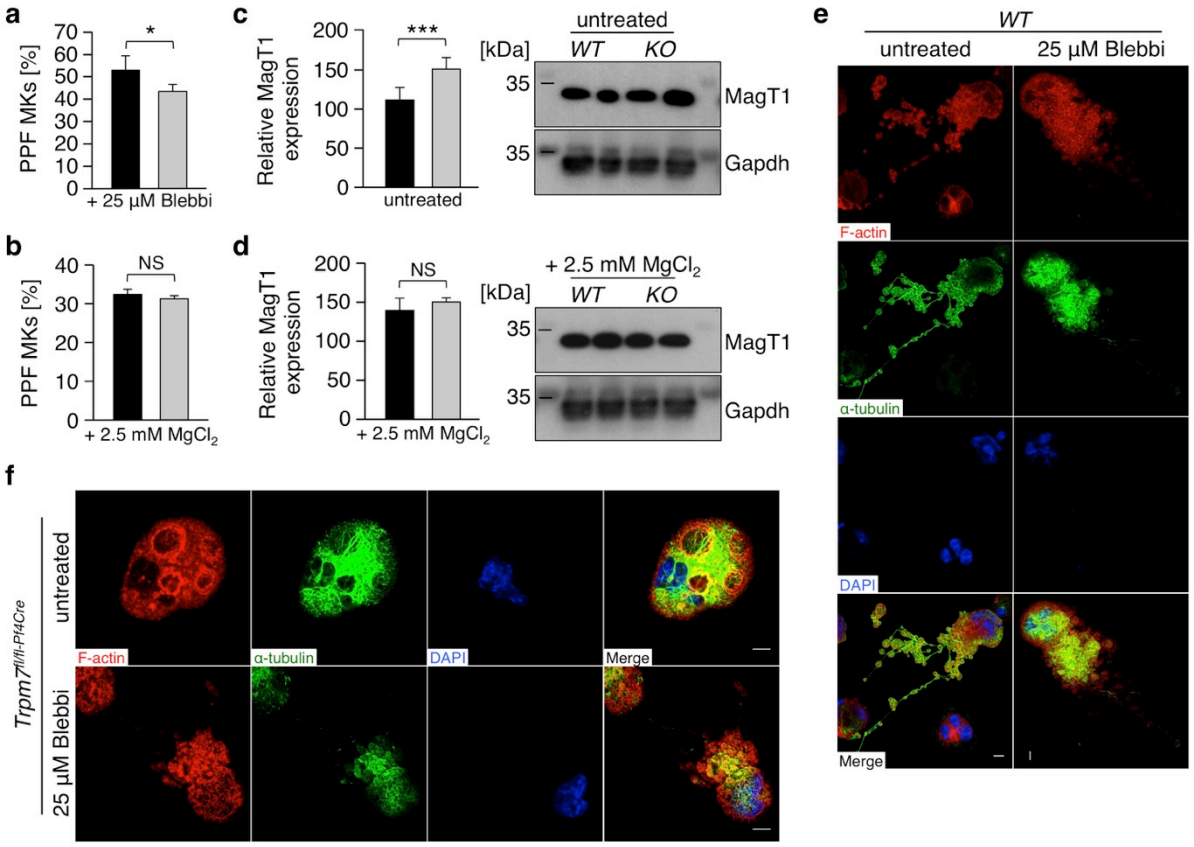

Figure 56 | Altered activity of NMMIIA accounts for the impaired proplatelet-formation of BM-derived *Trpm7*$^{fl/fl\text{-}Pf4Cre}$ MKs. (**a, b**) Pretreatment of fetal liver-derived MKs with 25 µM blebbistatin (**a**) or 2.5 mM $MgCl_2$ (**b**) rescued proplatelet formation. Values are mean ± s.d. (n = 6). Black bars, *WT* controls. Grey bars, *Trpm7*$^{fl/fl\text{-}Pf4Cre}$ MKs. PPF, *proplatelet-forming*. (**c, d**) MagT1 expression was determined under normal culture conditions (**c**) and in Mg^{2+}-supplemented cultures (**d**). Values are mean ± s.d. (n = 6). Black bars, *WT* controls. Grey bars, *Trpm7*$^{fl/fl\text{-}Pf4Cre}$ MKs. (**e, f**) Confocal images of untreated or blebbistatin-treated (25 µM) fetal liver-derived MKs from control (**e**) and *Trpm7*$^{fl/fl\text{-}Pf4Cre}$ (**f**) mice stained for F-actin (red), α-tubulin (green) and DAPI (blue). Scale bars, 10 µm. All images are representative of at least 5 animals. Unpaired Student's t-test; ***$P < 0.001$; *$P < 0.05$; NS, non-significant. (Stritt *et al.*, submitted)

4.5.7. Increased NMMIIA activity alters the cytoskeleton in *Trpm7*$^{fl/fl\text{-}Pf4Cre}$ platelets

Similarly to mutant MKs, immunostaining (Fig. 57a) and electron microscopy (Fig. 57b) revealed an increased number of aberrantly organized microtubules in *Trpm7*$^{fl/fl\text{-}Pf4Cre}$ platelets as compared with controls. This was due to an increased presence of highly dynamic tyrosinated tubulin (Fig. 57c) leading to accelerated and uncontrolled microtubule polymerization (Fig. 57a, d) while an increased stability of microtubules could be excluded (Fig. 57c). Interestingly, pretreatment of platelets with EDTA mimicked these cytoskeletal alterations (Fig. 57e, f) changes that could also be reverted by blebbistatin (Fig. 57g), thus further supporting the notion that reduced $[Mg^{2+}]_i$ alters the subcellular localization and activity of NMMIIA and results in cytoskeletal dysorganization. In support of this hypothesis, impaired polymerization of filamentous actin upon platelet activation (Fig. 57h) and an increased surface area of spread *Trpm7*$^{fl/fl\text{-}Pf4Cre}$ platelets was observed (Fig. 57i, j) reflecting the rapid degradation of NMMIIA and consequently the absence of coherent cytoplasmic contractile forces normally generated by activated NMMIIA.[202,281]

4.5.8. The p.C721G variant impairs TRPM7 channel function and causes macrothrombocytopenia in humans

The above-described findings raised the question, whether some DNA variants of extreme low frequency affecting TRPM7 channel function might also cause macrothrombocytopenia in humans. Examining the results of genome sequencing of 702 cases with *bleeding and platelet disorders* (BPD) of unknown genetic basis in the BRIDGE database of the *National Institute for Health Research* (NIHR) BioResource – Rare Diseases revealed three cases with a coding variant with consequences unobserved in nearly 81,000 control DNA samples (Table 1).

Unique case number (UCN)	0012 (patient 5)	0025	0110
Platelet count ($x10^9$ L^{-1}; N: 150-400)	94	50	409
Mean platelet volume (fL; N: 7.0-10.0)	11.5	10.5	Not applicable
HPO – Hematology terms	Increased mean platelet volume, thrombocytopenia, abnormal hemoglobin	Thrombocytopenia, abnormal hemoglobin	Impaired ADP-/epinephrine-induced platelet aggregation, abnormal platelet granules, subcutaneous hemorrhage, epistaxis, menorrhagia, post-partum hemorrhage, prolonged bleeding after dental extraction
Variant coordinate	50903409	50899402	50884374
Reference allele	T	C	G
Alternate allele	G	T	A
Effect on amino acid sequence	p.C721G (c.2161T>G)	p.R902C (c.2704C>T)	p.G1353D (c.4058G>A)
Combined annotation dependent depletion (CADD) score	24.80	20.40	15.68

Table 1 | BRIDGE-BPD study database entries. *Human phenotype ontology* (HPO) coded clinical and laboratory characteristics of the three index cases with variants in *TRPM7*. Data was kindly provided by NIHR BioResource – Rare Diseases and the associated BRIDGE genome sequencing projects.

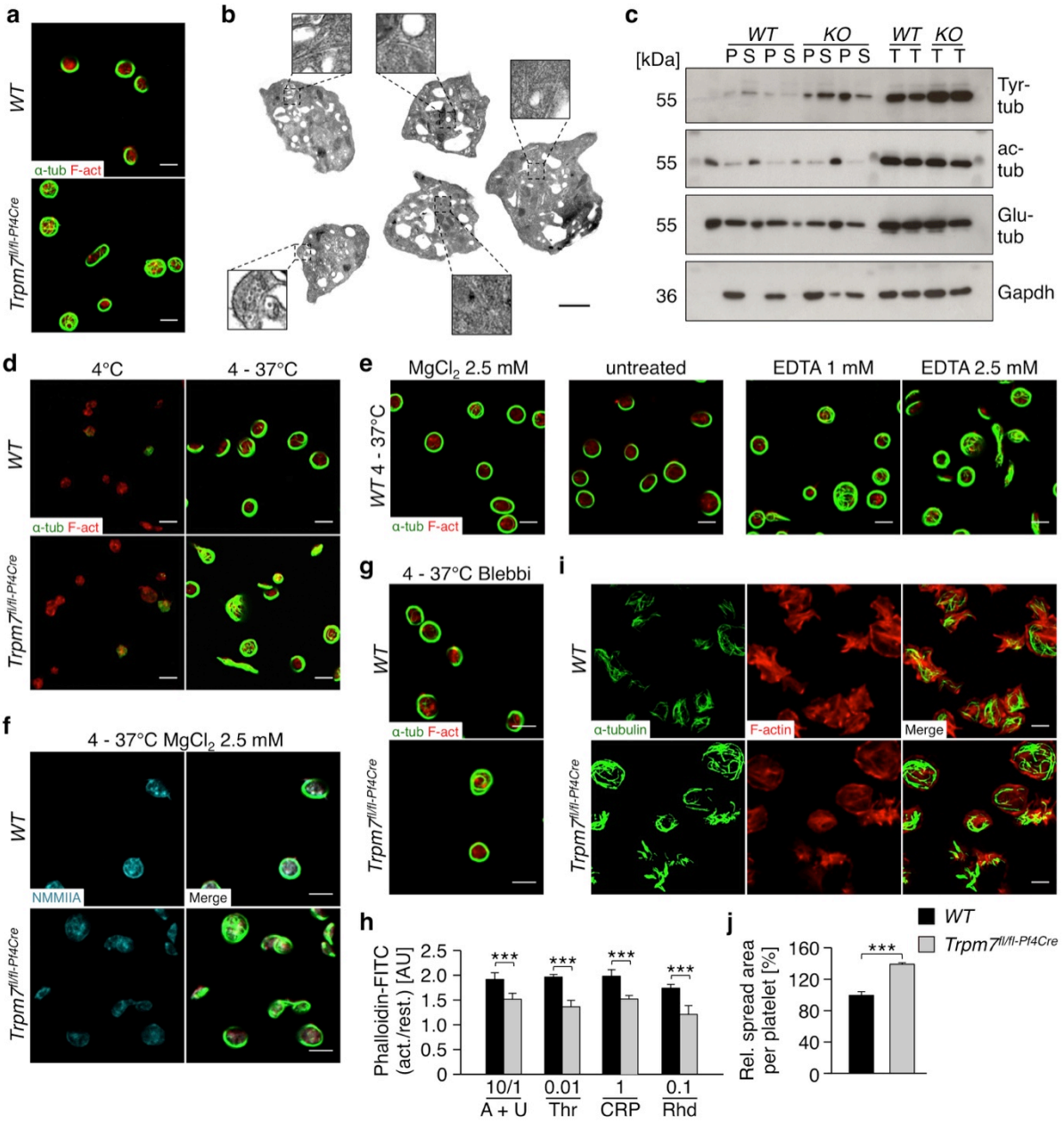

Figure 57 | Altered cytoskeletal organization in *Trpm7*$^{fl/fl\text{-}Pf4Cre}$ platelets. (**a**) Confocal images of resting platelets. α-tubulin, green; F-actin, red. Scale bars, 3 µm. (**b**) TEM analysis of resting *Trpm7*$^{fl/fl\text{-}Pf4Cre}$ platelets. Scale bar, 1 µm. (**c**) Tubulin cytoskeleton of resting platelets was isolated via ultracentrifugation and immunoblotted against dynamic Tyr-tubulin and post-translational modifications of stable microtubules, acetylated (ac)- or detyrosinated (Glu)-tubulin. Gapdh served as loading control. Insoluble fraction (*pellet*, P); soluble fraction (*supernatant*, S); T, *total protein*. (**d**) Platelets were incubated for 3 h at 4°C and if indicated rewarmed at 37°C, fixed on poly-L-lysine-coated coverslips and stained for F-actin (red) and α-tubulin (green). (**e**) Resting control platelets were incubated for 3 h at 4°C supplemented with the indicated reagents. After rewarming to 37°C platelets were fixed, on poly-L-lysine-coated coverslips and stained for α-tubulin (green) and F-actin (red). (**f**) Mg^{2+} supplementation does not restore NMMIIA localization in *Trpm7*$^{fl/fl\text{-}Pf4Cre}$ platelets after cold challenge with subsequent rewarming. (**g**) Rewarming of chilled and blebbistatin-pretreated (25 µM) *Trpm7*$^{fl/fl\text{-}Pf4Cre}$ platelets restored cytoskeletal organization. Scale bars, 3 µm. (**h**) The ratio of polymerized actin in activated versus resting platelets was determined. A+U, 10 µM *ADP* and 1 µM *U46619*; Thr, 0.01 U mL^{-1} *thrombin*; CRP, 1 µg mL^{-1} *collagen-related peptide* Rhd, 0.1 µg mL^{-1} *rhodocytin*. Values are mean ± s.d. (n = 6). (**I, j**) The relative spread surface area of platelets was determined using F-actin staining (**i**) as a measure. Values are mean ± s.d. (n = 6; 200 platelets). All images are representative of at least 5 animals. Unpaired Student's t-test; ***$P < 0.001$. (Stritt *et al.*, submitted)

Two of these three cases showed low platelet counts and macrothrombocytopenia. Interestingly, the p.G1353D (c.4058G>A) variant in *TRPM7* of index patient UCN 0110 was located close to the α-kinase domain and the absence of macrothrombocytopenia is in agreement with the results on the *Trpm7*^{KI} mice (Table 1 and Fig. 49).

Unfortunately, index case UCN 0025 with a p.R902C (c.2704C>T) variant was unavailable for further studies. In contrast, index case UCN 0012 with a p.C721G (c.2161T>G) variant and pedigree members were engaged in a further study, which showed macrothrombocytopenia and the p.C721G mutation in a highly conserved region of the channel domain for three patients, while other blood parameters were normal (Table 1, 2 and Fig. 58a). For patient 2, now deceased, macrothrombocytopenia was detected during her life (Fig. 58a).

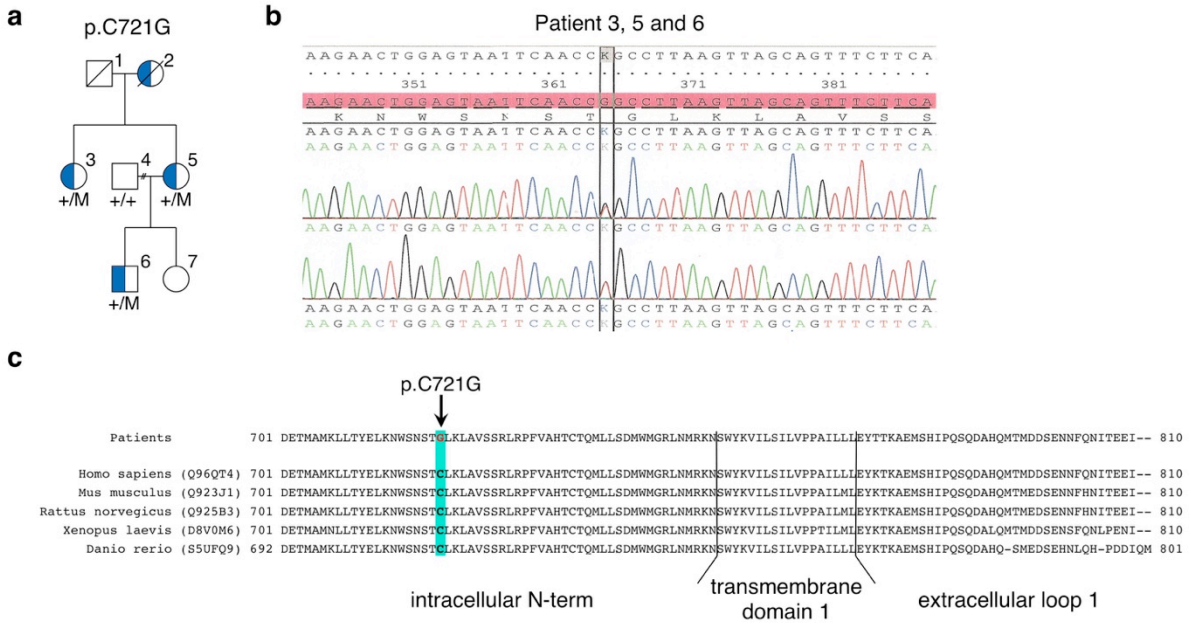

Figure 58 | The *TRPM7* p.C721G variant co-segregates with macrothrombocytopenia. (**a**) A heterozygous p.C721G variant of *TRPM7* was first identified by whole exome sequencing in index patient 5. Sanger sequencing then confirmed that this variant (M) co-segregated with the macrothrombocytopenia (blue coloration) in the family pedigree. Open symbols indicate that no macrothrombocytopenia was observed. The genotype +/M indicates that the family member was a carrier of the *TRPM7* variant. +/+ indicates that no variant was detected at that locus and no symbol that genotyping was not performed. (**b**) Sequencing results of heterozygous patients 3, 5 and 6. (**c**) Sequence alignment of *TRPM7* coding sequence from different species of different taxa highlighting the high sequence conservation. Co-segregation studies were performed in collaboration with Dr. Rémi Favier, Paris, France. (Stritt *et al.*, submitted)

Despite the reduced platelet numbers, aggregation responses and platelet life span were grossly normal for all patients and a bleeding tendency was only reported for patients 3 and 5 during surgery. Furthermore, the patients did not suffer from malignancies. Strikingly, paroxysmal atrial fibrillation was also present for the index case and her mother now deceased.

Pedigree	p.C721G		
Patient	3	5	6
Gender	F	F	M
Year of birth	1964	1965	1985
Platelet count ($x10^9$ L^{-1}; N: 150-400)	100	80	123
Mean platelet volume (fL; N: 7.0-10.0)	12.3	11.2	11.1
Plateletcrit (%; N: 0.19-0.40)	0.12	0.09	0.14
Red blood cell count ($x10^{12}$ L^{-1}; N: 4.0-6.2)	5.15	5.25	5.41
Hemoglobin (g dL^{-1}; N: 12-18)	15.7	14.6	15.4
Hematocrit (%; N: 45.0-55.0)	44.1	43.1	46.1
White blood cell count ($x10^9$ L^{-1}; N: 4.0-10.0)	9.52	6.83	5.80
Neutrophil count ($x10^9$ L^{-1}; N: 1.5-7.0)	5.94	4.62	3.21
Lymphocyte count ($x10^9$ L^{-1}; N: 1.5-4.0)	3.01	1.50	1.72
Monocyte count ($x10^9$ L^{-1}; N: 0.1-1.0)	0.36	0.45	0.44
Eosinophil count ($x10^9$ L^{-1}; N: 0.1-0.7)	0.14	0.20	0.33

Table 2 | Demographic information and blood parameters of the patient cohort. Blood parameters of patients 3, 5 and 6 were determined in ACD-A anticoagulated whole blood with an automated cell analyzer. Clinical parameters and phenotypes were analyzed in collaboration with Dr. Paquita Nurden (Pessac, France) and Dr. Rémi Favier (Paris, France). (Stritt *et al.*, submitted)

Similarly to *Trpm7*$^{fl/fl\text{-}Pf4Cre}$ mouse platelets, a reduced content of Mg^{2+} and an increased concentration of Ca^{2+} was found in platelets from the patients as compared with healthy controls (Fig. 59a). Patch clamp studies on HEK293 cells confirmed that the p.C721G variant reduced TRPM7 channel activity by 85% ± 4% as compared with *WT* controls (Fig. 59b-d).

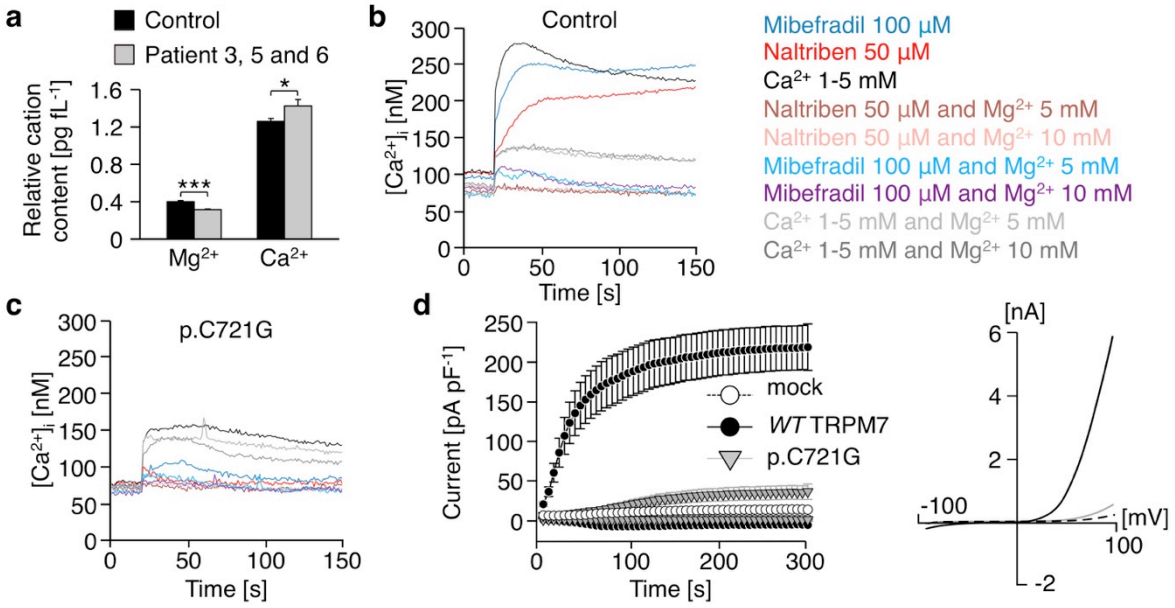

Figure 59 | The p.C721G variant impairs TRPM7 channel function and perturbs Mg^{2+} and Ca^{2+} homeostasis. (**a**) Total platelet cation content of healthy controls and patient 3, 5 and 6 was determined by inductively coupled mass spectrometry. Values are mean ± s.d. (n = 5 healthy controls). Unpaired Student's t-test; ***P< 0.001; *P< 0.01. (**b, c**) Fura-2 fluorescence was recorded from eGFP-positive HEK293 cells, either expressing *WT* TPRM7 or the p.C721G variant. (**d**) Whole cell patch clamp measurements on mock transfected HEK293 (n = 8), and cells overexpressing *WT* TRPM7 (n = 13) or the p.C721G variant (n = 13) revealed impaired channel activity. Left panel: The depletion of intracellular Mg^{2+} leads to the development of characteristic TRPM7-like currents in *WT* TRPM7 overexpressing HEK293 cells, whereas TRPM7 currents were abolished in mock-transfected, or p.C721G overexpressing HEK293 cells. Values are normalized to cell size as pA pF^{-1} and represent mean ± SEM. Right panel: *WT* TRPM7 overexpressing HEK293 cells show an I V^{-1}-relationship characteristic for TRPM7 (black trace), which are absent in mock-transfected (dashed black trace) or p.C721G overexpressing HEK293 cells (grey trace). Electrophysiology measurements were performed in collaboration with Dr. Vladimir Chubanov, Munich, Germany. (Stritt *et al.*, submitted)

4.5.9. p.C721G platelets display aberrant granules and cytoskeletal alterations

Platelets from all tested patients displayed an increased size, a spherical shape with numerous vacuoles, aberrant distribution of granules and an increased number and anarchic organization of microtubules (Fig. 60a). The abnormal cytoskeletal organization could be confirmed by immunostaining on resting platelets (Fig. 60b, c) and was not attributed to an increased stability of microtubules (Fig. 60b). However, similarly to *Trpm7*$^{fl/fl\text{-}Pf4Cre}$ mouse platelets, microtubules in platelets from patients with the p.C721G variant of TRPM7 were less prone to colchicine-induced disassembly (Fig. 60c).

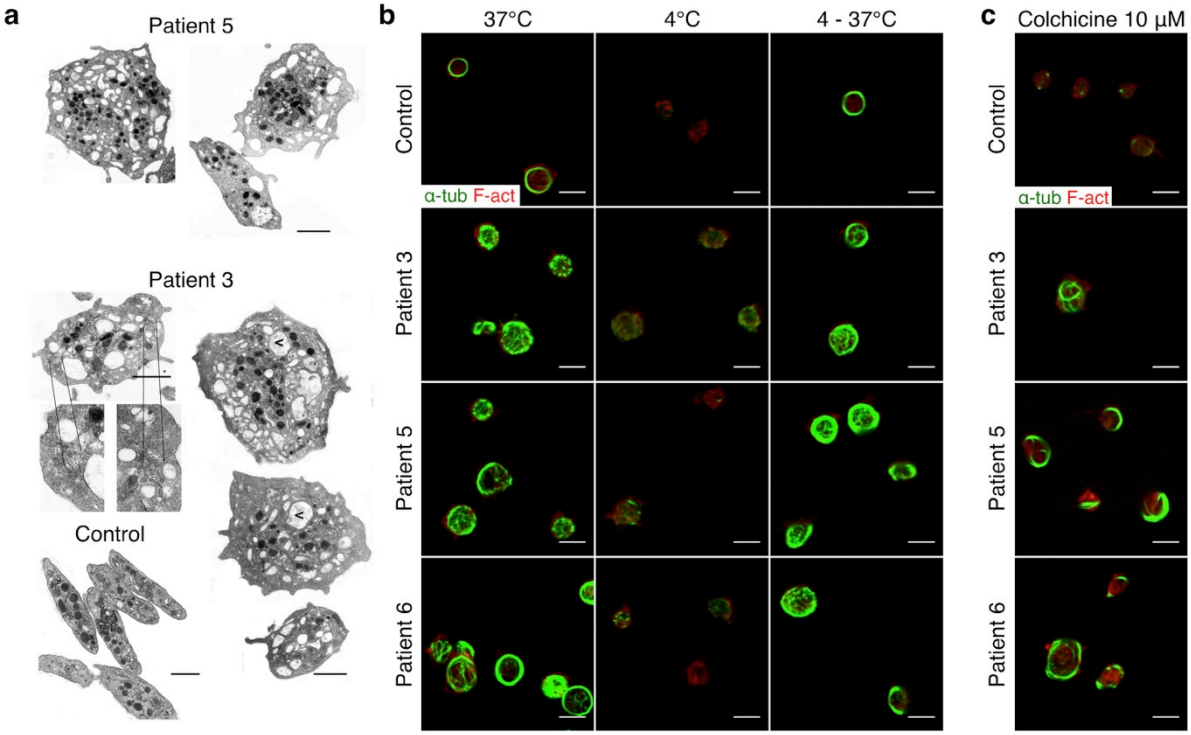

Figure 60 | Platelets from patients with the p.C721G variant strongly resemble those of *Trpm7*$^{fl/fl\text{-}Pf4Cre}$ mice. (**a**) Transmission electron microscopic analyses of resting platelets from controls (lower left) or patients carrying the p.C721G variant of TRPM7. V, *vacuole*. Scale bars, 1 µm. (**b, c**) Resting platelets of healthy controls and patients 3, 5 and 6 were subjected to cold-challenge for 3 h at 4°C with or without subsequent rewarming at 37°C (**b**) or incubated with 10 µM colchicine (**c**), fixed, allowed to adhere to poly-L-lysine-coated coverslips and stained for α-tubulin (green) and F-actin (red). Analysis was performed by confocal microscopy. (Stritt *et al.*, submitted)

4.5.10. Blebbistatin prevents loss of NMMIIA in p.C721G platelets

Since the ultrastructure of human platelets from individuals carrying the p.C721G variant strongly resembled that of *Trpm7*$^{fl/fl\text{-}Pf4Cre}$ mouse platelets, the distribution and stability of NMMIIA was analyzed. Whereas in resting control platelets NMMIIA localized to the marginal band, it was homogenously distributed throughout the cytoplasm of platelets from the patients (Fig. 61a). In line with the observations on *Trpm7*$^{fl/fl\text{-}Pf4Cre}$ mouse platelets, spread plate-

lets from the patients showed an increased surface area, a strong decrease in NMMIIA and an increased content of microtubules (Fig. 61b-d).

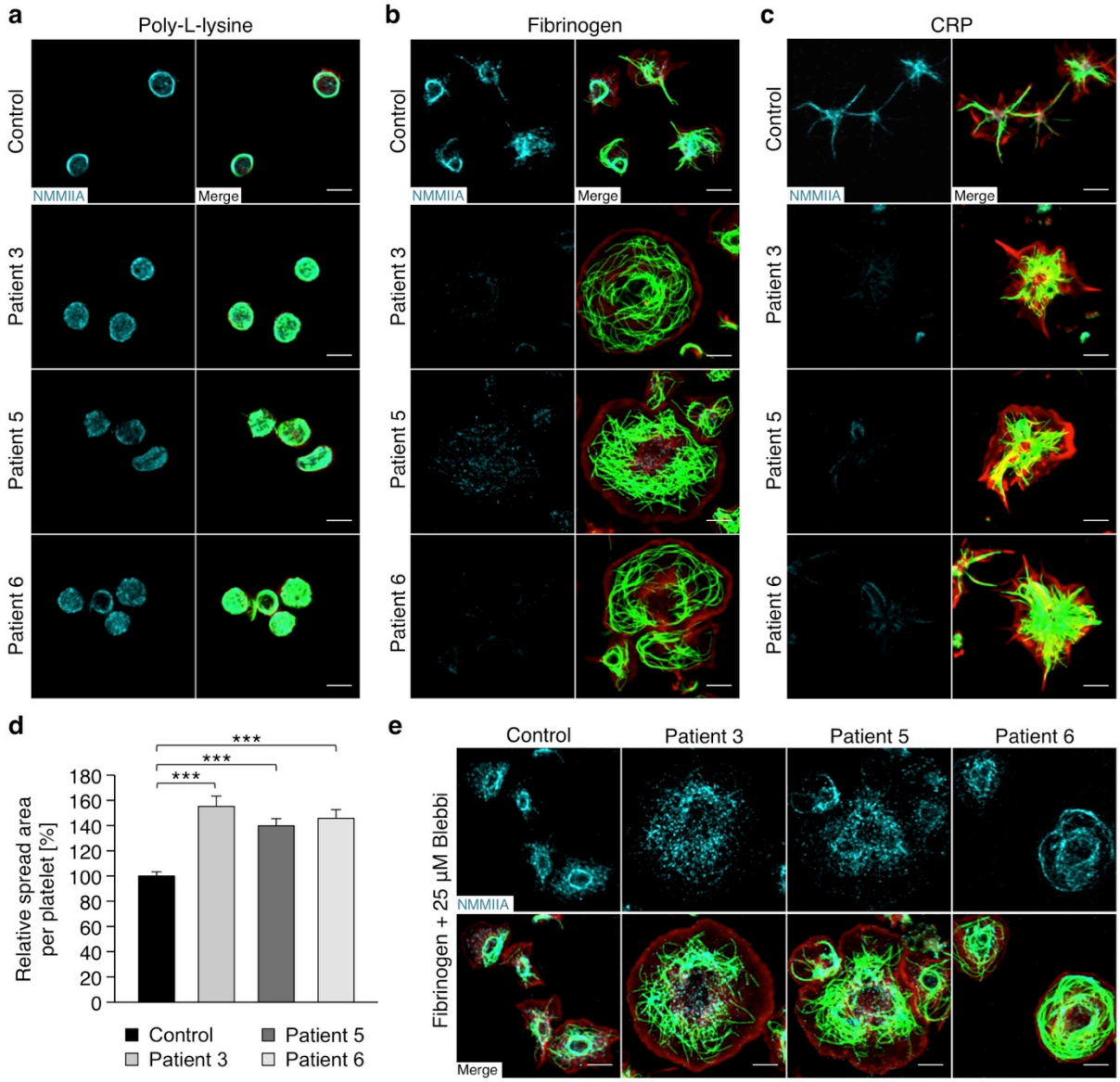

Figure 61 | Altered localization and accelerated degradation of NMMIIA in platelets from patients with the p.C721G variant of TRPM7. (**a**) On poly-L-lysine-immobilized resting platelets from controls or patients 3, 5 and 6 were stained for F-actin (red) α-tubulin (green), NMMIIA (cyan) and analyzed by confocal microscopy. (**b, c**) NMMIIA is degraded in platelets from patient 3, 5 and 6 but not in controls, upon spreading on fibrinogen (**b**; 100 µg mL^{-1}) or *collagen-related peptide* (**c**; CRP; 10 µg mL^{-1}). (**d**) The relative spread surface area of platelets form controls and patients 3, 5 and 6 was determined using F-actin staining (**b**) as a measure. Values are mean ± s.d. (at least 240 platelets per individual). Unpaired Student's t-test; ***P< 0.001. (**e**) Pretreatment of platelets with 25 µM blebbistatin prevented the degradation of NMMIIA in spread platelets (100 µg mL^{-1} fibrinogen) from patients. Scale bars, 3 µm. (Stritt *et al.*, submitted)

4.5.11. Blebbistatin treatment rescues the cytoskeletal organization of platelets from patients with variants in *TRPM7*

As described for the mouse model, blebbistatin prevented loss of NMMIIA upon spreading (Fig. 61e) and rescued the cytoskeletal organization of resting patients' platelets after cold challenge (Fig. 62). As mentioned above, patients 2 and 5 suffered from atrial fibrillation which might be associated with alterations in $[Mg^{2+}]_i$[282] and is likely caused by the reduced channel activity of TRPM7 (Fig. 59b-d). This observation is further supported by recent studies by Du *et al.* and Sah *et al.*, which revealed a role of TRPM7 in the development of atrial fibrillation in mice by regulating myofibroblast dedifferentiation and cardiac automaticity.[180,191]

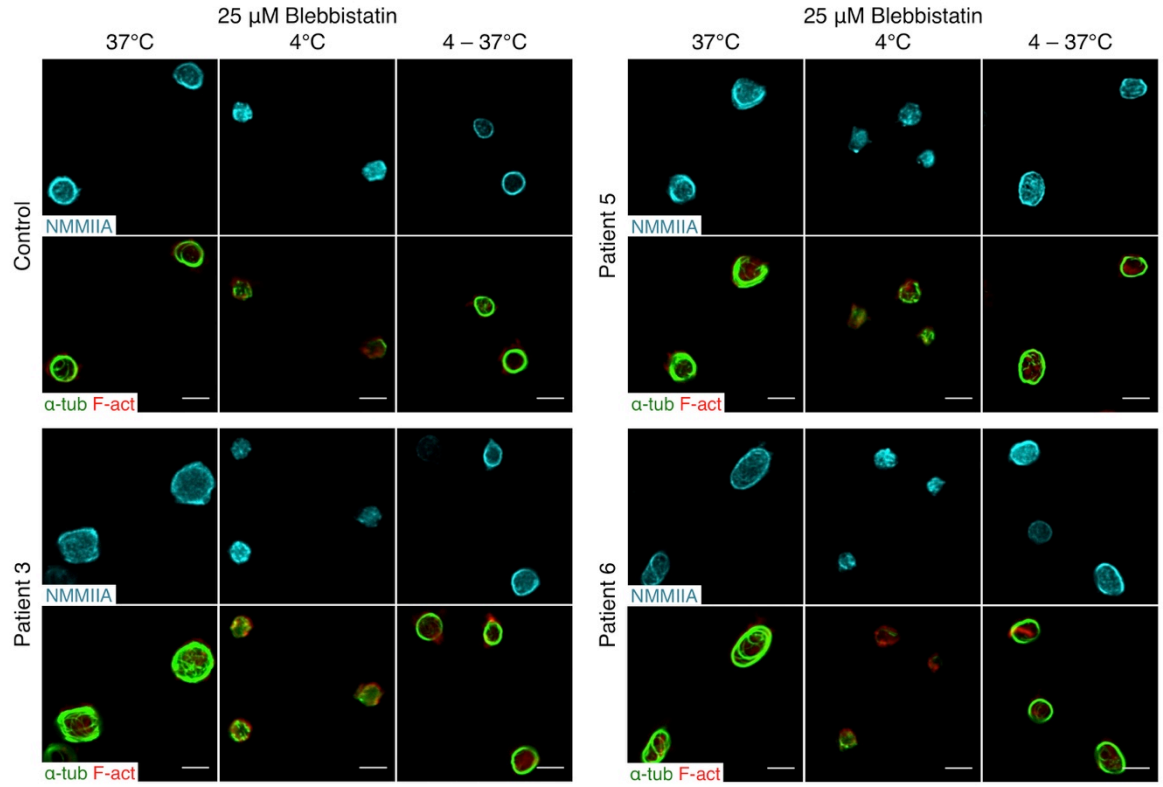

Figure 62 | Blebbistatin pretreatment restores the cytoskeletal architecture of platelets from patients with the *TRPM7* p.C721G variant upon rewarming. Resting platelets of healthy control, patient 3, 5 and 6 were treated with 25 µM blebbistatin and subjected to cold challenge with subsequent rewarming, fixed and stained for α-tubulin (green), F-actin (red) and NMMIIA (cyan). Scale bars, 3 µm. (Stritt *et al.*, submitted)

In conclusion, these results clearly demonstrate that defects in TRPM7 channel function cause macrothrombocytopenia in humans and mice. Decreased $[Mg^{2+}]_i$ leads to deregulated NMMIIA activity and altered cytoskeletal dynamics. These results reveal for the first time a critical role of Mg^{2+} in thrombopoiesis and of TRPM7 in the regulation of Mg^{2+} and Ca^{2+} homeostasis in MKs and platelets.

4.5.12. Mg^{2+} supplementation improves cell growth of Trpm7-deficient cells

To further assess the cause of thrombocytopenia in the absence of TRPM7 and to identify possible treatments the human chronic myelogenous leukemia cell line K562 was used. Cas9-induced DNA double strand breaks activated cellular DNA repair mechanisms and resulted in non-homologous end joining in 10 clones characterized by the deletion or insertion of up to 200 bp that may lead to a frame shift mutation and/or a non-functional protein (Fig. 63a). Mutant cells displayed an altered morphology and an increased size (Fig. 63b, c). In line with previous reports mutant cells could almost not survive under normal culture conditions, whereas control K562 cells showed normal growth (Fig. 63d).[182] Mg^{2+} supplementation promoted the proliferation of some clones thus providing a further line of evidence for successful disruption of TRPM7 function (Fig. 63e). Similar observations were made when control and mutant cells were dedifferentiated into MKs by the addition of PMA (Fig. 63f, g).

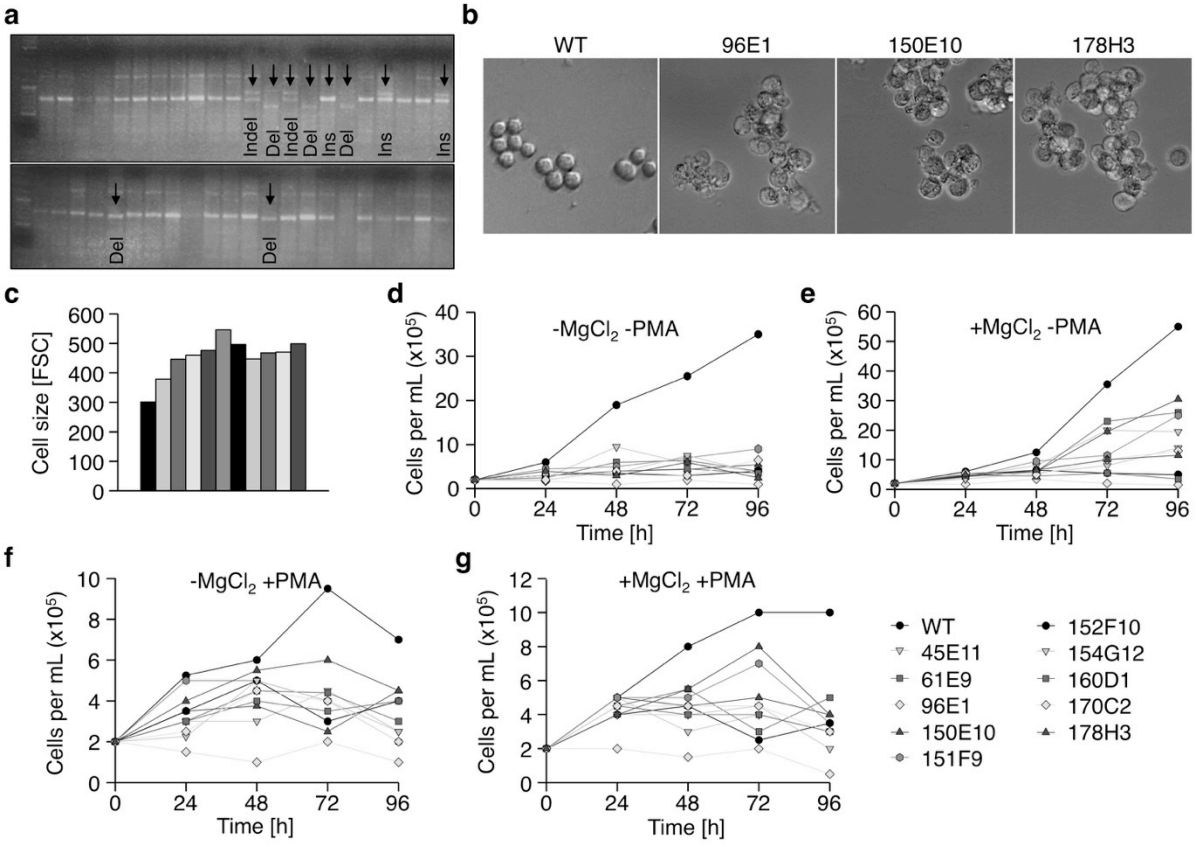

Figure 63 | Successful targeting of TRPM7 in K562 cells using the CRISPR-Cas9 system. (**a**) Genotyping PCR of CRISPR-Cas9-treated K562 cell clones yielded a 691 bp band for the *WT* allele. Arrows indicate larger *insertions* (Ins), *deletions* (Del), or both (Indel). (**b-e**) Cell morphology (**b**), size (**c**) and growth with (**e**) or without (**d**) Mg^{2+} supplementation were determined. (**f, g**) Growth rates were assessed upon PMA-induced (100 nM) dedifferentiation of the different cell clones into MKs. (Stritt *et al.*, unpublished observation)

5. DISCUSSION

Recent advances in whole exome sequencing identified numerous variants in genes encoding cytoskeletal/cytoskeleton-associated proteins as causes for bleeding or platelet disorders of so far unknown genetic origin in patients. Among these genes, *WAS*, *MYH9*, *FLNA*, *FERMT3*, *ACTN1*, *TUBB1, TPM4* and *DIAPH1* have been implicated to account for the observed clinical symptoms.[97,200,283-286] Although the above-mentioned genes have been identified, the underlying molecular mechanisms that lead to the observed abnormalities grossly remained elusive. A better molecular understanding and knowledge of the respective pathogenesis may help to identify new therapeutic or diagnostic approaches and improve personalized health care.

Similarly, it is well known that the actin and microtubule cytoskeleton play central roles in megakaryopoiesis and thrombopoiesis, however, the mechanisms orchestrating these complex processes are still poorly understood. Actin-binding or -associated proteins have previously been implicated as critical regulators of cytoskeletal rearrangements and are required for proper platelet formation; however, key regulators such as Pfn1 or Twf2a have been out of focus.[27,55,56,97,110,114,196,202,284,287]

Furthermore, the correct localization and the ability to protrude proplatelets into bone marrow sinusoids are prerequisites for proper platelet supply by MKs. Integrins and NMMIIA-mediated contractility of the cytoskeleton play pivotal roles in the latter process. Both are essential for cell migration and for the formation cytoskeletal superstructures, such as podosomes that serve the degradation of the ECM and are thought to grant proplatelets access to vascular sinusoids within the BM. Among others Mg^{2+} and the α-kinase of TRPM7 are regulators of NMMIIA actvitiy.[159,164,278] While PLD was revealed as critical regulator of podosome formation,[38,43] RIAM was proposed to be essential for β1 and β3 integrin activation.[238,240,241,243]

5.1. Megakaryocyte-specific Profilin1-deficiency alters microtubule stability and causes a Wiskott-Aldrich syndrome-like platelet defect

In the first part of this thesis, the molecular role of the small actin-binding protein Pfn1 in platelet production and function was analyzed. The results presented here reveal an unexpected function of Pfn1 as a regulator of microtubule organization and point to a previously unrecognized mechanism underlying the platelet formation defect in WAS patients.

5.1.1. *Pfn1*$^{fl/fl\text{-}Pf4Cre}$ mice recapitulate key features of the WAS

Mutations in the *WAS* gene cause a complex syndrome including microthrombocytopenia,[192] but the underlying molecular mechanisms have not been elucidated. Unexpectedly, *Wasp*$^{-/-}$ or *WIP*$^{-/-}$ mice do not completely reproduce the clinical symptoms described for WAS patients, particularly with respect to the severe microthrombocytopenia,[27,192,263] suggesting that WASp-deficiency may not directly, but rather indirectly affect platelet size determination through so far undefined mechanisms. In this thesis it was shown for the first time that *Pfn1*$^{-/-}$ mice do fully reproduce the MK and platelet phenotype found in WAS patients. In addition, the here presented data establish Pfn1 as a new and highly relevant regulator of microtubule stability and reorganization. These findings indicate that the MK/ platelet phenotype in WAS might be caused by altered Pfn1 function and/ or localization (Fig. 26a). In support of this, platelets of all four WAS patients contained severely misarranged and hyper-stable microtubules comparable to *Pfn1*$^{-/-}$ platelets that might represent the molecular cause of the reduced platelet size. To date, no Pfn1-null patients have been reported, most likely due to embryonic lethality as described for constitutive Pfn1-deficient mice.[138]

5.1.2. Pfn1 is an indirect regulator of microtubule stability

Even though indications for a co-localization of Pfn1 and platelet microtubule coils were found, no direct binding of Pfn1 to microtubules could be detected (Fig. 26c). However, it is likely that Pfn1 might be indirectly linked to microtubules by a protein complex consisting of one or more of its over 50 interaction partners (Fig. 64).[123] For example, Pfn1 might be indirectly linked to the microtubule cytoskeleton via its interaction with formins, which are well described to bind microtubules.[288] Moreover, it was reported that large amounts of tubulin were found in the Pfn1 complex, but direct Pfn1-tubulin binding was also not detected.[132] A possible hypothesis is that Pfn1 binds to phospholipids in the membrane and orchestrates microtubule stabilization/ rearrangement within a multi-protein complex, possibly involving WASp and/or WIP (Fig. 64). Even though Pfn1 was reported to interact with the ubiquitously expressed WASp homolog, N-WASp,[135] no direct interaction with hematopoietic WASp has been reported so far. Pfn1, however, is known to indirectly couple to WASp via WIP,[136] which could also be shown in this thesis by co-immunoprecipitation of Pfn1 and WASp (Fig. 26b), thus further linking Pfn1 to WAS.

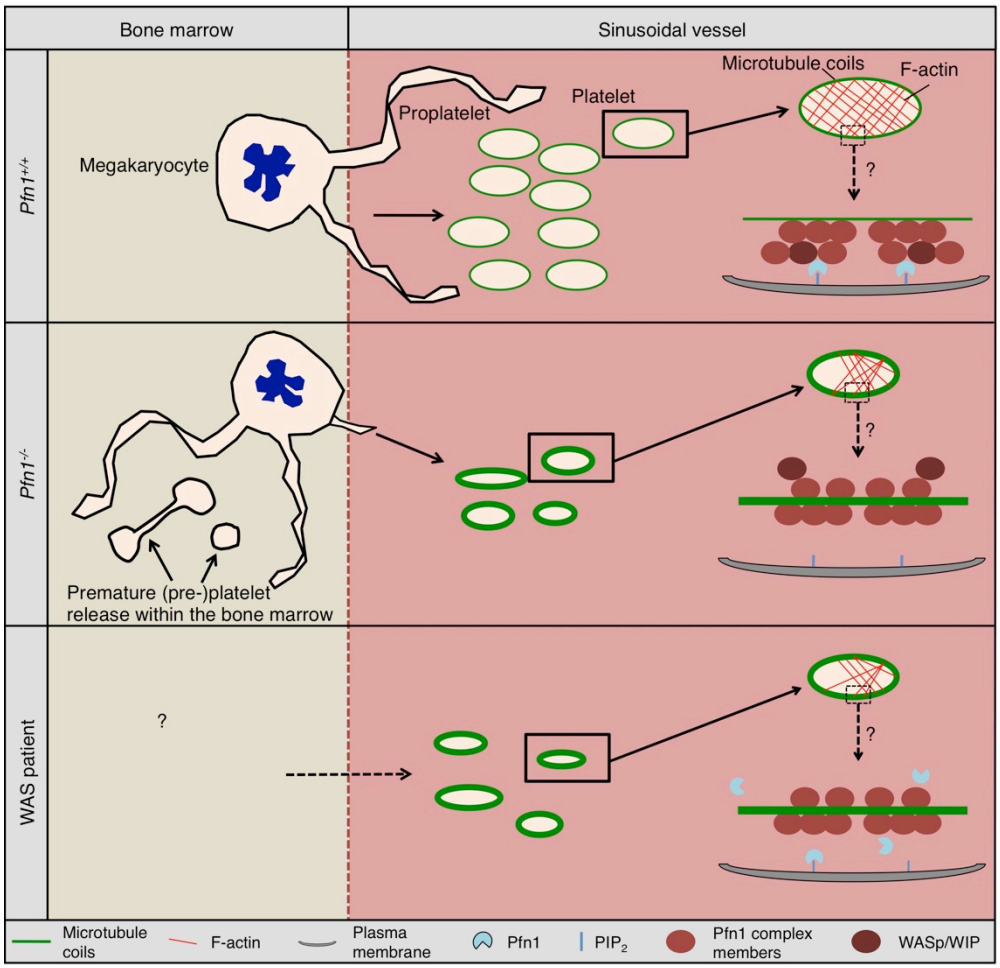

Figure 64 I **Hypothetical model.** Control BM MKs form proplatelets into the sinusoidal vessel where platelets are released from proplatelets. MT coils form a 'ring-like' structure designated as the marginal band. Pfn1 can bind to PIP_2 at the membrane and regulate via its interaction partners, including WASp/WIP, microtubule reorganization. *Pfn1*$^{-/-}$ mice display premature platelet release into the BM compartment. *Pfn1*$^{-/-}$ MKs produce less and smaller-sized platelets into the circulation, which have a thicker marginal band and a partially disrupted actin cytoskeleton. Lack of Pfn1 results in unrestrained function of Pfn1-interaction partners with consequent defective MT reorganization. Less is known about platelets derived from BM MKs of WAS patients. WAS patients display a microthrombocytopenia as observed in *Pfn1*$^{-/-}$ mice. Increased MT stability in platelets of WAS patients might be caused by altered localization and function of Pfn1 and Pfn1-interaction partners. (Bender* & Stritt* *et al. Nat Commun* 2014)[40]

Moreover, it has been suggested that Pfn1 might act as a direct activator of WASp or formins.[123] Consequently, the striking similarities between platelets of *Pfn1*$^{-/-}$ mice and WAS patients, along with the close localization of Pfn1 to microtubules observed in T-cells (Fig. 65a) and to a lesser extent in fibroblasts (Fig. 65b), point to a potential involvement of Pfn1 in the pathogenesis of the WAS. Therefore, it will be interesting to investigate a possible contribution of Pfn1-mediated alteration of microtubule stability to the development of immunodeficiency in WAS patients.

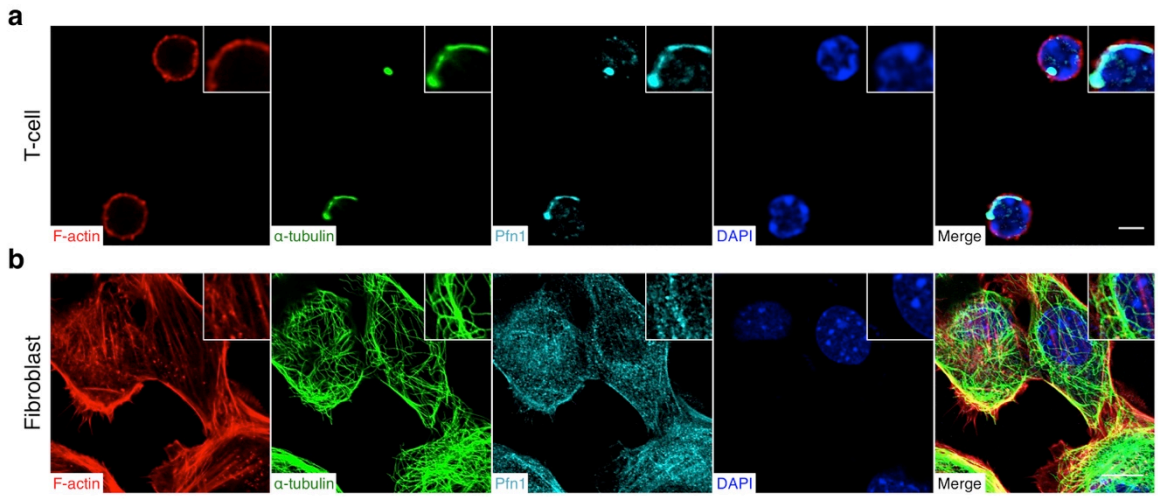

Figure 65 | Pfn1 co-localizes with microtubules in T-cells and mouse embryonic fibroblasts. (**a**) T-cells were allowed to adhere to poly-L-lysine-coated slides or (**b**) fibroblasts were grown on coverslips, fixed and stained for F-actin (red), α-tubulin (green), Pfn1 (cyan) and DAPI (blue). Scale bars, 3 µm (in **a**). Scale bars, 10 µm (in **b**). (Bender* & Stritt* *et al. Nat Commun* 2014)[40]

The differences between WAS patients and *Wasp*$^{-/-}$ mice (severity of thrombocytopenia, platelet size, microtubule reorganization) remain enigmatic. It was previously hypothesized that small platelets in WAS patients may escape splenic macrophages, and that the lack of small platelets, as well as the only moderate thrombocytopenia in *Wasp*$^{-/-}$ mice results from the in general smaller-sized mouse platelets as compared to human platelets. However, it has to be noted that in contrast to WAS patients microtubule stability was unaltered in platelets from WASp- (Fig. 23b, c) or WIP-deficient mice (Fig. 66).

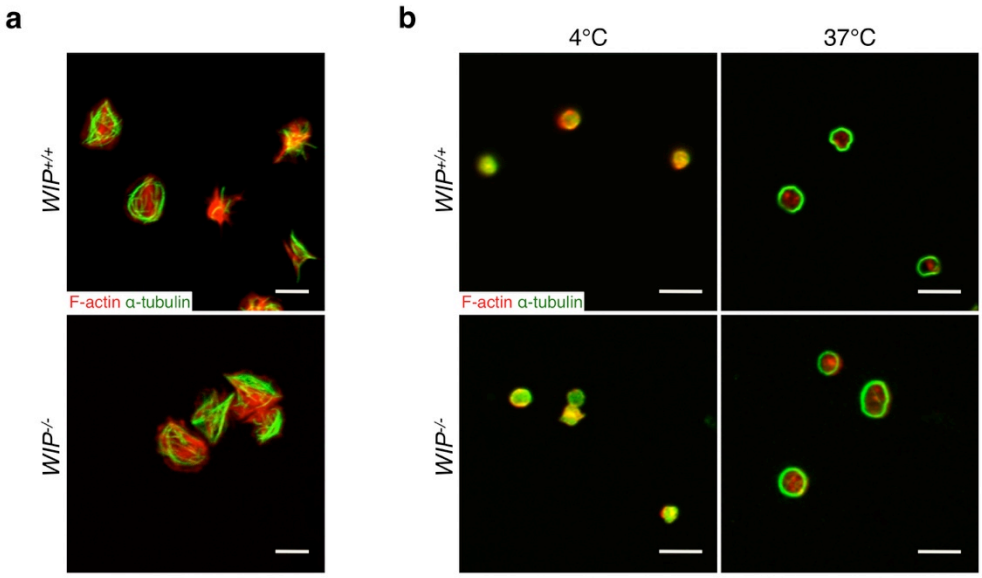

Figure 66 | Normal microtubule organization in *WIP*$^{-/-}$ mice. Control and *WIP*$^{-/-}$ platelets were allowed to (**a**) spread (15 min) on fibrinogen or (**b**) were incubated for 3.5 h at 4°C, fixed on poly-L-lysine-coated slides, stained for F-actin (red) and α-tubulin (green) and analyzed by confocal microscopy. Images are representative of at least 3 individuals. Scale bars, 3 µm. Images were acquired by Dr. Markus Bender. (Bender* & Stritt* *et al. Nat Commun* 2014)[40]

A possible role of the WASp homolog N-WASp in these processes needs to be determined. Additional support for a possible involvement of Pfn1 in the pathogenesis of WAS is provided by the growing evidence that abnormal microtubule rearrangement contributes to the development of diseases, e.g. as recently shown for Parkinson's disease.[289,290]

In summary, in this thesis it was shown that *Pfn1*$^{-/-}$ mice display a microthrombocytopenia strongly resembling the platelet phenotype of WAS patients. In addition, a central role for Pfn1 in preserving the integrity of the microtubule cytoskeleton was identified. Similarly to *Pfn1*$^{-/-}$ platelets, altered microtubule rearrangement and organization in platelets of WAS patients was revealed, which may serve as a diagnostic marker for the differential diagnosis of WAS. Based on these findings, it is tempting to speculate that WASp acts as a modulator of Pfn1 function in MKs, and that this process is disturbed in WAS patients leading to the known platelet formation defect.

5.2. Twinfilin2a is a central regulator of platelet reactivity and turnover

In the second part of this thesis the role of the small-actin binding protein Twf2a in the orchestration of platelet formation and particularly function were investigated. The here presented results establish Twf2a as a novel regulator of platelet reactivity and platelet turnover in mice and highlight Twf2a as an actin assembly-promoting factor in platelets.

5.2.1. Age dependent macrothrombocytopenia in *Twf2a*$^{-/-}$ mice

Previous studies on Twf1-deficient mice suggested that Twf1 is dispensable for platelet production and function (Stritt *et al.*, unpublished observation). However, isoform expression profiling in platelets revealed a prominent expression of both, Twf1 and Twf2a, whereas Twf2b was not detected. (Fig. 28a, b). These findings strongly suggested that the functional redundant isoforms compensate for each other in a single-deficient background. Nevertheless, besides an initial biochemical characterization and the description of a knockout mouse model, no information on the *in vivo* functions of Twf2a are available.[149,150] Surprisingly, Twf2a-deficient mice developed an age-dependent macrothrombocytopenia, suggesting that Twf1, whose expression was not upregulated, cannot completely compensate for the lack of Twf2a (Fig. 28b-f). In contrast the unaltered numbers and distribution of white blood cells suggested that Twf2a is not critical for immune cell development (Fig. 29). To further characterize this, Twf isoform expression profiling on different immune cell subsets needs to be performed. The thrombocytopenia could be ascribed to a marked reduction in platelet half-life that was however not associated with autoantibodies or an increased macrophage mediated platelet clearance (Fig. 30). Interestingly, it was recently shown that aged, desialylated platelets are cleared from the circulation by the Ashwell-Morell receptor on hepatocytes.[68] Hence it would be interesting to determine platelet desialylation to further elucidate a possible contribution of this alternative platelet clearance mechanism to the thrombocytopenia in *Twf2a*$^{-/-}$ mice.

5.2.2. Platelet hyper-reactivity might account for thrombocytopenia in *Twf2a*$^{-/-}$ mice

The pronounced hyper-reactivity of Twf2a-deficient platelets towards agonist stimulation together with the increased association of Tln-1 with β3 integrin tails strongly suggested increased platelet consumption as cause for the observed thrombocytopenia (Fig. 31 and 34). In support of this, increased thrombin generation was observed *in vitro* that appeared, however, to be independent of PS exposure on the platelet surface (Fig. 32). In line with this, it has been shown that thrombin generation does not directly correlate with PS exposure on

the outer leaflet of the platelet membrane, which led to the hypothesis of platelet microdomains that regulate the formation of coagulation complexes.[291,292]

Taken into account that PS exposure strongly depends on sustained Ca^{2+} signaling, the decreased PS exposure on activated Twf2a-deficient platelets strongly suggested an aberrant Ca^{2+} homeostasis. In agreement with this, integrin closure, depending on Ca^{2+}-dependent calpain-mediated cleavage of β3 integrin tails, was delayed in *Twf2a*$^{-/-}$ platelets (Fig. 33). To provide further evidence for increased platelet consumption due to sustained platelet aggregation, analysis of the microvasculature in histological sections will be performed. Moreover, to confirm perturbation of Ca^{2+} signaling in the absence of Twf2a Ca^{2+} measurements will be carried out and the cleavage of β3 integrin tails will be determined by immunoblot analysis.[272]

5.2.3. Twf2a promotes actin assembly in platelets

The precise role of Twf2a in actin dynamics *in vivo* is still under debate. On the one hand, Twf was shown to inhibit barbed end growth by capping of actin filaments and to inhibit pointed end growth by sequestering G-actin monomers.[152] On the other hand, its interaction with CP prevents filament disassembly and is thought to localize actin monomers to places of rapid actin turnover.[149,152,153,155] In support of the latter, impaired actin polymerization was observed in stimulated *Twf2a*$^{-/-}$ platelets thus revealing for the first time an actin assembly promoting function of Twf2a *in vivo* (Fig. 35e, f). However, it needs to be noted that the impaired actin assembly could also be attributed to Twf1, whose inhibitory function on actin assembly may become more evident in the absence of Twf2a. Together, one may speculate that Twf2a negatively regulates the inhibitory effects of Twf1 on actin dynamics. Furthermore, the accelerated spreading in the absence of Twf2a points to decreased coherent cytoplasmic contractile forces that are normally generated by activated NMMIIA (Fig. 31c, d and 35b). However, so far no direct link between Twf2a and NMMIIA exists and consequently further investigations are required to explain the accelerated spreading of *Twf2a*$^{-/-}$ platelets.[281]

Besides impaired actin assembly, also a reduced stability of microtubules was observed upon spreading or colchicine treatment of Twf2a-deficient platelets (Fig. 35b, d). Since the subcellular localization of Twfs depends on the small Rho-GTPases Rac1 and particularly Cdc42, Twfs are indirectly linked to the microtubule cytoskeleton.[148] Particularly in MKs and platelets a critical role of Rac1 and Cdc42 in regulating microtubule dynamics was shown.[293] Further investigations on the role of Twf in the regulation of microtubules are required. Furthermore, there is growing evidence that microtubules orchestrate actin polymerization and

organization and *vice versa*, thus suggesting that the alterations in the microtubule cytoskeleton in *Twf2a*$^{-/-}$ platelets could also be attributed to defects in the actin cytoskeleton.[294] In agreement with the cytoskeletal alterations in platelets, aberrant MK morphology with signs of increased fragmentation was observed (Fig. 37a, g).

Taking into account that Twf1 deficiency did neither perturb platelet production nor function (Stritt *et al.*, unpublished observation), the results presented here clearly demonstrate a critical function of Twf2a in thrombopoiesis and platelet function. Moreover, these results provide for the first time *in vivo* evidence for an actin assembly-promoting function of Twf2a and point to a possible involvement of Twf2a in the regulation of the microtubule cytoskeleton. However, to further elucidate the function of Twfs in cytoskeletal dynamics and to test a possible competition between Twf1 and Twf2a, MK-/platelet-specific Twf1-deficient mice were bred into a constitutive Twf2a-deficient background (further referred to as *Twf1/2a*$^{-/-}$).

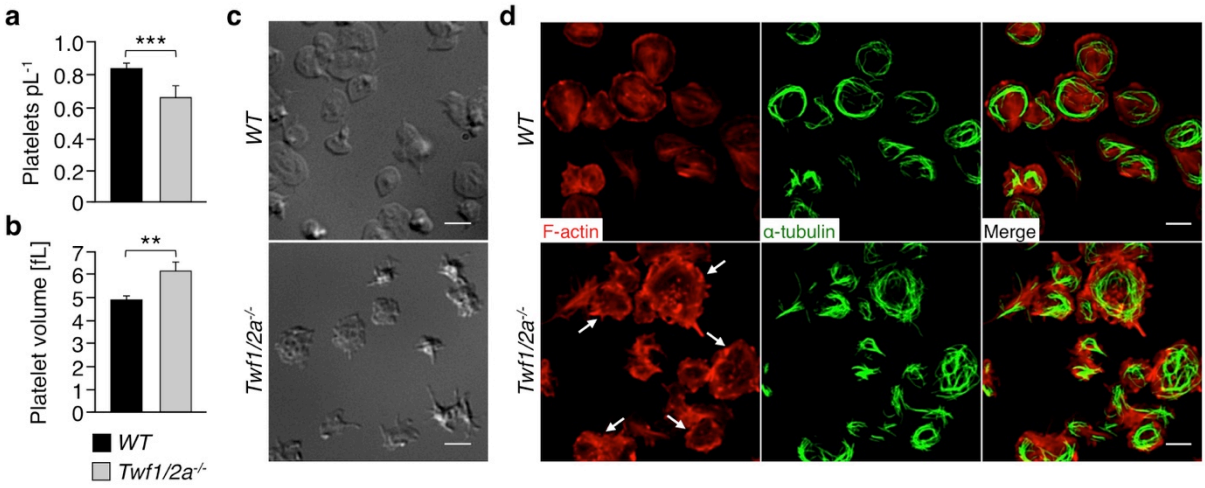

Figure 67 | Severe cytoskeletal defects in *Twf1/2a*$^{-/-}$ platelets. (**a, b**) Platelet count (**a**) and size (**b**) was determined on an automated blood cell analyzer. Values are mean ± s.d. (n = 6). Unpaired Student's *t*-test: ***$P < 0.001$; **$P < 0.01$. (**c, d**) On fibrinogen spread (15 min) platelets were visualized by DIC microscopy (**c**) or stained for F-actin (red) and α-tubulin (green) and analyzed by confocal microscopy (**d**). Arrows mark thickened cortical actin patches. Scale bars, 3 µm. Images are representative of at least 6 individuals. (Stritt *et al.*, unpublished observation)

Similar to mice lacking Twf2a, macrothrombocytopenia was observed in *Twf1/2a*$^{-/-}$ mice (Fig. 67a, b). In addition, spreading of Twf1/2a double-deficient platelets was impaired and yielded a highly aberrant morphology (Fig. 67c). Immunostaining revealed an uncontrolled polymerization and misorientation of actin filaments and microtubules leading to a rough platelet shape (Fig. 67d). The actin cytoskeleton was organized into thickened cortical actin patches and dot like structure, possible representing actin nodules.[295] This is in agreement with a report on Twf mutant *Drosophila melanogaster* where similar observations were made for the bristle morphology.

Together these findings strongly support the above raised hypothesis that Twf2a overcomes the inhibitory function Twf1, e.g. by competing in binding to actin monomers. Consequently, deficiency in both Twf1 and Twf2a results in a large proportion of free G-actin monomers that in turn promotes spontaneous actin nucleation and leads to uncontrolled actin polymerization. Further studies on the *Twf1/2a*$^{-/-}$ mice will provide a more detailed understanding on the role Twfs in actin dynamics *in vivo* and will prove or disprove the above raised hypothesis of a possible competition between Twf1 and Twf2a in platelet actin dynamics.

Furthermore, Twf is also thought to compete with ADF/cofilin in binding to ADP-G-actin monomers upon ADF/cofilin-mediated filament disassembly.[111,146,147] To put this hypothesis to a test, MK- and platelet-specific Twf1- and cofilin-deficient mice were intercrossed to generate double-deficient mice (further referred to as *Twf1/cof*$^{-/-}$). Similarly to cofilin single deficient mice, *Twf1/cof*$^{-/-}$ mice displayed normal platelet numbers with a highly increased size (Fig. 68a, b). In contrast, *Twf1/cof*$^{-/-}$ platelets were unable to spread fully and showed a severely reduced filopodia formation on vWF (Fig. 68c), reminiscent of strongly impaired cytoskeletal dynamics. Similarly to Twf2a-deficient platelets, microtubule numbers in spread *Twf1/cof*$^{-/-}$ platelets were also markedly reduced (Fig. 68d) and *in situ* analysis of BM MKs demonstrated a pronounced megakaryocytosis (Fig. 68e).

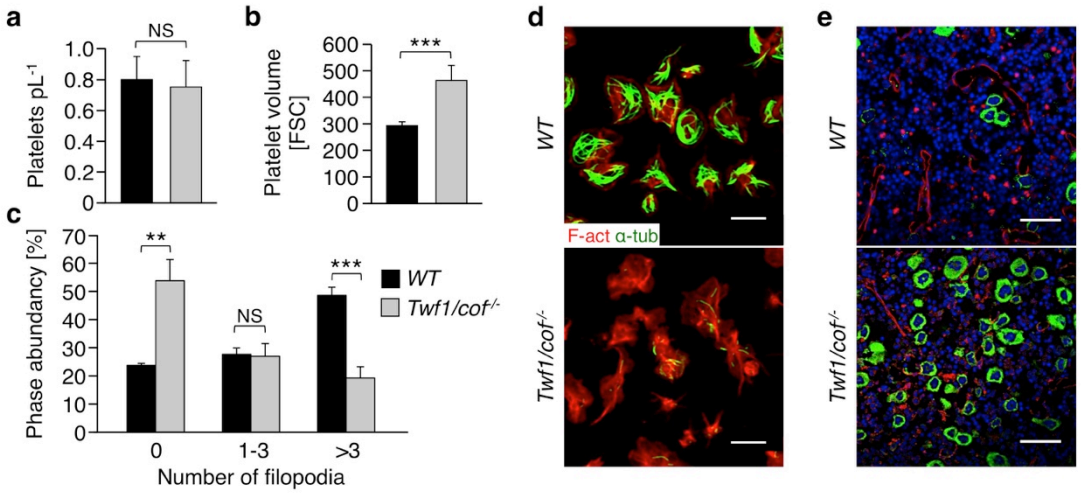

Figure 68 | Impaired cytoskeletal rearrangements and megakaryocytosis in *Twf1/cof*$^{-/-}$ mice. (**a, b**) Platelet count (**a**) and size (**b**) was determined on an automated blood cell analyzer. (**c**) Quantification of filopodia number per platelet of on vWF spread (15 min) platelets. Values are mean ± s.d. (n = 6). Unpaired Student's *t*-test: ***P< 0.001; **P< 0.01; NS, non-significant (**d**) Spread platelets (15 min, 100 µg mL^{-1} fibrinogen) were stained for F-actin (red) and α-tubulin (green) and analyzed by confocal microscopy. Scale bars, 3 µm. (**e**) Confocal microscopic images of immunostained BM sections. Scale bars, 50 µm. MKs, proplatelets and platelets are shown by GPIb staining in green color. Endoglin staining (red) labels vessels. DAPI, blue. Images are representative of at least 6 individuals. (Stritt *et al.*, unpublished observation)

These results reveal a critical role for the hypothesized competition of Twf1 and cofilin in platelets that cannot be overcome by closely related actin-binding proteins such as ADF or

Twf2a. Furthermore, the pronounced megakaryocytosis highlights Twf1 and cofilin as key molecules for the regulation of proper megakaryo- and thrombopoiesis. A detailed analysis of the defects and the underlying mechanisms will help to advance the current understanding of the regulatory network allowing tightly regulated actin dynamics.

5.3. Rap1-GTP-interacting adaptor molecule (RIAM) is dispensable for platelet integrin activation and function in mice

5.3.1. RIAM deficiency is not compensated by other MRL-family members

The unaltered inside-out and outside-in integrin activation in RIAM-deficient platelets, strongly suggested that loss of its function is compensated by other MRL-family members. However, in agreement with previous reports,[243] no lamellipodin expression (135 kDa) could be detected in platelets lysates, whereas Mig-10 is only found in *Caenorhabditis elegans* (Fig. 69).[241,245]

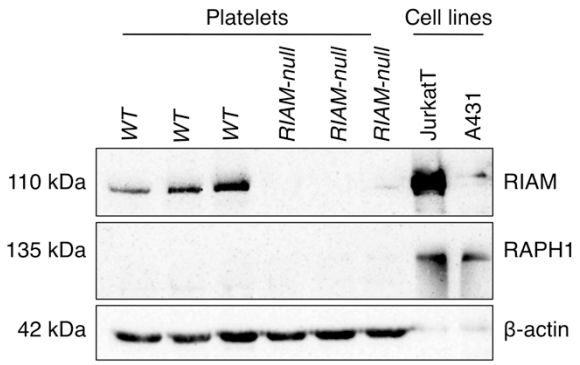

Figure 69 | Lamellipodin (RAPH1) is not expressed in mouse platelets. *WT* and *RIAM-null* platelet lysates were separated by SDS-PAGE and probed for RIAM and RAPH1 expression. β-actin served as loading control and Jurkat T-cell and A431 cell lysates as positive controls for RAPH1. (Stritt *et al.* unpublished observation)

5.3.2. RIAM deficiency does not interfere with Tln-1 recruitment to β3 integrins

Tln-1 and its recruitment to β3 integrin tails is indispensable for integrin activation,[236] and RIAM has been implicated as key molecule in this process.[238,240,241] In contrast to results obtained in cell culture approaches,[238,240,241] Tln-1 was normally recruited to β3 integrins in spread *RIAM-null* platelets (Fig. 70). Consequently, Tln-1 might be recruited to integrins via alternative pathways, e.g. by interaction with the exocyst complex, or by binding to the focal adhesion kinase.[296,297] In support of this, Han and colleagues showed in CHO cells that Tln-1 alone was sufficient to mediate β1 and β3 integrin activation, while RIAM and other Rap1 effectors were not.[238] Moreover, since platelets lacking Rap1b or CalDAG-GEFI did not show a complete block of αIIbβ3 integrin activation, alternative mechanisms for platelet integrin activation beyond RIAM-mediated recruitment of Tln-1 must be postulated.[243,275]

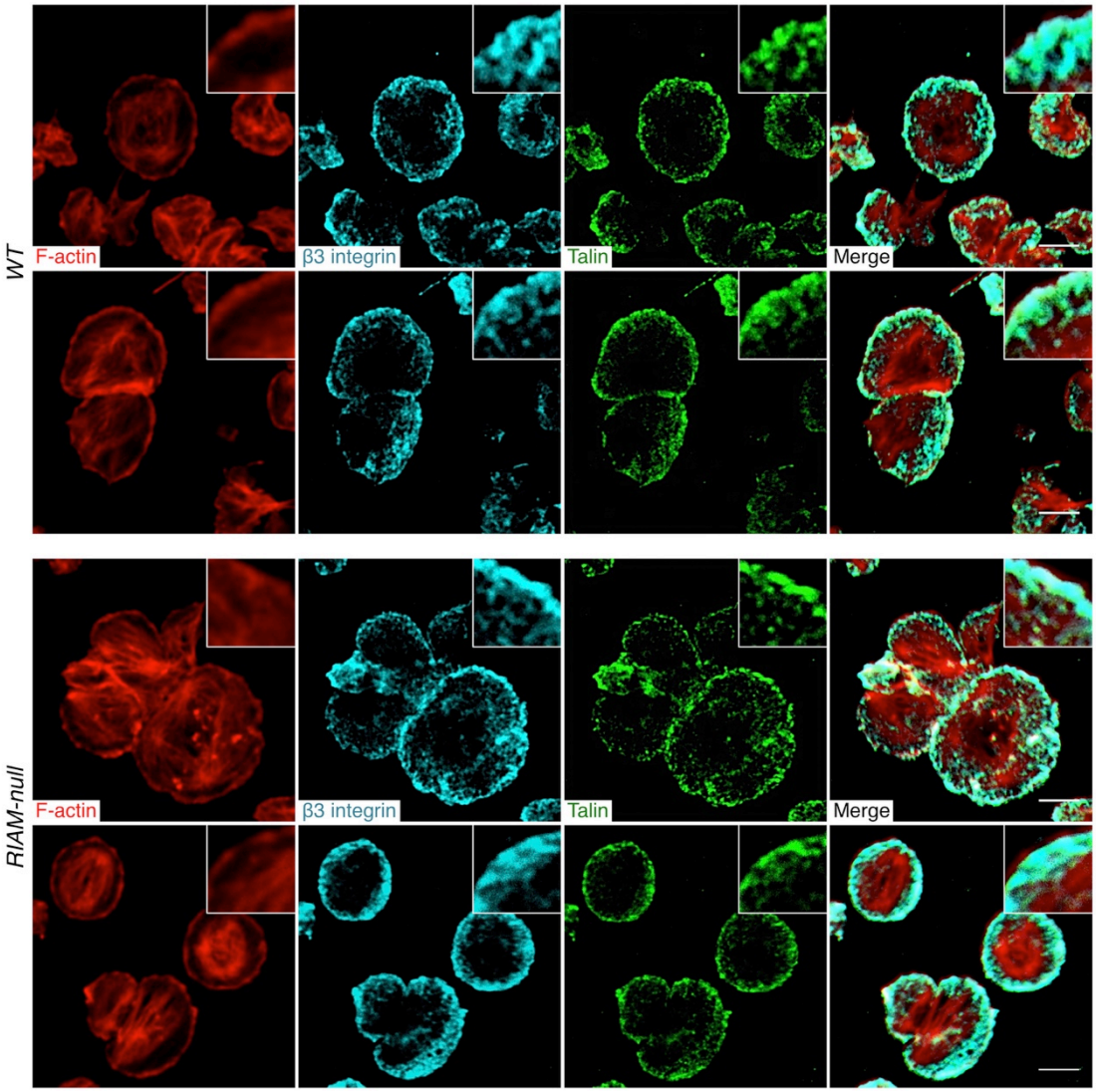

Figure 70 | Tln-1 is normally recruited to β3 integrins in RIAM-deficient platelets. Control and *RIAM-null* platelets were allowed to spread for 15 min on fibrinogen-coated (100 µg mL^{-1}) coverslips and stained for F-actin (red), β3 integrins (cyan) and Tln-1 (green). Images were acquired by confocal microscopy as described previously.[298] Scale bars, 3 µm. Images are representative of n = 5 animals. (Stritt *et al. Blood* 2015)[247]

The question on how Tln-1 is recruited to the membrane and consequently to β integrin tails might be answered by extensive biochemical studies that serve the identification of Tln- or Rap1-associated proteins in stimulated *RIAM-null* and control platelets, e.g. by mass spectrometry. In addition, this needs to be compared for different cell types beyond platelets, to exclude cell-type-specific functions of RIAM in integrin activation.

In further support of alternative pathways of Tln-1 recruitment, *RIAM-null* mice displayed no obvious immune defects and the distribution and numbers of white cells was normal (Fig. 38f). However, it has to be noted that the mice have not been challenged with different pathogens as they were maintained under almost pathogen-free conditions. One may speculate that the effects of RIAM on integrin activation are not required in normal physiology, but

take effect in diseased conditions. Consequently, the role of RIAM in immune cells needs to be elucidated in different settings and in response to different challenges.

In addition, besides Tln-1 also kindlin-3 was shown to be critical for platelet integrin activation.[239] However, it is still not known why both Tln-1 and kindlin-3 are required to enable integrin activation and how they work in concert in this process.[251]

The interaction with Tln, Ena/Vasp and Pfn1 via the PLP stretches of RIAM furthermore links it to cytoskeletal rearrangement. In line with this, knockdown of RIAM interfered with cell spreading and lamellipodia formation.[245] In contrast to previous reports, no defects in cytoskeletal organization and rearrangements in activated platelets were observed as the morphology (Fig. 40b) as well as the polymerization of F-actin (2.15 ± 0.11 fold increase in *WT* and 2.08 ± 0.06 fold increase in phalloidin-binding in *RIAM-null* mice) and the F/G-actin ratios were indistinguishable from controls (Fig. 71).

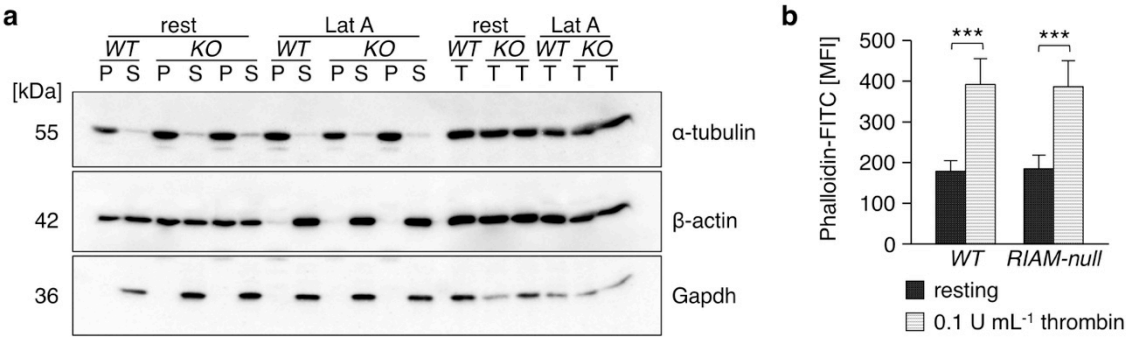

Figure 71 | Normal cytoskeletal dynamics in *RIAM-null* platelets. (**a**) Actin and tubulin cytoskeleton was isolated via ultracentrifugation and immunoblotted against α-tubulin or β-actin. Gapdh served as loading control. Insoluble fraction (*pellet*, P), soluble fraction (*supernatant*, S); rest: *resting*, Lat A: 2.5 µM *latrunculin A*, depolymerizes F-actin; T: *total protein*. (**b**) F-actin content of resting and activated (thrombin 0.1 U mL^{-1}) platelets was determined by flow cytometry. Values are mean ± s.d. (n = 9). (Stritt *et al.* unpublished observation)

Using the first *Apbb1ip*$^{-/-}$ (RIAM-null) genetic knockout mouse model, the results presented here clearly showed that RIAM is dispensable for platelet integrin function *in vivo* and that its role in platelet integrin activation needs to be reconsidered. Drs. Edward Plow and Jun Qin referred to theses findings as "…the study by Stritt *et al*., showing that platelet integrin function is apparently normal in RIAM-null mice, comes as a surprise and is potentially paradigm shifting".[299]

5.4. Phospholipase D is a central regulator of collagen I-induced cytoskeletal rearrangement and podosome formation in megakaryocytes

MK podosome formation has been proposed to be a requirement for proper platelet production and is thought to account for the premature platelet release within the BM of *Wasp*$^{-/-}$ and *Pfn1*$^{-/-}$ mice. To put the role of podosomes during proplatelet formation to a test, PLD-deficient mice were used as model. Together, the findings presented here point to a specific function of PLD in actin dynamics as well as podosome formation and size determination in MKs on a collagen I matrix. The normal platelet number in PLD-deficient mice, however, suggests the existence of compensatory mechanisms *in vivo* that overcome the defective podosome formation observed *in vitro*.

5.4.1. PLD1 and 2 are critical regulators of actin rearrangements in mouse MKs

There's growing evidence that PAs generated by PLDs are important regulators of cell adhesion, cytoskeletal dynamics and consequently cell migration and spreading.[37,38,41,42] In line with this, PLD deficiency in macrophages or MKs resulted in a reduced content of F-actin that translated into severe defects of the cytoskeletal architecture (Fig. 41).[39,43] Remarkably, PLD activity was shown to be regulated by small *ADP ribosylation factor* (Arf) and Rho-GTPases, thus linking PLD and the generation of PA to cytoskeletal rearrangements. Since spread *Pld2*$^{-/-}$ and *DKO*, but not *Pld1*$^{-/-}$ MKs displayed a marked reduction in the prevalence of F-actin, the results presented here reveal a specific role of PLD2 in actin assembly (Fig. 41a, c). However, the organization of actin filaments into podosomes as well as podosome size was impaired for MKs of all three mutants, thus suggesting cooperative functions for PLDs in the formation of actin superstructures (Fig. 41g). In support of this, PA-generation by PLD was shown to positively regulate NMMIIA activity. Consequently, abolition of PLD-mediated PA generation should result in a decreased NMMIIA contractility, which could also account for the impaired formation of podosomes.[43] However, neither chemical inhibition, nor deficiency in NMMIIA affected podosome numbers or size on different matrices and thus rather excludes a contribution of NMMIIA to the observed defects.[26]

5.4.2. The role of podosomes in MKs put to a test

Considering the proposed role of podosomes for proplatelet formation, the markedly impaired podosome formation of PLD-deficient MKs was very surprising as the mice displayed normal platelet counts and unaltered platelet production *in vitro* and *in vivo* (Fig. 44). This observation suggests that podosome formation *in vivo* can be promoted by additional stimuli via other surface receptors such as GPVI or αIIbβ3 integrins. In support of this, normal podosome

formation was found for mutant MKs upon spreading on fibrinogen or CRP (Fig. 45). The unaltered podosome formation upon spreading on CRP (Fig. 45f-j) strongly suggested that the defect seen on collagen I was attributed to defective outside-in signaling via α2β1 integrins. This would further be in agreement with previous reports on WASp- or Pfn1-deficient MKs that similarly displayed a reduced F-actin content and impaired podosome formation.[26,27,40] In *Wasp*$^{-/-}$ as well as in *Pfn1*$^{-/-}$ mice the abolished podosome formation is thought to result from defective outside-in signaling via α2β1 integrins and to account for the premature platelet release within the BM compartment. The indirect association of PLD and WASp via Grb2 further suggests hat PLD and WASp might act in concert to regulate MK actin dynamics and podosome formation in response to collagen I- mediated signaling downstream of α2β1 integrins.[37,38] However, despite reduced spreading, *Itga2*$^{-/-}$ MKs showed a normal podosomes density, thus clearly excluding impaired outside-in signaling via α2β1 as cause for the impaired podosome formation and premature platelet release observed in PLD1/2-, WASp- and Pfn1-deficient mice.[40,287,295] Interestingly, Nishimura *et al.* recently reported a IL-1α-dependent mechanism of platelet biogenesis, by which platelets are quickly released from MKs in an non-polarized fashion, partially also into the bone marrow that serves the quick restoration of platelet counts during acute platelet needs.[69,70] Rupture-type platelet production might also occur or even predominate in *Wasp*$^{-/-}$ and *Pfn1*$^{-/-}$ mice, where a reduced platelet life span may trigger IL-1α release and could account for the observed premature platelet release (Fig. 15b, e). Consequently, assessment of IL-1α levels in these mice would be highly interesting. Furthermore, so far it has not been assessed whether IL-1α may also trigger the formation of podosomes or podosome-like structure that serve the secretion of MMP and ECM degradation.

Another possible and provocative hypothesis that might explain the normal platelet number in the *DKO* mice could be that podosome formation by MKs, which has so far only been observed *in vitro*, may not be essential for (pro)platelet formation *in vivo*. The fact that collagen I is generally assumed to inhibit proplatelet formation, but induces the formation of podosomes, which is believed to be a pre-stage of proplatelets in MKs, further argues against a role of podosomes in (pro)platelet formation.

5.5. Defects in TRPM7 channel function result in deregulated thrombopoiesis through altered cellular Mg^{2+} homeostasis and cytoskeletal architecture

Besides the degradation of ECM components also integrin- and NMMIIA-mediated locomotion might be essential for platelet production by MKs. In support of this, NMMIIA has been proposed to inhibit proplatelet formation downstream of α2β1 integrins.[300] Both, integrin activation and NMMIIA activity critically depend on Mg^{2+}, whose concentration is mainly regulated via TRPM7 in MKs. In conclusion, the presented data provides compelling evidence that defects in TRPM7 channel function cause macrothrombocytopenia in humans and mice. Decreased $[Mg^{2+}]_i$ leads to deregulated NMMIIA activity and altered cytoskeletal dynamics that perturb thrombopoiesis.

5.5.1. Tightly regulated $[Mg^{2+}]_i$ is critical for normal thrombopoiesis

Although expression profiling of Mg^{2+} channels and transporters revealed expression of *MagT1*, *Tusc3* and *Trpm7* in mouse platelets, this study clearly reveals TRPM7 is the major regulator of Mg^{2+} levels in MKs and platelets, since neither MagT1, nor Tusc3 could compensate for the lack or the impaired channel activity of TRPM7 and restore $[Mg^{2+}]_i$ (Fig. 47a, d, 50a and 59). Decreased intracellular Mg^{2+} levels (Fig. 50a and 59a) led to the development of macrothrombocytopenia in TRPM7-deficient mice and in patients with variants in *TRPM7* (Fig. 48, 58 and Table 1 and 2). Furthermore, decreased $[Mg^{2+}]_i$ resulted in an aberrant morphology of α-granules, which either indicates defective packing of granules or that Mg^{2+} is stored in α-granules and that the aberrant morphology could be attributed to the decreased $[Mg^{2+}]_i$ (Fig. 50a, b, and 59). However, it is rather unlikely that defective packaging of granules accounts for the reduced electron density of α-granules, since the prevalence of tested α-granular proteins was normal or, in line with the enlarged size of *Trpm7*$^{fl/fl\text{-}Pf4Cre}$ platelets, mildly increased (Fig. 50c-e).

Strikingly, platelet production by TRPM7-deficient MKs was markedly reduced, which could be attributed to an increased NMMIIA activity and accounted for the observed macrothrombocytopenia (Fig. 52f, g and 56a, b). Several lines of evidence support the notion of an increased NMMIIA activity: (I) treatment with the NMMIIA inhibitor blebbistatin, or (II) Mg^{2+} supplementation could almost fully restore proplatelet formation in TRPM7-deficient MKs and (III) thick and densely packed proplatelets in BM sinusoids with signs of apoptosis, reflecting impaired proplatelet fragmentation and release of preplatelets from *Trpm7*$^{fl/fl\text{-}Pf4Cre}$ MKs, were observed (Fig. 52n and 56a, b).

Of note, Mg^{2+} was recently shown to inhibit NMMIIA activity by reducing the ADP release rate

and its affinity to actin.[164] Consequently, it is likely that reduced $[Mg^{2+}]_i$ in *Trpm7*$^{fl/fl\text{-}Pf4Cre}$ MKs leads to increased NMMIIA activity that is known to inhibit proplatelet formation.[187,188] Mg^{2+} supplementation is thought to increase $[Mg^{2+}]_i$, presumably mediated by MagT1 (Fig. 56c, d). In support of this, Deason-Towne *et al.* showed that upregulation of MagT1 expression and Mg^{2+} supplementation in TRPM7-deficient DT40 B-cells could improve, but not rescue cell growth.[182] Similar observations were made upon CRISPR-Cas9 mediated disruption of *TRPM7* expression in the myelogenous K562 cell line, where Mg^{2+} supplementation could similarly improve cell growth (Fig. 63). Unfortunately, MagT1 expression levels in K562 cells under different conditions have not yet been determined. These findings may raise the question why MK numbers were increased in the described mouse model (Fig. 52b and 54b). However, in the presented study a conditional targeting strategy of *Tprm7* was applied, for which Cre-recombinase is specifically expressed under the control of the *Pf4* promoter and hence induction of the knockout occurs rather late and possibly does not perturb MK lineage commitment (Fig. 47b and 52e). In addition, residual TRPM7 protein may persist from precursors up to the early MK stages and thus regulate Mg^{2+} homeostasis. However, in favor of this hypothesis, one out of 11 cells, showed a typical, but reduced TRPM7-like current, while it was abolished for all other tested MKs in a whole cell patch clamp setup (Fig. 47d). Unfortunately, up to date no specific antibody against TRPM7 is available that would allow to test this hypothesis. A recent report by Spinler *et al.* further provides an explanation for the impaired preplatelet shedding from proplatelets of *Trpm7*$^{fl/fl\text{-}Pf4Cre}$ MKs due to sustained NMMIIA activity, by showing that shear stress and NMMIIA inhibition increased the release of platelet-like particles form human $CD34^+$ cell-derived MKs *in vitro*.[187] Although TRPM7 α-kinase has been implicated as a critical regulator of NMMIIA and consequently cytoskeletal dynamics, the observed defects in MKs and platelets were independent of TRPM7 α-kinase activity, as a kinase-dead knock-in mouse model did not show these alterations (Fig. 49).

Interestingly, an aberrant localization and an activation-dependent decrease in NMMIIA levels was observed in MKs and platelets of TRPM7-deficient mice and patients with the p.C721G variant (Fig. 55 and 61). Of note, so far it is not clear whether NMMIIA is degraded or if the epitope becomes masked by posttranslational modifications or binding to other proteins. However, in support of a functional NMMIIA inactivation, accelerated spreading and an increased prevalence of microtubules that are thought to exert the protrusive forces during spreading, were observed upon decrease of NMMIIA in the *Trpm7*$^{fl/fl\text{-}Pf4Cre}$ platelets.[301] Similarly, in studies on MKs and platelets derived from patients with MYH-RD a reduced prevalence of NMMIIA in MKs and absent or only weak expression was determined in platelets.[203,302,303] The unaltered mRNA stability strongly suggests that increased degradation

of mutant NMMIIA might account for the decreased protein levels in platelets and MKs from patients with MYH9-RD.[302] One may speculate that similar to the results presented here on MKs and platelets from TRPM7 mutant mice and patients, NMMIIA degradation in patients with MYH9-RD might serve the inactivation of constitutive active NMMIIA mutants. In support of this, Chen *et al.* determined impaired proplatelet formation due to increased contractile forces in MKs from 10 patients with different variants in *MYH9*. Furthermore, proplatelet formation as well as MK ultrastructure could be rescued by blebbistatin treatment *in vitro*. Hence it was concluded that increased activity, altered assembly of NMMIIA, or both account for the macrothrombocytopenia in patients with variants in *MYH9*.[187,206]

Importantly, it has to be noted that the here-described human disorder, associated with the p.C721G variant in *TRPM7* is clearly distinguishable from *MYH9*-related platelet disease, which can be associated with hearing loss, cataracts, and renal failure.[200] However, patients with variants in *TRPM7* and *MYH9* both display macrothrombocytopenia with more spherical platelets and partially, increased actomyosin contractility.[187]

This study provides for the first time several independent lines of evidence that proper regulation of Mg^{2+} homeostasis in MKs by TRPM7 plays a critical role in thrombopoiesis and platelet sizing, both in humans and mice by interfering with NMMIIA activity. Collectively, these results highlight the clinical need to carefully control platelet count and size in patients with deregulated Mg^{2+} homeostasis and ultimately, these findings suggest Mg^{2+} supplementation as a potential treatment for the management of thrombocytopenia in patients with increased activity of NMMIIA. Furthermore, the fact that two of the patients in the presented study also suffered from paroxysmal atrial fibrillation suggests *TRPM7* as a candidate causing altered Mg^{2+} levels in cardiac cells. In support of this, it has recently been shown that defects of TRPM7 in mice lead to the development of atrial fibrillation by regulating myofibroblast dedifferentiation and cardiac automaticity by controlling the expression levels of HCN4.[179,180,191]

5.6. Concluding remarks and future perspectives

The findings presented in this thesis provide new insights into the regulation of cytoskeletal dynamics and its implications in platelet production and function in humans and mice.

The conditional Pfn1-deficient mouse represents the first mouse model recapitulating key features of the WAS. Furthermore, for the first time, a role of Pfn1 in the regulation of microtubule stability and organization in platelets and MKs was identified. Strikingly, similar alterations were found in platelets of four WAS patients, independent of their *WAS* variant. In conclusion, these findings point to a possible involvement of Pfn1 in the pathogenesis of the WAS. The identification of the twisted and bent microtubules in platelets from WAS patients might serve as a novel differential diagnostic test in patients with microthrombocytopenia, justifying sequence analysis of the *WAS* gene. However, the molecular link between Pfn1 and WASp, as well as the precise role of Pfn1 in the development of WAS remains elusive. To decipher the underlying mechanisms leading to the cytoskeletal alterations and hence microthrombocytopenia, retroviral reconstitution experiments will be carried out. To this end, different functional mutants of Pfn1 were generated (Fig. 6) and a retroviral transduction system for HSCs has been established in the course of this thesis. Furthermore, inducible mouse embryonic fibroblast knockout cell lines were generated by intercrossing *Pfn1*$^{fl/fl}$ mice with B6.129-*Gt(ROSA)26Sor*$^{tm1(cre/ERT2)Tyj}$/J mice (kindly provided by Prof. Antje Gohla (Würzburg, Germany)) and will complement afore mentioned *in vivo* experiments.

Of note, histone acetylation is known to increase gene expression and could account for the elevated WASp levels in PBMCs from WAS carriers (Fig. 27). In support of this, de-/ acetylation of both histones and microtubules is control by the same group of acetyltransferases and deacetylases.[89] Further studies on the overall acetylation pattern of proteins from WAS carriers' cells will help to understand this observation and possibly the pathogenic mechanism underlying the immunological defects in the WAS.

In addition, Twf2a was established as a central regulator of platelet reactivity and platelet turnover. The decreased platelet half-life was most likely attributed to the marked hyperreactivity of *Twf2a*$^{-/-}$ platelets characterized by sustained integrin activation that translated into accelerated thrombus formation *in vivo*. The impaired actin polymerization in Twf2a-defcient platelets upon stimulation provides the first evidence for a positive regulatory role of Twf2a in actin assembly. Furthermore, these results suggest a possible competition between Twf1 and Twf2a in actin dynamics. Future work will focus on the role of Twf2a in megakaryopoiesis and Ca^{2+} signaling. Besides this, functional redundancies of Twf1 and Twf2a as well as the rivalry between Twf1 and cofilin will be analyzed in *Twf1/2a*$^{-/-}$ and *Twf1/cof*$^{-/-}$ mice

(Fig. 67 and 68). These studies will help to clarify the role of Twfs in actin dynamics respectively and allow the identification of redundant functions and possible competitions between the two proteins. The marked hyper-reactivity stimulated further studies on the regulation of integrin activation and on a possible involvement of RIAM, which was suggested as key regulator therein. However, studies on the first constitutive RIAM-deficient mouse strain clearly showed that RIAM is dispensable for the activation of β1 and β3 integrins, at least in platelets. The absence of obvious immunological defects suggests that this is also true for immune cells, but will be ascertained and represents the focus of future studies. Besides this, alternative pathways of Tln-1 recruitment via the Rap1b pathway in the absence of RIAM, as well as the role of kindlin-3 therein will be analyzed.

During megakaryo- and thrombopoiesis outside-in signaling by integrins and other surface receptors transmits inhibitory and activating signals that regulate MK migration, but also the proplatelet formation. In this thesis, PLD was revealed as a critical regulator of actin dynamics and podosome formation in MKs. The normal platelet counts and platelet production upon challenge in *Pld1/2*$^{-/-}$ mice, as well as the absence of a premature platelet release in *Itga2*$^{-/-}$ mice, question the role of podosomes in platelet production and on the other hand raise the need to reconsider the proposed inhibitory signaling by α2β1 integrins on proplatelet formation. Future research will focus on alternative signaling pathways that account for the premature platelet release in *Pfn1*$^{-/-}$ and *Wasp*$^{-/-}$ mice. In addition, the existence and relevance of podosomes needs to be tested *in vivo*.

Moreover, NMMIIA has been implicated as a downstream effector of the inhibitory signals transmitted via α2β1 integrins. Besides Rho-GTPase signaling, also Mg^{2+} and TRPM7 α-kinase are known regulators of NMMIIA activity. In the course of this thesis, TRPM7 was identified as the major regulator of Mg^{2+} homeostasis in MKs and platelets. Furthermore, decreased $[Mg^{2+}]_i$ led to deregulated NMMIIA activity and altered cytoskeletal dynamics that perturbed thrombopoiesis and resulted in macrothrombocytopenia in humans and mice. Further research will focus on the role of Mg^{2+} homeostasis in platelets and MKs and its influence on platelet production and function. To this end, MagT1 and TRPM7 double-deficient mice will be generated and possible compensatory mechanisms will be analyzed. In addition, generation of a p.C721G TRPM7 mutant mouse represents a key step to prove a role of the p.C721G variant in the pathogenesis of atrial fibrillation that could not be reproduced in the used conditional knockout model. Finally, the data presented here strongly suggests Mg^{2+} supplementation as possible therapy for patients suffering from MYH9-RD with an increased activity of NMMIIA.

6. REFERENCES

1. Long, M.W. Megakaryocyte differentiation events. *Semin Hematol* **35**, 192-199 (1998).
2. Machlus, K.R., Thon, J.N. & Italiano, J.E., Jr. Interpreting the developmental dance of the megakaryocyte: a review of the cellular and molecular processes mediating platelet formation. *Br J Haematol* **165**, 227-236 (2014).
3. Lambert, M.P., Sullivan, S.K., Fuentes, R., French, D.L. & Poncz, M. Challenges and promises for the development of donor-independent platelet transfusions. *Blood* **121**, 3319-3324 (2013).
4. Malara, A.*, et al.* Extracellular matrix structure and nano-mechanics determine megakaryocyte function. *Blood* **118**, 4449-4453 (2011).
5. Malara, A.*, et al.* Megakaryocyte-matrix interaction within bone marrow: new roles for fibronectin and factor XIII-A. *Blood* **117**, 2476-2483 (2011).
6. Avecilla, S.T.*, et al.* Chemokine-mediated interaction of hematopoietic progenitors with the bone marrow vascular niche is required for thrombopoiesis. *Nat Med* **10**, 64-71 (2004).
7. Bunting, S.*, et al.* Normal platelets and megakaryocytes are produced in vivo in the absence of thrombopoietin. *Blood* **90**, 3423-3429 (1997).
8. Kaushansky, K., Fox, N., Lin, N.L. & Liles, W.C. Lineage-specific growth factors can compensate for stem and progenitor cell deficiencies at the postprogenitor cell level: an analysis of doubly TPO- and G-CSF receptor-deficient mice. *Blood* **99**, 3573-3578 (2002).
9. Mendez-Ferrer, S.*, et al.* Mesenchymal and haematopoietic stem cells form a unique bone marrow niche. *Nature* **466**, 829-834 (2010).
10. Bruns, I.*, et al.* Megakaryocytes regulate hematopoietic stem cell quiescence through CXCL4 secretion. *Nat Med* **20**, 1315-1320 (2014).
11. Zhao, M.*, et al.* Megakaryocytes maintain homeostatic quiescence and promote post-injury regeneration of hematopoietic stem cells. *Nat Med* **20**, 1321-1326 (2014).
12. Tomer, A. Human marrow megakaryocyte differentiation: multiparameter correlative analysis identifies von Willebrand factor as a sensitive and distinctive marker for early (2N and 4N) megakaryocytes. *Blood* **104**, 2722-2727 (2004).
13. Chagraoui, H.*, et al.* SCL-mediated regulation of the cell-cycle regulator p21 is critical for murine megakaryopoiesis. *Blood* **118**, 723-735 (2011).
14. Geddis, A.E., Fox, N.E., Tkachenko, E. & Kaushansky, K. Endomitotic megakaryocytes that form a bipolar spindle exhibit cleavage furrow ingression followed by furrow regression. *Cell Cycle* **6**, 455-460 (2007).
15. Lordier, L.*, et al.* RUNX1-induced silencing of non-muscle myosin heavy chain IIB contributes to megakaryocyte polyploidization. *Nat Commun* **3**, 717 (2012).
16. Tomer, A., Harker, L.A. & Burstein, S.A. Purification of human megakaryocytes by fluorescence-activated cell sorting. *Blood* **70**, 1735-1742 (1987).
17. Raslova, H.*, et al.* Megakaryocyte polyploidization is associated with a functional gene amplification. *Blood* **101**, 541-544 (2003).
18. Behnke, O. An electron microscope study of the megacaryocyte of the rat bone marrow. I. The development of the demarcation membrane system and the platelet surface coat. *J Ultrastruct Res* **24**, 412-433 (1968).
19. Schulze, H.*, et al.* Characterization of the megakaryocyte demarcation membrane system and its role in thrombopoiesis. *Blood* **107**, 3868-3875 (2006).
20. Chen, Y.*, et al.* Loss of the F-BAR protein CIP4 reduces platelet production by impairing membrane-cytoskeleton remodeling. *Blood* **122**, 1695-1706 (2013).
21. Eckly, A.*, et al.* Biogenesis of the demarcation membrane system (DMS) in megakaryocytes. *Blood* **123**, 921-930 (2014).

22. Mazharian, A. Assessment of megakaryocyte migration and chemotaxis. *Methods Mol Biol* **788**, 275-288 (2012).
23. Niswander, L.M., Fegan, K.H., Kingsley, P.D., McGrath, K.E. & Palis, J. SDF-1 dynamically mediates megakaryocyte niche occupancy and thrombopoiesis at steady state and following radiation injury. *Blood* **124**, 277-286 (2014).
24. Pitchford, S.C., Lodie, T. & Rankin, S.M. VEGFR1 stimulates a CXCR4-dependent translocation of megakaryocytes to the vascular niche, enhancing platelet production in mice. *Blood* **120**, 2787-2795 (2012).
25. Psaila, B., Lyden, D. & Roberts, I. Megakaryocytes, malignancy and bone marrow vascular niches. *J Thromb Haemost* **10**, 177-188 (2012).
26. Schachtner, H.*, et al.* Megakaryocytes assemble podosomes that degrade matrix and protrude through basement membrane. *Blood* **121**, 2542-2552 (2013).
27. Sabri, S.*, et al.* Deficiency in the Wiskott-Aldrich protein induces premature proplatelet formation and platelet production in the bone marrow compartment. *Blood* **108**, 134-140 (2006).
28. Gawden-Bone, C.*, et al.* Dendritic cell podosomes are protrusive and invade the extracellular matrix using metalloproteinase MMP-14. *J Cell Sci* **123**, 1427-1437 (2010).
29. Schachtner, H., Calaminus, S.D., Thomas, S.G. & Machesky, L.M. Podosomes in adhesion, migration, mechanosensing and matrix remodeling. *Cytoskeleton (Hoboken)* **70**, 572-589 (2013).
30. Murphy, D.A. & Courtneidge, S.A. The 'ins' and 'outs' of podosomes and invadopodia: characteristics, formation and function. *Nat Rev Mol Cell Biol* **12**, 413-426 (2011).
31. Li, A.*, et al.* The actin-bundling protein fascin stabilizes actin in invadopodia and potentiates protrusive invasion. *Curr Biol* **20**, 339-345 (2010).
32. Linder, S., Hufner, K., Wintergerst, U. & Aepfelbacher, M. Microtubule-dependent formation of podosomal adhesion structures in primary human macrophages. *J Cell Sci* **113 Pt 23**, 4165-4176 (2000).
33. Destaing, O., Saltel, F., Geminard, J.C., Jurdic, P. & Bard, F. Podosomes display actin turnover and dynamic self-organization in osteoclasts expressing actin-green fluorescent protein. *Mol Biol Cell* **14**, 407-416 (2003).
34. van den Dries, K.*, et al.* Interplay between myosin IIA-mediated contractility and actin network integrity orchestrates podosome composition and oscillations. *Nat Commun* **4**, 1412 (2013).
35. Evans, J.G., Correia, I., Krasavina, O., Watson, N. & Matsudaira, P. Macrophage podosomes assemble at the leading lamella by growth and fragmentation. *J Cell Biol* **161**, 697-705 (2003).
36. Jurdic, P., Saltel, F., Chabadel, A. & Destaing, O. Podosome and sealing zone: specificity of the osteoclast model. *Eur J Cell Biol* **85**, 195-202 (2006).
37. Chae, Y.C.*, et al.* Phospholipase D activity regulates integrin-mediated cell spreading and migration by inducing GTP-Rac translocation to the plasma membrane. *Mol Biol Cell* **19**, 3111-3123 (2008).
38. Gomez-Cambronero, J. The exquisite regulation of PLD2 by a wealth of interacting proteins: S6K, Grb2, Sos, WASp and Rac2 (and a surprise discovery: PLD2 is a GEF). *Cell Signal* **23**, 1885-1895 (2011).
39. Stritt, S., Thielmann, I., Dutting, S., Stegner, D. & Nieswandt, B. Phospholipase D is a central regulator of collagen I-induced cytoskeletal rearrangement and podosome formation in megakaryocytes. *J Thromb Haemost* **12**, 1364-1371 (2014).
40. Bender, M.*, et al.* Megakaryocyte-specific Profilin1-deficiency alters microtubule stability and causes a Wiskott-Aldrich syndrome-like platelet defect. *Nat Commun* **5**, 4746 (2014).
41. Exton, J.H. Regulation of phospholipase D. *Biochim Biophys Acta* **1439**, 121-133 (1999).

42. Oude Weernink, P.A., Lopez de Jesus, M. & Schmidt, M. Phospholipase D signaling: orchestration by PIP2 and small GTPases. *Naunyn Schmiedebergs Arch Pharmacol* **374**, 399-411 (2007).
43. Ali, W.H.*, et al.* Deficiencies of the lipid-signaling enzymes phospholipase D1 and D2 alter cytoskeletal organization, macrophage phagocytosis, and cytokine-stimulated neutrophil recruitment. *PLoS One* **8**, e55325 (2013).
44. Elvers, M.*, et al.* Impaired alpha(IIb)beta(3) integrin activation and shear-dependent thrombus formation in mice lacking phospholipase D1. *Sci Signal* **3**, ra1 (2010).
45. Thielmann, I.*, et al.* Redundant functions of phospholipases D1 and D2 in platelet alpha-granule release. *J Thromb Haemost* **10**, 2361-2372 (2012).
46. Stegner, D.*, et al.* Pharmacological inhibition of phospholipase D protects mice from occlusive thrombus formation and ischemic stroke--brief report. *Arteriosclerosis, thrombosis, and vascular biology* **33**, 2212-2217 (2013).
47. Behnke, O. An electron microscope study of the rat megacaryocyte. II. Some aspects of platelet release and microtubules. *J Ultrastruct Res* **26**, 111-129 (1969).
48. Italiano, J.E., Jr., Stewart, M. & Roberts, T.M. Localized depolymerization of the major sperm protein cytoskeleton correlates with the forward movement of the cell body in the amoeboid movement of nematode sperm. *J Cell Biol* **146**, 1087-1096 (1999).
49. Zhang, L.*, et al.* A novel role of sphingosine 1-phosphate receptor S1pr1 in mouse thrombopoiesis. *J Exp Med* **209**, 2165-2181 (2012).
50. Bender, M.*, et al.* Microtubule sliding drives proplatelet elongation and is dependent on cytoplasmic dynein. *Blood* **125**, 860-868 (2015).
51. Patel, S.R.*, et al.* Differential roles of microtubule assembly and sliding in proplatelet formation by megakaryocytes. *Blood* **106**, 4076-4085 (2005).
52. Richardson, J.L., Shivdasani, R.A., Boers, C., Hartwig, J.H. & Italiano, J.E., Jr. Mechanisms of organelle transport and capture along proplatelets during platelet production. *Blood* **106**, 4066-4075 (2005).
53. Stritt, S. & Nieswandt, B. In vitro platelets in sight. *Blood* **124**, 1849-1850 (2014).
54. Thon, J.N.*, et al.* Platelet bioreactor-on-a-chip. *Blood* **124**, 1857-1867 (2014).
55. Bender, M.*, et al.* ADF/n-cofilin-dependent actin turnover determines platelet formation and sizing. *Blood* **116**, 1767-1775 (2010).
56. Eckly, A.*, et al.* Abnormal megakaryocyte morphology and proplatelet formation in mice with megakaryocyte-restricted MYH9 inactivation. *Blood* **113**, 3182-3189 (2009).
57. Bender, M.*, et al.* Dynamin 2-dependent endocytosis is required for normal megakaryocyte development in mice. *Blood* **125**, 1014-1024 (2015).
58. Junt, T.*, et al.* Dynamic visualization of thrombopoiesis within bone marrow. *Science* **317**, 1767-1770 (2007).
59. Italiano, J.E., Jr. & Shivdasani, R.A. Megakaryocytes and beyond: the birth of platelets. *J Thromb Haemost* **1**, 1174-1182 (2003).
60. Leven, R.M. & Yee, M.K. Megakaryocyte morphogenesis stimulated in vitro by whole and partially fractionated thrombocytopenic plasma: a model system for the study of platelet formation. *Blood* **69**, 1046-1052 (1987).
61. Zhang, L.*, et al.* Sphingosine kinase 2 (Sphk2) regulates platelet biogenesis by providing intracellular sphingosine 1-phosphate (S1P). *Blood* **122**, 791-802 (2013).
62. Behnke, O. & Forer, A. From megakaryocytes to platelets: platelet morphogenesis takes place in the bloodstream. *Eur J Haematol Suppl* **61**, 3-23 (1998).
63. Thon, J.N.*, et al.* Cytoskeletal mechanics of proplatelet maturation and platelet release. *J Cell Biol* **191**, 861-874 (2010).
64. Potts, K.S.*, et al.* Mouse prenatal platelet-forming lineages share a core transcriptional program but divergent dependence on MPL. *Blood* (2015).
65. Potts, K.S.*, et al.* A lineage of diploid platelet-forming cells precedes polyploid megakaryocyte formation in the mouse embryo. *Blood* **124**, 2725-2729 (2014).

66. Kaufman, R.M., Airo, R., Pollack, S. & Crosby, W.H. Circulating megakaryocytes and platelet release in the lung. *Blood* **26**, 720-731 (1965).
67. Kaufman, R.M., Airo, R., Pollack, S., Crosby, W.H. & Doberneck, R. Origin of Pulmonary Megakaryocytes. *Blood* **25**, 767-775 (1965).
68. Grozovsky, R.*, et al.* The Ashwell-Morell receptor regulates hepatic thrombopoietin production via JAK2-STAT3 signaling. *Nat Med* **21**, 47-54 (2015).
69. Nishimura, S.*, et al.* IL-1alpha induces thrombopoiesis through megakaryocyte rupture in response to acute platelet needs. *J Cell Biol* **209**, 453-466 (2015).
70. Nieswandt, B. & Stritt, S. Megakaryocyte rupture for acute platelet needs. *J Cell Biol* **209**, 327-328 (2015).
71. Hartwig, C.*, et al.* Elevated phenylalanine levels interfere with neurite outgrowth stimulated by the neuronal cell adhesion molecule L1 in vitro. *FEBS Lett* **580**, 3489-3492 (2006).
72. Ng, A.P.*, et al.* Mpl expression on megakaryocytes and platelets is dispensable for thrombopoiesis but essential to prevent myeloproliferation. *Proc Natl Acad Sci U S A* **111**, 5884-5889 (2014).
73. Fitch-Tewfik, J.L. & Flaumenhaft, R. Platelet granule exocytosis: a comparison with chromaffin cells. *Front Endocrinol (Lausanne)* **4**, 77 (2013).
74. Flaumenhaft, R. Molecular basis of platelet granule secretion. *Arterioscler Thromb Vasc Biol* **23**, 1152-1160 (2003).
75. Michelson, A.D. Thrombin-induced down-regulation of the platelet membrane glycoprotein Ib-IX complex. *Semin Thromb Hemost* **18**, 18-27 (1992).
76. White, J.G. Interaction of membrane systems in blood platelets. *Am J Pathol* **66**, 295-312 (1972).
77. White, J.G. Effects of colchicine and vinca alkaloids on human platelets. II. Changes in the dense tubular system and formation of an unusual inclusion in incubated cells. *Am J Pathol* **53**, 447-461 (1968).
78. White, J.G. Effects of colchicine and Vinca alkaloids on human platelets. I. Influence on platelet microtubules and contractile function. *Am J Pathol* **53**, 281-291 (1968).
79. White, J.G. & Estensen, R.D. Degranulation of discoid platelets. *Am J Pathol* **68**, 289-302 (1972).
80. Harrison, P. & Cramer, E.M. Platelet alpha-granules. *Blood Rev* **7**, 52-62 (1993).
81. Fletcher, D.A. & Mullins, R.D. Cell mechanics and the cytoskeleton. *Nature* **463**, 485-492 (2010).
82. Alberts, B.J., A; Lewis, J. . *Molecular Biology of the Cell*, (Garland Science, 2007).
83. Weisenberg, R.C. Microtubule formation in vitro in solutions containing low calcium concentrations. *Science* **177**, 1104-1105 (1972).
84. Chretien, D., Metoz, F., Verde, F., Karsenti, E. & Wade, R.H. Lattice defects in microtubules: protofilament numbers vary within individual microtubules. *J Cell Biol* **117**, 1031-1040 (1992).
85. Desai, A. & Mitchison, T.J. Microtubule polymerization dynamics. *Annu Rev Cell Dev Biol* **13**, 83-117 (1997).
86. Patel-Hett, S.*, et al.* Visualization of microtubule growth in living platelets reveals a dynamic marginal band with multiple microtubules. *Blood* **111**, 4605-4616 (2008).
87. Walker, R.A.*, et al.* Dynamic instability of individual microtubules analyzed by video light microscopy: rate constants and transition frequencies. *J Cell Biol* **107**, 1437-1448 (1988).
88. Mitchison, T. & Kirschner, M. Dynamic instability of microtubule growth. *Nature* **312**, 237-242 (1984).
89. Song, Y. & Brady, S.T. Post-translational modifications of tubulin: pathways to functional diversity of microtubules. *Trends Cell Biol* **25**, 125-136 (2015).
90. Kalebic, N.*, et al.* alphaTAT1 is the major alpha-tubulin acetyltransferase in mice. *Nat Commun* **4**, 1962 (2013).

91. Perdiz, D., Mackeh, R., Pous, C. & Baillet, A. The ins and outs of tubulin acetylation: more than just a post-translational modification? *Cell Signal* **23**, 763-771 (2011).
92. Witt, O., Deubzer, H.E., Milde, T. & Oehme, I. HDAC family: What are the cancer relevant targets? *Cancer Lett* **277**, 8-21 (2009).
93. Yang, P.H., Zhang, L., Zhang, Y.J., Zhang, J. & Xu, W.F. HDAC6: physiological function and its selective inhibitors for cancer treatment. *Drug Discov Ther* **7**, 233-242 (2013).
94. Prota, A.E.*, et al.* Structural basis of tubulin tyrosination by tubulin tyrosine ligase. *J Cell Biol* **200**, 259-270 (2013).
95. Vale, R.D. The molecular motor toolbox for intracellular transport. *Cell* **112**, 467-480 (2003).
96. Schwer, H.D.*, et al.* A lineage-restricted and divergent beta-tubulin isoform is essential for the biogenesis, structure and function of blood platelets. *Curr Biol* **11**, 579-586 (2001).
97. Kunishima, S., Nishimura, S., Suzuki, H., Imaizumi, M. & Saito, H. TUBB1 mutation disrupting microtubule assembly impairs proplatelet formation and results in congenital macrothrombocytopenia. *Eur J Haematol* **92**, 276-282 (2014).
98. Breitsprecher, D.*, et al.* Rocket launcher mechanism of collaborative actin assembly defined by single-molecule imaging. *Science* **336**, 1164-1168 (2012).
99. Chesarone, M.A., DuPage, A.G. & Goode, B.L. Unleashing formins to remodel the actin and microtubule cytoskeletons. *Nat Rev Mol Cell Biol* **11**, 62-74 (2010).
100. Pollard, T.D. Regulation of actin filament assembly by Arp2/3 complex and formins. *Annu Rev Biophys Biomol Struct* **36**, 451-477 (2007).
101. Drenckhahn, D. & Pollard, T.D. Elongation of actin filaments is a diffusion-limited reaction at the barbed end and is accelerated by inert macromolecules. *J Biol Chem* **261**, 12754-12758 (1986).
102. McCullough, B.R., Blanchoin, L., Martiel, J.L. & De la Cruz, E.M. Cofilin increases the bending flexibility of actin filaments: implications for severing and cell mechanics. *J Mol Biol* **381**, 550-558 (2008).
103. De La Cruz, E.M.*, et al.* Polymerization and structure of nucleotide-free actin filaments. *J Mol Biol* **295**, 517-526 (2000).
104. Carlier, M.F. & Pantaloni, D. Direct evidence for ADP-Pi-F-actin as the major intermediate in ATP-actin polymerization. Rate of dissociation of Pi from actin filaments. *Biochemistry* **25**, 7789-7792 (1986).
105. Lassing, I. & Lindberg, U. Specific interaction between phosphatidylinositol 4,5-bisphosphate and profilactin. *Nature* **314**, 472-474 (1985).
106. Palmgren, S., Ojala, P.J., Wear, M.A., Cooper, J.A. & Lappalainen, P. Interactions with PIP2, ADP-actin monomers, and capping protein regulate the activity and localization of yeast twinfilin. *J Cell Biol* **155**, 251-260 (2001).
107. Bamburg, J.R. Proteins of the ADF/cofilin family: essential regulators of actin dynamics. *Annu Rev Cell Dev Biol* **15**, 185-230 (1999).
108. Hartwig, J.H. & DeSisto, M. The cytoskeleton of the resting human blood platelet: structure of the membrane skeleton and its attachment to actin filaments. *J Cell Biol* **112**, 407-425 (1991).
109. Tablin, F., Castro, M. & Leven, R.M. Blood platelet formation in vitro. The role of the cytoskeleton in megakaryocyte fragmentation. *J Cell Sci* **97 (Pt 1)**, 59-70 (1990).
110. Hartwig, J.H. Mechanisms of actin rearrangements mediating platelet activation. *J Cell Biol* **118**, 1421-1442 (1992).
111. Paavilainen, V.O., Bertling, E., Falck, S. & Lappalainen, P. Regulation of cytoskeletal dynamics by actin-monomer-binding proteins. *Trends Cell Biol* **14**, 386-394 (2004).
112. Safer, D. & Nachmias, V.T. Beta thymosins as actin binding peptides. *Bioessays* **16**, 473-479 (1994).

113. Rosenberg, S., Stracher, A. & Lucas, R.C. Isolation and characterization of actin and actin-binding protein from human platelets. *J Cell Biol* **91**, 201-211 (1981).
114. Falet, H.*, et al.* A novel interaction between FlnA and Syk regulates platelet ITAM-mediated receptor signaling and function. *J Exp Med* **207**, 1967-1979 (2010).
115. Kovacsovics, T.J. & Hartwig, J.H. Thrombin-induced GPIb-IX centralization on the platelet surface requires actin assembly and myosin II activation. *Blood* **87**, 618-629 (1996).
116. Carlsson, L., Nystrom, L.E., Sundkvist, I., Markey, F. & Lindberg, U. Actin polymerizability is influenced by profilin, a low molecular weight protein in non-muscle cells. *J Mol Biol* **115**, 465-483 (1977).
117. Cooley, L., Verheyen, E. & Ayers, K. chickadee encodes a profilin required for intercellular cytoplasm transport during Drosophila oogenesis. *Cell* **69**, 173-184 (1992).
118. Honore, B., Madsen, P., Andersen, A.H. & Leffers, H. Cloning and expression of a novel human profilin variant, profilin II. *FEBS Lett* **330**, 151-155 (1993).
119. Hu, E., Chen, Z., Fredrickson, T. & Zhu, Y. Molecular cloning and characterization of profilin-3: a novel cytoskeleton-associated gene expressed in rat kidney and testes. *Exp Nephrol* **9**, 265-274 (2001).
120. Obermann, H.*, et al.* Novel testis-expressed profilin IV associated with acrosome biogenesis and spermatid elongation. *Mol Hum Reprod* **11**, 53-64 (2005).
121. Lambrechts, A.*, et al.* Profilin II is alternatively spliced, resulting in profilin isoforms that are differentially expressed and have distinct biochemical properties. *Mol Cell Biol* **20**, 8209-8219 (2000).
122. Rothkegel, M.*, et al.* Plant and animal profilins are functionally equivalent and stabilize microfilaments in living animal cells. *J Cell Sci* **109 (Pt 1)**, 83-90 (1996).
123. Witke, W. The role of profilin complexes in cell motility and other cellular processes. *Trends Cell Biol* **14**, 461-469 (2004).
124. Metzler, W.J., Bell, A.J., Ernst, E., Lavoie, T.B. & Mueller, L. Identification of the poly-L-proline-binding site on human profilin. *J Biol Chem* **269**, 4620-4625 (1994).
125. Mahoney, N.M., Rozwarski, D.A., Fedorov, E., Fedorov, A.A. & Almo, S.C. Profilin binds proline-rich ligands in two distinct amide backbone orientations. *Nat Struct Biol* **6**, 666-671 (1999).
126. Goldschmidt-Clermont, P.J.*, et al.* The control of actin nucleotide exchange by thymosin beta 4 and profilin. A potential regulatory mechanism for actin polymerization in cells. *Mol Biol Cell* **3**, 1015-1024 (1992).
127. Pring, M., Weber, A. & Bubb, M.R. Profilin-actin complexes directly elongate actin filaments at the barbed end. *Biochemistry* **31**, 1827-1836 (1992).
128. Pantaloni, D. & Carlier, M.F. How profilin promotes actin filament assembly in the presence of thymosin beta 4. *Cell* **75**, 1007-1014 (1993).
129. Southwick, F.S. & Young, C.L. The actin released from profilin--actin complexes is insufficient to account for the increase in F-actin in chemoattractant-stimulated polymorphonuclear leukocytes. *J Cell Biol* **110**, 1965-1973 (1990).
130. Goldschmidt-Clermont, P.J., Machesky, L.M., Baldassare, J.J. & Pollard, T.D. The actin-binding protein profilin binds to PIP2 and inhibits its hydrolysis by phospholipase C. *Science* **247**, 1575-1578 (1990).
131. Goldschmidt-Clermont, P.J., Kim, J.W., Machesky, L.M., Rhee, S.G. & Pollard, T.D. Regulation of phospholipase C-gamma 1 by profilin and tyrosine phosphorylation. *Science* **251**, 1231-1233 (1991).
132. Witke, W.*, et al.* In mouse brain profilin I and profilin II associate with regulators of the endocytic pathway and actin assembly. *EMBO J* **17**, 967-976 (1998).
133. Auerbuch, V., Loureiro, J.J., Gertler, F.B., Theriot, J.A. & Portnoy, D.A. Ena/VASP proteins contribute to Listeria monocytogenes pathogenesis by controlling temporal

and spatial persistence of bacterial actin-based motility. *Mol Microbiol* **49**, 1361-1375 (2003).
134. Suetsugu, S., Miki, H. & Takenawa, T. Distinct roles of profilin in cell morphological changes: microspikes, membrane ruffles, stress fibers, and cytokinesis. *FEBS Lett* **457**, 470-474 (1999).
135. Suetsugu, S., Miki, H. & Takenawa, T. The essential role of profilin in the assembly of actin for microspike formation. *EMBO J* **17**, 6516-6526 (1998).
136. Ramesh, N., Anton, I.M., Hartwig, J.H. & Geha, R.S. WIP, a protein associated with wiskott-aldrich syndrome protein, induces actin polymerization and redistribution in lymphoid cells. *Proc Natl Acad Sci U S A* **94**, 14671-14676 (1997).
137. Verheyen, E.M. & Cooley, L. Profilin mutations disrupt multiple actin-dependent processes during Drosophila development. *Development* **120**, 717-728 (1994).
138. Witke, W., Sutherland, J.D., Sharpe, A., Arai, M. & Kwiatkowski, D.J. Profilin I is essential for cell survival and cell division in early mouse development. *Proc Natl Acad Sci U S A* **98**, 3832-3836 (2001).
139. Lambrechts, A.*, et al.* Profilin-I-ligand interactions influence various aspects of neuronal differentiation. *J Cell Sci* **119**, 1570-1578 (2006).
140. Bottcher, R.T.*, et al.* Profilin 1 is required for abscission during late cytokinesis of chondrocytes. *EMBO J* **28**, 1157-1169 (2009).
141. Beeler, J.F., LaRochelle, W.J., Chedid, M., Tronick, S.R. & Aaronson, S.A. Prokaryotic expression cloning of a novel human tyrosine kinase. *Mol Cell Biol* **14**, 982-988 (1994).
142. Beeler, J.F., Patel, B.K., Chedid, M. & LaRochelle, W.J. Cloning and characterization of the mouse homolog of the human A6 gene. *Gene* **193**, 31-37 (1997).
143. Rohwer, A., Kittstein, W., Marks, F. & Gschwendt, M. Cloning, expression and characterization of an A6-related protein. *Eur J Biochem* **263**, 518-525 (1999).
144. Goode, B.L., Drubin, D.G. & Lappalainen, P. Regulation of the cortical actin cytoskeleton in budding yeast by twinfilin, a ubiquitous actin monomer-sequestering protein. *J Cell Biol* **142**, 723-733 (1998).
145. Palmgren, S., Vartiainen, M. & Lappalainen, P. Twinfilin, a molecular mailman for actin monomers. *J Cell Sci* **115**, 881-886 (2002).
146. Poukkula, M., Kremneva, E., Serlachius, M. & Lappalainen, P. Actin-depolymerizing factor homology domain: a conserved fold performing diverse roles in cytoskeletal dynamics. *Cytoskeleton (Hoboken)* **68**, 471-490 (2011).
147. Paavilainen, V.O.*, et al.* Structural conservation between the actin monomer-binding sites of twinfilin and actin-depolymerizing factor (ADF)/cofilin. *J Biol Chem* **277**, 43089-43095 (2002).
148. Vartiainen, M.K., Sarkkinen, E.M., Matilainen, T., Salminen, M. & Lappalainen, P. Mammals have two twinfilin isoforms whose subcellular localizations and tissue distributions are differentially regulated. *J Biol Chem* **278**, 34347-34355 (2003).
149. Nevalainen, E.M., Skwarek-Maruszewska, A., Braun, A., Moser, M. & Lappalainen, P. Two biochemically distinct and tissue-specific twinfilin isoforms are generated from the mouse Twf2 gene by alternative promoter usage. *Biochem J* **417**, 593-600 (2009).
150. Nevalainen, E.M.*, et al.* Twinfilin-2a is dispensable for mouse development. *PLoS One* **6**, e22894 (2011).
151. Ojala, P.J.*, et al.* The two ADF-H domains of twinfilin play functionally distinct roles in interactions with actin monomers. *Mol Biol Cell* **13**, 3811-3821 (2002).
152. Helfer, E.*, et al.* Mammalian twinfilin sequesters ADP-G-actin and caps filament barbed ends: implications in motility. *EMBO J* **25**, 1184-1195 (2006).
153. Falck, S.*, et al.* Biological role and structural mechanism of twinfilin-capping protein interaction. *EMBO J* **23**, 3010-3019 (2004).

154. Carlier, M.F., *et al.* Actin depolymerizing factor (ADF/cofilin) enhances the rate of filament turnover: implication in actin-based motility. *J Cell Biol* **136**, 1307-1322 (1997).
155. Moseley, J.B., *et al.* Twinfilin is an actin-filament-severing protein and promotes rapid turnover of actin structures in vivo. *J Cell Sci* **119**, 1547-1557 (2006).
156. Wahlstrom, G., *et al.* Twinfilin is required for actin-dependent developmental processes in Drosophila. *J Cell Biol* **155**, 787-796 (2001).
157. Balduini, C.L., Pecci, A. & Savoia, A. Recent advances in the understanding and management of MYH9-related inherited thrombocytopenias. *Br J Haematol* **154**, 161-174 (2011).
158. Vicente-Manzanares, M., Ma, X., Adelstein, R.S. & Horwitz, A.R. Non-muscle myosin II takes centre stage in cell adhesion and migration. *Nat Rev Mol Cell Biol* **10**, 778-790 (2009).
159. Clark, K., *et al.* TRPM7 regulates myosin IIA filament stability and protein localization by heavy chain phosphorylation. *J Mol Biol* **378**, 790-803 (2008).
160. Ikebe, M. & Hartshorne, D.J. Reverse reaction of smooth muscle myosin light chain kinase. Formation of ATP from phosphorylated light chain plus ADP. *J Biol Chem* **261**, 8249-8253 (1986).
161. Ikebe, M., Hartshorne, D.J. & Elzinga, M. Identification, phosphorylation, and dephosphorylation of a second site for myosin light chain kinase on the 20,000-dalton light chain of smooth muscle myosin. *J Biol Chem* **261**, 36-39 (1986).
162. Even-Faitelson, L. & Ravid, S. PAK1 and aPKCzeta regulate myosin II-B phosphorylation: a novel signaling pathway regulating filament assembly. *Mol Biol Cell* **17**, 2869-2881 (2006).
163. Dulyaninova, N.G., Malashkevich, V.N., Almo, S.C. & Bresnick, A.R. Regulation of myosin-IIA assembly and Mts1 binding by heavy chain phosphorylation. *Biochemistry* **44**, 6867-6876 (2005).
164. Swenson, A.M., *et al.* Magnesium modulates actin binding and ADP release in myosin motors. *J Biol Chem* **289**, 23977-23991 (2014).
165. de Baaij, J.H., Hoenderop, J.G. & Bindels, R.J. Magnesium in man: implications for health and disease. *Physiol Rev* **95**, 1-46 (2015).
166. Paravicini, T.M., Chubanov, V. & Gudermann, T. TRPM7: a unique channel involved in magnesium homeostasis. *Int J Biochem Cell Biol* **44**, 1381-1384 (2012).
167. Mei, Z.Z., Xia, R., Beech, D.J. & Jiang, L.H. Intracellular coiled-coil domain engaged in subunit interaction and assembly of melastatin-related transient receptor potential channel 2. *J Biol Chem* **281**, 38748-38756 (2006).
168. Clapham, D.E. TRP channels as cellular sensors. *Nature* **426**, 517-524 (2003).
169. Runnels, L.W., Yue, L. & Clapham, D.E. TRP-PLIK, a bifunctional protein with kinase and ion channel activities. *Science* **291**, 1043-1047 (2001).
170. Monteilh-Zoller, M.K., *et al.* TRPM7 provides an ion channel mechanism for cellular entry of trace metal ions. *J Gen Physiol* **121**, 49-60 (2003).
171. Bae, C.Y. & Sun, H.S. TRPM7 in cerebral ischemia and potential target for drug development in stroke. *Acta Pharmacol Sin* **32**, 725-733 (2011).
172. Jin, J., *et al.* Deletion of Trpm7 disrupts embryonic development and thymopoiesis without altering Mg2+ homeostasis. *Science* **322**, 756-760 (2008).
173. Ryazanova, L.V., *et al.* TRPM7 is essential for Mg(2+) homeostasis in mammals. *Nat Commun* **1**, 109 (2010).
174. Kaitsuka, T., *et al.* Inactivation of TRPM7 kinase activity does not impair its channel function in mice. *Sci Rep* **4**, 5718 (2014).
175. Desai, B.N., *et al.* Cleavage of TRPM7 releases the kinase domain from the ion channel and regulates its participation in Fas-induced apoptosis. *Dev Cell* **22**, 1149-1162 (2012).

176. Nunez-Villena, F.*, et al.* Increased expression of the transient receptor potential melastatin 7 channel is critically involved in lipopolysaccharide-induced reactive oxygen species-mediated neuronal death. *Antioxid Redox Signal* **15**, 2425-2438 (2011).
177. Liu, W.*, et al.* TRPM7 regulates gastrulation during vertebrate embryogenesis. *Dev Biol* **350**, 348-357 (2011).
178. Jin, J.*, et al.* The channel kinase, TRPM7, is required for early embryonic development. *Proc Natl Acad Sci U S A* **109**, E225-233 (2012).
179. Sah, R.*, et al.* Ion channel-kinase TRPM7 is required for maintaining cardiac automaticity. *Proc Natl Acad Sci U S A* **110**, E3037-3046 (2013).
180. Sah, R.*, et al.* Timing of myocardial trpm7 deletion during cardiogenesis variably disrupts adult ventricular function, conduction, and repolarization. *Circulation* **128**, 101-114 (2013).
181. Abed, E. & Moreau, R. Importance of melastatin-like transient receptor potential 7 and magnesium in the stimulation of osteoblast proliferation and migration by platelet-derived growth factor. *Am J Physiol Cell Physiol* **297**, C360-368 (2009).
182. Deason-Towne, F., Perraud, A.L. & Schmitz, C. The Mg2+ transporter MagT1 partially rescues cell growth and Mg2+ uptake in cells lacking the channel-kinase TRPM7. *FEBS Lett* **585**, 2275-2278 (2011).
183. Schmitz, C.*, et al.* Regulation of vertebrate cellular Mg2+ homeostasis by TRPM7. *Cell* **114**, 191-200 (2003).
184. Su, L.T.*, et al.* TRPM7 regulates polarized cell movements. *Biochem J* **434**, 513-521 (2011).
185. Guilbert, A.*, et al.* Transient receptor potential melastatin 7 is involved in oestrogen receptor-negative metastatic breast cancer cells migration through its kinase domain. *Eur J Cancer* **49**, 3694-3707 (2013).
186. Middelbeek, J.*, et al.* TRPM7 is required for breast tumor cell metastasis. *Cancer Res* **72**, 4250-4261 (2012).
187. Spinler, K.R., Shin, J.W., Lambert, M.P. & Discher, D.E. Myosin-II repression favors pre/proplatelets but shear activation generates platelets and fails in macrothrombocytopenia. *Blood* **125**, 525-533 (2015).
188. Favier, R. & Raslova, H. Progress in understanding the diagnosis and molecular genetics of macrothrombocytopenias. *Br J Haematol* (2015).
189. Visser, D., Middelbeek, J., van Leeuwen, F.N. & Jalink, K. Function and regulation of the channel-kinase TRPM7 in health and disease. *Eur J Cell Biol* **93**, 455-465 (2014).
190. Coombes, E.*, et al.* Pathophysiologically relevant levels of hydrogen peroxide induce glutamate-independent neurodegeneration that involves activation of transient receptor potential melastatin 7 channels. *Antioxid Redox Signal* **14**, 1815-1827 (2011).
191. Du, J.*, et al.* TRPM7-mediated Ca2+ signals confer fibrogenesis in human atrial fibrillation. *Circ Res* **106**, 992-1003 (2010).
192. Thrasher, A.J. & Burns, S.O. WASP: a key immunological multitasker. *Nat Rev Immunol* **10**, 182-192 (2010).
193. Villa, A.*, et al.* X-linked thrombocytopenia and Wiskott-Aldrich syndrome are allelic diseases with mutations in the WASP gene. *Nat Genet* **9**, 414-417 (1995).
194. Symons, M.*, et al.* Wiskott-Aldrich syndrome protein, a novel effector for the GTPase CDC42Hs, is implicated in actin polymerization. *Cell* **84**, 723-734 (1996).
195. de la Fuente, M.A.*, et al.* WIP is a chaperone for Wiskott-Aldrich syndrome protein (WASP). *Proc Natl Acad Sci U S A* **104**, 926-931 (2007).
196. Falet, H.*, et al.* Platelet-associated IgAs and impaired GPVI responses in platelets lacking WIP. *Blood* **114**, 4729-4737 (2009).
197. Snapper, S.B.*, et al.* Wiskott-Aldrich syndrome protein-deficient mice reveal a role for WASP in T but not B cell activation. *Immunity* **9**, 81-91 (1998).

198. Lanzi, G.*, et al.* A novel primary human immunodeficiency due to deficiency in the WASP-interacting protein WIP. *J Exp Med* **209**, 29-34 (2012).
199. Curcio, C.*, et al.* WIP null mice display a progressive immunological disorder that resembles Wiskott-Aldrich syndrome. *J Pathol* **211**, 67-75 (2007).
200. Seri, M.*, et al.* Mutations in MYH9 result in the May-Hegglin anomaly, and Fechtner and Sebastian syndromes. The May-Heggllin/Fechtner Syndrome Consortium. *Nat Genet* **26**, 103-105 (2000).
201. Matsushita, T.*, et al.* Targeted disruption of mouse ortholog of the human MYH9 responsible for macrothrombocytopenia with different organ involvement: hematological, nephrological, and otological studies of heterozygous KO mice. *Biochem Biophys Res Commun* **325**, 1163-1171 (2004).
202. Leon, C.*, et al.* Megakaryocyte-restricted MYH9 inactivation dramatically affects hemostasis while preserving platelet aggregation and secretion. *Blood* **110**, 3183-3191 (2007).
203. Kunishima, S., Hamaguchi, M. & Saito, H. Differential expression of wild-type and mutant NMMHC-IIA polypeptides in blood cells suggests cell-specific regulation mechanisms in MYH9 disorders. *Blood* **111**, 3015-3023 (2008).
204. Pecci, A.*, et al.* Position of nonmuscle myosin heavy chain IIA (NMMHC-IIA) mutations predicts the natural history of MYH9-related disease. *Hum Mutat* **29**, 409-417 (2008).
205. Zhang, Y.*, et al.* Mouse models of MYH9-related disease: mutations in nonmuscle myosin II-A. *Blood* **119**, 238-250 (2012).
206. Chen, Y.*, et al.* The abnormal proplatelet formation in MYH9-related macrothrombocytopenia results from an increased actomyosin contractility and is rescued by myosin IIA inhibition. *J Thromb Haemost* **11**, 2163-2175 (2013).
207. Ruggeri, Z.M. Von Willebrand factor, platelets and endothelial cell interactions. *J Thromb Haemost* **1**, 1335-1342 (2003).
208. Turitto, V.T.M., R.; Baumgartner, H.R. Physical factors influencing platelet deposition on subendothelium: Importance of blood shear rate. in *The Behavior of Blood and its Components at Interfaces*, Vol. 283 (ed. Vroman, L.L., E.) 284-292 (Annals of the New York Academy of Sciences, New York, 1977).
209. Ruggeri, Z.M., Orje, J.N., Habermann, R., Federici, A.B. & Reininger, A.J. Activation-independent platelet adhesion and aggregation under elevated shear stress. *Blood* **108**, 1903-1910 (2006).
210. Canobbio, I., Balduini, C. & Torti, M. Signalling through the platelet glycoprotein Ib-V-IX complex. *Cell Signal* **16**, 1329-1344 (2004).
211. Varga-Szabo, D., Pleines, I. & Nieswandt, B. Cell adhesion mechanisms in platelets. *Arteriosclerosis, thrombosis, and vascular biology* **28**, 403-412 (2008).
212. Nieswandt, B. & Watson, S.P. Platelet-collagen interaction: is GPVI the central receptor? *Blood* **102**, 449-461 (2003).
213. Watson, S.P., Herbert, J.M. & Pollitt, A.Y. GPVI and CLEC-2 in hemostasis and vascular integrity. *J Thromb Haemost* **8**, 1456-1467 (2010).
214. Dutting, S., Bender, M. & Nieswandt, B. Platelet GPVI: a target for antithrombotic therapy?! *Trends Pharmacol Sci* **33**, 583-590 (2012).
215. Varga-Szabo, D., Braun, A. & Nieswandt, B. Calcium signaling in platelets. *J Thromb Haemost* **7**, 1057-1066 (2009).
216. Harper, M.T. & Poole, A.W. Diverse functions of protein kinase C isoforms in platelet activation and thrombus formation. *J Thromb Haemost* **8**, 454-462 (2010).
217. Spalton, J.C.*, et al.* The novel Syk inhibitor R406 reveals mechanistic differences in the initiation of GPVI and CLEC-2 signaling in platelets. *J Thromb Haemost* **7**, 1192-1199 (2009).
218. Lorenz, V.*, et al.* Targeted downregulation of platelet CLEC-2 occurs through Syk-independent internalization. *Blood* (2015).

219. Coughlin, S.R. Thrombin signalling and protease-activated receptors. *Nature* **407**, 258-264 (2000).
220. Sambrano, G.R., Weiss, E.J., Zheng, Y.W., Huang, W. & Coughlin, S.R. Role of thrombin signalling in platelets in haemostasis and thrombosis. *Nature* **413**, 74-78 (2001).
221. Offermanns, S. Activation of platelet function through G protein-coupled receptors. *Circ Res* **99**, 1293-1304 (2006).
222. Offermanns, S., Toombs, C.F., Hu, Y.H. & Simon, M.I. Defective platelet activation in G alpha(q)-deficient mice. *Nature* **389**, 183-186 (1997).
223. Badolia, R., Manne, B.K., Dangelmaier, C., Chernoff, J. & Kunapuli, S.P. Gq-mediated Akt translocation to the membrane: a novel PIP3-independent mechanism in platelets. *Blood* **125**, 175-184 (2015).
224. Hart, M.J.*, et al.* Direct stimulation of the guanine nucleotide exchange activity of p115 RhoGEF by Galpha13. *Science* **280**, 2112-2114 (1998).
225. Cantley, L.C. The phosphoinositide 3-kinase pathway. *Science* **296**, 1655-1657 (2002).
226. Clapham, D.E. & Neer, E.J. G protein beta gamma subunits. *Annu Rev Pharmacol Toxicol* **37**, 167-203 (1997).
227. Yang, J.*, et al.* Loss of signaling through the G protein, Gz, results in abnormal platelet activation and altered responses to psychoactive drugs. *Proc Natl Acad Sci U S A* **97**, 9984-9989 (2000).
228. Butenas, S., Orfeo, T. & Mann, K.G. Tissue factor in coagulation: Which? Where? When? *Arterioscler Thromb Vasc Biol* **29**, 1989-1996 (2009).
229. Geddings, J.E. & Mackman, N. New players in haemostasis and thrombosis. *Thromb Haemost* **111**, 570-574 (2014).
230. Fox, J.E. The platelet cytoskeleton. *Thromb Haemost* **70**, 884-893 (1993).
231. Jackson, S.P. The growing complexity of platelet aggregation. *Blood* **109**, 5087-5095 (2007).
232. Sachs, U.J. & Nieswandt, B. In vivo thrombus formation in murine models. *Circ Res* **100**, 979-991 (2007).
233. Shattil, S.J. & Newman, P.J. Integrins: dynamic scaffolds for adhesion and signaling in platelets. *Blood* **104**, 1606-1615 (2004).
234. Nieswandt, B., Varga-Szabo, D. & Elvers, M. Integrins in platelet activation. *J Thromb Haemost* **7 Suppl 1**, 206-209 (2009).
235. Calderwood, D.A., Campbell, I.D. & Critchley, D.R. Talins and kindlins: partners in integrin-mediated adhesion. *Nat Rev Mol Cell Biol* **14**, 503-517 (2013).
236. Nieswandt, B.*, et al.* Loss of talin1 in platelets abrogates integrin activation, platelet aggregation, and thrombus formation in vitro and in vivo. *J Exp Med* **204**, 3113-3118 (2007).
237. Tadokoro, S.*, et al.* Talin binding to integrin beta tails: a final common step in integrin activation. *Science* **302**, 103-106 (2003).
238. Han, J.*, et al.* Reconstructing and deconstructing agonist-induced activation of integrin alphaIIbbeta3. *Curr Biol* **16**, 1796-1806 (2006).
239. Moser, M., Nieswandt, B., Ussar, S., Pozgajova, M. & Fassler, R. Kindlin-3 is essential for integrin activation and platelet aggregation. *Nat Med* **14**, 325-330 (2008).
240. Lee, H.S., Lim, C.J., Puzon-McLaughlin, W., Shattil, S.J. & Ginsberg, M.H. RIAM activates integrins by linking talin to ras GTPase membrane-targeting sequences. *J Biol Chem* **284**, 5119-5127 (2009).
241. Watanabe, N.*, et al.* Mechanisms and consequences of agonist-induced talin recruitment to platelet integrin alphaIIbbeta3. *J Cell Biol* **181**, 1211-1222 (2008).
242. Wynne, J.P.*, et al.* Rap1-interacting adapter molecule (RIAM) associates with the plasma membrane via a proximity detector. *J Cell Biol* **199**, 317-330 (2012).

243. Chrzanowska-Wodnicka, M., Smyth, S.S., Schoenwaelder, S.M., Fischer, T.H. & White, G.C., 2nd. Rap1b is required for normal platelet function and hemostasis in mice. *J Clin Invest* **115**, 680-687 (2005).
244. Krause, M.*, et al.* Lamellipodin, an Ena/VASP ligand, is implicated in the regulation of lamellipodial dynamics. *Dev Cell* **7**, 571-583 (2004).
245. Lafuente, E.M.*, et al.* RIAM, an Ena/VASP and Profilin ligand, interacts with Rap1-GTP and mediates Rap1-induced adhesion. *Dev Cell* **7**, 585-595 (2004).
246. Ermekova, K.S.*, et al.* The WW domain of neural protein FE65 interacts with proline-rich motifs in Mena, the mammalian homolog of Drosophila enabled. *J Biol Chem* **272**, 32869-32877 (1997).
247. Stritt, S.*, et al.* Rap1-GTP-interacting adaptor molecule (RIAM) is dispensable for platelet integrin activation and function in mice. *Blood* **125**, 219-222 (2015).
248. Jenzora, A., Behrendt, B., Small, J.V., Wehland, J. & Stradal, T.E. PREL1 provides a link from Ras signalling to the actin cytoskeleton via Ena/VASP proteins. *FEBS Lett* **579**, 455-463 (2005).
249. Patsoukis, N.*, et al.* RIAM regulates the cytoskeletal distribution and activation of PLC-gamma1 in T cells. *Sci Signal* **2**, ra79 (2009).
250. Yang, J.*, et al.* Conformational activation of talin by RIAM triggers integrin-mediated cell adhesion. *Nat Commun* **5**, 5880 (2014).
251. Shattil, S.J., Kim, C. & Ginsberg, M.H. The final steps of integrin activation: the end game. *Nat Rev Mol Cell Biol* **11**, 288-300 (2010).
252. Hernandez-Varas, P.*, et al.* Rap1-GTP-interacting adaptor molecule (RIAM) protein controls invasion and growth of melanoma cells. *J Biol Chem* **286**, 18492-18504 (2011).
253. Nieswandt, B.*, et al.* Acute systemic reaction and lung alterations induced by an antiplatelet integrin gpIIb/IIIa antibody in mice. *Blood* **94**, 684-693 (1999).
254. Nieswandt, B., Bergmeier, W., Rackebrandt, K., Gessner, J.E. & Zirngibl, H. Identification of critical antigen-specific mechanisms in the development of immune thrombocytopenic purpura in mice. *Blood* **96**, 2520-2527 (2000).
255. Bergmeier, W.*, et al.* Flow cytometric detection of activated mouse integrin alphaIIbbeta3 with a novel monoclonal antibody. *Cytometry* **48**, 80-86 (2002).
256. Massberg, S.*, et al.* A crucial role of glycoprotein VI for platelet recruitment to the injured arterial wall in vivo. *The Journal of experimental medicine* **197**, 41-49 (2003).
257. Nieswandt, B.*, et al.* Long-term antithrombotic protection by in vivo depletion of platelet glycoprotein VI in mice. *The Journal of experimental medicine* **193**, 459-469 (2001).
258. May, F.*, et al.* CLEC-2 is an essential platelet-activating receptor in hemostasis and thrombosis. *Blood* **114**, 3464-3472 (2009).
259. Hofmann, S., Vogtle, T., Bender, M., Rose-John, S. & Nieswandt, B. The SLAM family member CD84 is regulated by ADAM10 and calpain in platelets. *J Thromb Haemost* **10**, 2581-2592 (2012).
260. Unkeless, J.C. Characterization of a monoclonal antibody directed against mouse macrophage and lymphocyte Fc receptors. *The Journal of experimental medicine* **150**, 580-596 (1979).
261. Tiedt, R., Schomber, T., Hao-Shen, H. & Skoda, R.C. Pf4-Cre transgenic mice allow the generation of lineage-restricted gene knockouts for studying megakaryocyte and platelet function in vivo. *Blood* **109**, 1503-1506 (2007).
262. Anton, I.M.*, et al.* WIP deficiency reveals a differential role for WIP and the actin cytoskeleton in T and B cell activation. *Immunity* **16**, 193-204 (2002).
263. Falet, H., Hoffmeister, K., Neujahr, R. & Hartwig, J. Normal Arp2/3 complex activation in platelets lacking WASp. *Blood* **100**, 2113-2122 (2002).
264. Rosenbaum, J. Cytoskeleton: functions for tubulin modifications at last. *Current biology : CB* **10**, R801-803 (2000).

265. Pollard, T. & Borisy, G. Cellular motility driven by assembly and disassembly of actin filaments. *Cell* **112**, 453-465 (2003).
266. Bender, M.*, et al.* ADF/n-cofilin-dependent actin turnover determines platelet formation and sizing. *Blood* **116**, 1767-1775 (2010).
267. Diagouraga, B.*, et al.* Motor-driven marginal band coiling promotes cell shape change during platelet activation. *The Journal of cell biology* **204**, 177-185 (2014).
268. Yamada, M.*, et al.* Determination of carrier status for the Wiskott-Aldrich syndrome by flow cytometric analysis of Wiskott-Aldrich syndrome protein expression in peripheral blood mononuclear cells. *J Immunol* **165**, 1119-1122 (2000).
269. Monroe, D.M., Hoffman, M. & Roberts, H.R. Platelets and thrombin generation. *Arterioscler Thromb Vasc Biol* **22**, 1381-1389 (2002).
270. Munnix, I.C.*, et al.* Segregation of platelet aggregatory and procoagulant microdomains in thrombus formation: regulation by transient integrin activation. *Arterioscler Thromb Vasc Biol* **27**, 2484-2490 (2007).
271. Cosemans, J.M., Iserbyt, B.F., Deckmyn, H. & Heemskerk, J.W. Multiple ways to switch platelet integrins on and off. *J Thromb Haemost* **6**, 1253-1261 (2008).
272. Mattheij, N.J.*, et al.* Dual mechanism of integrin alphaIIbbeta3 closure in procoagulant platelets. *J Biol Chem* **288**, 13325-13336 (2013).
273. Critchley, D.R. Biochemical and structural properties of the integrin-associated cytoskeletal protein talin. *Annu Rev Biophys* **38**, 235-254 (2009).
274. Lenter, M.*, et al.* A monoclonal antibody against an activation epitope on mouse integrin chain beta 1 blocks adhesion of lymphocytes to the endothelial integrin alpha 6 beta 1. *Proceedings of the National Academy of Sciences of the United States of America* **90**, 9051-9055 (1993).
275. Crittenden, J.R.*, et al.* CalDAG-GEFI integrates signaling for platelet aggregation and thrombus formation. *Nature medicine* **10**, 982-986 (2004).
276. Colo, G.P.*, et al.* Focal adhesion disassembly is regulated by a RIAM to MEK-1 pathway. *Journal of cell science* **125**, 5338-5352 (2012).
277. Nishikimi, A.*, et al.* Sequential regulation of DOCK2 dynamics by two phospholipids during neutrophil chemotaxis. *Science* **324**, 384-387 (2009).
278. Clark, K.*, et al.* TRPM7, a novel regulator of actomyosin contractility and cell adhesion. *EMBO J* **25**, 290-301 (2006).
279. Houk, A.R.*, et al.* Membrane tension maintains cell polarity by confining signals to the leading edge during neutrophil migration. *Cell* **148**, 175-188 (2012).
280. Shin, J.W., Swift, J., Spinler, K.R. & Discher, D.E. Myosin-II inhibition and soft 2D matrix maximize multinucleation and cellular projections typical of platelet-producing megakaryocytes. *Proc Natl Acad Sci U S A* **108**, 11458-11463 (2011).
281. Cai, Y.*, et al.* Nonmuscle myosin IIA-dependent force inhibits cell spreading and drives F-actin flow. *Biophys J* **91**, 3907-3920 (2006).
282. Shalev, H., Phillip, M., Galil, A., Carmi, R. & Landau, D. Clinical presentation and outcome in primary familial hypomagnesaemia. *Arch Dis Child* **78**, 127-130 (1998).
283. Kuijpers, T.W.*, et al.* LAD-1/variant syndrome is caused by mutations in FERMT3. *Blood* **113**, 4740-4746 (2009).
284. Kunishima, S.*, et al.* ACTN1 mutations cause congenital macrothrombocytopenia. *Am J Hum Genet* **92**, 431-438 (2013).
285. Kwan, S.P., Hagemann, T.L., Blaese, R.M., Knutsen, A. & Rosen, F.S. Scanning of the Wiskott-Aldrich syndrome (WAS) gene: identification of 18 novel alterations including a possible mutation hotspot at Arg86 resulting in thrombocytopenia, a mild WAS phenotype. *Hum Mol Genet* **4**, 1995-1998 (1995).
286. Nurden, P.*, et al.* Thrombocytopenia resulting from mutations in filamin A can be expressed as an isolated syndrome. *Blood* **118**, 5928-5937 (2011).

287. Shcherbina, A.*, et al.* WASP plays a novel role in regulating platelet responses dependent on alphaIIbbeta3 integrin outside-in signalling. *Br J Haematol* **148**, 416-427 (2010).
288. Palazzo, A.F., Cook, T.A., Alberts, A.S. & Gundersen, G.G. mDia mediates Rho-regulated formation and orientation of stable microtubules. *Nat Cell Biol* **3**, 723-729 (2001).
289. Law, B.*, et al.* A Direct Interaction between Leucine-rich Repeat Kinase 2 and Specific β-Tubulin Isoforms Regulates Tubulin Acetylation. *The Journal of biological chemistry* **289**, 895-908 (2014).
290. Lin, X.*, et al.* Leucine-rich repeat kinase 2 regulates the progression of neuropathology induced by Parkinson's-disease-related mutant alpha-synuclein. *Neuron* **64**, 807-827 (2009).
291. Sumner, W.T., Monroe, D.M. & Hoffman, M. Variability in platelet procoagulant activity in healthy volunteers. *Thromb Res* **81**, 533-543 (1996).
292. Walsh, P.N. & Lipscomb, M.S. Comparison of the coagulant activities of platelets and phospholipids. *Br J Haematol* **33**, 9-18 (1976).
293. Pleines, I.*, et al.* Defective tubulin organization and proplatelet formation in murine megakaryocytes lacking Rac1 and Cdc42. *Blood* **122**, 3178-3187 (2013).
294. Preciado Lopez, M.*, et al.* Actin-microtubule coordination at growing microtubule ends. *Nat Commun* **5**, 4778 (2014).
295. Poulter, N.S.*, et al.* Platelet actin nodules are podosome-like structures dependent on Wiskott-Aldrich syndrome protein and ARP2/3 complex. *Nat Commun* **6**, 7254 (2015).
296. Thapa, N.*, et al.* Phosphoinositide signaling regulates the exocyst complex and polarized integrin trafficking in directionally migrating cells. *Developmental cell* **22**, 116-130 (2012).
297. Lawson, C.*, et al.* FAK promotes recruitment of talin to nascent adhesions to control cell motility. *The Journal of cell biology* **196**, 223-232 (2012).
298. Kasirer-Friede, A.*, et al.* ADAP interactions with talin and kindlin promote platelet integrin alphaIIbbeta3 activation and stable fibrinogen binding. *Blood* **123**, 3156-3165 (2014).
299. Plow, E.F. & Qin, J. The role of RIAM in platelets put to a test. *Blood* **125**, 207-208 (2015).
300. Chen, Z.*, et al.* The May-Hegglin anomaly gene MYH9 is a negative regulator of platelet biogenesis modulated by the Rho-ROCK pathway. *Blood* **110**, 171-179 (2007).
301. Even-Ram, S.*, et al.* Myosin IIA regulates cell motility and actomyosin-microtubule crosstalk. *Nat Cell Biol* **9**, 299-309 (2007).
302. Deutsch, S.*, et al.* Asp1424Asn MYH9 mutation results in an unstable protein responsible for the phenotypes in May-Hegglin anomaly/Fechtner syndrome. *Blood* **102**, 529-534 (2003).
303. Pecci, A.*, et al.* Pathogenetic mechanisms of hematological abnormalities of patients with MYH9 mutations. *Hum Mol Genet* **14**, 3169-3178 (2005).

7. APPENDIX

7.1. Abbreviations

ACD	Acid citrate dextrose
ADF	Actin depolymerizing factor
ADF-H	ADF-homology domain
ADP	Adenosine diphosphate
AEC	3-amino-9-ethylcarbazole
α	Alpha/ anti
α-TAT1	α-tubulin N-acetyltransferase 1
Akt	Protein kinase B
Ang-1	Angiopoietin-1
Anxa5	Annexin V
Apbb1ip	Amyloid beta (A4) precursor protein binding, family B, member 1
APC	Adenomatous polyposis coli
APS	Ammonium persulfate
Arf	ADP ribosylation factor
Arp2/3	Actin-related proteins 2/3
ARPC	Arp2/3 complex
ASAP1	ArfGAP with SH3 domain, ankyrin repeat and PH domain 1
ATP	Adenosine triphosphate
BC	Bone marrow compartment
β	Beta
BM	Bone marrow
BMC	BM cell
BSA	Bovine serum albumin
BPD	Bleeding and platelet disorders
Ca^{2+}	Calcium cation
CA	Central/acidic domain
CADD	Combined annotation dependent depletion
CalDAG-GEFI	Ca^{2+}-dependent DAG-regulated guanine nucleotide exchange factor
cAMP	Cyclic adenosine diphosphate
CAP	Cyclase-associated protein
CD	Cluster of differentiation
Cdc42	Cell division control protein 42
CIP4	Cdc42 interacting protein 4

CLEC-2	C-type lectin-like type II transmembrane receptor
c-Mpl	Myeloproliferative leukemia virus oncogene
Cof	Cofilin
Colchi	Colchicine
Coll	Collagen
CRISPR	Clustered regularly interspaced short palindromic repeats
CRP	Collagen-related peptide
CP	Capping protein
CVX	Convulxin
CXCL	Chemokine (C-X-C Motif) Ligand
DAG	Diacylglycerol
DAPI	4'-6-Diamidino-2-phenylindole
°C	Degree Celsius
Del	Deletion
DIAPH	Mammalian Diaphanous
DIC	Differential interference contrast
$DiOC_6$ (3)	3,3′-dihexyloxacarbocyanine iodide
DNA	Deoxyribonucleic acid
dNTP	Deoxynucleotide triphosphates
DMEM	Dulbecco's Modified Eagle's Medium
DMS	Demarcation membrane system
DMSO	Dimethylsulfoxide
DPBS	Dulbecco's phosphate-buffered saline
DPFC	Diploid platelet-forming cells
DTS	Closed-channel dense tubular system
EC	Endothelial cell
ECL	Enhanced chemiluminescence
ECM	Extracellular matrix
EDTA	Ethylenediaminetetraacetic acid
e.g.	*Exempli gratia*
EGTA	Ethylene glycol tetraacetic acid
ELC	Essential light chain
ELISA	Enzyme-linked immunosorbent assay
et al	*Et alii*
ETP	Endogenous thrombin potential

F	Coagulation factor
F-actin	Filamentous actin
FasL	Fas-ligand
FCS	Fetal calf serum
FcR	Fc receptor
FGN	Fibrinogen
Fig	Figure
FITC	Fluorescein-isothiocyanate
FIPI	5-fluoro-2-indolyl deschlorohalopemide
FlnA	FilaminA
FN	Fibronectin
FSC	Forward scatter
g	Gravitation force
G-actin	Globular actin
γ-TuRC	γ-tubulin-ring complex
GAPDH	Glycerinaldehyd-3-phosphat-Dehydrogenase
GEF	Guanine nucleotide-exchange factor
GMF	Glia maturation factor
GP	Glycoprotein
GPCR	G-protein coupled receptors
Grb2	Growth factor receptor-bound protein2
gRNA	guide RNA
GTP	Guanosine triphosphate
HCN4	Hyperpolarization activated cyclic nucleotide gated K^+ channel 4
HDAC	Histone deacetylase
HE	Hematoxylin and eosin
HEK	Human embryonic kidney
Hem	Hematopoietic protein
HEPES	N-2-Hydroxyethylpiperazine-N'-2-ethanesulfonic acid
HPO	Human phenotype ontology
HRP	Horseradish peroxidase
HSC	Hematopoietic stem cells
5-HT	5-hydroxytryotamine/ serotonin
Ig	Immunoglobulin
IHC	Immunohistochemistry

IL	Interleukin
IMDM	Iscove's Modified Dulbecco's Media
IMS	Invaginated membrane system
Ins	Insertion
IP	Immunoprecipitation
IP_3	Inositol-1,4,5-triphosphate
IRES	Internal ribosome entry site
ITAM	Immunoreceptor tyrosine-based activation motif
i.v.	Intravenously
kb	Kilo base pairs
kDa	Kilo Dalton
LAT	Linker of activated T-cells
LatA	Latrunculin A
LPR1	Lipid-phosphatase-related protein-1
M/N	Molar
MAPF	microtubule-associated proteins
mDia	Mammalian Diaphanous
MEF	Mouse embryonic fibroblast
Mena	Mammalian Ena orthologue
MEP	MK-erythroid precursor cells
MFI	Mean fluorescence intensity
$[Mg^{2+}]_i$	Intracellular Mg^{2+} concentration
min	Minute
MK	Megakaryocyte
MLC	Myosin light chain
MMP	Matrix metalloproteases
MOPS	3-(N-morpholino) propanesulfonic acid
MRL	Mig-10/RIAM/Lamellipodin family
MT	Microtubule
MTOC	Microtubule-organizing center
MYH	Non-muscle myosin heavy chain
MYH9-RD	MYH9-related disorder/disease
N	Number of chromosome sets
NAD	Nicotinamide adenine dinucleotide
Neo	Neomycin

NIHR	National Institute for Health Research
NMMIIA	Non-muscle myosin IIA
NP-40	Nonidet P-40
OCS	Open canalicular system
Orai1	Ca^{2+} release-activated calcium channel protein 1
ORF	Open reading frame
P	Phosphorylation/ Pellet
PA	Phosphatidic acid
PAA	Polyacrylamide
PAGE	Polyacrylamide gel electrophoresis
PAK	p21/Cdc42/Rac1-activated kinase
PAR	Protease activated receptors
PBMC	Peripheral blood mononuclear cells
PBS	Phosphate buffered saline
PCR	Polymerase chain reaction
PDGF	Platelet-derived growth factor
PE	R-phycoerythrin
PF4	Platelet factor 4
PFA	Paraformaldehyde
Pfn	Profilin
PGI_2	Prostacyclin
PH	Pleckstrin homology domain
P_i	Inorganic phosphate
PI	Propidium iodide/ protease inhibitors
PI3K	Phosphoinositide 3-kinase
PIP_2	Phosphatidylinositol 4,5-bisphosphate
PIP_3	Phosphatidylinositol-3,4,5-trisphosphate
PIPES	Piperazine-N,N′-bis(2-ethanesulfonic acid)
PK	Proteinkinase
PL	Phospholipase
PLP	Poly-L-proline
PMA	Phorbol 12-myristate 13-acetate
PMSF	Phenylmethylsulphonylfluorid
PNK	Polynucleotide kinase
Profilactin	ATP-G-actin bound to Pfn

PRP	Platelet rich plasma
PP	Proplatelet
PPF	Proplatelet-forming
PVDF	Polyvinylidene difluoride
PRP	Platelet-rich plasma
PS	Phosphatidylserine
RA	Ras-association domain
Rac1	Ras-related C3 botulinum toxin substrate 1
Rap1	Ras-proximate-1
RBC	Red blood cell
Rest	Resting
Rhd	Rhodocytin
RhoA	Ras homolog gene family, member A
Rho-GEF	Rho-specific guanine nucleotide exchange factor
Rho-GTPase	Ras-homologue-guanine triphosphatase
RIAM	Rap1-GTP-interacting adaptor molecule
RLC	Regulatory light chain
RNA	Ribonucleic acid
ROCE	Receptor-operated Ca^{2+} entry
ROCK	RhoA kinase
rpm	Rotation per minute
RT	Room temperature
RT-PCR	Reverse transcription polymerase chain reaction
RUNX-1	Runt-Related Transcription Factor 1
S	Soluble
SCF	Stem cell factor
SDF-1α	Stromal cell-derived factor-1α
SDS-PAGE	Sodium dodecyl sulfate polyacrylamide gel electrophoresis
SFFV	Spleen focus-forming virus
SH2	Src-homology 2
SIN	Sinusoidal/ self-inactivating
SIRT	Sirtuin
SLP-76	SH2 domain-containing leukocyte protein of 76 kDa
SN	Supernatant
SOCE	Store-operated Ca^{2+} entry

S1p	Sphingosine 1-phosphate
S1pR1	S1p-receptor 1
STED	Stimulated emission depletion
STIM	Stromal interaction molecule
Syk	Spleen tyrosine kinase
T	Total
TBS	TRIS buffered saline
TEM	Transmission electron microscopy
TEMED	Tetramethylethylenediamine
TF	Tissue factor
TGF-β1	Transforming growth factor-β1
Thpo	Thrombopoietin
Thr	Thrombin
Tks5	Tyrosine kinase substrate with five SH3 domains
Tln-1	Talin-1
TMB	3,3,5,5-tetramethylbenzidine
Tmsb4x	β4-thymosin
TRIS	Tris(hydroxymethyl)aminomethane
TTL	Tubulin-tyrosine kinase
TLLL	TTL-like family member
TRPM7	Transient receptor potential melastatin-like 7
TSA	Trichostatin A
Twf	Twinfilin
TxA_2	Thromboxane A_2
U46	U46619
V	Verproline homology motif
VASP	Vasodilator-stimulated phosphoprotein
VOF	Visual observed field
VS	Vascular sinus
vWF	Von Willebrand factor
WAS	Wiskott-Aldrich syndrome
WASp	Wiskott-Aldrich syndrome protein
WAVE	WASp family verprolin-homologous protein
WIP	WASp-interacting protein
WT	Wild-type

7.2. Acknowledgement

The work presented here was accomplished at the Department of Experimental Biomedicine Vascular Medicine, University Hospital and Rudolf Virchow Center for Experimental Biomedicine, University of Würzburg, in the group of Prof. Dr. Bernhard Nieswandt between August 2012 and July 2015. Some results summarized in this thesis have been published, as indicated in the respective result sections.

Many persons supported me throughout my PhD studies, whom I would like to thank:

My supervisor, Prof. Dr. Bernhard Nieswandt, for giving me the opportunity to pursue my PhD projects in his group, for his critical and valuable scientific input, constant encouragement, ideological and financial support and basing my scientific network and career.

The members of my thesis committee: Prof. Dr. Antje Gohla and Prof. Dr. Manfred Gessler for fruitful discussions and reviewing this thesis.

Drs. Paquita and Alan Nurden and Prof. Dr. Harald Schulze for many valuable discussions, science lessons and for sharing their unlimited scientific knowledge and network with me.

Dr. Attila Braun, Dr. Markus Bender, Dr. Sebastian Dütting and Dr. David Stegner for the numerous valuable discussions, critical input on projects, inspiration, support and joint efforts in various projects.

Dr. Dr. Katharina Remer and all animal care takers for their excellent work - without you many of these studies would not have been possible!

Members and friends of ‘Office 3’: Carsten, Daniela, Deya, Ina, Judith, Kiran, Mari, Michi, Sarah and Viola for critical discussions but also way to many fun moments and making the last three years an unforgettable experience.

Members of ‘Team Twinfilin’: Sarah and ‘Tiny Tim’ for their support, many fun moments and fruitful discussions.

Judith, Karen and Sarah for the fruitful collaborations and support with 2PM microscopy and *in vivo* models of thrombosis.

Dominic, Judith, Karen, Mari, Michi and Sarah for carefully proofreading this thesis.

Birgit, Jonas, Juliana, Steffi, Sylvia for their valuable support, discussions during the morning hours and efforts to keep the lab running.

All present and former members of the Nieswandt lab, who have not been mentioned here by name, but spent their time and shared their knowledge with me, for the excitatory, cooperative and supporting working atmosphere as well as for the great social intercourse and many fun moments besides work.

All patients that agreed (written informed, for sure) to participate in our studies and without whom many results of this thesis would not have been achieved.

All collaborators that have not been mentioned here by name, for their support and valuable contributions to the different studies.

The team of the Graduate School of Life Sciences for organizing and offering the transferable skill courses and the coordination of the PhD study program.

The German Excellence Initiative and the Graduate School of Life Sciences for providing my fellowship that allowed me to attend and participate in scientific conferences, to communicate my research and enabling the numerous site visits to analyze patient samples.

The Bioimaging Centre (Rudolf Virchow Center) for providing technical infrastructure and support and for the numerous and stimulating hours in the cold darkness.

Last, I owe my deepest gratitude and love to my wife Stephi, my parents and my brother who always supported and believed in me. You were, and will always be there when I need you. I owe you everything.

7.3. Publications

7.3.1. Original articles

Stritt S, Nurden P, Favier R, Favier M, Gotru SK, Eeuwijk JMM, Schulze H, Nurden AT, Lambert MP, Turro E, Burger-Stritt S, Matsushita M, Ferioli S, Mittermeier L, Ballerini P, Zierler S, NIHR BioResource, Chubanov V, Laffan MA, Gudermann T, Nieswandt B, Braun A. Defects in TRPM7 channel function result in deregulated thrombopoiesis through altered cellular Mg^{2+} homeostasis and cytoskeletal architecture. *Submitted*.

- **Stritt S***, Nurden P*, Turro E*, Greene D, Jansen SB, Westbury SK, Petersen R, Astle WJ, Marlin S, Bariana TK, Kostadima M, Lentaigne C, Maiwald S, Papadia S, Kelly AM, Stephens JC, Penkett CJ, Ashford S, Tuna S, Austin S, Bakchoul T, Collins P, Favier R, Lambert MP, Mathias M, Millar CM, Mapeta R, Perry DJ, Schulman S, Simeoni I, Thys C, BRIDGE-Bleeding and Platelet Disorders (BPD) Consortium, Gomez K, Erber WN, Stirrups K, Rendon A, Bradley JR, van Geet C, Raymond LC, Laffan MA, Nurden AT, Nieswandt B, Richardson S, Freson K*, Ouwehand WH*, Mumford AD*. A gain-of-function variant in *DIAPH1* causes dominant macrothrombocytopenia and hearing loss. *Submitted*.
  **these authors contributed equally*

- Lorenz V, Stegner D, **Stritt S**, Vögtle T, Kiefer F, Witke W, Schymeinsky J, Watson SP, Walzog B, Nieswandt B. Targeted downregulation of platelet CLEC-2 occurs through Syk-independent internalization. *Blood* 2015; doi: 10.1182/blood-2014-11-611905.
  accompanied by an Inside Blood Commentary

- **Stritt S**, Wolf K, Lorenz V, Vögtle T, Gupta S, Bösl MR, Nieswandt B. Rap1-GTP-interacting adaptor molecule (RIAM) is dispensable for platelet integrin activation and function in mice. *Blood* 2014; doi: 10.1182/blood-2014-08-597542.
  highlighted as plenary paper and accompanied by an Inside Blood Commentary

- Bender M*, **Stritt S***, Nurden P, van Eeuwijk JMM, Zieger B, Kentouche K, Schulze H, Morbach H, Stegner D, Heinze K, Dütting S, Gupta S, Witke W, Falet H, Fischer A, Hartwig JH, Nieswandt B. Megakaryocyte-specific Profilin1-deficiency alters microtubule stability and causes a Wiskott–Aldrich syndrome-like platelet defect. *Nat Commun* 2014; doi: 10.1038/ncomms5746.
  **these authors contributed equally*

- **Stritt S**, Thielmann I, Dütting S, Stegner D, Nieswandt B. Phospholipase D is a central regulator of collagen I-induced cytoskeletal rearrangement and podosome formation in megakaryocytes. *J Thromb Haemost* 2014; doi: 10.1111/jth.12623.

- van Dieck J, Schmid V, Heindl D, Dziadek S, Schraeml M, Gerg M, Massoner P, Engel AM, Tiefenthaler G, Vural S, **Stritt S**, Tetzlaff F, Soukupova M, Kopetzki E, Bossenmaier B, Thomas M, Klein C, Mertens A, Heller A, Tacke M. Development of Bispecific Molecules for the In Situ Detection of Protein-Protein Interactions and Protein Phosphorylation. *Chemistry & Biology* 2014; doi: 10.1016/j.chembiol.2013.12.018.

7.3.2. Research commentaries

- Nieswandt B, **Stritt S**. Megakaryocyte rupture for acute platelet needs. *J Cell Biol* 2015; doi: 10.1083/jcb.201504026.

- **Stritt S**, Nieswandt B. *In vitro* platelets in sight. *Blood* 2014; doi: 10.1182/blood-2014-08-592493.

7.3.3. Oral presentations

- How many platelets are required to maintain the vascular integrity in mice. 56th ASH® Annual Meeting and Exposition of the American Society of Hematology at the ICIS Breakfast Meeting, December 5-9, 2014, San Francisco, USA, CA.

- Aberrant microtubule organization and Wiskott-Aldrich syndrome-like defects in platelets and megakaryocytes of profilin1-deficient mice. Platelets 2014, 8th International Symposium in conjunction with Platelets 2014 Educational Course, June 2-6, 2014, Ma'ale Hachamisha, Israel.

- Profilin1 is a regulator of platelet size and microtubule stability. 8th International Symposium organized by the Students of the Graduate School of Life Sciences, October 9-10, 2013, Würzburg, Germany.

- Microthrombocytopenia and impaired platelet integrin function in conditional profilin1-deficient mice XXIVth Congress of the International Society on Thrombosis and Haemostasis (ISTH) and 59th Annual Scientific and Standardization Committee (SSC) Meeting, June 29 to July 4, 2013, Amsterdam, The Netherlands.
  Winner of Young Investigator's Award

7.3.4. Poster presentations

- Impaired platelet production and aberrant microtubule organization in megakaryocyte-specific TRPM7-deficient mice. Cell Biology of Megakaryocytes and Platelets, Gordon Research Conference 2015, April 19-24, 2015, Lucca (Barga), Italy.

- Twinfilin2a is a central regulator of platelet reactivity and turnover. 9th International Symposium organized by the Students of the Graduate School of Life Sciences, October 14-15, 2014, Würzburg, Germany.

- Aberrant microtubule organization and Wiskott-Aldrich syndrome-like defects in platelets and megakaryocytes of profilin1-deficient mice. Platelets 2014, 8th International Symposium in conjunction with Platelets 2014 Educational Course, June 2-6, 2014, Ma'ale Hachamisha, Israel.

- Profilin1 is a regulator of platelet size and microtubule stability. 8th International Symposium organized by the Students of the Graduate School of Life Sciences, October 9-10, 2013, Würzburg, Germany

- Profilin1 plays a critical role in platelet sizing and function. 7th International Symposium organized by the Students of the Graduate School of Life Sciences, October 16-17, 2012, Würzburg, Germany.

7.4. Curriculum Vitae

7.5. Affidavit

I hereby confirm that my thesis entitled “The role of the cytoskeleton in platelet production and the pathogenesis of platelet disorders in humans and mice” is the result of my own work. I did not receive any help or support from commercial consultants. All sources and/or materials applied are listed and specified in the thesis.

Furthermore, I confirm that this thesis has not yet been submitted as part of another examination process neither in identical nor in similar form.

Würzburg, August 2015 _____

Simon Stritt

Eidesstattliche Erklärung

Hiermit erkläre ich an Eides statt, die Dissertation “Die Rolle des Zytoskeletts in der Thrombopoese und der Pathogenese von Thrombozytopathien im Menschen und der Maus” eigenständig, d.h. insbesondere selbständig und ohne Hilfe eines kommerziellen Promotionsberaters, angefertigt und keine anderen als die von mir angegebenen Quellen und Hilfsmittel verwendet zu haben.

Ich erkläre außerdem, dass die Dissertation weder in gleicher noch in ähnlicher Form bereits in einem anderen Prüfungsverfahren vorgelegen hat.

Würzburg, August 2015 _____

Simon Stritt